UNIVERSITÀ DI PARMA

UNIVERSITA' DEGLI STUDI DI PARMA

DOTTORATO DI RICERCA IN

"SCIENZE E TECNOLOGIA DEI MATERIALI"

CICLO XXXVI

ANTIFOULING COATINGS FOR MARINE APPLICATIONS

Coordinatore:
Chiar.mo Prof. Enrico Dalcanale

Tutore:
Chiar.ma Dott.ssa Mariarosa Raimondo

Dottoranda: Maria Caruso

Anni Accademici 2020/2021 – 2022/2023

CONTENT

ABSTRACT

This work has focused on the design and fabrication of superhydrophobic coatings (SHS) and Slippery Liquid Porous Surfaces (SLIPS) for marine applications. The coatings were obtained by deposition of ceramic nanoparticles (Al_2O_3, SiO_2-X) and chemical modification with low surface energy compounds (< 23mN/m). I designed the synthesis of SiO_2 nanoparticles that are inherently superhydrophobic by sol-gel in isopropyl alcohol and ethyl alcohol, respectively with fluorinated and alkyl chains. I characterized nanoparticles in terms of size and Z potential using DLS and ELS technology.

The one-step synthesis has been design the synthesis of flower-like boehmite (Al_2O_3) in hydrothermal route, in an aqueous solution, evaluating the morphology as different reaction conditions.

Two deposition techniques have been explored, dip coating and spray coating. After the deposition of nanoparticles, a heat treatment was necessary. Heat treatment has been optimized for some more sensitive materials such as steel and fiberglass. The proposed coatings involve the combination of a first inorganic layer alumina based, which after boiling water treatment has flower-like structure, and an organic layer is deposited with fluorinated or alkyl functionality. The second type of coating has a layer composed of silica nanoparticles intrinsically superhydrophobic. To obtain a SLIPS type surface it is necessary to infuse a lubricant inside the porosities. Fluorinated lubricating oils, alkanes with long alkyl chains and silicon oils were chosen.

The coatings have been characterized in terms of wettability properties (static contact angle WCA and dynamic contact angle CAH) with water. After I determined the surface morphology with FESEM observation, determining the particle size, coating homogeneity, and thickness.

The superhydrophobic coatings were subjected to cell adhesion test (MTT cell viability assay) and cytotoxicity tests (Actin/DAPI), also evaluating the strength of the superhydrophobic properties after test.

The antifouling properties of the coating was tested with larvae settlement test (no choice assay), and the leaching toxicity of the coatings molecules was evaluated. Finally, the coatings were to the open sea to assess the antifouling qualities under more drastic conditions. Moreover, the durability of the superhydrophobic properties in underwater conditions has been monitored.

Coatings have been designed to reduce wall friction in underwater conditions. The tests were conducted on aluminum panels, suitably microstructured with hierarchical structured and functionalized with fluorine-free compounds. The reduction of wall friction was measured in the cavitational tunnel, evaluating the reduction of wall hydrodynamic force as the water flow speed increased. Hydrodynamic force tests are conducted on surface rotors of a suitably nanostructured and functionalized rheometer for the alternative evaluation of morphological potentials easily applicable in future perspective. The ultimate goal was to find a superhydrophobic coating that combined antifouling and friction reduction properties.

LIST OF ABBREVIATIONS

ACA Advancing Contact Angle

AFM Atomic Force Microscope

APTES 3-aminopropyltriethoxysilane

ATR Attenuated total reflectance

CA Contact Angle

CAH Contact Angle Hysteresis

CRT Control

CVD Chemical vapor deposition

DAPI 4',6-diamidino-2-ylindole, dihydrochloride

DLS Dynamic Light Scattering

DSA drop shape analyzer

EAcAc ethyl acetoacetate

ELS Electrophoretic Light Scattering

Epox Epoxy resin

EPS extracellular Polymer Substance

EtOH ethanol

FAS Fluoroalkylsilane

Fb Fiberglass

FBS Fibroblast

FCRs Foul Release Coatings

FNSW natural seawater filtered

FTIR Fourier Transform Infrared Spectroscopy

HTS Hexadecyltrimethoxysilane

IMO International Marine Organizations

IPA Isopropyl alcohol

iPrOH Isopropyl alcohol

K Krytox

MTES methyl triethoxysilane

MTT 3-(4,5-dimethylthiazol-2-yl)-2,5-diphenyltetrazolium bromide

OTS octadecyltrichlorosilane

PBS Phosphate Buffered Saline

PDI Poly dispersion Index

PFOTS 1H,1H,2H,2H-perfluoroctyltriethoxysilane

PFPE perfluoropolyether

PVC polyvinylchloride

PVD Physics Vapor Deposition

RCA Receding Contact Angle

Ref benchmark

SE surface energy

SEM Scanning Electron Microscope

SHS Superhydrophobic Surface

SLIPS Slippery Liquid Infused Porous Surface

TBT tributyltin

TEOS tetraethyl orthosilicate

TGA Thermo gravimetric analyses

TT thermal treatment

WCA Static Contact Angle

XRD X- ray diffraction

γ_{SG} Surface Energy

1. INTRODUCTION

Surface science, as a specialized subfield of materials science, is primarily concerned with the study and understanding of properties and behavior of material interface when in contact with the surrounding environments in working conditions. Surface science is a complex interdisciplinary field that deals with the chemical and physical interactions that occur at the interface between two or more phases.

In this framework, this thesis deals with the formulations, properties and behavior of thin layers. The dimensional range of thin layers is defined between 1nm to 1µm as shown in Fig.1.

The thin layer is deposited on different substrates of industrial interest looking at the interaction between solid-gas, solid-liquid, solid-vacuum, liquid-gas, etc. As freestanding structures, two-dimensional thin films have advantages over bulk materials due to their large surface to volume ratios, desirable for application requiring enhanced surface interaction.

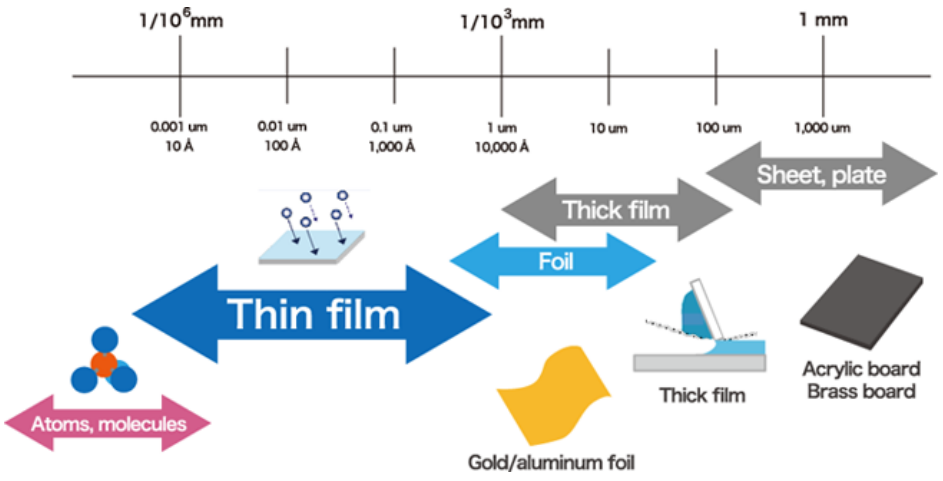

Figure 1 *Thin film thickness range.*

According to the composition of their external surface, thin-layered coated materials have numerous industrial applications, for example, protective coatings against component wearing and tearing phenomena, corrosion, and more generally speaking environmental damages. In the aerospace sector, the surface modification could enable to increase the flight, and safety during take-off/leading operations avoiding ice deposition[1], while in maritime applications to prevent the attack of biological species and limit corrosion in underwater conditions[2,3]. Other tribological effects can be reduced by presence of thin layer, such as reduction of friction[4] between mechanical parts of the surface and the contact medium (water, fluids, air).

Surface modifications allow to make of the same material (the substrate) a new one for specific or wider applications, as mentioned above.

In recent years, advances in characterization techniques allowed a deeper understanding of the role of thin films through the determination of surface chemistry, crystallinity, morphology, and roughness, which brought to the possibility of combining them in the most suitable way for a given application.

1.1 Biomimetic approach to surface modifications

Surface modification through a biomimetic approach has a tremendous development in recent years. Among scientists, the biomimetic approach has played a key role in the design of thin films with innovative properties for industrial purposes. In nature, there is a variety of organisms (plants and animals) that have developed over the centuries exclusive surface properties and features that have allowed their survival. One of the most widespread properties of natural living organisms and plants is their ability to repel water, or other liquid and fluid in a wide range of surface tension 20-73 (mN/m). The best-known example is the repellence of the *Lotus effect*. The lotus flower, belonging to the Nelumbo genus of aquatic plants, is renowned for its consistently pristine and immaculate leaves, even when growing in the typically muddy surroundings. This exceptional state of unsullied perfection is made possible by the remarkable wetting properties of the lotus leaf's surface. Whenever a water droplet falls on the Lotus leaf, it maintains its spherical shape and effortlessly rolls off, leaving no trace of adhesion. In this process, any residual dust or dirt particle residing on the leaf's surface is swept away, leaving the leaf in a state of absolute cleanliness.

The first two researchers observing the peculiar microstructure of the Lotus leaf, and then describing the phenomenon of "superhydrophobicity", were Bartholott and Ehler in 1997. The investigation of the surface morphology of lotus leaves was conducted using a Scanning Electron Microscope (SEM), revealing an intriguing structure (Fig 2). This structure consisted of small protrusions known as papillae, measuring approximately 10-20 µm in height and 10-15 µm in width, evenly distributed across the surface. At higher magnification levels, the superficial papillae exhibit nano-scale epicuticular waxes. As will be elucidated later, this dual-scale, hierarchical structure plays a vital role in conferring the property of water repellency, often referred to as "superhydrophobicity". Furthermore, it is worth noting that the surface waxes are chemically stable and do not engage in any form of chemical interaction with water, in other words, they exhibit low surface energy, which in the second crucial requirement for achieving superhydrophobicity[5].

Another well-known example is the sharkskin, a microstructure that repels water and reduce the skin friction so thus enhancing animal speed in marine environment. The surface micrometer sized features, are interconnected to form a non-smooth surface[6]. In addition, the grooves present on the ribs are parallel to the longitudinal axis of the shark's body and covered with mucus. This conformation reduces friction with water and increases the handling speed[7].

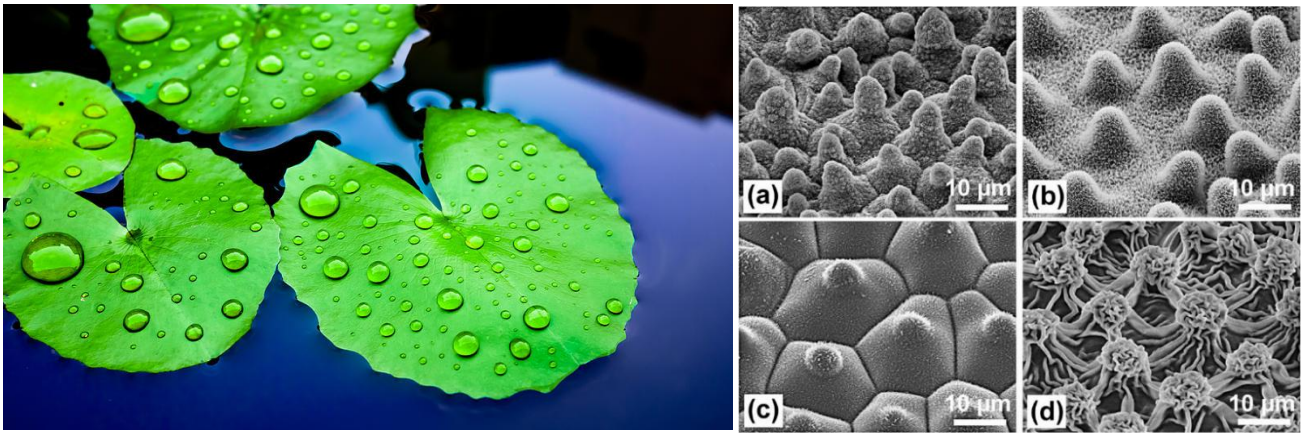

Figure 2 *Lotus leaf and SEM images of the papillose leaf surfaces of Nelumbo Nucifera (Lotus-Leaf)[1].*

Other natural patterns include the gecko's legs, which have more than five thousand setae divided into hundreds of spatulas. This conformation shows superhydrophobicity and high adhesion properties[8].

Butterfly wings present neat grooves and microgrooves side by side on the stairs. This system allows water droplets to easily slide away[9]. However, if droplets slip the opposite way, the drop strongly adheres to the surface. Something similar to the mechanism of the butterfly's wings are the rice leaves, which thanks to grooves allow the directional gliding of water[3]. Other animals and plants, such as caterpillars, loquat leaves, rose petals, etc., all show excellent repellence against water.

Another fascinating biomimetic model that has taken hold for the progress of superhydrophobic synthetic surfaces is given by the carnivorous plant Nepenthes Pitcher (Fig.3). This type of plants covers the surface with a waxy layer that plays an important role in catching insects. The mechanism of the Nepenthes launcher inspired many researchers such as Wong et al[10], who propose a porous structure in which a liquid, immiscible with the liquid to be repelled, is infused to replace the air inside the pores. These infused surfaces named SLIPS (Slippery Liquid Infused Porous Surfaces) have been proposed for severe environments (high pressure, temperature, and humidity) in which the Lotus leaf based materials failed. The principle of building slippery surfaces is very simple consisting in the infusion of a liquid on a porous superhydrophobic under-layer surface.

The liquid to be infused must have the following properties: the liquid must enter the cavities due to the roughness of the surfaces, the liquid must be chemically compatible with the layer of low surface energy deposited previously, and finally must not be miscible with the liquid to be rejected[10].

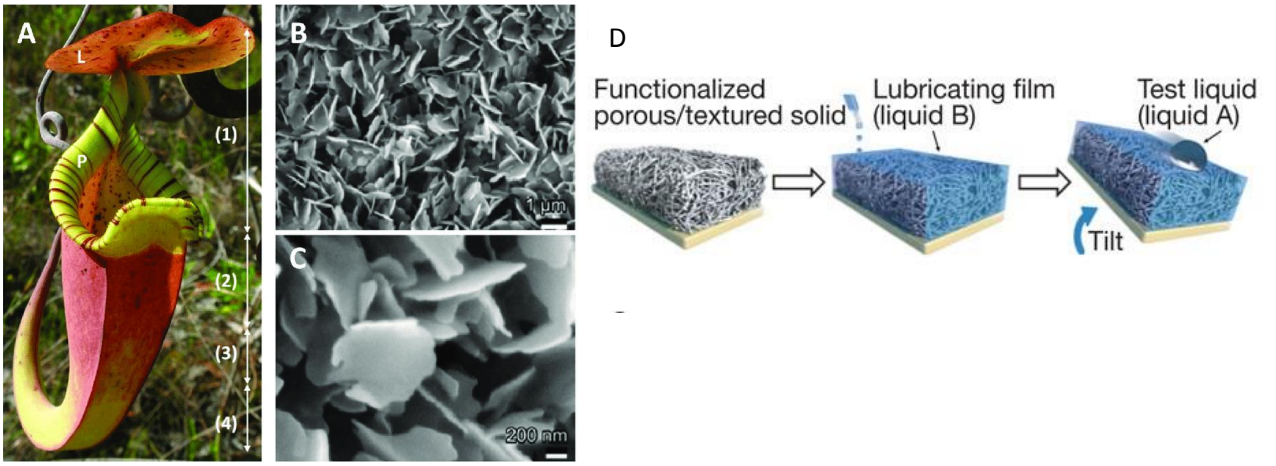

Figure 3 *A) Nepenthes Pitcher plant B) Scanning electron microscopy of the upper wax layer C) Scanning electron microscopy of wax crystal of the upper wax layer[8] D) Scheme of the fabrications of a SLIPS surfaces devised by Wong et al.[7]*

The biomimetic models mentioned above acted as inspiration tools for this thesis work. In particular, the research work of this thesis has taken inspiration from two natural models of Lotus leaf and SLIPS surfaces. There are several techniques for the fabrication of wettability-controlled surfaces; however, it is necessary to have control over the structure and morphology. Two approaches can be distinguished: the first is the surface modification of an intrinsically hydrophobic material. The second is based on the deposition of a coating by modifying the morphology and/or chemical composition. Several deposition techniques distinguish themselves for their simplicity of application, versatility across surfaces of all sizes, and absolute control over morphology. Among the most used techniques for the deposition of coatings are: chemical and physical vapor deposition (CVD and PVD)[11,12], plasma [13], sol-gel coating[14–16], layer-by-layer [17,18], and self-assembled monolayer[19]. In addition to those listed, there are numerous other techniques; and it is possible to combine several techniques to obtain superhydrophobic coatings.

1.2 Fouling phenomena in marine environment

The marine environment has a high degree of complexity due to the simultaneous presence of a multitude of microorganisms and chemical species involved in an enormous number of chemical processes. The fouling phenomenon is promoted by the organisms present in a given habitat and depends on the substratum, geographical location, season, and other factors including competition and predation.

In general, the marine environment is a highly aggressive environment, where surfaces are subject to multiple degradation phenomena, including microbiologically affected corrosion (MIC) and degradation resulting from biofouling adhesion and growth[20]. The phenomenon known as marine biofouling occurs because of the settlement and growth of microorganisms, plants, and animals. Various fouling organisms easily attach to ships, oil platforms, and breeding facilities in the ocean[2]. Fouling adhesion leads to an increase in the weight of hulls or other components (including propulsion systems) as well as significant changes in surface topography (roughness). This results in increasing wall friction with subsequent negative effects on navigation speed, fuel consumption, cleaning, and maintenance operation, harmful chemicals, and prolonged navigation stops[21–23]. The same negative effects of fouling accumulation offshore platforms leads to the obstruction of drainage pipes, posing threats to the safety and service life of marine facilities. As the human marine economy continues to expand, the economic losses attributable to marine fouling organisms are increasing. Consequently, there is growing attention towards developing effective and economically viable prevention methods[24].

Figure 4 *Hull surface fouling process and main fouling organisms.*

The process of fouling accumulation is typically divided into several steps, which contribute to making this process difficult for future prevention (Fig.4):

- **Conditioned film**: when a substrate is immersed in seawater, film formation occurs through the adsorption of organic such as proteins, polysaccharides, proteoglycans, and inorganic molecules. This thin film reduces the surface energy of the substrate, thus achieving a new state of equilibrium. The adsorption process is reversible and promoted by various physical forces: including hydrogen bonding, electrostatic, and Van der Waals forces. Generally, the resulting film is a negatively charged protein film with high adhesion.

The conditioned film is crucial as it provides the necessary conditions for microorganisms to adhere to the substrate[25].

- **Biofilm:** in the presence of the conditioned film, bacteria, and diatoms present in seawater tend to adhere to the substrate even if, during the adhesion process, some microorganisms may detach due to the shearing forces exerted by the seawater. The stage of biofilm formation is unstable as the interactions between the microorganisms and the conditioned film are dynamic and evolving. Acting forces at play, including adhesion and detachment, contribute to the ever-changing and transitional nature of the biofilm.
- **Micro fouling**: in the early stages of biofilm formation, bacteria and microorganisms on the substrate's surface establish robust adhesion and undergo rapid reproduction. These microorganisms secrete extracellular polymeric substances that facilitate their attachment to the conditioned membrane, obtaining a stable biofilm. The formation of biofilm is a pivotal event and a significant concern in the context of marine fouling. The stability and persistence of the biofilm contribute to the challenges associated with marine fouling, emphasizing the relevance of understanding and managing this process.
- **Macro fouling**: as micro-pollution continues to grow, the variety of species adhering to the membrane surface expands. Simultaneously, because of the cutting forces in the ocean, a dynamic balance between attachment and detachment is achieved. Larvae of larger fouling organisms, suspended in seawater, encounter the biofilm. When contact occurs organisms bind chemically and, mechanically with the biofilm. This interaction firmly secures them to the biofilm, resulting in the formation of a biofouling community. The amalgamation of different organisms of the biofouling community characterizes the macro-fouling phase[26,27].

It is misleading to assume that the colonization of a surface implies a direct causal relationship among different stages as well. To assume that controlling or blocking the initial colonization stages will certainly lead to the reduction or elimination of macrofouling[28]. To identify fouling prevention strategies, studies must focus on the mechanisms of adhesion of various organisms. The adhesion process of bacteria is intricate and dynamic, influenced by many factors, including, the specific bacteria species, its shape and size, and the chemical and physical composition of the bacterial surface. The combination of all these factors means that we have to face up a multifaceted phenomenon that varies across bacterial types and environmental conditions. Understanding these factors is essential for comprehending bacterial adhesion and its implications, especially when biofilm and marine fouling are concerned.

In addition, bacteria play a crucial role in producing the Extracellular substrates of the Polymer Substance (EPS). These EPS substrates contain nutrients that help both the initial attack and the subsequent growth. Once attached to the surface, microorganisms continue to produce EPS substrate, thereby contributing to the ongoing development of the biofilm. This ongoing production and accumulation of EPS substrate can exacerbate fouling and its associated challenges[29]. In both static and dynamic marine environments, fouling organisms employ the secretion of macromolecular-binding polymers to adhere to surfaces effectively. Thus, antifouling strategies should aim to reduce the molecular adhesion of microorganisms or at least, inhibit their action their molecular adhesion. According to the current state of the art, the achievement of efficient antifouling materials involves synergistic approaches combining both chemical and physical elements. On one hand, the antifouling agent has to work by disrupting the binding ability of the polymers secreted by fouling organisms inhibiting their formation altogether. On the other hand, tuning the coating's surface energy and their structural organization at different dimensions (micro-nanostructure) can additionally deter fouling by making the surface less attractive or challenging for fouling organisms to adhere to. By integrating chemical agents, tailored surface properties, and dimensional features at different levels, antifouling strategies can be optimized for higher efficiency, ultimately mitigating fouling in marine environments[28].

1.3 Antifouling strategies

Over time, antifouling strategies have been improved, approaching the problem from different points of view including the removal process, electrochemical methods, and anti-fouling coatings.

Several strategies have been used to mitigate the effects of marine biofouling. These approaches can prevent and/or delay the development of biofilm and the attack of macrofoulers or even eliminate them; Figure 5 illustrates three different strategies for these new methods of prevention/elimination with of fouling with the use of coating with specific characteristics. A range of criteria should be evaluated to select the most suitable marine antifouling strategy, including effectiveness, safety, and biosecurity, compatibility with the materials of devices (equipment and feasibility).

Over the centuries, the research analyzed different types of treatment and coating typologies that can prevent the attack and accumulation of marine organisms. The antifouling strategies adopted to try to limit these phenomena can be summarized on three principal levels:

- Prevention of the attack on exposed surfaces of organisms that cause biofouling (fouling resistant).
- Reduction of biofilm adhesion strength (fouling release).
- Biocidal actions against the responsible organisms (fouling decrease).

Figure 5 *Schematic illustration of three principal antifouling strategies 1) fouling resistant, 2) fouling release and 3) fouling degrading [30].*

Several strategies have been found over time for the removal and prevention of hull, initially using a mixture of natural minerals and natural resin to wrap the hull of ship or manually remove hull [31,32].

Anti-fouling coatings

An anti-fouling coating is a specialized paint formulation designed to hinder the attachment and proliferation of biofouling organisms on the surface where it is applied. These coatings play a crucial role in minimizing the likelihood of exotic marine species settling and spreading. The maritime industry commonly employs two primary categories of anti-fouling coating: biocidal anti-fouling coatings and non-biocidal foul release coatings. Both varieties are designed to avoid or prevent the attachment and persistence of biofouling organisms on submerged surfaces. However, their optimal performance relies on appropriate vessel speed, above all, and their effectiveness diminishes over time[33].

Biocidal anti-fouling coatings

For many years, the identification and deposition of treatments with biocidal action have been the most widespread routes.

These are characterized by the use of paints, whose antifouling activity is attributable to the presence of active ingredients capable of killing with different mechanisms (attack of the respiratory centers, breakdown of the cell wall, etc.) the microorganisms responsible for this phenomenon.

The effectiveness of these paints is determined by the concentration of the active ingredient and the duration of the biocidal effect, which turn is regulated by the release of the active chemical species. Biocidal compounds that contain lead, arsenic, mercury, or organic derivatives were previously used in paint products, but now they are prohibited due to their significant environmental impact.

In the 1950s, much attention was paid to tributyltin (TBT) as an effective biocide whose activity was very similar to that of heavy metals. The broader utilization of self-cleaning coatings in the marine environment started in the 1970s and, introduced hydrolyzable formulations based on acrylic or methacrylic copolymers. These products loaded with TBT can reduce surface roughness and ensure the release rate control (leaching) of the biocidal product. The percentage of release is controlled by the consumption of the resin in which it is contained by hydrolysis, which in turn depends on the composition of the chains of resin[34,35]. International Maritime Organizations (IMO) later banned the use of TBT in 2003 due to the bioaccumulation of tin and subsequent malformations detected in many species in the marine ecosystem. In addition, UV or bacterial-induced degradation of TBT in the environment gives rise to hydrolysis products that cause serious environmental damage[36]. The ban on the use of TBT has triggered the search for innovative antifouling solutions for the marine industry with lower environmental impact. Copper and zinc were selected as excellent alternatives to tin-based compounds, whether in metal forms, alloy, or oxide, the latter in both metallic and alloy or oxide forms. To improve the durability of these metal-based coatings, due to a non-controlling dissolution of these, they have been added in the formulation of organic compounds based on nitrogen, halogens, aromatics, carbamates, phenol, amines, and phosphorous compounds. The inclusion of these boosters counteracts the growth of algae as organic compounds [2]. Among the best-known copper-based biocides are Irgarol 1051, TMCS-pyridine, and DCOIT 211, which, however, over time have caused accumulation phenomena in the harbor, resulting in toxicity related to high concentrations that interfere with algae photosystems.

To overcome the limitations associated with the use of biocidal paints, the scientific community and the marine and shipping industry have shared efforts in search of solutions to reduce the impact of biofouling.

Non-biocidal and non-toxic antifouling solution

Foul-release coatings (FCRs) are non-biocidal and possess surface properties that minimize the adhesion of biofouling organisms while facilitating their removal through water flow[33,37]. The surface of FCRs is characterized by smoothness and low friction coefficient attributed to their low surface energy. Materials surface energy plays a key role in the colonization process, where lower surface energy diminishes the adhesion strength of fouling organisms[38]. The relationship between surface-free energy and surface adhesion has been well established and is often represented by the Baier curve, as described in various studies. This curve illustrates the optimal resistance to fouling organisms at a surface energy range of 22-24 mN/m (Fig 6). At this range, fouling organisms exhibit the lowest adhesion to the substrate surface. Baier was one of the pioneering researchers to investigate this relationship and introduced the well-known "Baier curve" to describe the relationship between surface energy and relative adhesion[39]. In turn, surface free energy depends on chemical composition and can be considered a key indicator of wettability changes. Generally, a surface with high free energy demonstrates good wetting ability, while a surface with low energy exhibits poor wetting ability. In terms of resisting biofouling, the prevailing theory correlates the strength of surface reaction to free energy. Coatings with low interfacial energy minimize adhesion strength between foul organisms and the substrate. This reduction in adhesion strength allows for the removal of organism settlements through hydrodynamic stress during navigation or via straightforward mechanical cleaning. Achieving coatings with specific interfacial properties within the range outlined by the Baier curve is instrumental in creating effective antifouling strategies in relation to the surface energy of the new coating formulation[39].

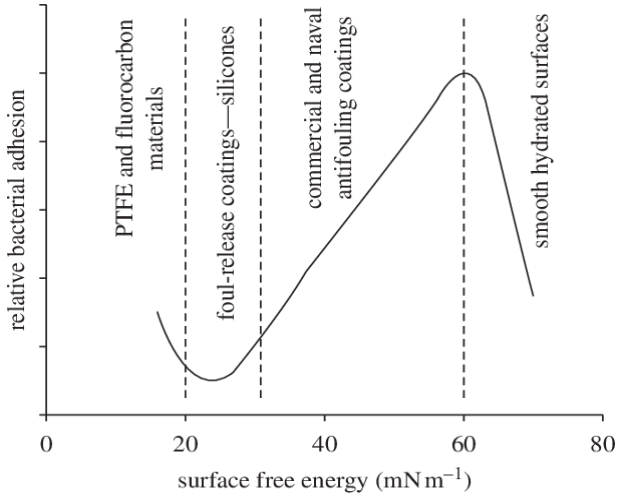

Figure 6 *Relationship between surface free energy and surface adhesion[40].*

Fluoropolymers and silicone elastomers are the most commonly used compounds in FCRs to achieve these desired surface properties, albeit with differing foul release mechanisms. The International Maritime Organization (IMO) has approved various commercial FCR products that are available on the international market. Notable examples include silicon-based coating such as Intersleek® 700, Sealion® and Bioclean®, fluoropolymer-based coating like Intersleek® 800, hybrid coating exemplified by Phasecoat® UFR, and hydrogels silicon coating like Hempasil® X3. Silicone based FRCs, characterized by thicker layers, allow for a more efficient pelleting action of the silicone away from marine adhesive. Researchers have also worked on developing hybrid silicone-based FRCs to improve durability and adhesion[2]. For instance, they have incorporated nanofillers, modified silicone matrix components such as polyurethane and epoxy resin, utilized the sol-gel process, introduced hydrogels, fluorinated segments, or incorporated biocides into the coating materials.

The microstructure of a surface indeed plays a critical role in resisting the adhesion of fouling organisms, as supported by various studies[41,42]. Research has demonstrated that microstructures with specific characteristics such as appropriate size, shape, height, spacing, and other relevant factors can effectively inhibit the adhesion of fouling organisms. These microstructures can disrupt the settling and attachment mechanisms of fouling organisms, making the surface less favorable for adhesion. By engineering surfaces with tailored microstructure, it becomes possible to create antifouling surfaces that actively deter fouling organism adhesion. The microstructures can create physical barriers on unfavorable surface conditions, reducing the ability of fouling organisms to firmly attach and grow on the surface. This approach, often referred to as “topography-based antifouling “ is a promising strategy in the field of antifouling coatings and materials[43]. In particular, materials with a hierarchical ceramic-like structure consisting of an inorganic-organic hybrid matrix are proposed. The inorganic coating is composed of ceramic nanoparticles synthesized by sol-gel route. The sol-gel coating process is of interest and it is conducted at low temperature; in addition, the coatings exhibit high biocompatibility making them particular effective for corrosion prevention for metal surfaces[44–46].

In recent years, numerous papers have been published investigating the potential of superhydrophobic surfaces in both reducing biofilm formation[3,47] and decreasing frictional resistance under laminar and turbulent flow condition[48,49].

Natural mechanisms serve as the foundation for biomimetic “bioinspired” coatings, with a primary focus on designs inspired by topographical features[50]. Many marine animals, from mollusk shells to the skin of sharks[51] and whales, exhibits intricate surface topography. Drawing inspiration from the “self-cleaning” Lotus-leaf effects. These ideas have supported research into various bioinspired surface designs, with the most prominent ones for marine applications being those that emulate biomimetic surfaces.

An alternative approach in the pursuit of non-toxic anti-fouling solutions involves the engineering of surface topography to hinder the attachment of fouling organisms or weaken their attachment strength. According to a recent review[52], surfaces with a hierarchical organization when compared to regular geometric features are the most effective solution to fight biofouling.

Many plants and animals in nature have evolved effective antifouling mechanisms to adapt to their environments, exhibiting excellent antifouling effects[53,54]. Lack of microorganisms at the surface results from the combination of topography and surface energy as the most relevant variables. It has been theorized by Schumacher et al[55] how different geometric structures affect the settlement of organisms. The hypothesis is that certain topography creates stress on the cell membrane and prevents initial contacts for settlement. In nature, one notable example is the Lotus plant, which grows in muddy riverbeds. The leaves of the Lotus plant possess remarkable self-cleaning properties, which have been revered and associated with purity since ancient times. This self-cleaning phenomenon known as the “Lotus effect” was carefully understood in the 1970s. The Lotus leaf’s surface is covered with tiny papillae and a layer of wax, creating a hydrophobic and non-absorbent surface. When the rain falls on the Lotus leaf, the water drops assume an almost perfect spherical shape thanks to the high value of the surface tension (73 mN/m). With a slight tilt of the leaf, these water droplets roll, picking up dust and debris, effectively achieving a self-cleaning effect. In recent years, numerous studies have aimed to replicate the self-cleaning properties of the lotus leaf[56–58].

Looking at potential application one of the most critical aspects is that under severe environmental conditions, the structure and surface chemistry are preserved, ensuring, for example, that the stability of the Cassie-Baxter state, remains immobilized within the nanometer cavities. In the underwater environment, the pressure exerted by the liquid can undermine the stability of the coatings to the point of complete degradation with water penetration inside the cavities. Research is constantly searching to overcome these limitations, searching for new formulations able to preserve their liquid-repellent properties even in extremely severe environmental conditions. In 2011, the so-called SLIPS[10] (Slippery Liquid-Infused Porous Surfaces) was first formulated.

The approach for generating SLIPS remains a biomimetic approach, which borrows the anti-adhesion and high-slippery mechanisms of some carnivorous plants such as the Nepenthes plant. SLIPS-type coatings consist of a porous matrix (often nanometer-sized) in whose cavities air pockets are replaced by a low surface tension, water-immiscible liquid that is infused during the manufacturing process. If the surface is properly designed, the infused liquid, whose role is in effect that of a lubricant, forms a homogenous layer on the surface, and by capillary effect, the liquid remains trapped in the cavity. The stability and durability of materials with coatings obtained by SLIPS approach have been the subject of many studies that in recent years have allowed their performance to be optimized even in environments where coating obtained by Lotus leaf based approach had failed. The most recent literature on the subject points to SLIPS coatings as the best solution for applications in marine environments, even when pressures become significant. Another aspect to be emphasized is the self-repair (self-healing) capability of SLIPS coatings: since the working interface is a “liquid” surface, the optimized viscosity value allows its spontaneous resetting on any damaged areas. The lubricant to be infused can be chosen from a wide range of solutions with different viscosities and surface tensions, which makes it possible to greatly expand the types of liquid/fluid toward which repellency is manifested. It is possible, for example, to design SLIPS coatings with superhydrophobic or even omniphobic (repellency of all polar and apolar liquids at different surface tension) behavior. When properly designed, the coatings show outstanding anti-adhesion properties, even against complex mixtures with significant solid loadings. To date, there are many articles available in the literature reporting the antifouling properties of SLIPS in the marine environment[59] as well as their ability to reduce frictional resistance[60,61].

Mechanical system for fouling removal

Various biofouling treatments have been employed, including thermal stress, osmotic shock, deoxygenation, UV and laser radiation, and hydrodynamic and acoustic cavitation[62–64]. The most common cleaning technologies include brushing, scraping, pressure cleaning with water/air jetting, or mechanical cleaning using wipers[62,63,65–67]. For instance cavitation technology, despite its dependence on surface material properties, liquid temperature, and tool distance, generally results in lower surface damage compared to brush-based method. Cleaning boats, ships, and other movable marine equipment can be carried out either in dry-dock or using in water cleaning technologies. In water, biofouling approaches may be cost effective but can pose higher chemical contamination and biosecurity risks, potentially increasing recolonization or surrounding surfaces[68]. Specific biofouling treatment methods include:

- UV- radiation: mainly used for sterilization treated water, it is effective against bacterial and planktonic fouling. However, it is more suitable as a pre-treatment and enhances the efficiency of biocides. Low maintenance is required.
- Acoustic energy (ultrasonic): pulsed acoustic energy inhibits biofilm formation and may prevent fouling species settlement in internal seawater system. However, its applicability is limited, and installation of ultrasonic treatment system is expensive.
- Low-level laser: laser irradiation in water can cause the dead of cells, but is not effective against established biofouling. It requires additional treatment for surviving organisms.
- Mechanical technologies: involve the removal of biofilm organisms from hull surfaces. Available mechanical cleaning solutions include:
    - Brushes/ abrasive pads or blades: handheld powered tools with brushes and pads can remove heavy fouling but may damage coatings. Rotating brushes are effective against soft/ erect fouling but not hard calcareous.
    - High pressure and cavitating water jets: divers can control jet direction, and water blasting efficiently removes biofouling organisms. Cavitating water jets incorporate microscopic air and bubbles, creating localized shear stress. However, inappropriate pressure or angle application may damage antifouling coatings.

2. OBJECTIVE OF THIS THESIS

During the Ph.D., The main focus was to obtain hybrid sol-gel coatings acquired from alumina and silica nanoparticles functionalized with different properties. The main goal is to carry superhydrophobic coatings with a single deposition process that have antifouling properties and are not hazardous to the environment. Two different biomimetic approaches inspired by the Lotus leaf and the carnivorous plant Nepenthes Pitcher were used, namely superhydrophobic surfaces (SHS) and Slippery Porous Surfaces (SLIPS). To modify a surface in a physic-chemical way it is necessary to start from a synthesis of nanoparticles, in particular, nanoparticles of alumina sol-gel previously optimized, and subsequently a designed synthesis of silica nanoparticles functionalized with silanes with different functional groups. Obtaining superhydrophobic coating with antifouling purposes will be designed in the literature, a further focus on fluorine-free proposal with functionalization of nanoparticles with organic compounds. The particles were characterized in terms of size distribution by Dynamic Light Scattering and Z-potential and were deposited on different substrates for dip coating and spray coating. For each type of substrate and coating selected, it is necessary to optimize the deposition parameters of the coating and its heat treatment, and at the end, Scanning Electron Microscopy (SEM) characterized the quality of the coating. To achieve super-hydrophobicity in the inorganic coating of nanoparticles, the first step was to modify the coating with low surface energy chemical compounds. Commercial fluoroalkylsilane (FAS) and long alkyl chain silane have been applied with dip-coating and spray-coating techniques.

The final goal is however, the design of a nanoparticle synthesis that gives a nanostructure to the coating with low surface energy. In this way, you will get a super hydrophobic coating with only one deposition process. The surfaces were then analyzed for their wettability properties, with a focus on assessing Water Contact Angle (WCA) and Contact Angle Hysteresis (CAH). Superhydrophobic surfaces have found widespread application in various industrial fields, with a particular focus on their antifouling properties.

Notably, in recent years, these surfaces have emerged as promising alternatives in the marine environment, aiming to replace the use of biocidal paints. While biocidal paints offer exceptional antifouling properties, they also carry significant environmental implications. The fundamental principle underlying the antifouling action of a superhydrophobic coating is elegantly straightforward: by preventing direct contact with water-containing marine microorganisms, it effectively averts surface degradation, thus preventing their subsequent growth. Wherefore, it is imperative to ensure a consistent and enduring performance of the coating, as it is subjected to the continuous movement of the surrounding water in which it is immersed. When using superhydrophobic surfaces for antifouling purposes, it is crucial to ensure three key aspects: long-term performance, ease of reapplying the coating once its properties are lost, and environmental safety, meaning that the release of substances from the coating does not harm marine fauna. In this study, we aimed to optimize the parameters for achieving superhydrophobic surfaces that ensure these three aspects. Initially, we conducted a preliminary assessment of the anti-adhesion properties of the proposed coating by evaluating their effectiveness against cellular-type organisms. Then, we subjected the coatings to direct evaluation using microorganisms. Finally, we tested them in a real marine environment.

In the initial phase, cell adhesion tests were performed using a murine fibroblast cell model. MTT cell viability assay was utilized for cytocompatibility tests. The samples were analyzed under the fluorescence microscope to confirm that the cells did not adhere to the modified surfaces.

In collaboration with the IAS-CNR Institute on Genoa, we evaluated the antifouling properties of the designed coatings. Specifically, we conducted a settlement test using "*Cypris*" larvae of *Amphibalanus Amphrite*. Subsequently, we conducted a raft test, subjecting the coatings to the marine environment for several months. Finally, we confirmed the coating's non-toxic nature through release tests.

Antifouling properties are not the sole consideration for materials intended for underwater application. Given the exposure to harsh underwater environments, the longevity of the coating is a crucial factor. Consequently, we evaluated the coatings in terms of wettability after having subjected them to static and dynamic immersion in seawater.

3. WETTING MODELS

Thomas Young conducted one of the earliest investigations into the wetting process of solid using a simple model to describe the equilibrium condition of a liquid droplet on ideal solid surfaces. However, he did not formalize his theory. The formulation of the Young equation (Eq.1), in fact, was fist accomplished by Gauss in 1830[69].

$$cos\theta = \frac{\gamma_{SG} - \gamma_{SL}}{\gamma_{LG}} \quad \text{[Eq.1]}$$

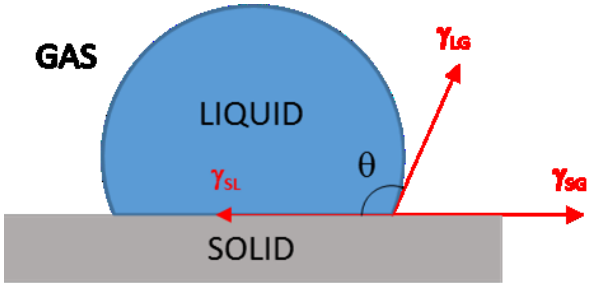

Figure 7 *Diagram of the forces at the three-phase contact line of a liquid droplet on a solid.*

When droplet is deposited on a solid surface the contact angle ϑ is defined as the angle formed by the tangent to the liquid gas interface at the three phase contactline[70] (Fig.7). The wetting of the solid surfaces the liquid (water) can be categorized according to their angles. Referring to water as liquid, when ϑ< 90°, the surfaces is defined hydrophilic, whereas if ϑ>90° it is labeled as hydrophobic. Among each region, there are specific ranges for static contact angle to differentiate between general and extreme wetting conditions.

Figure 7 illustrate the forces that contribute to determining the contact angle ϑ. γ_{SL} denotes the interfacial tension between the solid and liquid phases, γ_{LG} represent the interfacial tension between the liquid and gas phases (also referred to as the liquid's surface tension), and γ_{SG} is the interfacial tension between the solid and gas phases (solid's surface energy). These forces intersect at the three-phase contact line.

Validity of Young's equation is limited to a smooth, chemically homogeneous, non-reactive flat surface. Although real surfaces are not ideal, Young's equation provides a basic understanding of the relationships between static contact angle and interfacial surface tensions.

For the rough real-world surface, two main wetting regimes are considered throughout the literature namely the Wenzel and Cassie Baxter ones. In the Wenzel regime, liquid droplet moves inside the surfaces roughness and the real surface area increases due to roughness, as shown in the Figure 8. Consequently, the actual interfacial area between the solid and liquid medium is much higher than the apparent geometric contact area, which makes the surface hydrophobicity level to increase compared to a smooth surface. The apparent contact angle (ϑ_{app}) was then proposed. While investigating the wetting characteristics of textiles, Wenzel[71] estimated that, in rough surfaces, the solid-liquid interfacial area is increased by a roughness factor r, defined as the ratio between the actual contact area and geometric one (Fig.8). Such situation is defined as Wenzel wetting state and the relative Wenzel equation [Eq. 2] is:

$$cos\theta_W = r \times cos\theta \text{ [Eq 2]}$$

The Wenzel equation underscores how surface roughness can intensify its wetting behavior.

For instance, a hydrophilic smooth surface experiences a heightened degree of hydrophilicity when its roughness is increased.

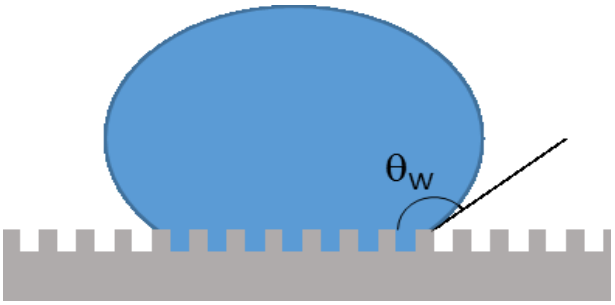

Figure 8 *Sketch of water drop resting on a rough surface in Wenzel wetting state.*

This means that the observable contact angle (ϑ_{app}), which represents the angle perceived at a macroscopic level, will be smaller than the contact angle ϑ of an equivalently smooth surface made of the same material. Conversely, a hydrophobic material can increase its ϑ_{app} by introducing roughness to its surface. Typically, smooth surfaces tend not to exhibit angle higher than 120°. Through surface roughening, ϑ_{app} can exceeds 150°, which corresponds to the conventional threshold for superhydrophobicity.

When a surface possesses the appropriate morphology and chemical composition, water finds it challenge to infiltrate surface irregularities. Instead, pockets of air are retained, resulting in the formation of combined interface involving liquid, solid and, air (in Fig.9). This phenomenon becomes particularly evident on porous surfaces. Cassie and Baxter[72] delineated this particular interface using the subsequent equation:

$$cos\theta_{CB} = f_1 cos\theta_1 + f_2 cos\theta_2 \text{ [Eq. 3]}$$

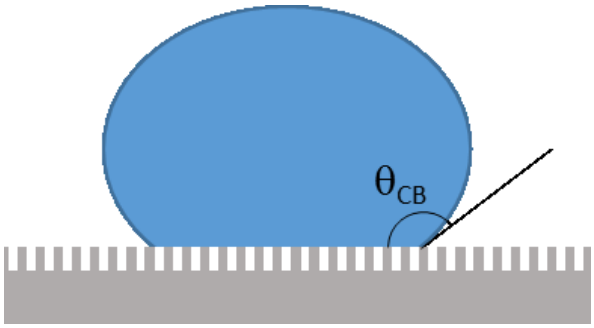

Figure 9 *Sketch of a liquid drop resting on a rough surface in Cassie-Baxter wetting state.*

In the equation, f_1 and f_2 correspond to the surface fractions with phase 1 and phase 2 respectively. ϑ_1 and $\vartheta 2$ denote the contact angles (as determinate by the Young equation) of the liquid on phase 1 and phase 2. If phase represents the solid while phase 2 is air, then ϑ_2 =180°. Moreover, when no other phase is present and the interfaces are flat[73]. It follows that f_2 =1- f_1. Therefore, Cassie-Baxter equation becomes:

$$cos\vartheta_{CB} = f(1 + cos\vartheta) - 1 \text{ [Eq. 4]}$$

As per Cassie-Baxter equation [Eq.4], the smaller the value of f, the larger the value of ϑ_{CB}.

For f→ 0, the surface will have ϑ_{CB}→ 180°. Drops in Cassie-Baxter state usually display very high $\vartheta_{app.}$

Both the Wenzel and Cassie-Baxter models exhibit certain limitation. For instance, the Cassie-Baxter model assumes a level liquid-gas interface beneath the drop. However Herminghaus[74] introduce adjustments that factor in small-scale roughness overlaying the surface structure. This correction is useful to explain the wetting behavior of hierarchically structured surface. The description of the model in a surface with micro and nanometric roughness (hierarchical type) can be more difficult than a mono-layer[75]. In fact Milne and Amirfazil[73] are suggested to use the Cassie-Baxter original form because of the surface morphological characteristics do not allow the planarity mentioned in the previous equation, which the sum of the area fraction f_1 and f_2 is greater than or equal to 1. This non-planarity is due to surface asperities, spikes, high hydrostatic pressure and partial penetration of the liquid in the features of the morphology.

$$cos\vartheta_{CB} = f_1 cos\vartheta_1 - f_2 \text{ [Eq 5]}$$

Gao and McCarthy describe the shape of the drop according to the shape of the porosity of the surface[75] also depending on the strength of the tension of the surface with the contact line[76], rather than contact area. However, Wenzel and Cassie-Baxter models remain the most widely used ones for the description of wetting behavior solid surface.

4. SOL-GEL SYNTHESIS OF NANOPARTICLES

The sol-gel process is a widely used approach for the production of highly pure materials for powders, fiber, films and monoliths. It is very versatile and scalable process used in industry for the production of inorganic materials. The sol-gel technique offers many advantages, such as control over composition, surface area, porosity and particle size. In addition, a process occurs at room temperature and atmospheric pressure. The process is divided into two phases, the first called “sol” is the formation of a colloidal suspension in which the nanoparticles are dispersed in a solvent, and the second phase “gel” bonds are formed between the particles by the removal of a molecule thus forming the desired product.

A colloid is a suspension in which the dispersed phase is so small (1-1000nm) that gravitational forces are negligible and interactions are dominated by short forces, such as Van Der Waals attraction and surface charges. A sol is a colloidal suspension of solid particles in a liquid[77]. Sol ceramic oxides are obtained from different precursor, inorganic and organic, The typical precursor for sol-gel synthesis is alkoxide $M(OR)_x$, where M is metal or metalloid and OR is an alkoxy ligand.

Metal alkoxides are popular precursors because they react readily with water. The reaction is called hydrolysis, because a hydroxyl ion becomes attached to metal atom, as in the following reaction:

$$M(OR)_x + H_2O \rightarrow M(OR)_{z-1}(OH) + ROH$$

This reaction catalyzed by acid[78] or basic[79] compounds. After hydrolysis, condensation reactions lead to form of M-O-M bonds and either a water or an alcohol molecule. Indeed, condensation is a polymerization reaction, whose product is a macromolecule:

$$M(OR)_{Z-1}(OH) + M(OR)_Z \rightarrow (RO)_{Z-1}M\text{-}O\text{-}M(OR)_{Z-1} + ROH$$

$$2M(OR)_{Z-1}(OH) \rightarrow (RO)_{Z-1}M\text{-}O\text{-}M(OR)_{Z-1} + H_2O$$

Condensations reaction can continue until are hydrolysable OR groups accessible.

As a macromolecule grows to a macroscopic size a transition from a sol state to a gel state takes place[80]. In a gel, the solid phase established continuity and encases a continuous liquid phase. Gelation can also result from the attractive dispersion forces among suspended particles, causing them to coalesce into a network- like structure. Moreover, depositing a sol onto a surface and then swiftly evaporating the solvent can lead to the formation of a gel film. The duration of gelation is influenced by factors including pH and other parameters.

Even following the process of gelation, hydrolysis and condensation reactions persist, involving the sol phase that remains confined within the continuous gel phase. This ongoing process is referred to as ageing. Simultaneously, the liquid phase undergoes evaporation, which leads to shrinkage and the concurrent development of elevated capillary pressures. Sol-gel syntheses are extensively employed in ceramic materials science due to their simplicity, non-demanding conditions, and their capacity to yield materials with distinctive attributes. Among the common oxides generated through sol-gel processes, silica (SiO_2)[81,82] , alumina (Al_2O_3)[83,84] and titanium oxide (TiO_2)[79,85], and numerous other oxides stand out[86,87]. The versatility of sol-gel methods allow for the creation of a wide range of oxide based materials with unique properties, making them invaluable in various applications within the field of material science[14,88].

The synthesized suspensions are stable over time so that there is no excessive waste of material, and the suspensions can be reused several times. Suspension are monitored over time by DLS technique. Once the particle diameter of the aged suspension is much larger than that of newly synthesized suspension (>50 nm) homogenization of the deposited film is not guaranteed.

My research group has focused over the year on the development of alumina based film, starting from sol-gel synthesis to coating optimization on different substrate[15,89]. However, silica-based nanoparticles are of interest; the replacement of its hydroxyl groups by alkyl chain with different end groups creates a new system with different wettability characteristics from silica as is[82,90,91]. In this way, it is possible in one-step to achieve superhydrophobicity performance that we require.

4.1 Alumina nanoparticles

The first sol-gel synthesis was on alcohol based one, with isopropyl alcohol (*iP*rOH) as solvent. The procedure was inspired by the work from Minami et al [83]. The synthesis is reported published by my group in 2015 [15].

The precursor was aluminum tri-sec-butoxide Al (O-*sec*-Bu)$_3$. Typically used as a precursor to sol-gel synthesis as it leads to a pure end result[83]. However, it is extremely sensitive to atmospheric humidity and immediately form Al(OH)$_3$ when exposed to air. Therefore, the presence of a ligand is necessary to stabilize it and allow for a controlled hydrolysis.

A chelating agent must be used to promote the stability of the alkoxide in the solvent. Excellent for aqueous or alcoholic media is ethyl acetoacetate. The chelating agent complexes the aluminum forming an extremely stable compound[92], this process slows the rate of hydrolysis but makes the complex still soluble in the solvent[93,94].

The EAcAc: Al ratio determines the size of the nanoparticles. Specifically, the higher the ratio the smaller the diameter will be, as increasing the chelating agent prevents the aggregation of the metal making and blocks the growth[95] (Fig.10).

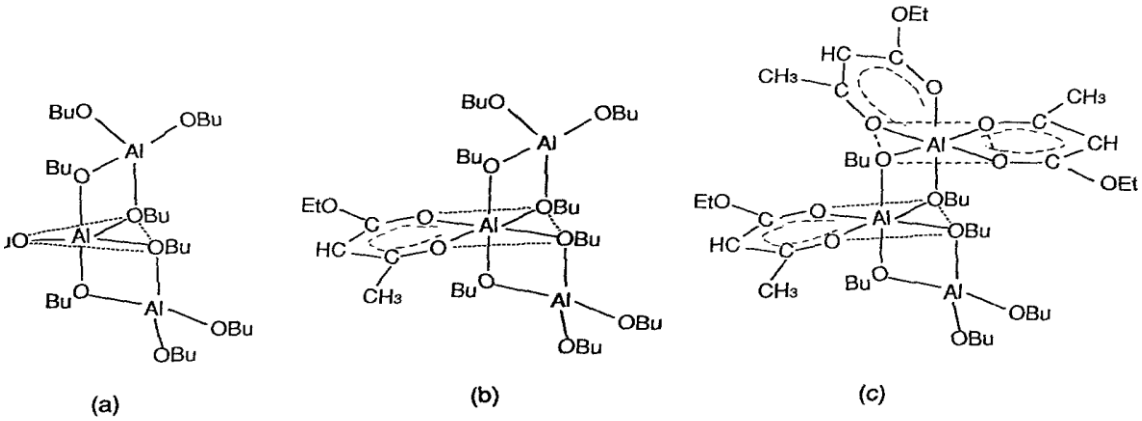

Figure 10 *Scheme of the formation the complex Al(O-sec-Bu)$_3$ and EAcAc. Image courtesy of Uchihashi et Al.* [83].

The synthesis was performed as follows. Aluminum tri-*sec*-butoxide (97%, Sigma-Aldrich) was added to isopropyl alcohol (99%, Sigma-Aldrich), while magnetically stirring to disperse the alkoxide, the synthesis is carried out in a humidity-controlled environment. After one hour, ethyl acetoacetate (> 99%, Sigma-Aldrich) was added, while stirring continued. In short time a change in the color of suspension is observed, from transparent to pale yellow due to the complexation that has taken place[94]. After 3 hours, a 1:1 v/v mixture of iPrOH and deionized water was added dropwise to mixture to start hydrolysis. The molar ratios of EAcAc, water and iPrOH with respect to Al were set to 1,4 and 20, respectively. The exact quantities are listed table 1.

Table 1 *Molecular weight, purity, density, volume, weight, moles, molar ratio with respect to Al and molarity of every reagents used in the synthesis of alcohol-based alumina suspension.*

	PM (g/mol)	Purity (%)	ρ (g/mL)	nX/nAl	n (mol)	m (g)	V (mL)
Al (O-sec-Bu)$_3$	130.14	100	1.03	1	0.059	7.71	7.50
EtOacac	246.33	97	0.96	1	0.059	15.0	15.6
H_2O	18.02	100	1.0	4	0.24	4.20	4.20
i-PrOH	60.1	0.99	0.78			74.04	94.0

After 24 hours, the reaction is completed and ready for characterization. Average particle size was determined by Dynamic Light Scattering (DLS, Zetasizer Nano S, Malvern Instrument). The measured distribution of hydrodynamic diameters is reported in Fig. 11.

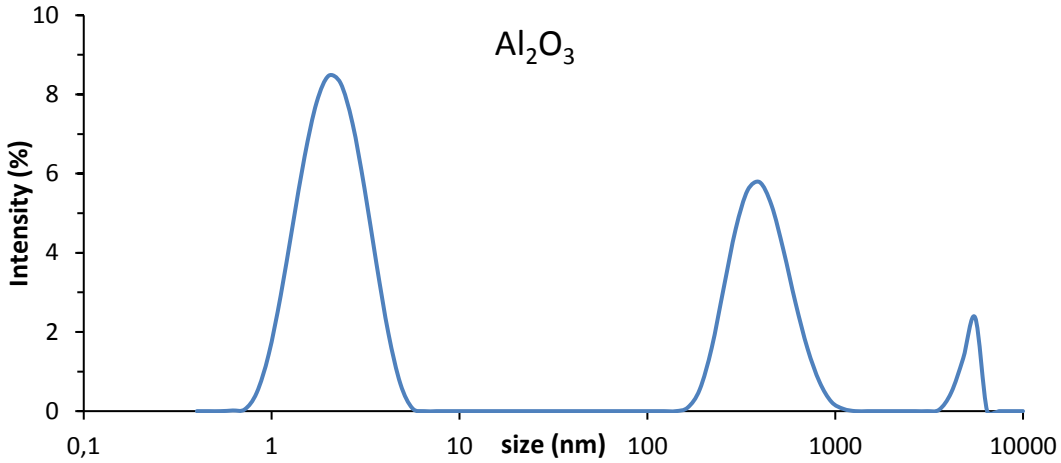

Figure 11 *Intensity of scattered light vs size distribution for as-synthesized alumina nanoparticles suspended in iPrOH.*

The analysis reports two peaks, of which the dimensions observed are d= 2.2 nm and d= 396 nm with smaller amounts of aggregated particles.

Surface tension γ for the suspension of nanoparticles was determined via pendant drop method. This technique calculates surface tension for a liquid drop by fitting its profile with a Laplacian curve[96]. The only data to be known for the measurement is the suspension density estimated at 0,777 g/mL. The number of measurement results in high accuracy of the standard deviation of the measurement by varying from 5 to 7 drops. The surface tension data γ= 21.3 ± 0.1 mN/m at room temperature (about 24°C).

The suspension has a lower surface tension than the solvent in which it is dispersed, in fact isopropanol alcohol has a surface tension of γ = 23.3 mN/m, therefore some of the components of the sol caused a small decrease in γ.

The possible responsible for this lowered value could be 2-butanol, a likely reaction product during hydrolysis. The respective reagents used as EAcAc and reacted water have a higher surface tension than isopropyl alcohol while the value of 2-butanol is γ=22.6 mN/m at 25°C. Therefore, the amount of 2-butanol is so low that it does not explain such a decisive lowering of surface tension. It is probable that the real responsible for the lowering of surface tension is the presence of hydrophilic nanoparticle; the influence of particles in a pure liquid is reported in literature[97,98], but such a small variation in the alcoholic medium nevertheless remains unexplained.

4.2 Silica nanoparticles

4.2.1 Synthesis of silica nanoparticles functionalize with fluorine silane

The synthesis of silica functionalized with fluorinated alkyl chain was conducted via sol-gel. The synthesis previously used by the group presented some problems[89]. Due to little stability of the synthesis, after a few days it formed sediments. The diameter of the nanoparticle turns out to be greater than >500 nm.

The previous synthesis was prepared as follows: ammonium hydroxide NH_4OH (30% Sigma-Aldrich) was added to ethanol (99%, Sigma Aldrich) and stirred to complete dissolution. Tetraethyl orthosilicate (TEOS 98%, Sigma-Aldrich) was introduced in the solution, then temperature was increased to 60°C. 1H,1H,2H,2H-perfluoroctyltriethoxysilane (PFOTS 98%, Sigma- Aldrich) was added dropwise to the solution, the molar ratio is reported in table 2. The suspension remain in agitation for about 100 minutes, and then cooled to room temperature[89]. The DLS analysis of the suspension showed a monodisperse size distribution with a single peak positioned at 481nm.

Table 2 *Molecular weight, purity, density, volume, weight, moles, molar ratio with respect to Al and molarity of every reagents used in the synthesis of alcohol-based silica suspension.*

	PM (g/mol)	Purity (%)	ρ (g/mL)	nX/nSi	n (mol)	m (g)	V (mL)
TEOS	208.3	98	0.94	1	0.16	33.8	36.7
PFOTS	510.4	97	1.33	0.6	0.010	5.05	36.0
NH_4OH	35.1	28	0.90	5.7	0.93	32.5	3.80
i-PrOH	60.1	100	0.78	25	4.1	245.2	312

To improve the quality of the synthesis and make it more stable over time, the following reaction parameters were studied:

- TEOS: PFOTS ratio
- Type of solvent

The new set-up, a hot plate, a three –necked flask and a cooling tube immersed in a glycol bath are used. The procedure of reagent insertion remains unchanged. The new synthesis set-up allows for a more uniform heat distribution, and the use of the magnetic stirring rod instead of mechanical paddle provides greater control plus homogeneity over stirring.

Six syntheses were conducted by studying the TEOS:PFOTS molar ratio from 1:0.2 mol: mol to 1:0.6 mol: mol, in the table3 by controlling the particle size a thanks to DLS.

Table 3 *List of fluorinated silica synthesis with different molar ratio.*

Sample	Molar ratio TEOS:PFTOS
SiO_2-F #1	1: 0.2
SiO_2-F #2	1: 0.3
SiO_2-F #3	1: 0.4
SiO_2-F #4	1: 0.5
SiO_2-F #5	1: 0.6

As shown in the table 4, the hydrodynamic radius of the particles does not vary much by changing the value of PFOTS but remains constant.

Table 4 *Particle size values for each synthesis with different TEOS: PFOTS molar ratio measured at day 0 from 14 day of aging of the synthesis.*

Sample	TEOS:PFTOS mol: mol	Size (nm) 0d	PDI	Size (nm) 7d	PDI	Size (nm) 14 d	PDI
SiO_2-F #1	1:0.2	243	0.1	251	0.1	243	0.121
SiO_2-F #2	1:0.3	313	0.06	265	0.04	267	0.078
SiO_2-F #3	1:0.4	227	0.1	239	0.01		
SiO_2-F #4	1:0.5	252	0.05	249	0.03	258	0.071
SiO_2-F #5	1:0.6	197	0.2	224	0.02	206	0.221

In Fig 12 and in table 4 it is deduced that to the dimension of the nanoparticles diminishes to increase of the molar ratio between TEOS and PFOTS, however, it seems not to be great variations of the hydrodynamic diameter of the nanoparticle to aging of the synthesis.

The last optimization was conducted to improve the stability of the synthesis over time. In the literature the combination of TEOS and Isopropyl alcohol is widely used, TEOS in this solvent needs to age about two month to achieve the desired performance[99].

It note as seen previously that the radius of the particle does not change during aging. It also observe that the hydrodynamic radius of fluorinated silica in isopropyl alcohol is smaller than for ethanol-dispersed nanoparticles.

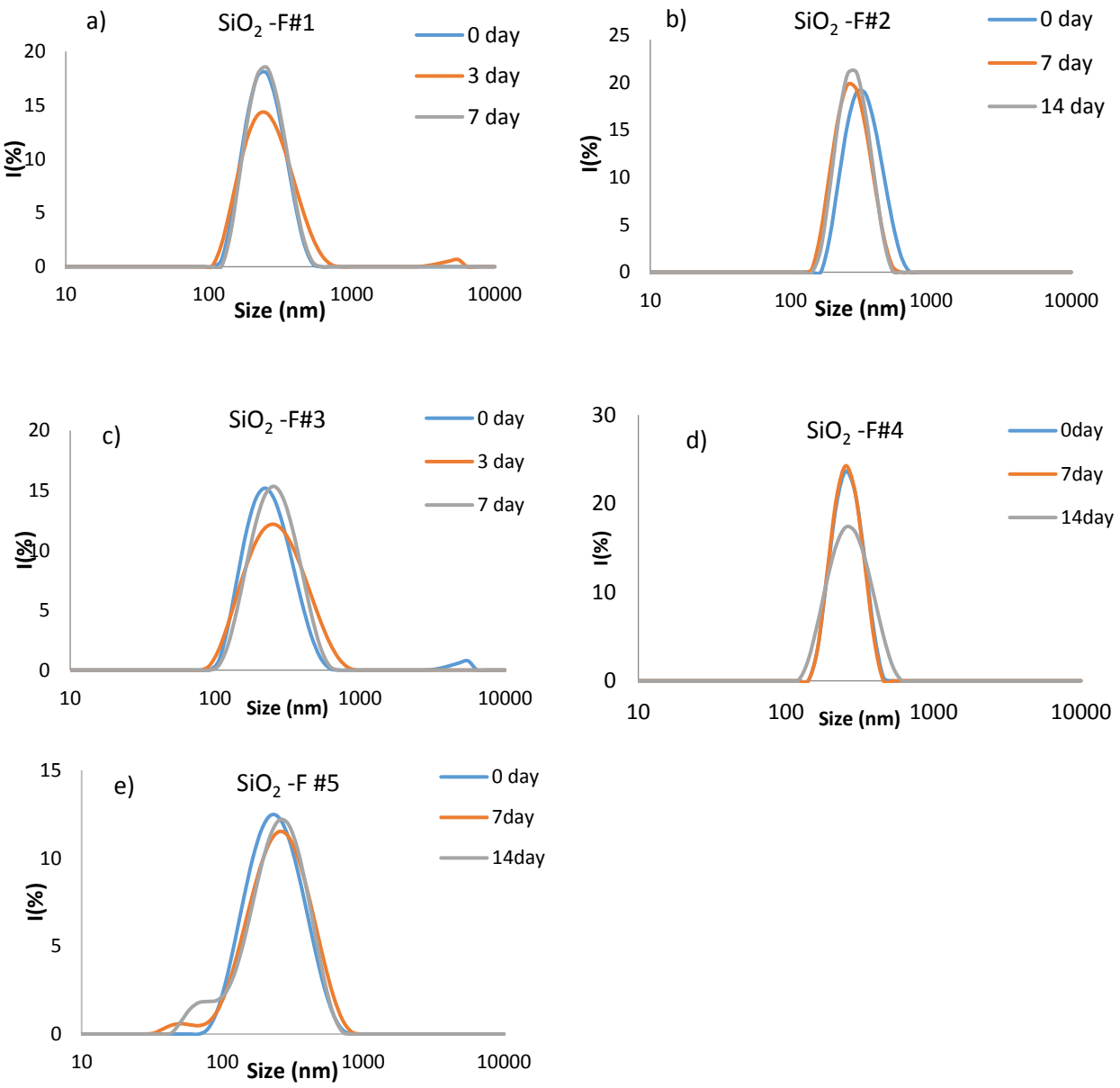

Figure 12 *Intensity of scattered light vs size distribution for SiO_2-F suspension in EtOH with different TEOS:PFOTS molar ratio a) SiO_2F #1 1:0.2 b) SiO_2F #2 1:0.3 c) SiO_2F #3 1:0.4 d) SiO_2F #4 1:0.5 e) SiO_2F #5 1:0.6.*

Same TEOS: EtOH molar ratio was used for the new synthesis, and the synthesis temperature was lowered to 50°C to avoid promoting boiling. The molar ratio TEOS: PFTOS used in this synthesis was 1:0.5. As before, particle size was monitored as the synthesis aged as shown in table 5. It is noted ad seen previously that the radius of the particle does not change aging. It also observed that the hydrodynamic radius of fluorinated silica in isopropyl alcohol is smaller than for ethanol-dispersed nanoparticles.

Table 5 *Particle size values for fluorinated silica synthetized in iPrOH.*

Sample	Day	Size (nm) 0d	PDI
SiO_2-F #6	0	150	0.1
	14	174	0.1
	60	160	0.3

A thermogravimetric analysis was conducted on the fluorinated silica nanoparticles. The analysis was conducted in Air/N_2 up to 700°C, to observe the amount of organic present on the nanoparticle.

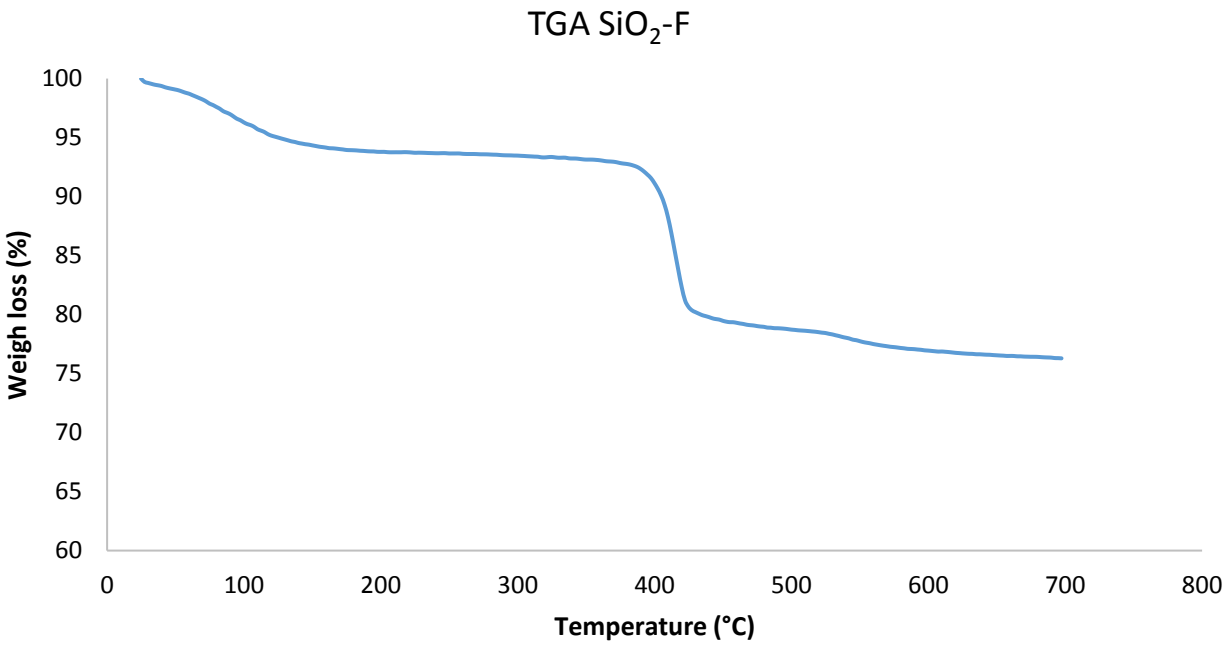

Figure 13 *TGA analysis of fluorinated silica nanoparticles (SiO_2F)*

The figure 13 shows the TGA analysis of silica nanoparticles, the graphs shows a 6% loss around 100°C, due to the evaporation of the solvent inside the powder. Instead, around 400°C is observed a 17% weight loss due to degradation of the organic part that covers the nanoparticles.

4.2.2 Synthesis of silica nanoparticles functionalize with amino silane

The synthesis of silica nanoparticles with alkyl chain with primary amine groups was conduct via sol-gel (Fig 14). This functional group will serve us later to improve the adhesion of nanoparticles to resin. To introduce the amine group into the silica nanoparticles one of the most widely used reagents in the literature was 3-aminopropyltriethoxysilane (APTES)[91,100,101].

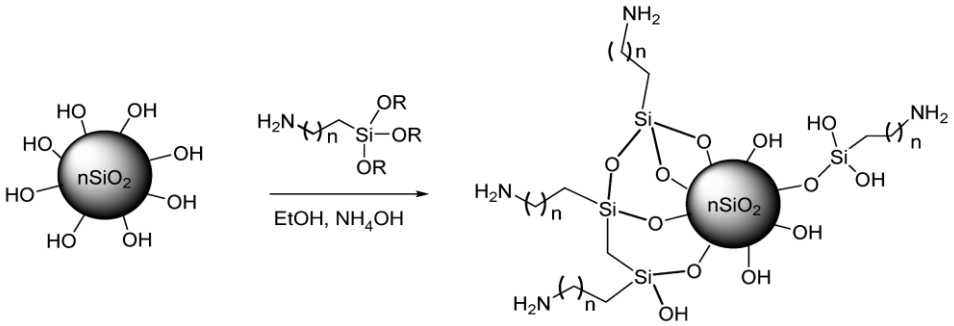

Figure 14 *Reaction scheme of functionalization of silica nanoparticles with amino group.*

The synthesis was performed as follows: the nanoparticles powder SiO_2 (10-20 nm, Sigma Aldrich) was used and dispersed in ethanol and the temperature was set to 60°C and under stirring. Once the temperature was reached, the 3-aminopropyltriethoxysilane (APTES, BRB Silanil® 919) was weight in the ratio APTES: SiO_2 1:2 (w: w) and dispersed in a small aliquot of ethanol until completely dissolved. APTES is added drop by drop, the synthesis remains in stirring for 100 minutes and then cooled to room temperature. The suspension was centrifuged to remove the supernatant liquid at 8000 rpm for 10 minutes. The powder was then allowed to dry at 60°C overnight. The exact quantities are listed in the table 6.

Table 6 *Molecular weight, purity, density, volume, weight, moles, molar ratio with respect to SiO_2 and molarity of every reagent used in the synthesis.*

	PM (g/mol)	**Purity (%)**	**□ (g/mL)**	**nX/nSi**	**m (g)**	**V (mL)**
SiO_2	60.08	100	/	1	4	/
APTES	221.37	97		4	2	
EtOH	46.08	100	0.78		80	100

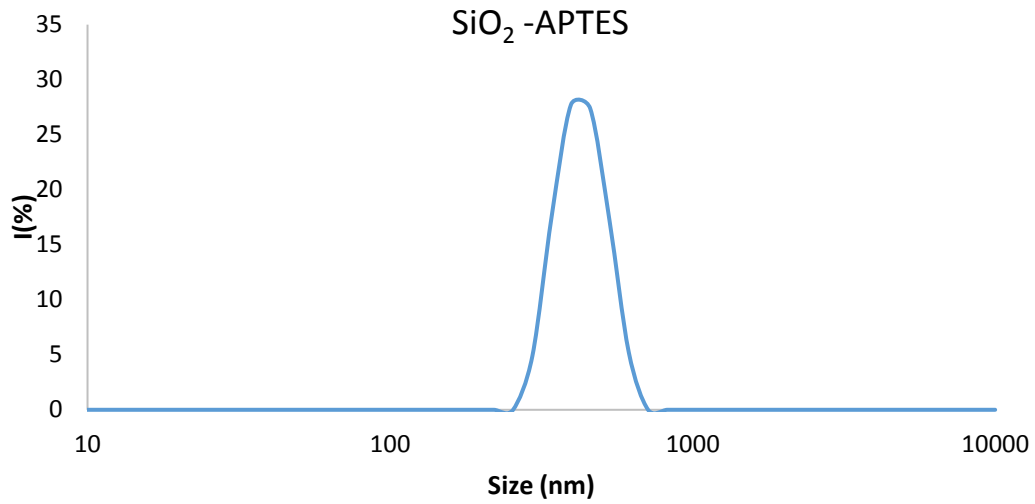

Figure 15 *Intensity of scattered light vs size distribution for SiO_2-APTES suspension in EtOH.*

DLS characterization of nanoparticles size was performed (Fig. 15). It can be seen in the figure 14 that the hydrodynamic diameter was greater than the nanopowder size of SiO_2 (20nm). This may be due to two reason: first, the steric hindrance of APTES was high considering the alkyl chain, also being an agent that promotes adhesion the particles will have aggregation. The particles size was 458 nm PDI 0.174.

In contrast, SiO_2 has a negative surface charge due to the presence of hydroxyls. The measurement of Z potential of functionalized nanoparticles allows verifying the achievement of functionalization of the nanoparticles with the amino group. Table 7 shows the respective Z potential of SiO_2 and silica after functionalization with APTES.

To facilitate understanding of the measurement, water was used as the dispersion solvent. A small of powder (~1mg) was taken and dispersed in distilled water. After that, the measurement was carried out.

The measurement of the Z potential in this synthesis was very important. As it was well known, the NH_4^+ groups has a positive surface charge so the Z potential of SiO_2 nanoparticles functionalized with amino group will turn out to have a positive Z potential.

The potentials were shown in the table 7 with the respective standard deviation.

Table 7 *Z potential measurements of the SiO_2 suspension and SiO_2 suspension in water.*

Sample	ZP (mV)	SD
SiO_2	-24	1.30
SiO_2-APTES	31	0.72

The table compares the Z potential of silica and silica functionalized with APTES, the Z potential of SiO_2-APTES is positive, confirming the effective functionalization of the nanoparticle with the amino group.

4.2.3 Synthesis of silica nanoparticles functionalize with silane with long alkyl chain

The synthesis of silica nanoparticles was conducted via sol-gel with silane with primary long-alkyl chain.

Functionalization of nanoparticle with long chain alkyl groups helps to achieve inherently hydrophobic particles without multilayer deposition or the use of fluorine-containing compounds. Among the most common long alkyl chain silanes used to modify silica nanoparticles rich in hydroxyl groups were: methyl triethoxysilane (MTES)[102], octadecyltrichlorosilane (OTS)[103] and hexadecyltrimethoxysilane (HTS)[102,104].

This type of sol-gel synthesis involves two steps: first the formation of silica nanoparticles by classical Stober method and then functionalization with silane[81]. The molar ratio of silica to HTS determines the hydrophobicity of the surface once the layer was deposited, indeed the higher the HTS:SiO_2 ratio with range 1:1< HTS:SiO_2 <4:1 the lower the surface energy of the coating will be[81,104].

First, the synthesis of Stober silica nanoparticles and its optimization was carried out. The synthesis was inspired by work published Q. Zhang et al 2021[105], and then optimized in our laboratory. First, tetraethyl orthosilicate (TEOS 98%, Sigma-Aldrich) was dispersed in ethanol (EtOH <99%, Sigma Aldrich) under magnetic stirring and recorded as solution A. The mixture of ammonia hydroxide (NH_4OH <30%, Sigma Aldrich), deionized water and ethanol was magnetically stirred at room temperature for 30 minute as solution B. Then, solution A was dripped into solution B, the drip time should be around 30 minute. Stirring time was designed to get the smallest particles in the short time. To ensure that once the reaction is over the particles diameter does not continue to increase due to unreacted ammonia, the particle were centrifuged and washed in ethanol three times. Once that was done, the powered is withdrawn and re-dispersed in an aliquot of 100 mL ethanol; the molar ratio is reported in table 8.

Table 8 *Molecular weight, purity, density, volume, weight, moles, molar ratio with respect to SiO_2 and molarity of every reagent used in the synthesis.*

	PM (g/mol)	Purity (%)	nX/nSi	n (mol)	m (g)	V (mL)
TEOS	208.33	98	1	0.04	8.3	8.5
NH_4OH	35.05	30	6.4	0.25	9.0	10
EtOH	46.08	99	1.4	0.060	89	100
H_2O	18.08	100	4.8	0.20	1.0	1.0

To monitor particle growth during the sol-gel reaction, a small aliquot was taken from the reaction flask every hour and analyzed at DLS. The particle size vs time was reported in the graph (Fig. 16).

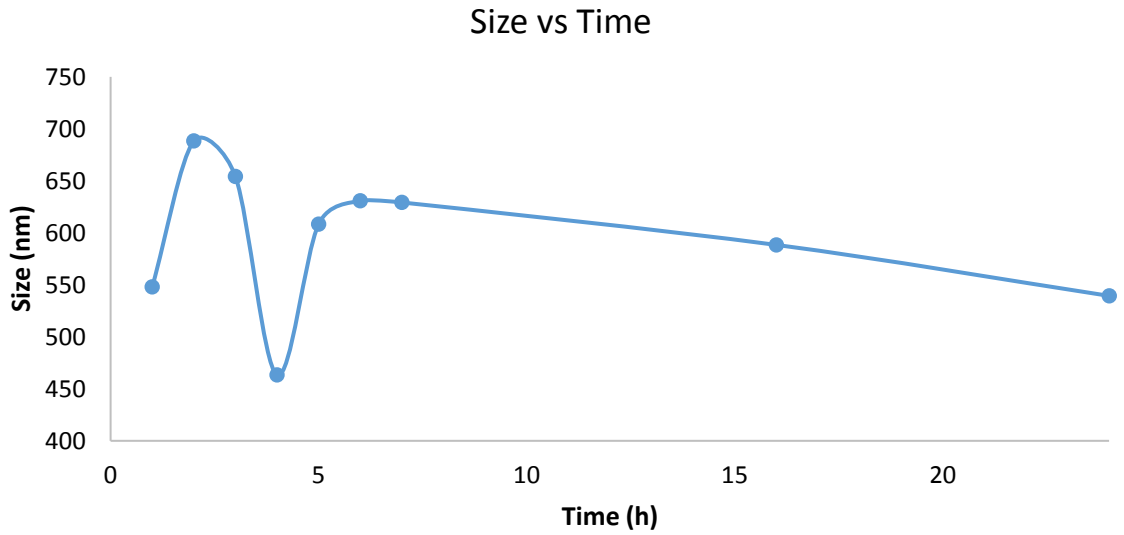

Figure 16 *Particle size vs time reaction of silica nanoparticles.*

In figure16, the hydrodynamic diameters of the silica nanoparticles obtained with the synthesis described above are shown. The reaction time determine the diameter, in particular it want to obtain the smallest diameter in the shortest possible time, but it also necessary to take into account the reaction yield. Reaction time of less than 600 nm in diameter are 1 hour (547 nm), 4 hours (463) and 24 hours (539 nm) respectively.

After 4 and 24 hours of reaction, diameters of less than 550 nm are obtained. The reaction yields has been calculated to determine the most suitable reaction time. Yield obtained after 4 hours of 36%, while after 24 hours is 40%. The percentage difference obtained is not decisive, but 4 hours has more advantages than 24 hours. For this reason, it was decided that the reaction time of silica nanoparticles obtained by this procedure is 4 hours.

Having then optimized the method of synthesis of silica nanoparticles, the process continued with the functionalization involving a silane with a long alkyl chain. The procedure unfolded as follows: a silica suspension was extracted and diluted fourfold in ethanol, and then heated to 60°C under magnetic stirred. Once the temperature was reached, the hexadecyltrimethoxysilane (HTS > 85%, Sigma Aldrich) was slowly dropped inside the reaction flask. After 100 minute, the reaction was cooled at room temperature. The molar ratio of SiO_2: HTS was 1:1; the particle size was 431 and PDI 0.042.

To get further confirmation of functionalization an FTIR spectrum of powder obtained by centrifugation and drying the suspension was made (Fig. 17).

A KBr pellet was prepared and subjected to FTIR (Fourier Transform Spectroscopy) analysis with instrument ThermoFisher Nicolet IS5.

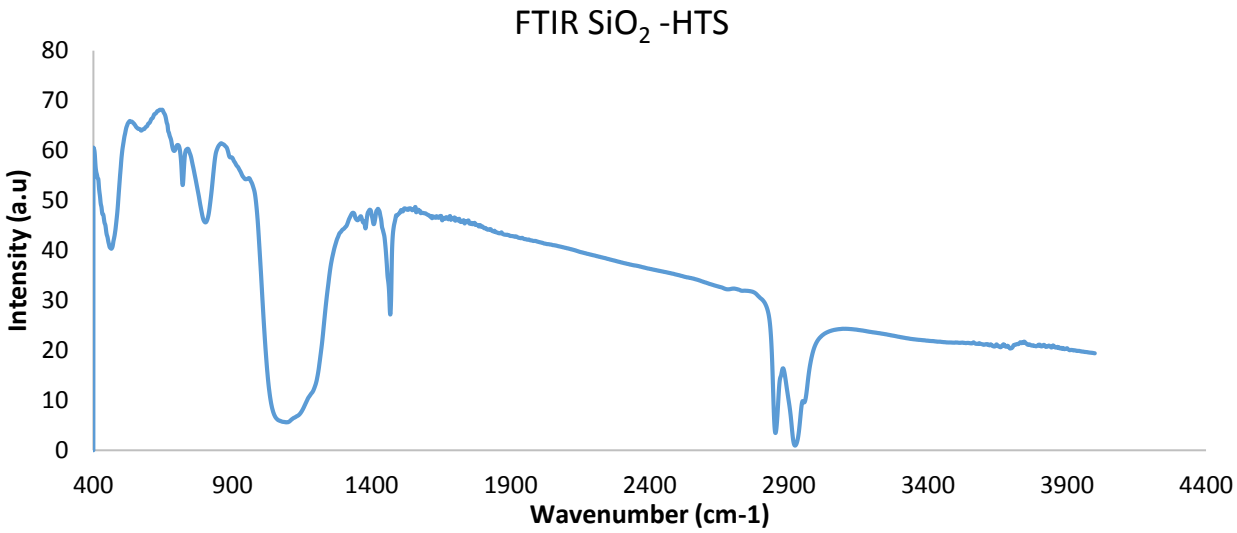

Figure 17 *FTIR analysis of SiO_2-HTS nanoparticles in reflectance in KBr pellets.*

From graph (Fig 17) the evident pikes in the 3000 cm^{-1} region represent the CH_3 and CH_2 of the alkyl chain of HTS, while the extended band around 1050-1100 cm^{-1} indicates Si-O-CH_x bonding.

FTIR spectroscopic analysis confirms the effective functionalization of silica nanoparticle with long alkyl chains thanks to the presence of CH_2 and CH_3 signals.

A thermogravimetric analysis was conducted on the fluorinated silica nanoparticles. The analysis was carried out in Air/N_2 up to 700°C, to observe the amount of organic present on the nanoparticle.

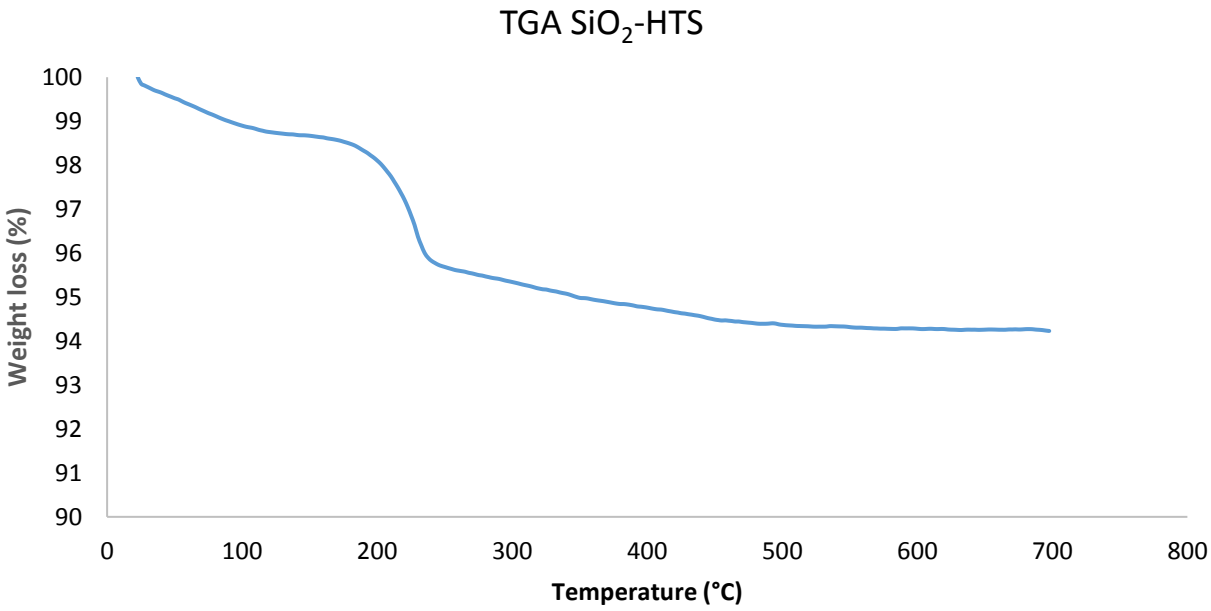

Figure 18 *TGA analysis of silica nanoparticles functionalized with fluorine-free chain (SiO_2-HTS)*

In the figure 18, the TGA analysis of silica nanoparticles functionalized with HTS, presents a loss of 2% at 100°C, due to solvent evaporation. In addition, a weight loss of 5% is observed at 250°C. This weight loss is attributable to organic present on the nanoparticles.

This analysis shows that functionalization with fluorine free organic chain did not take place completely. During the reaction, 50% of HTS was introduced compared to SiO_2 nanoparticles, but only 5% of HTS reacted during the functionalization process. Future prospects, include a review of the synthesis to improve both the yield to obtain the nanoparticles of SiO_2, that the reaction of functionalization with fluorine-free chain.

5. COATING DEPOSITION PROCESSES

5.1 Theory of film deposition

The coating deposition techniques used are easily transferable to industry. In particular, the technique of dip coating and spray coating were explored.

These techniques make it possible to coat objects of any size. The dip-coating technique has a very simple process; the sample was dipped into the suspension at certain speed and for a specific time. Despite being a seemingly simple technique, controlling a few parameters allows for. Landau and Levich found the basic parameters needed to control coating thickness as a function of emersion rate[106].

$$h = \frac{0.94\eta^{2}/_{3}}{\gamma^{1}/_{6}(\rho g)^{1}/_{2}}\, u^{\,2}/_{3}$$ [Eq 6]

η, γ, ρ are sol viscosity, surface tension and density, respectively [Eq.6]. This correlation was achieved at withdrawal velocities exceeding 1mm/s. In such condition, viscous drag by gravity was the predominant factor (viscous regime). At lower speeds (draining regime), evaporation becomes faster than the motion of drying line, prompting the sol from the coating reservoir to be drawn in though capillary. In fact, for speeds around 0.1 mm/s the trend was reversed, resulting in an increase in film thickness as speed decrease. Grosso et al.[16,107] published paper detailing this phenomenon and subsequently established a more precise relationship between *u* and *h*.

$$h = k\left(\frac{E}{Lu} + Du^{\,2}/_{3}\right)$$ [Eq 7]

In this equation [Eq. 7], *k* is a composition constant (proportional to concentration), while *E* is the evaporation rate, *L* is the substrate length and *D* contains the physical-chemical characteristics of the coating solution. Both the capillary regime (E/u term) and viscous regime (Du $^{2/3}$ term) contribute to final thickness. Consequently, the curve illustrating thickness versus withdrawal speed will exhibit a minimum at a specific velocity value. This curve's position can be adjusted by altering the surface temperature during deposition or by modifying the sol concentration. Precise control of coating thickness holds paramount importance for materials like glass, where optical transparency must remain unaffected. Thin sol-gel coating, featuring thickness smaller than the wavelength of visible light, possess the ability to preserve or even augment transparency, serving as anti-reflective coatings[108,109]. Another deposition technique used is the spray technique. Compared to the dip technique, which involves the use of large suspension volumes for filling the tank, the main advantage of this technique is the use of a reduce suspension volume. The technique used in the thesis is of manual type; with a precision airbrush containing a volume of 5 mL, thanks to the adjustment of the needle-nozzle distance, it was possible to decide the nozzle opening to have a larger or smaller spray cone as needed. Another important parameter was to decide the distance between the needle and the sample. If the distance was large (60cm), the recompression area will be larger, while for small distances the recompression was smaller.

This technique has disadvantages; first, it was not possible to use it with any type of suspension in particular unstable suspension that settle risk clogging the nozzle. In addition, it was not always possible to obtain homogeneous coatings since the thickness was so small that it was not visible to the naked eye and there was no quality control in the immediate.

5.1.1 Dip coating

The dip coating process was performed with automated dip coater available at CNR-ISSMC (Fig.19). In particular, dip coater was purchased from Aurel Automation (Modigliana (FC), Italy). This dip coater was a customized solution tailored to the specific requirements of the research group. Its design and development were guided the group's needs. The coater boasts an expansive chamber, with internal dimensions measuring 1700 x 1000x 700 mm. It incorporates two interconnected steel arms that traverses along a rail, powered by an electric motor. A specialized clam was provided to secure samples, although various other configurations were employed bases on the shape of the sample. All operations were meticulously controlled by computer interface, enabling the user to define critical parameters such as dipping and withdrawal speeds, immersion duration, initial, intermediate, and immersion position, as well as drying times. This level of control ensures the utmost consistency in the dipping process. The size limitations for samples primarily stem from the chosen contains, which also dictates the required volume of coating solution.

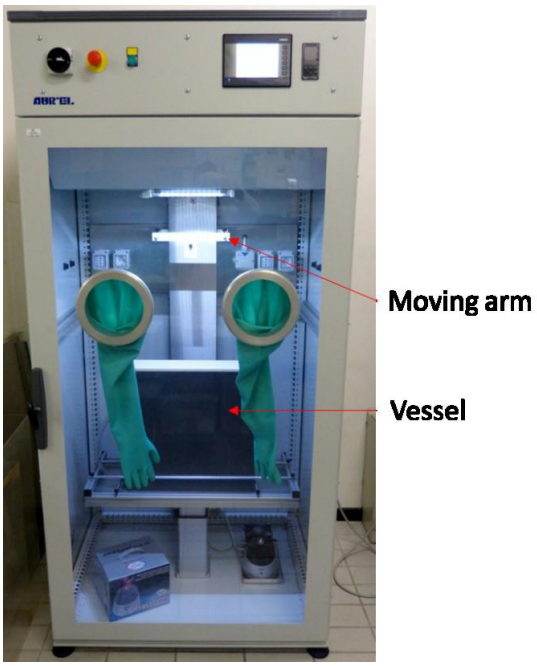

Figure 19 *Large automated dip coater designed by Aurel Automation.*

After dip coating, the samples are left to air dry for the time necessary for the solvent to evaporate and for the type of substrate. Subsequently we proceed with the heat treatment.

5.1.2 Spray coating

The deposition of coatings by spraying is widely used because it allows coating to be deposited on samples of different morphology. A technique has a broad spectrum of fluids with different rheology, particle size and solvent. This technique offer the opportunity to fine-tune the system to deposit virtually any type of solution and achieve the desired film properties.

However, there are some parameters to optimize to obtain the desired coating. One is the size of the needle. A needle with a small diameter allows very punctual and precise spraying; a needle with larger dimension allows you to cover a larger area with a wider spray.

Another parameter is the needle position. The position of needle is fundamental. The less it is exposed the wider the jet opening will be. On the contrary, the more visible the needle is, the more punctual the spraying will be.

Airbrush sample distance is another important parameter. A very small distance between the substrate and the airbrush allows for very punctual and precise spraying, while moving further away the spraying area increase.

The spray technique was executed using a precision airbrush. The sample was positioned within the enclosure of the dip coater, determining the optimal distance between airbrush and the sample, along with the desired speed for sample movement. This endeavor aims to mechanize the manual process to the greatest extent possible, thereby enhancing the reproducibility of these hands-on techniques (Fig. 20).

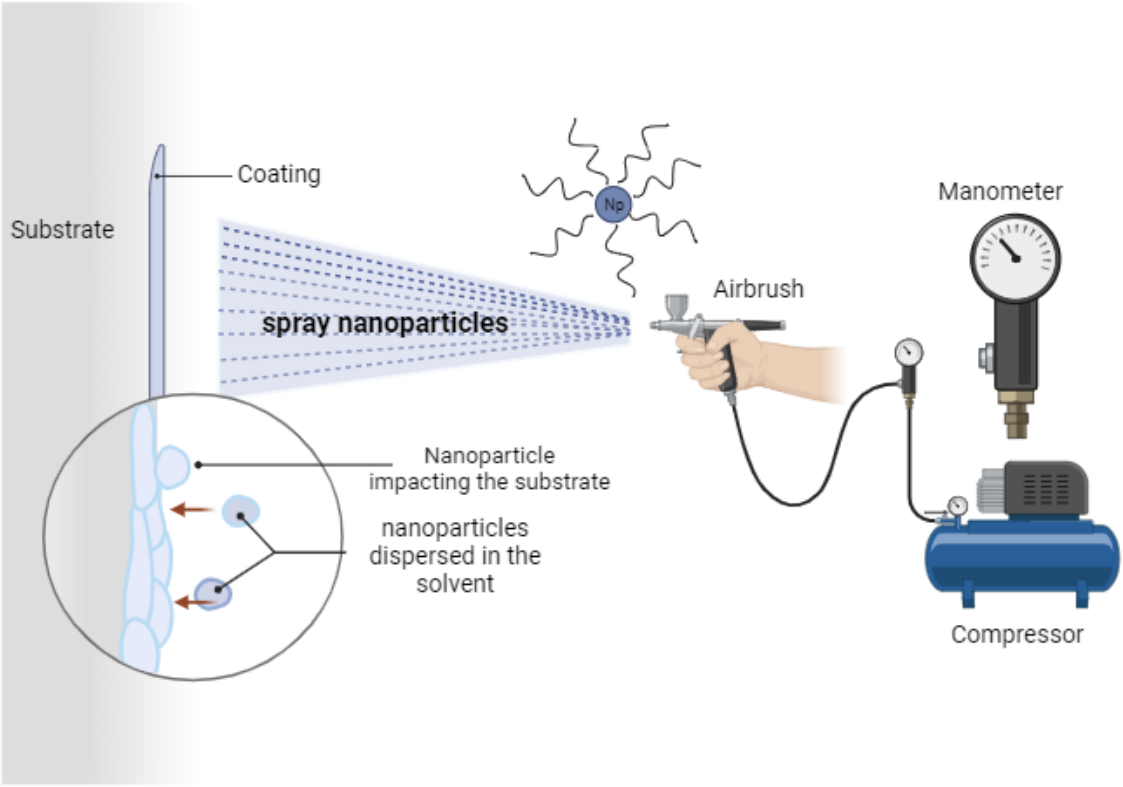

Figure 20 *Operating diagram of the spraying technique.*

5.2 Thermal treatment of coatings

The air-dried ceramic coating underwent a heat-treatment process within a furnace. This annealing stage facilitated thorough film drying, elimination of organic compounds, accomplishment of condensation and densification process, resulting in beneficial enhancements to the mechanical process[110].

Kozuka et al. [111,112]conducted comprehensive research on the cracking phenomena in gel films. Their investigations highlight that the inherent stress that arises during heating reaches its peaks during the condensation stage of treatment. Nevertheless, when depositing a well-established nanoparticle suspension, condensation was restricted, leading to diminished cracking. Consequently, cracking was primarily attributed to disparities in potential thermal expansion coefficients between the substrate (resulting in thermal stress) and capillary pressure stemming from solvent vaporization. The authors also underscored the constructive influence of chelating agents in mitigating the occurrence of crack during the heating process.

The selection of temperature was significantly influenced by substrate material. As will be elaborated upon in the concluding section of this chapter, the substrate has the potential to develop structured phases that could disrupt the coating's surface morphology.

Consequently, it becomes essential to conduct a tailored optimization of thermal processes for each specific material upon which the coating was applied.

Two different instruments were used for the heat treatment. The first system used for heat treatment is a laboratory furnace model FSV 64 of Nannetti S.r.l, with a maximum operating temperature of 1100°C and heating ramp 150°C/h.

The second is a ventilated stove that allows the temperature to be kept constant below 100°C without any changes. The stove is used for heat treatments in which the coated substrate is plastic. These substrates require heat treatments with temperature below their glass transition temperature to ensure non-deformation of the sample during treatment. The ventilated stove is mod OPV 30 from Nannetti S.r.l. with a maximum operating temperature of 300°C.

6. CONTACT ANGLE MEASURMENTS

6.1 Static and dynamic contact angle

As already mentioned in the previous chapter, the contact angle ϑ is characterized as the angle created by the tangent at the liquid-gas interface where it meets the three phase contact line[70]. Numerous techniques were available for contact angle measurements[113], with the sessile drop method being the most commonly employed. This approach is straightforward and was supported by numerous commercially accessible automated system, which can execute the measurements swiftly and yield high reproducibility.

In this methodology, a liquid droplet with volume was placed onto the surface. A light source, such as a lamp, illuminates the droplet from the side, generating an image that was captured by camera's objective lens. In automated set up, software was employed to automatically identify the droplet's profile and match it with the selected analytical technique. The angle formed between the baseline and the tangent to the fitting curve at the point of contact was the quantified contact angle. An illustrative instance of contact angle measurements is depicted in Figure 21.

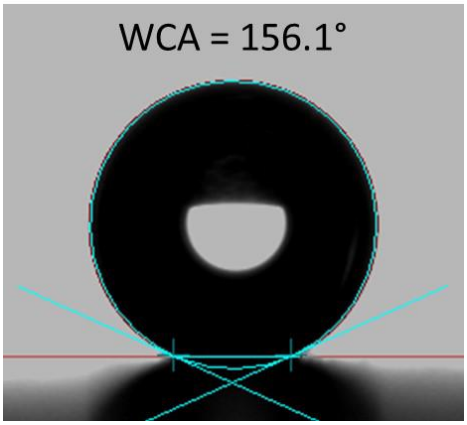

Figure 21 *Fitting of a drop profile with ellipse method and calculation of contact angle. The red straight line is the baseline, the blue curve is the fitted drop profile and the blue inclined lines are the tangents of a drop profile at the contact points (blue crosses).*

The selection of a fitting method can significantly influence the determined contact angle value[113,114]. Goniometric measurement directly assessing the tangent often introduce substantial errors. In the case of an axisymmetric drop, employing automated axisymmetric drop shape (ADSA) analysis facilitates the acquisition of the drop profile[115]. A theoretical curve described by the Laplace equation is fitted to the experimental profile (Fig. 22). The tangent or polynomial method allows the contact angle to be then calculated based on the slope of the theoretical curve at the contact point. This method proves to be the most accurate, considering its incorporation of gravity-induced deformation in the drop. For an ideal surface, characterized by uniformity, solidity, smoothness, and chemical internees, the contact angle with a specific liquid remains consistent and relies solely on interfacial tension, as outlined by the Young equation. However, real surfaces exhibit defects and micro-roughness, leading to variations in the contact angle. Consequently, the contact angle may seemingly assume different values.

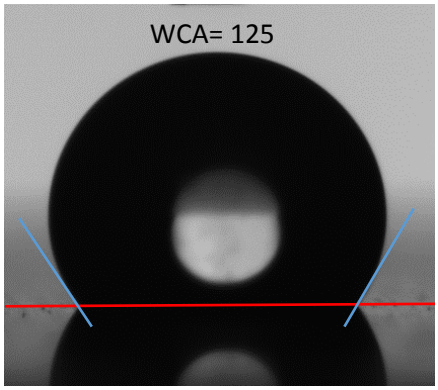

Figure 22 *Fitting a drop profile with tangent method and calculation of contact angle. The red straight line is the base line; the blue line is the tangent of the angle to form in three-phase system.*

Another interesting way to calculate the contact angle was by changing the volume of the drop or tilting the contact surface. In this way it was possible to identify two types of angle during the measurement: the advancing contact angle ACA ϑ_A referred to the movement of contact angle line towards a non-wetted area; the receding contact angle RCA ϑ_R referred to the movement of contact line towards a wetted part of the surface[113]. It will always be true that ACA≥RCA. The difference between ACA and RCA is termed as a contact angle hysteresis (CAH) or $\Delta\vartheta$, which correlates with the movement of droplets on the surface: a lower CAH, the higher the mobility.

The measurement of the hysteresis angle allows determining whether a surface was of Wenzel or Cassie Baxter types. In particular, if the hysteresis angle was very high and pinned phenomenon occurs, the drop penetrates the structure and remains blocked. On the contrary, drops in the Cassie-Baxter state have the liberty to move on the mixed solid-gaseous surface; therefore, hysteresis will be low, usually below 10°. As previously alluded, there exist predominantly two techniques for quantify ACA and RCA. The initial approach involves placing a droplet on the surface and inclining it until the droplet initiates its motion. At the point of initial movement, the measured contact angle corresponds to RCA; while the angle measured downhill correspond ACA. This method was referred to as the tilted plate technique[116].

However, the most commonly method used to determine CAH involves a stationary sessile droplet remaining affixed to a needle. The droplet's volume is increased by injection; the ϑ value noted when the contact point instigates motion is designated as ACA. This value ought to remain constant as the droplet volume increases over a certain threshold. Subsequently, the droplet's volume is diminished using suction, causing the contact line to retreat. From that moment on, the plateau value of ϑ is recognized as RCA. The measurement of the RCA value strongly depends on the measurement method used. However, the tilting method requires more complex instrumentation than the sliding angle method, and the sliding method is reproducible and reliable for the measurement we perform. In particular, in this work, we will perform both static contact angle and hysteresis measurement.

6.2 Surface energy

Another important parameter is the surface energy of the solid (denoted as γ_{SG} in the Young equation), which can be described as the energy required to generate a surface from a bulk material[117]. In general, a higher the value of γ_{SG} typically corresponds to a diminished contact angle when in contact with specific liquid.

Among the various techniques available for the measurement of surface energy, contact angle measurement are considered the simplest, the most commonly employed[118]. However, the absolute value of γ_{SA} is inadequate to delineate the surface wetting by a liquid. In fact, the solid-liquid interaction strongly depend in the chemical composition of both phases. For this reason, surface tension is often divided into components to express the relative contributions by different types of interaction. The nature of these components depends on the chosen model. The most common one is Owens-Wendt-Kealble (OWK) model[119,120]. In this model, γ_{SG} and γ_{LG} are each divided into a polar component (due to hydrogen bond and dipole-dipole interactions) and dispersive component (Wan Der Waals force) [Eq.8]. There is interaction only between correspondent components:

$$\gamma_{SL} = \gamma_{SG} + \gamma_{LG} - 2\sqrt{\gamma_{SG}^{d}\,\gamma_{LG}^{d}} - 2\sqrt{\gamma_{SG}^{p}\,\gamma_{LG}^{p}} \quad \text{[Eq 8]}$$

Combing this equation with Young equation gives:

$$\gamma_{LG}\,(1 + cos\vartheta)\gamma_{SL} = \gamma_{SG} + 2\sqrt{\gamma_{SG}^{d}\,\gamma_{LG}^{d}} - 2\sqrt{\gamma_{SG}^{p}\,\gamma_{LG}^{p}} \quad \text{[Eq 9]}$$

In this equation [Eq. 9], unknown variables are γ_{SG}^{d} and γ_{SG}^{p}. It is necessary to measure ϑ for two liquid with known γ_{SG} components, usually water (large γ_{SG}^{p}) and hexadecane (large γ_{SG}^{p}) and solve the system. However, all models designed for the computation of surface energy operate under numerous assumptions, such as the applicability of the Young equation to the surface. As a result, these models hold validity solely in the context of smooth surfaces. When for rough surfaces, calculated surface energy values are useful only as an assessment of changes in chemical composition.

7. CHARACTERIZATION

The characterization is fundamental step in materials science to understand the properties of the artifact. Wettability is the property most studied in this thesis work, to achieve the desired performance a combination of several properties is necessary. The study of the synthesis to obtain a given morphology and the characterization of the suspension obtained.

First, characterization of the synthesized suspension in the laboratory is necessary; knowledge of the nano properties of the materials allows anticipation of subsequent macro properties.

In fact, it is essential to know the size and Z-potential of the nanoparticles to ensure the efficiency of the synthesis carried out. In addition, spectroscopic characterization allows one to understand whether the functionalization process occurred during the synthesis.

The wettability and surface energy properties of a material have been described extensively the ADSA instrument is essential. However, to study the morphology of the coating the most widely used instrument is the scanning electron microscope (SEM), which allows accurate study both at the nano level, assessing the actual diameter of the nanoparticles and their shape, and a study at the macro level such as the homogeneity of the deposited coating and any defects on the surface.

Roughness is another key parameter in surface science. Many phenomena are related to the presence of asperity, defects and non-homogeneity of the coating. Investigating this parameter allows us to understand where to act to obtain a coating with better morphological characteristics. The instruments used for this property are non-contact profilometry for micron scales and Atomic Force Microscope (AFM) for nanometric scales.

7.1 Dynamic Light Scattering

Detection of light scattering from matter is useful technique with applications in numerous scientific applications, where, depending on the light source and detector, specific properties of molecules can be studied. In a typical light –scattering experiment, the sample is exposed to a monochromatic wave of light and an appropriate detector detects the signal. Einstein and Smoluchowski also established Brownian motion theory explaining molecular motion of particles. He established that particles were subject to random forces due to constant collision with solvent molecules resulting in random walk of particles, and that the mean squared displacement of particles due to Brownian motion is proportional to time[121].

When a monochromatic light beam interacts with a solution containing macromolecules, the light scatters in various direction based on the size and shape of the molecules. In static light scattering, the intensity of scattered light is analyzed as time averaged intensity, providing information about molecular weight and hydrodynamic diameter. On the other hand, by analyzing the intensity fluctuations caused by Brownian motion of macromolecules in solution, it is possible to obtain the diffusion coefficient, which is related to hydrodynamic size of the macromolecules.

The speed of Brownian motion is influenced by particle size, sample viscosity and temperature. In particular, the smaller the particle is, the more rapid the Brownian motion becomes.

Contrarily the larger the particle is, the slower the Brownian motion becomes. Moreover the higher temperature the more rapid the Brownian motion.

The translational Diffusion coefficient (D) can be converted into a particle size using Stokes-Einstein equation [Eq 10]:

$$D_H = \frac{kT}{3\pi\eta D} \text{ [Eq 10]}$$

Where d_H is the hydrodynamic diameter, k is the Boltzmann's constant, T is defined as the absolute temperature, η is the viscosity and D is the diffusion coefficient. Therefore, DLS analysis allows us to obtain hydrodynamic diameter of nanoparticles and not equal diameter. The hydrodynamic diameter is defined as size of the particle on any surface structure, as well as the type and concentration of any ions in the medium[122].

To make a measurement at DLS, the laser placed at 173° emits a beam of monochromatic light that goes into the cuvette (containing the suspension) and light is scattered. The scattered light is collected by a photon-counting device that converts the intensity of scattered light into the hydrodynamic mean diameter of the particle, the scheme represented in the Figure 23 below.

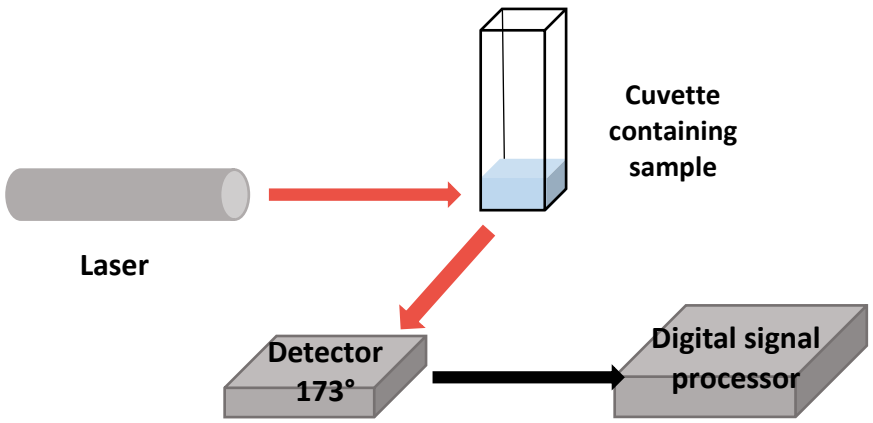

Figure 23 *Components of Dynamic Light Scattering Instrument.*

Electrophoretic light scattering (ELS) is a technique used to measure the electrophoretic mobility of particles in dispersion, or molecules in solution. This mobility is often converted to Zeta potential to enable comparison of materials under different experimental conditions. The fundamental physical principal is that of electrophoresis.

A dispersion is introduced into a cell containing two electrodes. An electrical field is applied to the electrodes, and particles or molecules that have a net charge, more strictly a net Zeta potential will migrate towards the oppositely charged electrode with a velocity, known as the mobility, that is related to their zeta potential[123].

The sample is collocated in the capillary cell. This cell consists of a tube joining larger chambers containing the electrodes. The tube is transparent, usually glass or quartz. This form of cell has the advantage that the electrodes can be large in area, which reduce the current density at the surface and ensure that any gas bubble produced is remote from the sample measurement performed in the central part of the capillary.

The relationship between frequency shift and mobility depends on the Q vector (optical arrangements and the electric field). If the field changing during the measurement due to polarization effects. Deriving Zeta potential or surface charge then depends on dealing with the effects of the ion cloud surrounding the sample particles[124].

Electrophoretic Light Scattering Technique (ELS) measures the Z potential of particles. The charged particles are put in motion by electrophoresis under the action of an electric field and their velocity is determined by the Laser Doppler Velocimetry (LDV) techniques by comparing the phase of the diffused light at 17° with that of a reference beam that does not cross the sample. From the velocity and the intensity of the electric field applied, the electrophoretic mobility was obtained. From such property, the zeta potential was derived based on a suitable model depending on the thickness of the electrical double layer. The zeta potential can be calculated from the electrophoretic velocity of the particles using the Helmholtz-Smoluchowski equation.

DLS and ELS measurement are made with Malvern Zetasizer Nano ZSP instrument. The suspension to be analyzed for particle size mixture are prepared by taking 1mL of pure suspension and diluting 10 times in the solvent in order, to prevent aggregation of nanoparticles and have false measurement. The diluted suspension (2mL) is taken and placed in the PCS8501 cuvette. For electrophoretic light scattering measurements, a few of diluted suspension is taken with a syringe and placed in the U-cell DTS1070.

7.2 Fourier Transformation Infrared (FTIR) spectroscopy

The Fourier Transformation infrared (FTIR) spectroscopy stand as the predominant approach for infrared spectroscopy. Due to its swifter pace, heightened sensitivity, and enhanced precision compared to antiquated methodologies[125]. Infrared (IR) spectroscopy serves as an analytical method grounded in the interplay between matter and infrared radiation, inducing vibrational shift in chemical bonds.

Infrared (IR) light constitutes electromagnetic radiation featuring wavelengths surpassing those of visible light yet falling short of radio waves, encompassing a span from 700 nm to 1 mm. The most captivating spectral range for spectroscopic investigations lies within 2.5 and 25µm, facilitating scrutiny into foundational vibrational pattern as well as rotational-vibrational behaviors among diminutive molecules[126] (Fig.24). Within this specific spectral domain, molecules engage in diverse vibration patterns: symmetrical or asymmetrical stretching which modifies bond lengths, alongside bending vibrations encompassing shifts in bond angle, achieved though twisting, rocking, wagging and scissoring motions (in Fig.24)[127]. A vibration mode absorbs light when the molecule's dipole moment undergoes cyclic alteration; these vibrations are denoted as being infrared active[128].

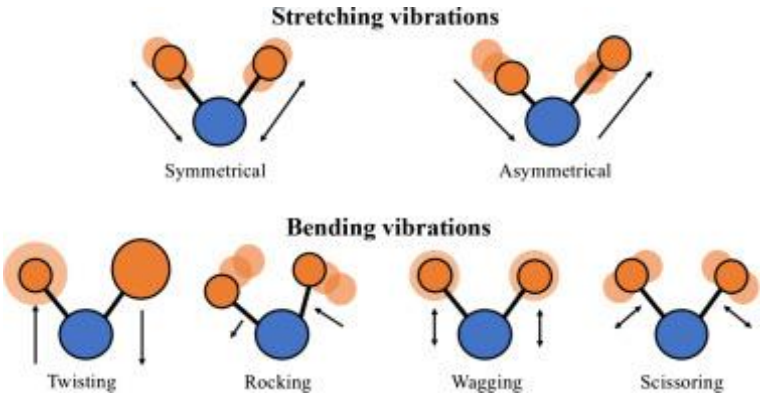

Figure 24 *Vibrational modes of bonds[78].*

IR spectroscopy finds application in the examination and characterization of functional groups presents in the sample. This is achieved by virtue of distinct functional groups exhibiting varying absorption frequencies of IR radiation, contingent upon the bond strengths and atomic masses inherent in the constituent elements. Each molecule possesses a unique spectrum, commonly termed as its "fingerprinting", enabling molecule identification through comparison with a spectral database[129]. Notably, IR spectroscopy proves highly advantageous for identifying and analyzing the structure of array of substances, spanning both organic and inorganic compounds.

Within a FTIR spectrometer, the IR light emanating from the source traverses a Michelson interferometer, composed of three mirrors, and subsequently encounters the sample. As the mobile mirror shifts its position over time, leading to alterations in light distribution, the transmittance of the sample undergoes temporal fluctuation.

The resultant light output is captured in the form of an "interferogram" which is transformed into a spectrum through Fourier transformation (in Fig 24). The presentation of an IR spectrum materializes as a graph (Fig. 25), with IR light absorbance/transmittance plotted along the vertical axis against wavenumber of frequency on the horizontal axis (expressed in cm^{-1})[130].

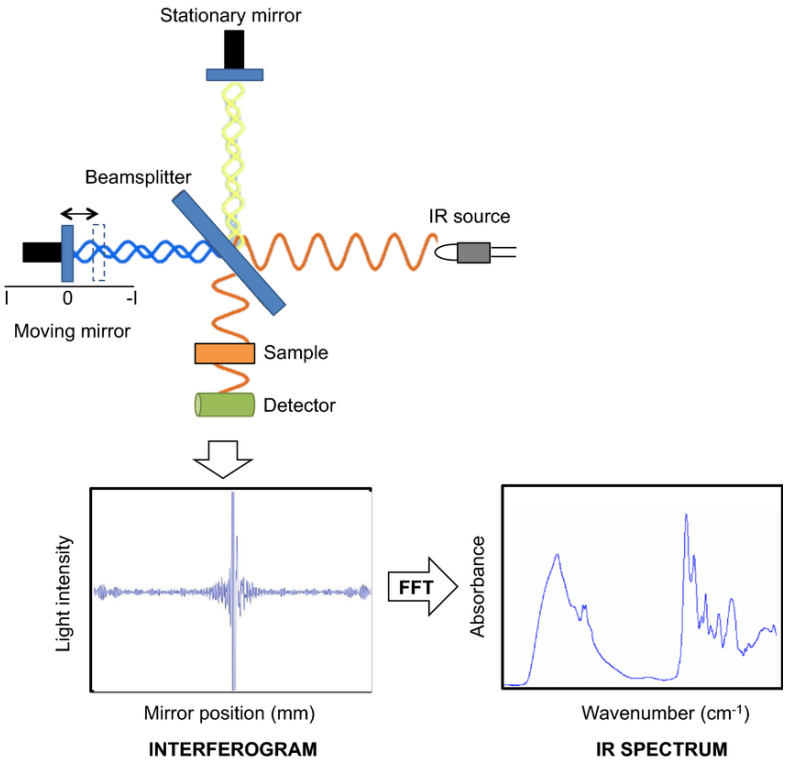

Figure 25 *Scheme of FT-IR spectrometer, highlighting the conversion of interferogram to IR through Fourier transform[130].*

Beyond the traditional absorption/transmission infrared spectroscopy, an alternative method rests on the principles of attenuated total reflectance (ATR). In this scenario, IR light traverses a high refractive index crystal, transparent to infrared, and undergoes numerous internal reflections. These internal reflections give rise to an evanescent wave that extends beyond the crystal's surface and into the adjacent sample, with which the crystal is in contact. Following interaction with the sample, the wave returns to the crystal, undergoing attenuation in IR light regions where the sample absorbs energy. Ultimately, the wave emerges from the opposite end of the ATR crystal and proceeds toward the detector[131].

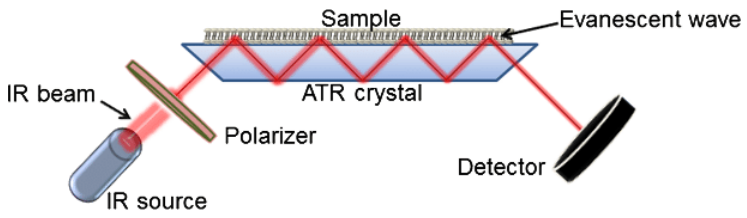

Figure 26 *Schematic representation of an ATR-FTIR system[132].*

The experimental setup employed in this study involved a FTIR spectrometer (Nicolet IS5, ThermoFisher Scientific, U.S.A.) (Fig. 26), coupled with an accessory designed for attenuated total reflectance (ATR) analysis, featuring a monolithic diamond crystal (iD7, ThermoFisher Scientific, U.S.A). This ATR technique enabled the analysis of liquid, bulk solids, and powder samples, circumventing the need for prolonged preparation procedures and addressing issue linked to the hygroscopic nature of common materials, (e.g. KBr) utilized in traditional FTIR analysis. Additionally, the typical errors originating from the viability of preparation methods could be minimized.

The ATR-FTIR analyses are done on samples in which nanometer layers have been deposited, given the transparent nature of organic layers to see any deposition or functionalization of nanoparticles after sol-gel synthesis, the coatings are subjected to FTIR analysis. All the spectra were acquired by accumulation of 16 scans covering the 4000 to 400 cm^{-1} range at resolution of $2cm^{-1}$.

7.3 Thermal Gravimetric Analysis

Thermogravimetric analysis, also known as thermal gravimetric analysis (TGA), is a thermo analytical method to use to track alterations in sample mass relative to temperature and duration, within a specified temperature regimen and under defined atmospheric condition. The TGA analyzer employs a thermo-balance (a fusion of an electronic microbalance with a furnace and suitable temperature control) to track changes in sample weight resulting from physical or chemical alterations such as dehydration, decomposition accompanied by volatile release, oxidation, or gas adsorption or desorption (represented in figure 27).

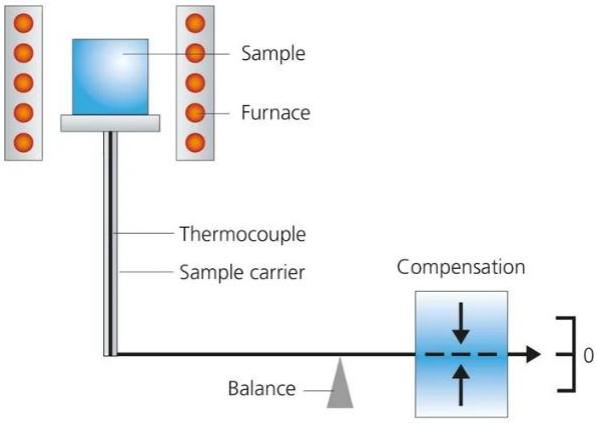

Figure 27 *Scheme of the measuring principal of thermogravimetric (TGA) analysis[133].*

The outcome is depicted as a thermogravimetric plot, or thermogravim, illustrating temperature or time on the x-axis against the absolute percentage change in mass on the y-axis.

In this study, TG analyses conducted using a STA analyzer (STA 449 C Jupiter, NETZSCH, Geräetebau GmbH, Germany), TGA was performed to examine the percentage of organic that is present on differently functionalized nanoparticles. The TGA tests were carried out

7.4 Scanning Electron Microscopy

Scanning electron microscopy (SEM) is one of the most employed imaging techniques in material science because it allows the observation of objects with magnification and resolution over 1000 times higher than optical microscopy. A scanning electron microscope (SEM) is an instrument that employs a focused beam of electrons to scan systematically the surface of a specimen in a patter resembling a grid, there by generating a high-resolution image.

Essential components of a typical SEM[134,135] (Fig. 28) are following:

- The electron source in a scanning electron microscope (SEM) consist of a cathode and an anode positioned at the top of the column. This source generates the electron beam crucial for imaging. There are two main categories of electron source: thermionic and field emission. In thermionic sources, the electron beam is emitted thermionically. This process involves applying a current to the cathode, causing it to heat up until its electrons acquire enough energy to escape the surface. Tungsten filaments are commonly employed in thermionic electron guns due to their high melting point and low vapor pressure. Alternatively, single crystal of LaB_6 and CeB_6 can also serve as emitters, although they necessitate high vacuum conditions, leading to increase costs.

Field Emission Guns (FEGs), on the other hand, utilize a potent electrostatic field applied to the sharp tip of a tungsten wire to induce electron emission. FEGs come in two types: cold-cathode, which employs single crystal emitters, and Schottky type. The latter employs tungsten single crystal coated with ZrO_2 and is thermally assisted. Schottky-type FEGs combine the advantages of both field emission and the thermionic effect. FEG sources have a smaller emission area compared to thermionic sources, resulting in improved image quality. However, the use of electrostatic fields in ultra-high vacuum conditions renders FEGs more expensive. The anode, positioned near the cathode, attracts the emitted electrons and accelerates them down the column.

- Electromagnetic lenses play a crucial role in a scanning electron microscope (SEM). they consist of several components(RIF):
    - Condenser lenses: there are composed of two lenses that work together to diminish the size of electron beam, effectively narrowing it down to a focus spot.
    - Scanning coils: these coils are responsible for deflecting the electron beam in both the horizontal (x) and Vertical (y) directions. By employing controlled deflections, the beam scans cross a rectangular area on the sample's surface.
    - Objective lens: the final lens in the electromagnetic system, the objective lens, is responsible for further concentrating the electron beam onto the sample's surface. This results in a further reduction of the spot size, contributing to higher resolution imaging.

  Collectively, these electromagnetic components work in harmony to manipulate the electron beam's size, position, and focus, enabling the SEM to create detailed and high-resolution images of sample's surface.

- Analysis chamber: this chamber is where the actual interaction between the electron beam and the sample occurs, and it operates under vacuum conditions to prevent electron scattering by air molecules.
- Detectors: various detectors are employed to gather the diverse signals produced because of the interaction between electrons and the sample. These signals encompass secondary electrons, backscattered electrons, X-ray, and others. The collected signals proved valuable information about the sample's surface morphology, composition and other characteristics.

- Software for image reconstructions: this software is responsible for processing the signals collected by the detectors. Each pixel in the resulting grayscale image corresponds to the positions of the electron beam on the analyzed sample. The resulting image serves as a distribution map, portraying the intensity of signals emitted from the scanned area. Through careful processing, this software generates a coherent and interpretable image that reveals valuable details about the sample 'surface characteristics.

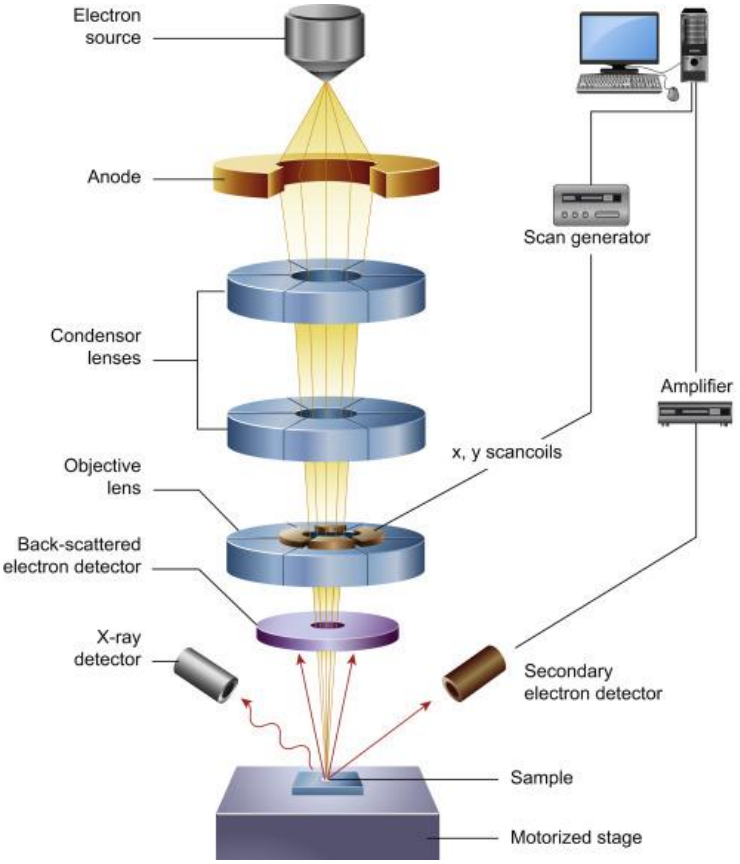

Figure 28 *Schematic of a Scanning Electron Microscope (SEM), showing the principal components*[136].

Upon impact of the primary electron beam onto the sample, a range of scattering phenomena and absorption occurs within a distinct teardrop-shaped volume termed the interaction volume (as shown in the Figure 29). The dimensions of this interaction volume can span from slightly less than 100 nanometers to around 5 micrometers into the materials. The depth and diameter of this volume are contingent upon factors such as the beam energy and the specimen's density. Specifically, the interaction volume will be more extensive for higher accelerating voltages, and for samples, comprising elements with a greater atomic number ($Z<90$)[135], it will be comparatively smaller.

The interaction between electrons and matter gives rise to various signals, as depicted in the figure 27 [135,135,137]. Of these signals, the most frequently examined ones include secondary electrons, backscattered electrons and X-rays.

- Secondary electrons (In Lens): these electrons are generated through inelastic interactions with the electron clouds surrounding sample atoms. This interaction prompts the emission of electrons from the sample. Secondary electrons have relatively low energy levels (less than 50 EV) and originate only a few nanometers beneath the surface. Consequently, they offer valuable insights into the sample's morphology and surface characteristics.
- Backscattered electrons (BSEs): BSE are electrons with relatively high energy levels (greater than 50 EV) that are reflected back after an elastic interaction between the electrons of the electron beam and the atomic nuclei within the sample. These electrons stem from deeper portions within the interaction volume. Although BSE are not particularly suitable for intricate morphological analysis, they serve as effective tools for discerning chemical compositional distinctions. This is due to the fact that heavy elements (with higher atomic numbers) tend to backscatter electrons more vigorously than lighter elements, leading to their brighter appearance in the resulting image.
- X-ray electrons: X-Ray are high-energy photons resulting from the excitation of deep electrons. They find application in elemental microanalysis.

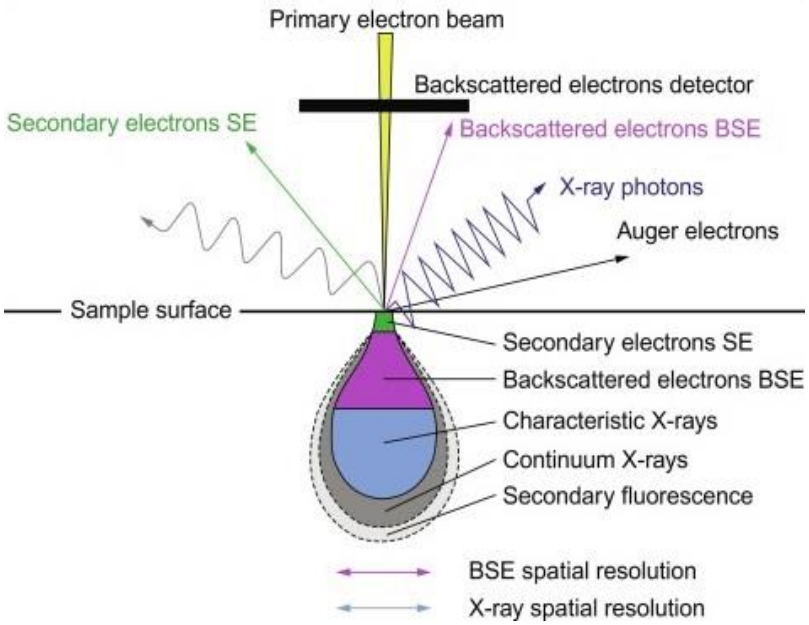

Figure 29 *Electron volume interaction with matter and various type of generated signals*[88].

This instrument then allows obtaining very high-resolution images, and specifically allows understanding both the surface defects and the shape of the nanoparticles that it have deposited on the surface. However, conventional SEM necessitates the use of solid materials that are conductive and can withstand the vacuum conditions typically within the range of 10^{-5} to 10^{-6} pressure units. This requirement established certain limitations on the types of materials that can be studied using the SEM. For insulating materials, such as those that do not readily conduct electricity, there are strategies to render their surfaces electrically conductive in order to be compatible with SEM analysis.

Specifically, for coatings deposited on non-conductive substrate a gold-base conductive layer is deposited.

The equipment employed in this work was a FE-SEM, i.e. field emission gun-scanning electron microscope, with W-ZrO_2, source with Schottky effect and hot cathode gun (Zeiss Sigma, Carl Zeiss Microscopy GmbH, Germany) equipped with detectors for secondary electrons SE2, low energy electrons SE1 and backscattered electrons BSE. For SEM analysis, all the samples were mounted on aluminum stubs with carbon tape. Non-conductive sample required a metal coating: non-conductive layer was coated a thin layer of 5nm of gold using a turbo-pumped sputter coater (Q150T ES, Quorum Technologies Ltd, UK).

7.4 Fluorescence Microscopy

A fluorescence microscope combines the magnification capabilities of an optical microscope with the fluorescence emitting properties of specimens' compounds. The process involves using a high intensity light source to illuminate the sample. The sample is treated with fluorophores, which absorb the intense light emitted by the source and re-emit it with a longer wavelength and lower energy. The resulting fluorescent light is separated from the surrounding radiation using specialized filters, allowing the observer to see only the fluorescing material. Fluorescence microscopy is widely used in biology[138].

The fundamental function of a fluorescence microscope is to allow excitation light to illuminate the specimen and subsequently distinguish the much weaker emitted light in the resulting image. This process involves the following steps:

- Excitation filter: the microscope is equipped with a filter that selectively permits radiation with a specific wavelength corresponding the fluorophore used.
- Excitation and emission. The excitation light interacts with the atoms in the specimen, causing electrons to be elevated to higher energy levels. When these electrons return to lower energy states, they emit light.
- Emission filter: to make the emitted fluorescence visible to the human eye, it is separated from the much brighter excitation light by a second filter. This separation works because the emitted light has a longer wavelength and lower energy compared to the illumination light[139].

The microscope used is the Ti-E microscope (Fig. 30) allows for detailed examination of specimens, such as cell cultures, biomaterials and, 3D cultures on innovative supports, both in bright field and fluorescence models. With fluorescence-labeled antibodies, it is possible to study not only cellular morphology but also to assess cellular activities by visualizing specific proteins and biomolecules of interest. Additionally, the Ti-E features a time-lapse system, enabling the real-time observation of live cells to study their behavior, for example, in response to a new release system like a drug delivery system. This microscope is equipped with exclusive Perfect focus System (PFS), which automatically corrects focus and, drift in real-time during extended time-lapse imaging session. For image analysis, the microscope used an advanced software called NIS Elements AR, which is comprehensive for 3D image acquisition. Moreover, the software includes a deconvolution module for digital image enhancement using a dedicated algorithm.

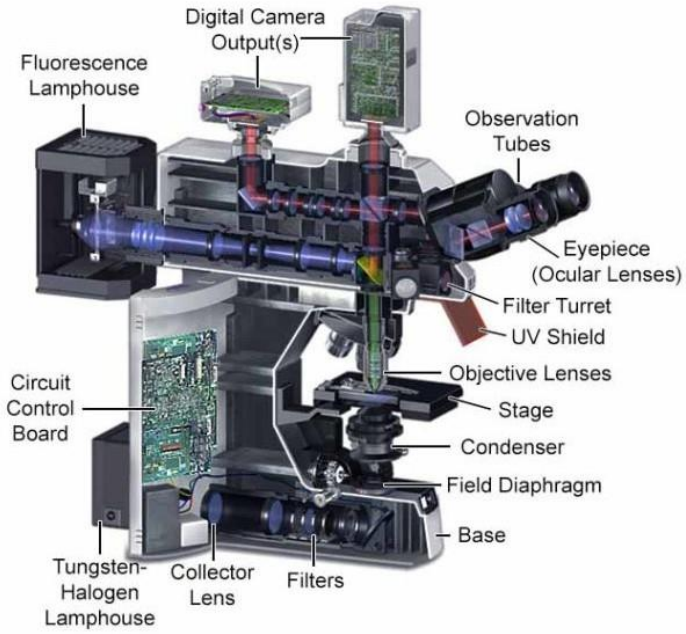

Figure 30 *Schematic of Fluorescence Microscope*[138].

7.5 Non-contact Profilometry

In this thesis, morphological analyses of surfaces where different layers were deposited were performed; the purpose of the analysis is to understand the thickness and roughness deposited through the selected technique. The instruments used is interferometric profilometer Contour GT-K 3D (Bruker, Germany) on sample with different measured. Then the data were analyzed using the commercial software Vision64 Map.

Profilometry represents a methodology employed to scan and chart the topography of an object's surface. In conventional contact profilometry, a mechanical stylus engages the surface to trace its features. Nevertheless, this approach runs the risk of modifying or potentially impairing those very features. In contrast, non-contact optical profilometry attains surfaces morphology without causing harm, thanks to its utilization of light as the probing mechanism. Optical profilometer encompass a diverse array of measurements principles, one of which is the interferometric measurement mode. This technique hinges on the concept of interferometry: the light beam sourced divides into two identical rays, each traversing distinct paths. One ray interacts with the sample's surface, while the other engages a mirror; subsequently, these rays reunite at the beam splitter before converging on the detector (CCD sensor).

The discrepancy in the optical paths taken by these rays induces a phase alteration, giving rise to an interference pattern[140]. A simplified representation of a interferometric profilometer is illustrated in Figure 31[141].

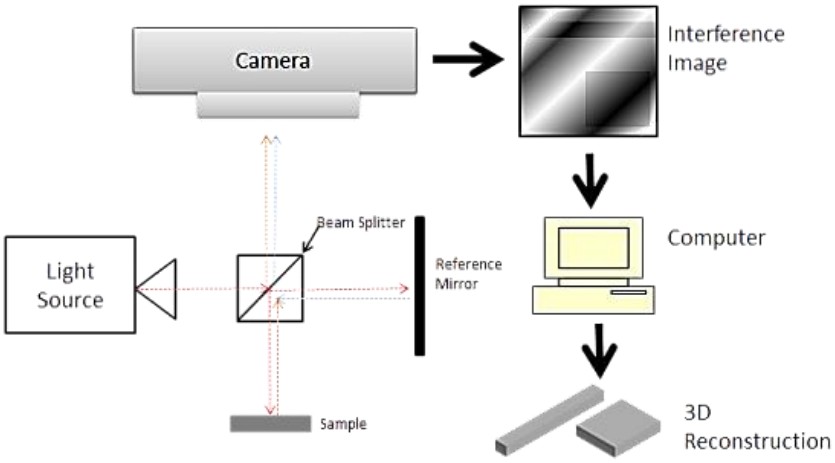

Figure 31 *Schematic of an interferometric profilometer[92].*

7.6 Atomic Force Microscope

The atomic force microscope (AFM) is an instrument capable of visualizing the surface topography of a material with nanometer resolution and providing information on mechanical, electrical, and magnetic properties of the surface of nano-materials such as nanodots, nanotubes and nanofibers. AFM scans the surfaces using a micrometers radius tip the end of a rod (cantilever). The tip interacts with the surface, flexing the cantilever. As the topography or other surface properties change, there is a change in the interaction with the tip, thus allowing the surface topography to be reconstructed. The use of these instruments for micro-nano structured surfaces allows to measure surface roughness, not possible with optical measurements.

The Atomic Force Microscope (AFM) stands out as a potent tool for exploring the surface properties and structure of materials at the nanometric scale. Unlike some techniques, the nature of the surface and the environment are not significant limitation in AFM. This device facilitates the determination of various material characteristics, such as conductivity or insulation, softness or hardness, and differentiation between inorganic and organic materials. Additionally, AFM allows for the measurement of geometrical morphology, adhesion, friction, surface impurities, identification of different regions of the surface, elasticity, distribution of the surface electrical charges, and the polarity of various electrical point[142,143].

The AFM device features an exceptionally sharp and delicate head attached to an elastic probe known as a cantilever. The opposite end of this cantilever is connected to a piezoelectric arm.

To enhance the reflection of the laser beam, crucial for informing the orientation of the cantilever in space, the back of the pulsar is coated with a thin metallic layer.

By applying suitable voltage to the piezoelectric arm in the x, y, and z directions, it becomes possible to precisely shift the cantilever attachment spot to any desired point in three-dimensional space with angstrom level precision[144].

The apparatus operates by employing a cantilever with a finely pointed tip to its extremity to traverse the sample surface (Fig. 32). During this, traversal attractive or repulsive forces manifest between the tip and the sample. These forces, often arising as Van Der Waals interactions but also encompassing alternatives such as electrostatic and hydrophobic/hydrophilic forces, prompt a deflection in the cantilever's position. This deflection is gauged using a laser (depicted in Fig.31), which is projected onto the cantilever and subsequently detected by photodiodes. The collection of additional light by one of the photodiodes generates an out but signal that is then processed, furnishing insights into the cantilever's vertical bending. This dataset is then relayed to a scanner that orchestrates the probe's height modulation as it navigates the surface. The scanner 'manipulation of height deviations is subsequently harassed to generate a three dimensional topographic depiction of the sample[145].

The mode to operate in the laboratory is tapping mode. In this mode, the cantilever is externally oscillated at its fundamental resonance frequency (Figure 31). A piezoelectric on top of the cantilever is used to adjust the amplitude of oscillation as the probe scans across the surface. The deviations in the oscillation frequency or amplitudes, there are due to interactions between the probe and surface are measured, and the surface providing information about the surface or types of material present in the sample. This method is gentler than contact AFM since the tip is not dragged across the surfaces, but does require longer scanning times. It also to provide higher lateral resolution than contact AFM[145].

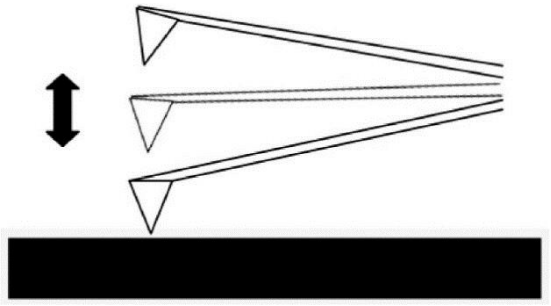

Figure 32 *Diagram of probe and surface interaction in tapping mode[145].*

The most common application of AFM is for morphological studies in order to attain an understanding of topography of the sample. In particular, it is used to have an idea of the thickness and roughness of the layer, and of the size of the nanoparticles on the surface.

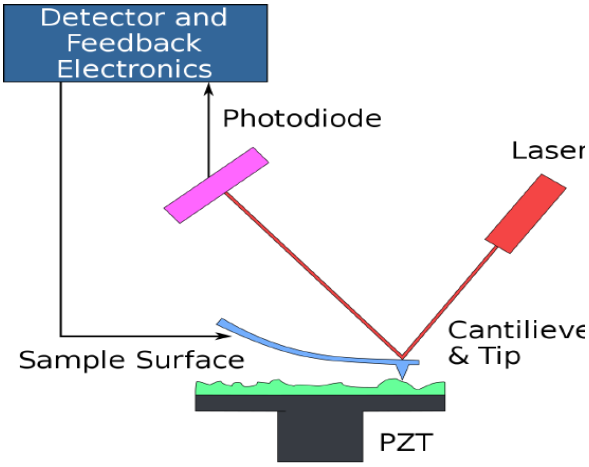

Figure 33 *Simple schematic of atomic force microscope (AFM) apparatus. Adapted H.G Hasma, department of Physics, University of California, Santa Barbara*[94].

The sample size analyzed with AFM have a dimension 2 x 2 cm and typical height of 1 mm. Coatings analyzed at AFM are first observed by SEM microscopy to see if they are homogeneous over entire surface so that during AFM analysis there is no risk of cantilever breakage (Fig 33).

8. COATINGS COMPOSITION PROCESSING

8.1 Alumina based coatings

Aluminum substrates

In my thesis project, different materials typically used as structural part or components of marine vehicles were selected and coated as described below. Aluminum alloy (Al) was the most studied one since already optimized process were made available from a previous knowledge development at ISSMC. The roughness of Al substrates, showed in Figure 34, expressed by Ra and Rz values, were, respectively, 0.231±0.037 µm and 1.327±0.394 µm as measured by the optical profilometer (BRUKER Contour GT-k 3D) on a 25 mm^2 area with Gaussian regression filters (cut-off filters: ʎ short =25µm and ʎ long =0.8 mm).

Aluminum samples were dip coated with alumina sol-gel, the synthesis of which is described in previous section 3.1.

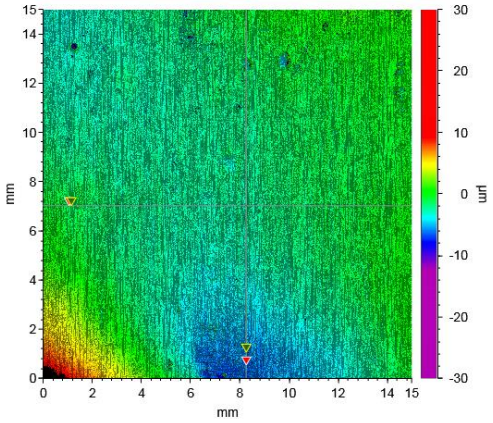

Figure 34 *Aluminum substrate surface profilometry, the surface is completely smooth, as indicated by the colorimetric scale.*

An immersion/withdraw the speed of 2 mm/s was adopted, with a soaking time is 5s. After dip coated, the samples underwent a first thermal treatment (TT) at 400°C for 1h. This annealing step allowed for a complete drying of the film, removal of organic components, completion of condensation and densification, with positive effects on mechanical properties[110].

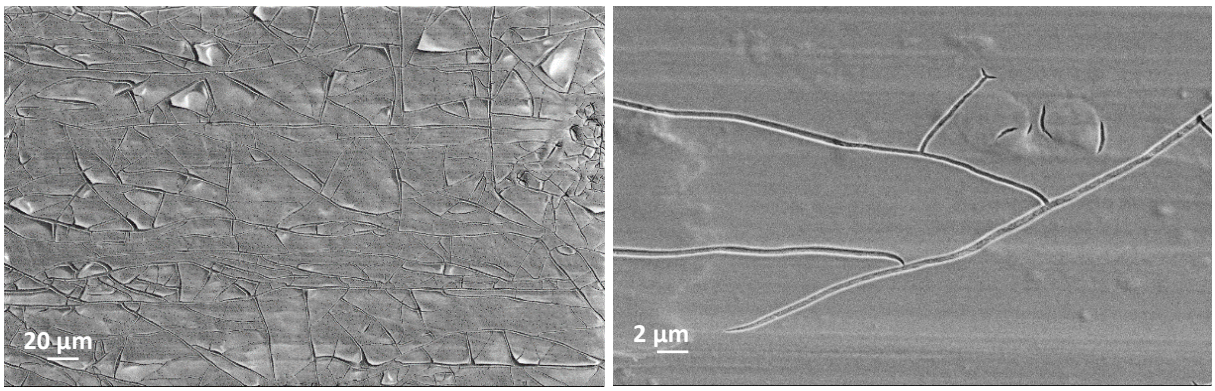

Figure 35 *SEM morphology of aluminum coated with Al_2O_3 in IPA after first heat treatment (400°C 1h).*

The morphology of the coating after the first heat treatment is shown in the micrographs of Fig. 35.

The alumina deposition and the heat treatment led to the formation of a smooth layer, which already presented some crack along the surface. The formation of intrinsic stresses, that could represent a critical issue, is maximum when the condensation takes place during the treatment.

By settling a more stable nanoparticle suspension, the occurrence of the condensation is restricted. As a result, the occurrence of cracks, primarily attributed to variations in thermal expansion coefficients between the substrate and capillary pressure due to evaporation of the solvent, will be minimized. For the same purposes, some authors[111,112] highlighted the beneficial influence of chelating agents in reducing cracks development during heating.

After the first TT, alumina based coated substrate were cooled in air environment and then treated in boiling water. The literature indicates that alumina (Al_2O_3) undergoes a reaction with hot water, resulting in the formation of boehmite (AlOOH) showcasing a distinct flower-like arrangement reminiscent of a desert rose[83]. This particular structure and the dimension of nano-sized pores among the lamellae, allow to entrap air and generate significant anti-wetting capillary pressure[146].

In this project, boehmite was formed through immersion for 30 minutes of alumina coated substrates in boiling deionized water. These conditions were adopted according to the work of Feng et al. [147], who indicated this timeframe as optimal for attaining superhydrophobicity on such a surfaces. Moreover, an additional thermal treatment was carried out to promote a thorough drying and consolidation of the coating to ensure the retention of the flower-like[148] morphology. Treatment temperature was the same as in the previous annealing step, but treatment time was shorted to 10 minutes, as no organic species had to be eliminated. The morphology after boiling treatment is depicted in figure 36.

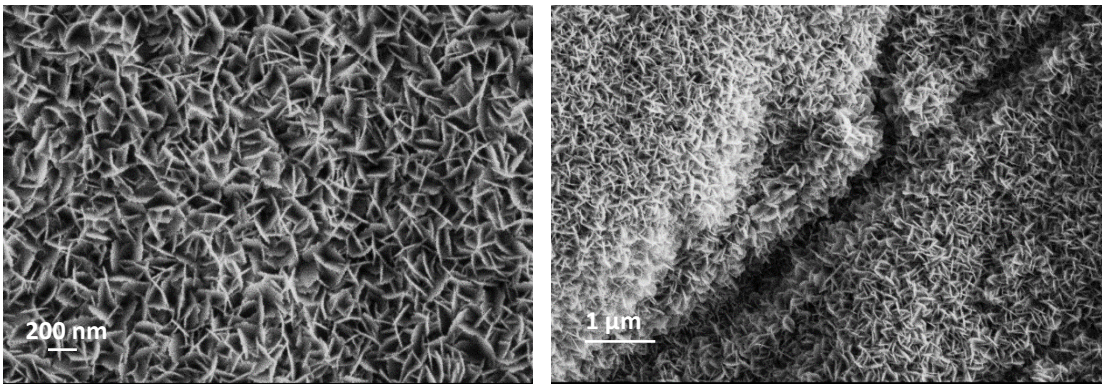

Figure 36 *Morphology SEM of aluminum coated with Al_2O_3 in IPA after boiling treatment (90°C 30 min).*

The flower like structure, with about 200 nm long nanopetals, is easily detectable, as is covers homogeneous the entire surface.

Steel substrate

The other substrate under investigations was AISI 316 stainless steel. The compositions of the alloy is shown in the table 9.

Table 9 *Composition of AISI 216 steel*

Components	Carbon	Chrome	Nickel	Molybdenum
%	0.03	16-18	8-13	2-3

Stainless steel substrates were coated as described for aluminum alloy in the previous paragraph. After processing, the Al_2O_3 coating is homogeneously on surfaces but there are more cracks on the surface it is formed during drying is quite evident (Fig. 37).

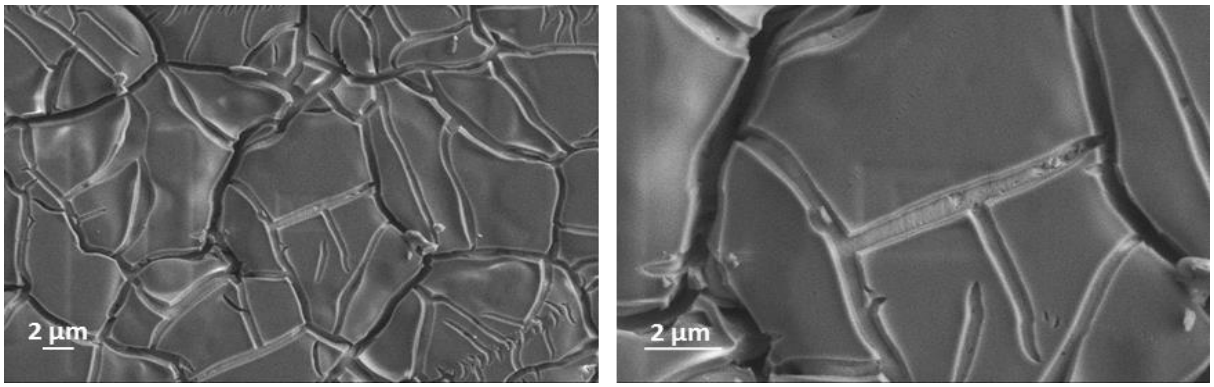

Figure 37 *SEM morphology of an Al_2O_3 (IPA) coated steel substrate after drying.*

Due to great difference between steel (1.7 x 10^{-5}/ °C) and for alumina is (8 x 10^{-6} /°C) thermal expansion coefficient, the thermal consolidation was performed at 200°C per 1h to avoid cracks formations.

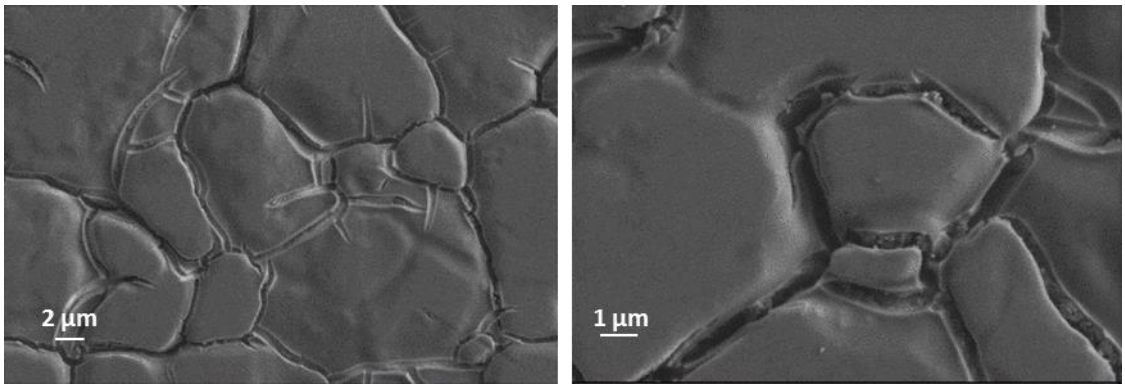

Figure 38 *SEM morphology of an Al_2O_3 (IPA) coated steel substrate after heat treatment at (200°C 1h).*

In the Figure 38, it is observed that the coating is still present after thermal treatment notwithstanding the presence of cracks on the surface. In this case, the flower-like structure is obtained by immersion of samples in water kept at 90°C. As reported by Tadanaga et al.[149] , it is not necessary to reach boiling temperature since the formation of oxide-hydroxide alumina begins even when the water reaches 60°C. Addition, boiling could damage the alumina coating if the adhesion between the substrate and the oxide layer is not optimized. On this aspect much work was done to activate the surface by chemically modifying it through, for example, a preliminary etching treatment[150].

A suggested by many authors, first etching treatment could involve the washing of surfaces in acetone for 10 minutes in an ultrasonic bath, followed by immersion in 2M HCl for 30 seconds. Then, the samples are treated with H_2O_2 35% wt (2mL), left in solution for 10 minutes and, finally washed in ethanol and air dried[150].

A second type of etching, according to N.U Taskin[151] (2021), involves the washing in ethanol for 10 minutes, a subsequent immersion in a 1:1 HNO_3/H_2O_2 solution for 7 minutes, then rinsing with distilled water and air-dried.

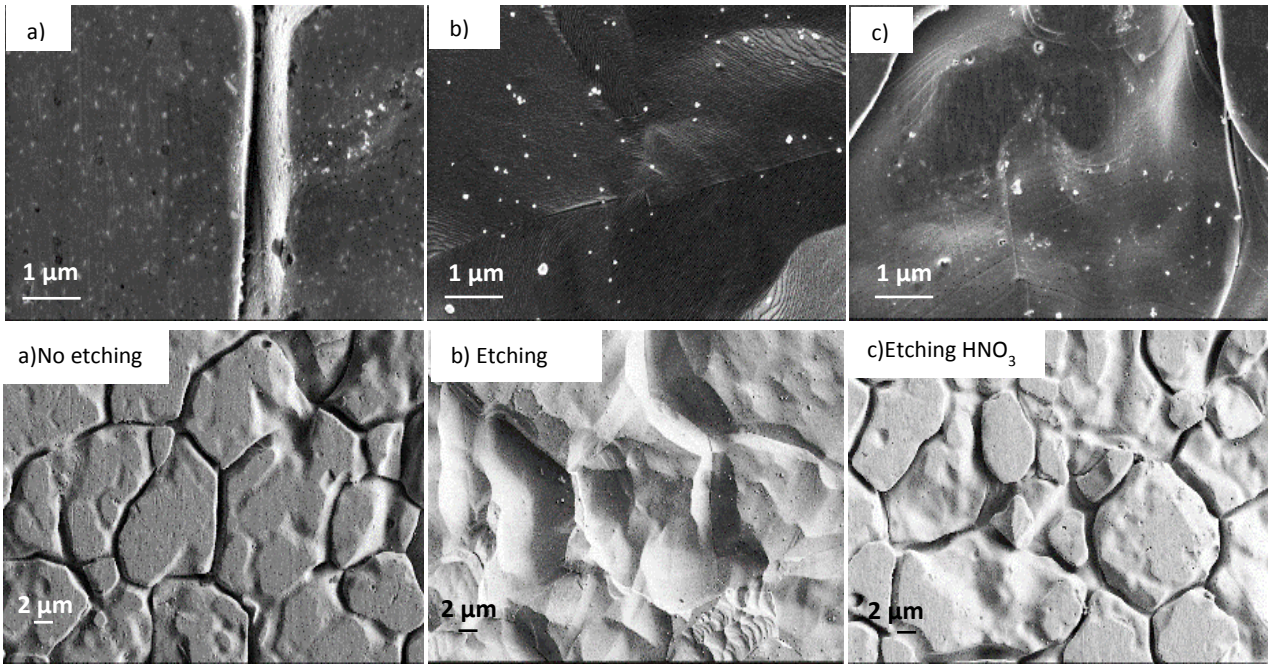

Figure 39 *SEM morphology of steel substrate a) without etching b) after etching treatment with HCl c) after etching with HNO_3.*

Figures 39 a), b) and c) compare, respectively an untreated steel with HCl and HNO_3 etched specimens. It can be observed that HCl treatment introduce significant surface roughness variation (Fig. 38 b), while the oxidizing one involves small morphological effects.

The same analyses were performed on steel surfaces after the deposition of alumina sol-gel film and thermal treatment. According to figure 40 a-c, when coating is deposited on samples that underwent preliminary acid etching (Figure 40 b and c), a reduction of both crack number and extension is detected.

The figure Fig. 40 below, one compares the coated samples after undergoing etching. One notices that in figure b and c where acid etching occurred, there is a reduction in crack formation, which also they appear to be less extensive.

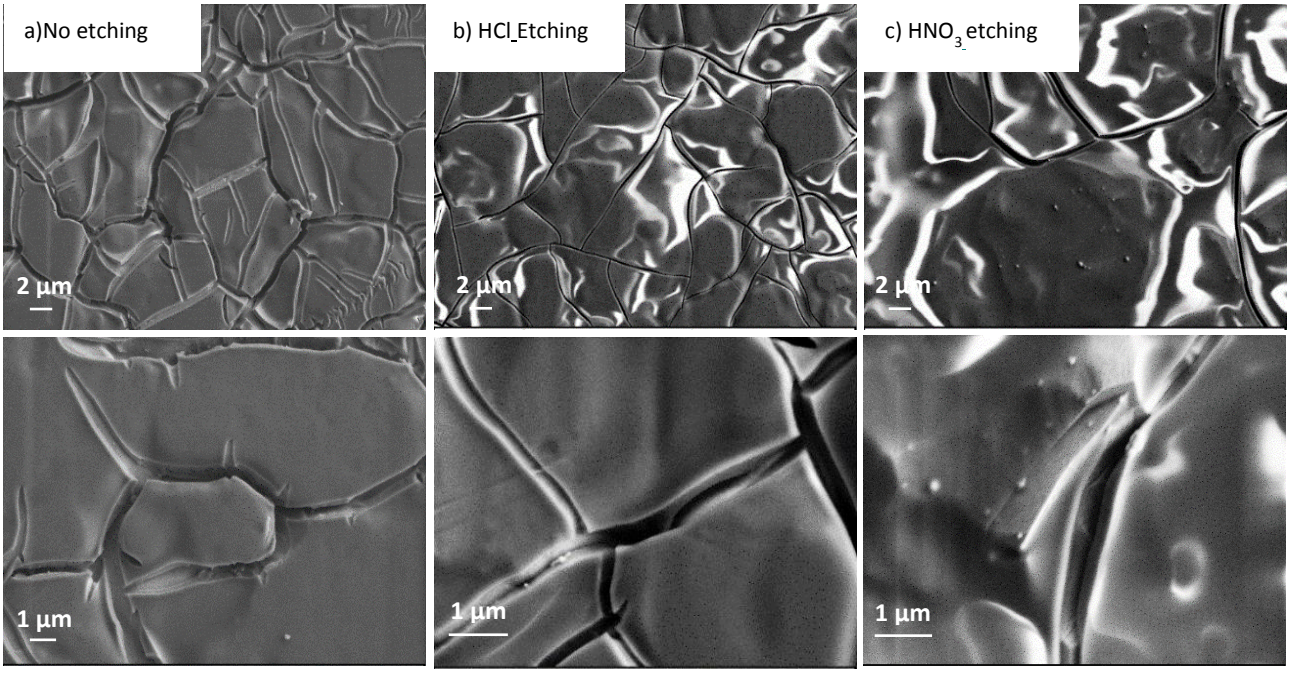

Figure 40 *SEM morphology of steel substrates coated with Al_2O_3 and heat treated at (200°C 1h) a) not etched substrate b) HCl etched c) HNO_3 etched.*

In addition, with hot water performed at 90°C on etched surfaces (Fig. 41) helps to avoid the exfoliation phenomenon and, so that the flower-like nanostructure is correctly obtained.

The boiling treatment was carried out only on the sample etched with HNO_3 acid, because the alumina coating deposited on steel after etching treatment has smaller cracks than both the untreated and the HCl etched ones.

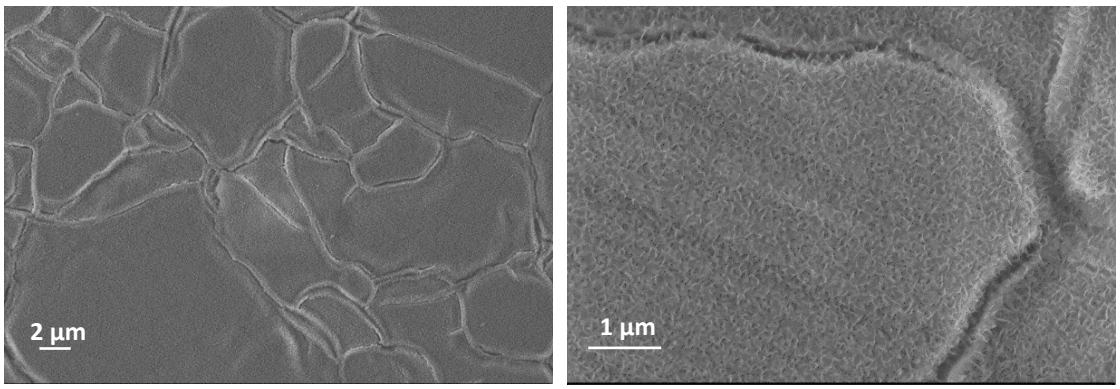

Figure 41 *SEM morphology of HNO_3 etched steel substrate coated with Al_2O_3 after hot water treatment (90°C 30 min). Higher magnification observation confirms the presence of flower like structure.*

Fiberglass substrate

The third material, selected in this work as substrate, is a low viscosity bisphenol A modified epoxy resin, adequately formulated for the infusion lamination process. The resin, which is a commercially available product, is cured with cycloaliphatic amine and furtherly modified with a post heat treatment after curing.

The composite consists of six layers of epoxy resin and glass fibers according to the lamination sequence. The material's face selected to be coated is the flat one (front) well distinguishable from the other one (back) appearing more wrinkled both visually and to the touch, with residual signs of the cushion mesh used and traces of release material.

The front face was observed under a scanning electron microscope (SEM) for a comparison of surface topography before and after coatings deposition. The uncoated surface appeared uneven, with micrometer-sized bumps as highlighted in Figure 42 A e B.

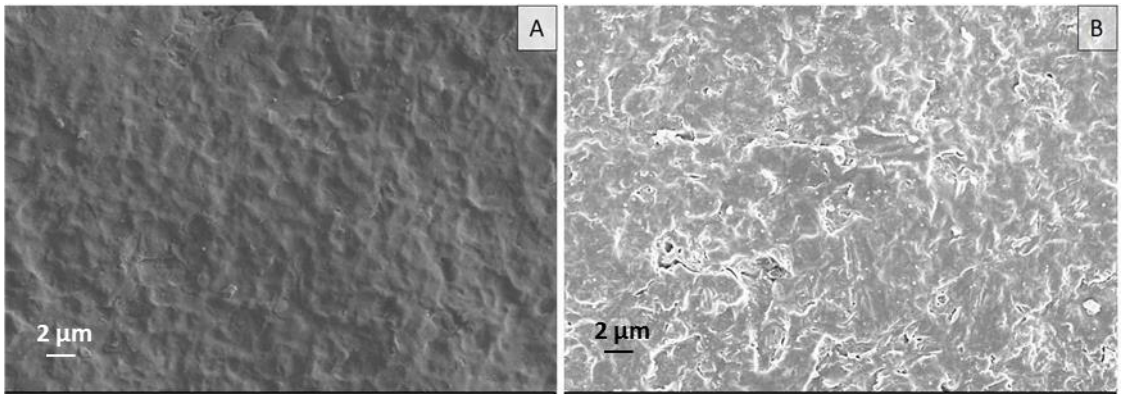

Figure 42 *SEM micrograph of the surface of the fiberglass epoxy composite. The image shown in A) was acquired with the secondary electron detector while the image in B) was reconstructed by the primary electron detector.*

Optical profilometry was used to evaluate the fiberglass roughness (Fig.43) without any coatings, for a later evaluation with inorganic coatings. The roughness parameters of fiberglass substrate measured at the profilometer and Ra = 2.53µm Rz (statistics) = 60.58 µm.

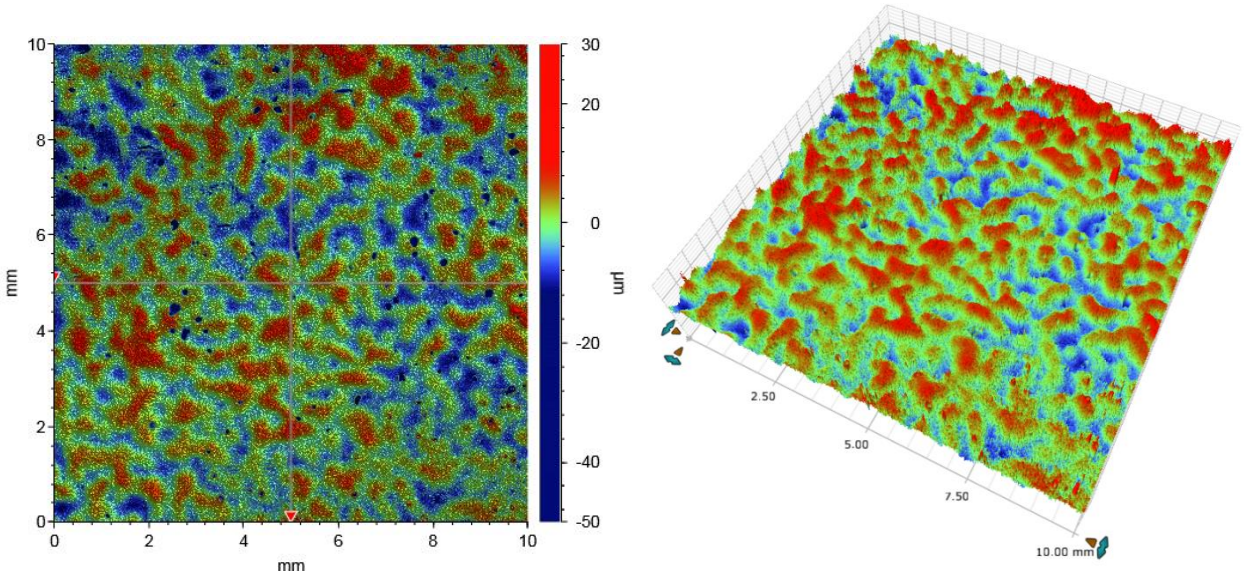

Figure 43 *Optical profilometer image of fiberglass substrate.*

The composite has the mechanical properties shown in table 10; in particular, the transition temperatures were taken into account for planning the deposition strategy of the superhydrophobic coating.

Table 10 *Mechanical properties of composite resin.*

Tensile strength (ASTM D 638)	65 ÷ 75 N/mm^2
Elongation at break	6.0 ÷ 7.0%
Tensile module (UNI5819)	2400 ÷ 3000 N/mm^2
Flexural strength (ASTM D790)	95 ÷ 110 N/mm^2
Hardness (ASTM D 15)	86/90
Flexural modulus (ASTM D790)	2400 ÷ 3200 N/mm^2
Compressive strength (UNI 4279)	90 ÷ 110 N/mm^2
Glass transition temperature	75 ÷ 85°C
Max transition temperature	70 ÷ 98°C
Water absorption [24h at room temperature]	0.1/0.2%
Water absorption [2h 100°C]	0.6/0.7%

Before coatings deposition, fiberglass substrates were preliminary washed with plenty of soap and water. They were then rinsed with deionized water and dried one by one with compressed air. Subsequently, they were washed with a great amount of ethanol in order to remove all the residual surfactant and then dried with compressed air.

The sequence of Al_2O_3 deposition steps on fiberglass was revised with respect to the previous one due to the nature of fiberglass itself and the peculiar mechanical properties; in particular, the deposition rate and the consolidation temperature were changed, while a treatment in the vapor phase (instead of liquid immersion) was introduced for the surface structuring.

Firstly, different emersion rates - from 1 to 16 mm/s – were adopted and thereafter, samples left upright until the solvents completely dried. The thermal consolidation was performed at 40°C for 24h, allowing, anyway, the complete solvent evaporation and the improvement of superficial adhesion. The data (to be presented later) showed that the optimal emersion rate is 4 mm/s. It is necessary to proceed with the treatment in hot water to obtain the flower-like morphology. The heat treatment in steam flow for 30 minutes ensured the formation of nanostructured boehmite over the whole surface of the sample keeping itself below the glass transition temperature during the process. The steam chamber was made with a holed basket of 30 cm in diameter inside which the samples were fixed with the face to be coated facing the direction of the steam flow. After the steam flow treatment, the samples were left to dry in a humidity-controlled chamber until completely drying. The figure 44 A-C shows the surface appearance (SEM micrographs) after the steam treatment.

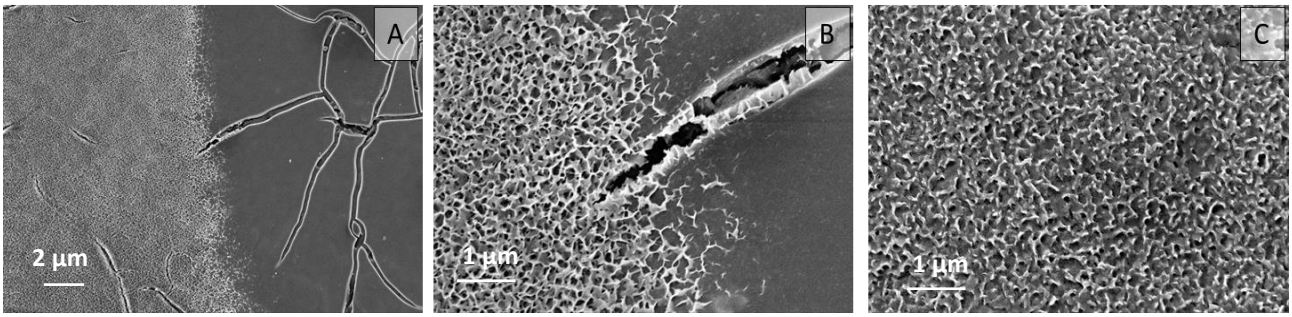

Figure 44 *SEM micrographs of fiberglass surface with nanostructure boehmite coating A) Area of the surface where both a properly coated (left side) and an uncoated are observed; B) detail of the transition area C) detail of the boehmite with flower-like nanostructure.*

8.1.1 Organic layer deposition

For any material, the increasing of hydrophobicity depends not only on physical modifications (increasing the roughness) but also on the chemistry of the surface aiming at lowering the surface energy.

In literature, numerous molecules have been shown to efficiently reduce surface energy, typically thought the introduction of non-polar C-C and C-H bonds or highly stable C-F bonds. For instance, many authors have reported successful modifications of metal oxides with long alkyl chain[103,104], fatty acid[1,152] and organic chains in which hydrogen has been replaced by fluorine. These types of compounds, however, form a weak bond with the underlying oxide. A promising alternative is the use of silane molecules functionalized with chains strengthening the bonds among layer. In addition, when compared with alkyl compounds, silanes have good thermal stability above 100°C[153]; whit this requirement being key point to consolidate coatings in high-performance manner. Two types of silane have been selected:

- The first is a fluoroalkylsilane (FAS) solution named Dynasylan SIVO Clear EC (manufactured by Evonik, Germany), that exhibits excellent superhydrophobic performance[154,155]. FAS is deposited by various techniques, specifically dip coating and spray coating. In this work, the use of commercial product in this case ensured the reproducibility.
- The second silane is a laboratory-prepared solution of silane with three methoxide group and an organic chain with 16 carbons, hexadecyltrimethoxysilane (95 % HTS, Sigma Aldrich). In order to have superhydrophobic performance, the chemical compound must be diluted. In previous work a 6% dilution in ethanol has been optimized. In this way, the methoxide chains will react with the underlying oxide, and on the surface, the long alkyl chain will be exposed. The dilution is necessary to ensure that the chains do not overlap with each other, achieving the desired wettability performance.

The solution was affixed to the samples through a dip coating method employing the same immersion withdrawal speed as the deposition of inorganic sol (2mm/s). However, the soaking time was extended to 2 minutes to facilitate the interaction between the inorganic layer and the molecules present in the solution. The lengthened soaking time does not influence the ultimate performance. Once the organic layer has been deposited it is necessary to proceed with a heat treatment. Given the organic nature of both the fluorinated and the alkyl compound, the consolidation takes place no later than 150°C for 30 minutes.

Optimization of organic coatings on metal and composite substrates after coating Al_2O_3

The dip-coating deposition of the above organic coatings has been optimized for steel and fiberglass substrates. For aluminum substrate, on the other hand, the deposition process has been optimized above, both for the fluoroalkylsilane and silane with a long alkyl chain.

The functionality of alumina coating with organic compounds is aimed at increasing the superhydrophobicity of the coating; in fact, the goodness of the deposition process is evaluated according to the static and dynamic contact angle.

The table 11 shown the wettability data of the coating of FAS and HTS deposited by dip-coating on alumina substrate coated with Al_2O_3 flower-like, with emersion withdrawal speed 2mm/s and stasis times 120s.

Table 11 *Static (WCA) and Dynamic contact angle(CAH) of different organic layer deposited on Al_2O_3 flower-like inorganic layer, standard deviation of data is also shown.*

Organic layer	WCA (°)	ACA (°)	RCA (°)	CAH (°)
FAS	172 ± 1	158 ± 1	157 ± 1	1 ± 1
HTS	171 ± 3	163 ± 3	159 ± 5	4 ± 3

Steel substrate

The deposition of organic layer is optimized for steel substrate. In a first step, the deposition conditions of fluoroalkylsilane remain unchanged, dipping/withdrawal speed 2mm/s and soaking time 120s. Previously the deposition and heat treatment of the alumina flower-like layer has been optimized. However, to evaluate the quality in terms of not only morphology but also wettability, for each variable changed a layer of organic fluorinated was deposited.

A scheme in table 12 of the deposition and treatment variables carried out on AISI 316L steel.

Table 12 *Sample of steel treated by different condition of heat treatment, boil conditions and etching pretreatment.*

Sample	u [mm/s]	I TT[°C]	Boil [°C]	Etching	NOTE
1	2	400	100	/	
2	2	200	100	/	
3	2	200	90	/	
4	2	200	90	HCl/H_2O_2	
5	2	200	90	HNO_3/ H_2O_2	
6	2	200	90	/	No II T.T post boiling
7	2	200	90	HNO_3/ H_2O_2	No II T.T post boiling

The static and dynamic contact angles measured with water and the surface energy calculated using hexadecane apolar liquid are reported in table 13.

Table 13 *Static (WCA) and Dynamic (CAH) and surface energy of steel coated with Al_2O_3- FAS treated at different conditions, standard deviation of data is also shown.*

Sample	WCA H_2O [°]	CAH H_2O [°]	γ_{SG} [Nm/m]
1	122 ± 4	79 ± 11	4.72
2	138 ± 8	43 ± 7	3.00
3	147 ± 5	67 ± 5	1.77
4	139 ± 5	103 ± 4	1.56
5	134 ± 3	85 ± 10	2.11
6	152 ± 1	90 ± 6	1.53
7	165 ± 4	9 ± 3	2.00

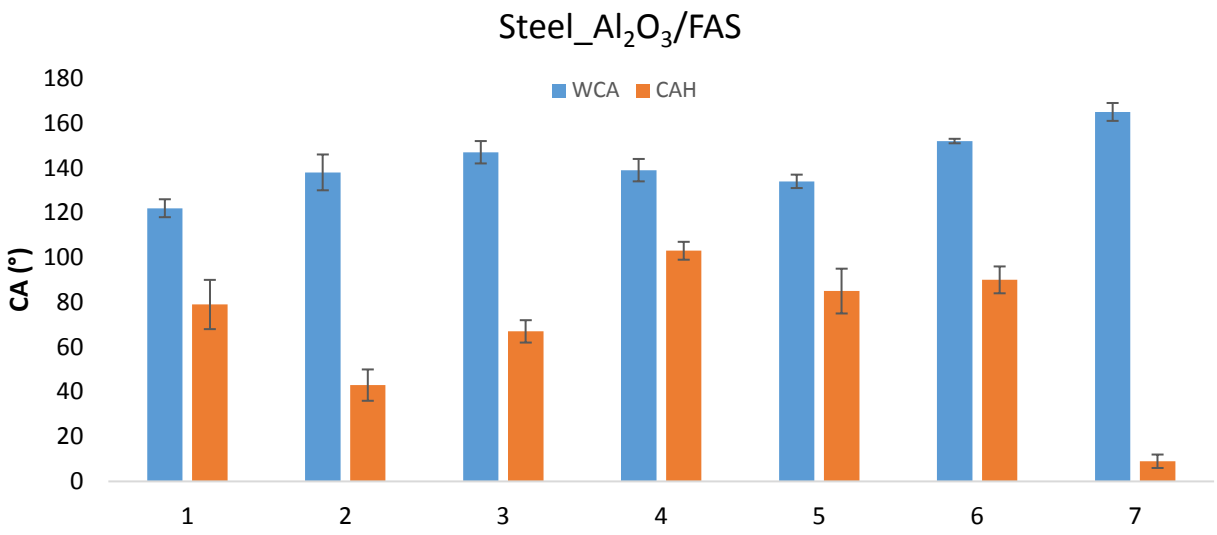

Figure 45 *Static (WCA blue) and dynamic (CAH orange) contact angle measurement on steel coated with Al_1O_3/FAS at different condition.*

From data shown in the table 12 and in the graph Fig. 45, it is clear that static wettability data are obtained in the range of the hydrophobic for any change made during the optimization process of the alumina structuring flower-like. However, an important improvement is achieved for the steel sample with etching HNO_3/H_2O_2, which after the boiling at 90°C has no exfoliation defects and an optimal static and dynamic wettability for superhydrophobicity. The surface energy of the coatings, excluding the sample 1, is less than 5 mN/m.

The deposition process of the alkyl silane on the steel substrate has been optimized. In this case, we worked on the parameters of withdrawal speed (1) and soaking time (2) during the dip-coating process. In addition, the HTS solution was diluted in alcohol to 6% (a) and 12% (b). For contact angle measurements, an inorganic coating based on alumina is deposited in order to best assess the hydrophobicity of the coating as follows: etching pretreatment with HNO_3/H_2O_2, dipping/withdrawal speed Al_2O_3 in IPA at 2mm/s and soaking time 5s, heat treatment at 200°C 1h, boiling 90°C for 30 min and air drying.

The table 14 shows the deposition parameters and immersion time for the alkyl layer and the contact angle.

Table 14 *Advancing (ACA), receding (RCA) and Hysteresis (CAH) contact angle of steel coated with Al_2O_3 and HTS at different conditions, standard deviation of data is also shown.*

Sample	% HTS	Deposition rate [mm/s]	Immersion time [min]	ACA(°)	RCA(°)	CAH (°)
1_0.1a	6	0.1	2	98 ± 7	83 ± 5	15 ± 3
1_0.1b	12	0.1	2	86 ± 1	34 ± 5	52 ± 4
1_2a	6	2	2	88 ± 3	52 ± 14	36 ± 16
1_2b	12	2	2	87 ± 2	26 ± 2	62 ± 2
1_10a	6	10	2	89 ± 2	52 ± 6	37 ± 3
1_10b	12	10	2	90 ± 2	72 ± 5	18 ± 5
2_5a	6	2	5	85 ± 1	37 ± 5	48 ± 5
2_5b	12	2	5	86 ± 2	36 ± 5	49 ± 5
2_30a	6	2	30	85 ± 1	44 ± 5	41 ± 5
2_30b	12	2	30	85 ± 1	40 ± 12	45 ± 12
2_60a	6	2	60	85 ± 2	32 ± 7	54 ± 8
2_60b	12	2	60	83 ± 1	50 ± 11	33 ± 11

Method_1: alumina process as describe above, immersion time HTS 120s and rising emersion rate (u): 0.1, 2 and 10 mm/s.

Method_2: alumina process as described above, immersion rate 2mm/s and stasis time in ascending order: 5, 30 and 60 min.

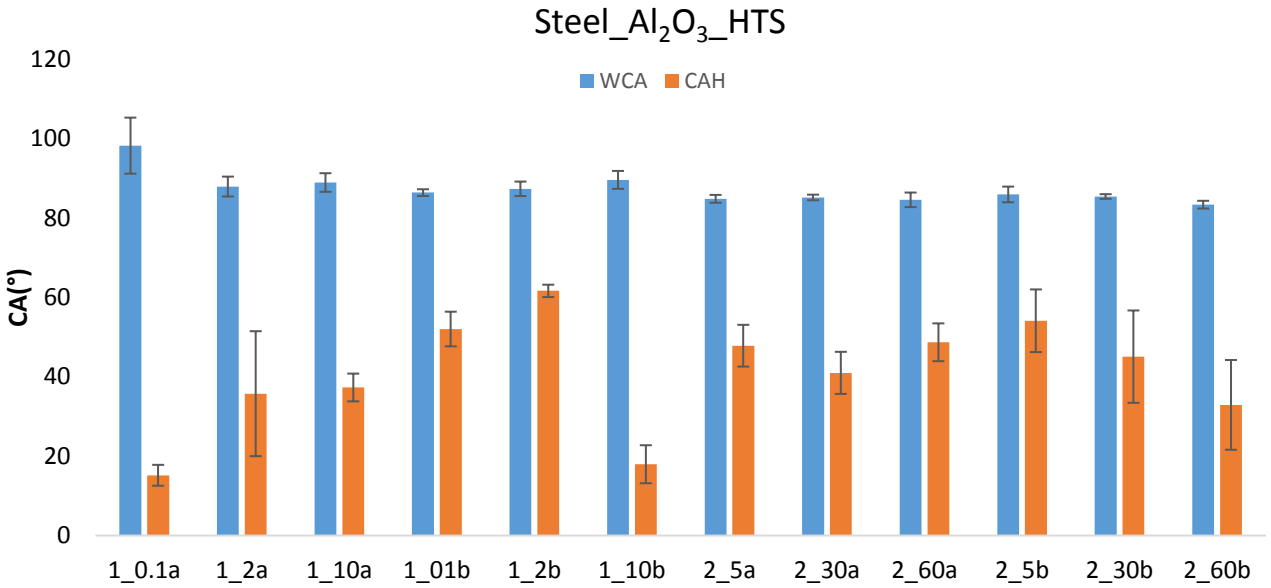

Figure 46 *Static (WCA blue) and dynamic (CAH orange) contact angle of Al_2O_3 –HTS coating with organic layer deposited at different conditions.*

From the Fig. 46 and the table 14 can be deduced that:

- The percentage of HTS in ethanol in order to obtain high performance coatings in terms of static and dynamic contact angle is 6%.
- Low-speed deposition (0.1mm/s) results in very low hysteresis (CAH=15°).
- Soaking time of more than 2 minutes, does not lead to any improvement in terms of superhydrophobicity of the coatings.

The deposition of hexadecyltrimethoxysilane on steel by dip-coating allow to obtain a hydrophobic coating (WCA~ 90°) if diluted to 6%, moreover the optimal conditions of deposition are 0.1 mm/s withdrawal speed and 2 minutes soaking time.

Fiberglass substrate

Given the particular nature of the substrate, the deposition process of Al_2O_3 has been extensively described in the previous paragraphs, introducing several changes both in the thermal consolidation phase and for the treatment in boiling water. The emerging rate of the alumina has been optimized, in particular the withdrawal speed from 1 to 16 mm/s have been adopted, keeping the soaking time unchanged at 5 seconds. After the previously described morphological characterization, to appreciate the wetting properties of the coating a fluorinated organic layer has been deposited with a withdrawal speed of 2mm/s and a soaking time of 2 minutes. In this case, the sample is left in air for 12h as thermal consolidation and ensure adequate grafting of the organic layer. Wettability and surface energy data of coating on fiberglass substrates where the inorganic layer has been deposited at different rates of deposition and FAS is deposited at V_{imm}=2 mm/s and t_{imm}=2 minutes.

Table 15 *Static contact angle (WCA) and surface energy of fiberglass coated with Al_2O_3 and fluoroalkylsilane deposited at different emersion rate, standard deviation of data is also shown.*

Sample	Emersion rate [mm/sec]	WCA [°]	γ_{SG} [Nm/m]
Al_2O_3-FAS_1	1	108 ± 15	15 ± 3
Al_2O_3-FAS_2	2	128 ± 18	12 ± 3
Al_2O_3-FAS_4	4	133 ± 6	8 ± 3
Al_2O_3-FAS_16	16	144 ± 14	1 ± 1

From the table 15 it can be deduce that the withdrawal speed of the dip-coating process of 4 mm/s allows the achievement of a satisfactory and homogeneous superhydrophobicity over the whole treated surface, in particular, a static contact angle (WCA) of more than 130° with less dispersion around the mean value.

8.1.2 Coating by SLIPS approach

The infusion with lubricating oil (Fig. 47) was conducted on all types of substrate already functionalized with hybrid coating Al_2O_3/FAS and Al_2O_3/HTS. Two types of lubricating oils have been used. The first one based on PTFE of the commercial series Krytox®, while, the second is a silicone oil with viscosity 100cst (Sigma-Aldrich). The selected lubricating oils have three different formulations Krytox®103, Krytox®105 and Krytox® 107. The increasing number indicates an increases in polymer length, which reflects an increase in oil viscosity (table 16).

The presence of fluorine in the oil makes it suitable for use as a lubricant for coatings that have fluorinated molecules as organic coating, to allow a chemical anchorage between the molecules and improve the oil retention capacity in porosity. Silicone oil 100CSt has been selected instead for SLIPS coatings that have organic fluorine free layer below, in order to improve the retention of lubricating oil.

The oil is deposited either with manual brush technique for the sample longer than 4 cm^2, or for spin coating for small samples (< 2 cm^2). After the lubricating film is deposited, the surfaces are left in air for about 24 hours in order to remove excess lubricant by dripping.

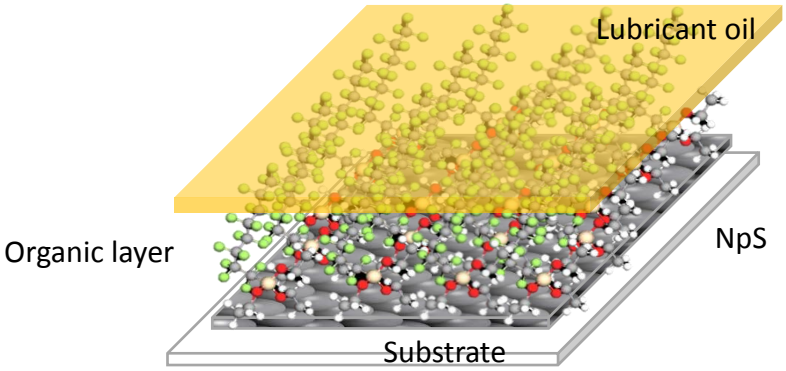

Figure 47 *Representation of different layer that composed the coating obtained by SLIPS approach. The substrate (white) is coated by an inorganic layer (grey) and organic layer (molecular structure), and infused with lubricant oil (orange).*

Table 16 *Physical characteristic of lubricant oil.*

Lubricant oil	Surface tension γ [mN/m]	Viscosity μ [cSt]	Density ρ [g/mL]
Krytox® 103	16.6 ± 0.04	7	1.87
Krytox® 105	17.4 ± 0.01	80	1.92
Krytox® 107	18.3 ± 0.08	550	1.94
Silicon oil 100	20.9	95-105	0.96

The lubricant replaces air of the nanoporosities of the inorganic coating. This allows having a dynamic repellence to liquids similar and better to the SHS surfaces improving the performance of resistance to higher-pressure loads, abrasion resistance and the ability of self-healing.

8.2 Silica based coatings

8.2.1 Fluorinated silica based coatings

Fluorinated silica was deposited on three substrates described earlier. It is necessary to distinguish two types of fluorinated silica in the two different solvents, namely ethanol and isopropyl alcohol.

As described above, the optimization of SiO_2-F synthesis in ethanol was assessed. Each fluorinated silica suspension was deposited on an aluminum substrate with withdrawal speed of 2 mm/s and soaking time 120s. The TT used is 150°C for 30 minutes. The choice of the most suitable silica synthesis was made on the basis of contact angle of coated specimens, contact angles provided during the suspension ageing, and surface morphology.

Table 17 takes overview of the molar ratio adopted by the different batches of SiO_2F synthesis.

Table 17 *Different batches of SiO_2F with different molar ratio.*

Sample	Molar ratio TEOS:PFTOS
SiO_2-F #1	1:0.2
SiO_2-F #2	1:0.3
SiO_2-F #3	1:0.4
SiO_2-F #4	1:0.5
SiO_2-F #5	1:0.6

The table 18 shown the static (WCA) and dynamic angle (CAH) values by the different SiO_2F batches.

Table 18 *Static (WCA) and dynamic (CAH) contact angle measurements by different SiO_2F batches after deposition on aluminum, standard deviation of data is also shown.*

Synthesis	WCA (°)	CAH (°)
SiO_2-F #1	152 ± 6	81 ± 14
SiO_2-F #2	158 ± 3	57 ± 11
SiO_2-F #3	149 ± 2	127± 14
SiO_2-F #4	154 ± 8	121 ± 10
SiO_2-F #5	128 ± 7	113 ± 9

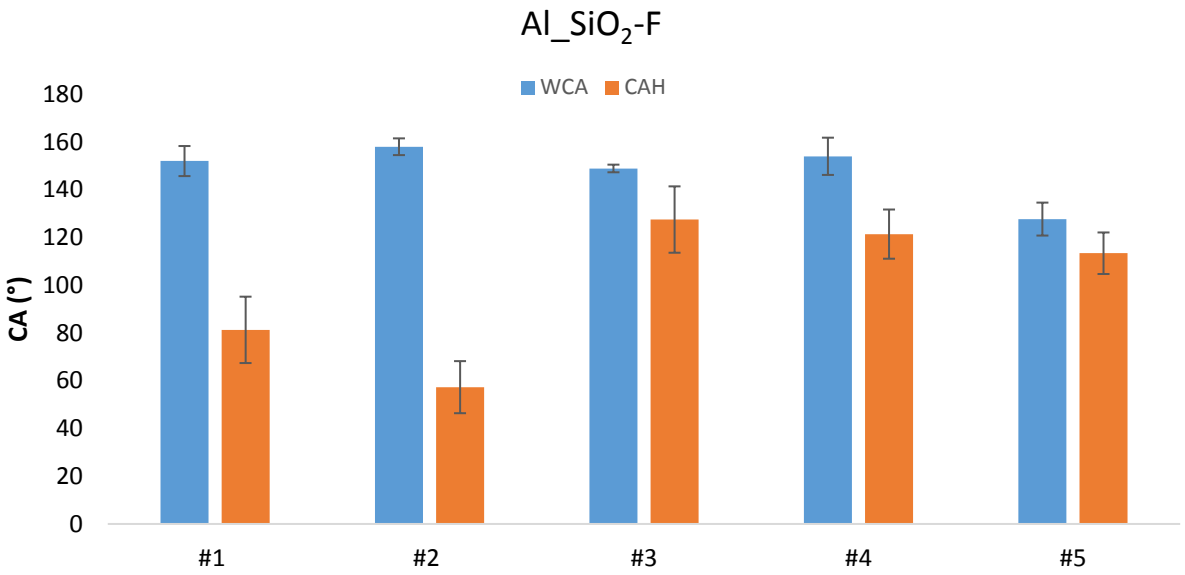

Figure 48 *Water Contact Angle (WCA) and contact Angle Hysteresis (CAH) value for aluminum coated with different synthesis of SiO_2F at time t0 aging.*

In Fig 48 show that the synthesis from #1- 4# the static angle values are about 150° with small standard deviations confirming the superhydrophobicity of the layer deposited with a single dip coating step. However, the dynamic angle is very high; in fact, it is observable during the measurements a pinning effect on the sample.

To see if the pinning phenomenon during synthesis aging is still observable, the dynamic contact angles at various significant times, specifically at 7, 15 days after synthesis, are measured.

Table 19 *Static and dynamic contact angle measurement of different SiO_2F synthesis at different aging, standard deviation of data is also shown.*

Aging	Day 0	Day 7	Day 15
Sample	**CAH (°)**	**CAH (°)**	**CAH (°)**
SiO_2-F #1	123 ± 6	119 ± 11	123 ± 19
SiO_2-F #2	57 ± 11	22 ± 16	24 ± 18
SiO_2-F #3	127 ± 14	81 ± 25	19 ± 3
SiO_2-F #4	121 ± 10	51 ± 3	22 ± 3
SiO_2-F #5	113 ± 9	128 ± 6	134 ± 3

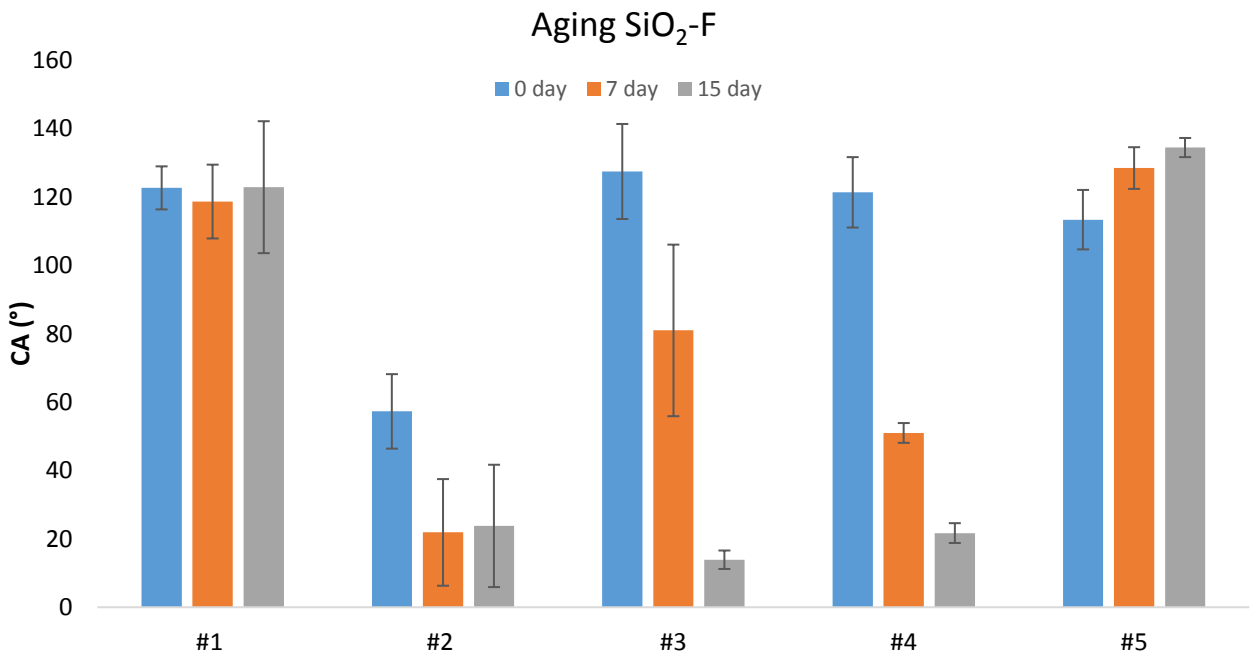

Figure 49 *Dynamic contact angle CAH of different fluorinated silica synthesis at different aging.*

The table 19 and graph in figure 49 show the dynamic contact angle of fluorinated silica coatings on aluminum at different synthesis aging times, namely 0, 7, and 15 days. The syntheses #1 and #6 having the lowest and highest molar ratio of TEOS: PFOTS tested for this synthesis show a contact angle that remains unchanged over days. On the other hand, for molar ratios between 1:0.2 and 1:0.6, lowering of the hysteresis angle and consequently a decrease in the pinning effect on the surface as the synthesis ages is noted in Fig 49.

It is important to observe the morphology of the coating that has deposited on the aluminum samples. The photos were taken with a SEM microscope.

From the photos SEM in the Fig. 50, it can be seen that:

- Some coating in figure 50 (a, b, c) are not homogeneous, in fact the substrate was seen.
- Two particles sizes are seen, one larger (400 nm) less present on the surface and one smaller (200 nm) that covers the surface.
- The presence of “amorphous” material is observed, a reagent that did not structure during the sol-gel reaction.

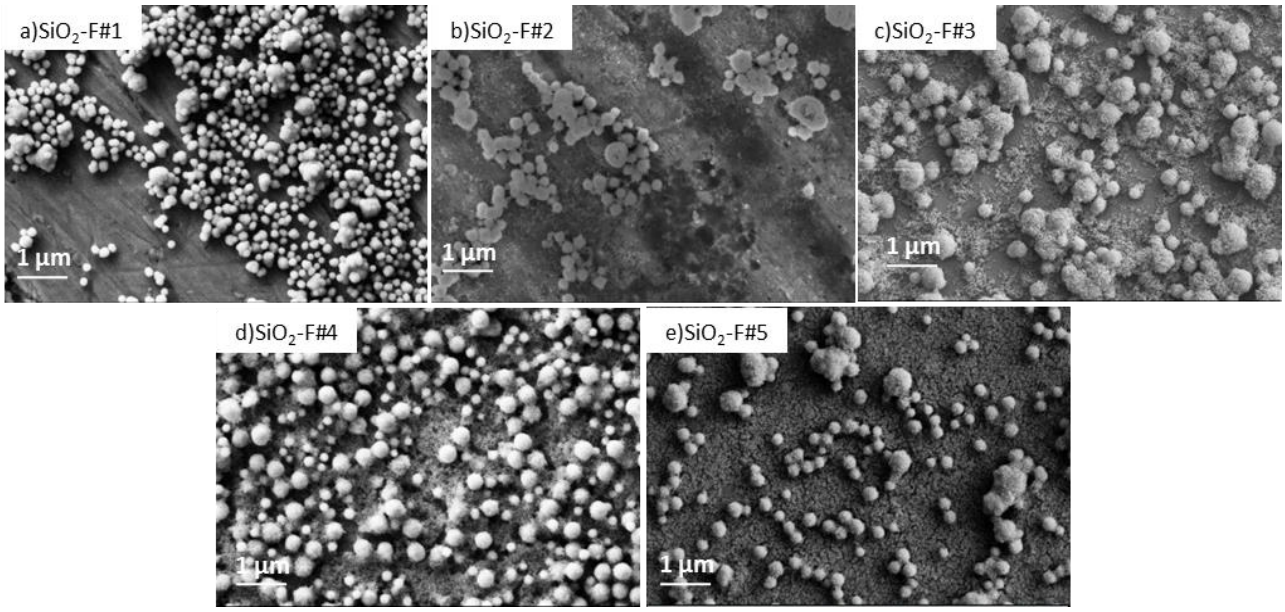

Figure 50 *SEM micrographs of SiO_2F deposited on aluminum a) Synthesis #1 b) Synthesis #2 c) Synthesis # d) Synthesis #4 e) Synthesis #5.*

The presence of amorphous material on the surface can explain why the fluorinated silica layers have a very static contact angle but a widespread pinning effect on the surface.

The reason for the change of solvent in the synthesis is due precisely to ensure that the entire reagent is structured during the sol-gel synthesis.

In the previous paragraph, the synthesis of fluorinated silica nanoparticle in isopropyl alcohol is described, presenting a nanoparticle size around 170 nm. The SiO_2-F in iPrOH is deposited by dip coating technique at 2 mm/s for 120s and TT is 150°C 30 min, on aluminum substrate. Static and dynamic wettability is monitored up to 60 days of ageing.

Table 20 *Static (WCA) and Dynamic (CAH) contact angle of SiO_2F #6 coating deposited at different aging of the synthesis, standard deviation is also shown.*

Sample	Day aging	WCA (°)	CAH (°)	γ_{SG} [Nm/m]
SiO_2-F #6	0	132 ± 3	113 ± 7	36
	7	148 ± 13	131 ± 25	26
	15	150 ± 3	26 ± 3	25
	60	172 ± 2	4 ± 4	23

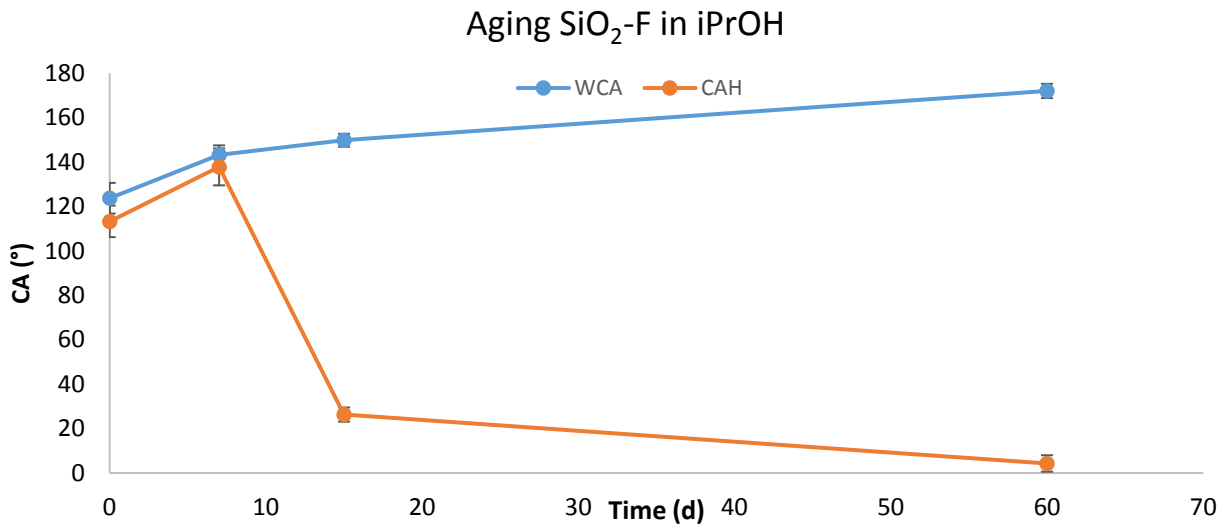

Figure 51 *Trend of static contact angle (WCA blue) and dynamic contact angle (CAH orange) of aluminum coated with SiO_2F in iPrOH aging at different time.*

The table 20 and figure 51 data reveal that, over the time, WCA of Al surface coated by fluorinated silica improves up to a maximum of about 170° while CAH value as low as 4-5° can be detected at the end of aging period, confirming that the pinning effect tends to disappear. The increasing of superhydrophobicity over the time is probably attributable to the improvement of F moieties on the nanoparticles surface. Correspondingly, in fact the surface energy 60 days the energy drops to 22mN/m. Figure 52 shows the morphology of the coating deposited on aluminum.

In figure 52, it can be seen that SiO_2F of different sizes are present on Al surface, smaller nanoparticles diameter being < 100nm. The layer is quite homogeneous over the entire surface with no amorphous phase seems to be present. Owing to all these factors, hereafter silica nanoparticles suspension in isopropyl alcohol based coatings have been adopted as suitable for the experimental work.

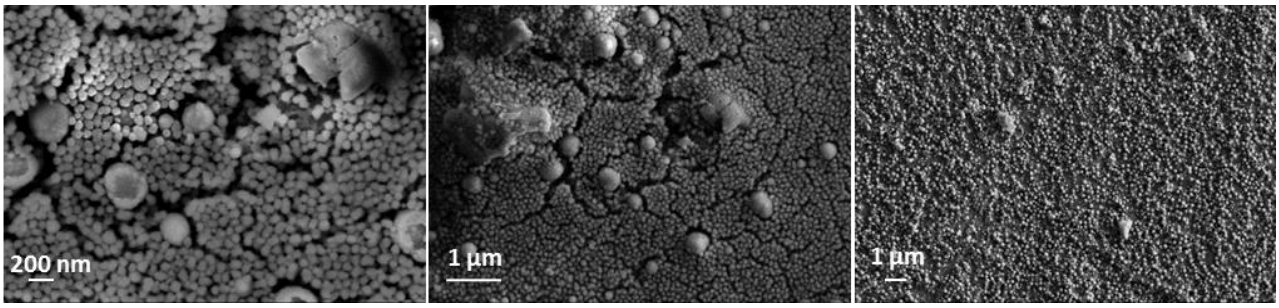

Figure 52 *SEM micrographs of aluminum coated with SiO_2F at different magnifications.*

Thickness of fluorinated silica nanoparticles based layer

The coating's thickness is a key variable for mechanical, optical and wettability properties. For this reason, coating thickness was measured as a function of withdrawal speed adopted during dip-coating. Samples were prepared by a dipping/withdrawal speed at withdrawal of 0.1, 2, 4, 10, 20 mm/s, and then their sections, analyzed by SEM. As the figure 53, a monolayer film is obtained at the minimum deposition speed 0.1 mm/s, then the thickness start to increase with the withdrawal speed. Due to the different size of nanoparticles, the coatings thickness could be different along the entire surface, as certificate by the quite high associated standard deviation.

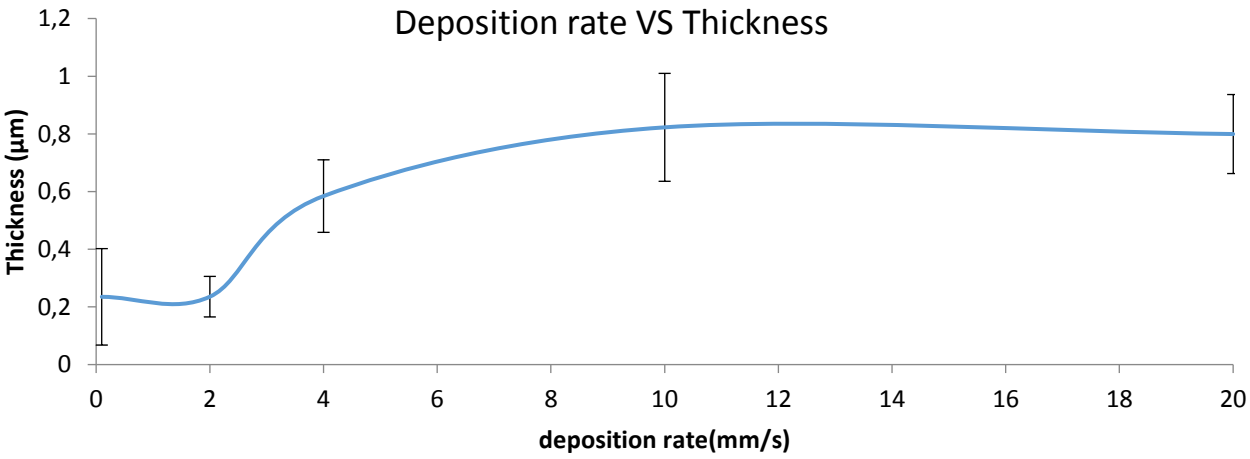

Figure 53 *Graph of deposition rate vs Thickness of SiO2-F deposited on glass.*

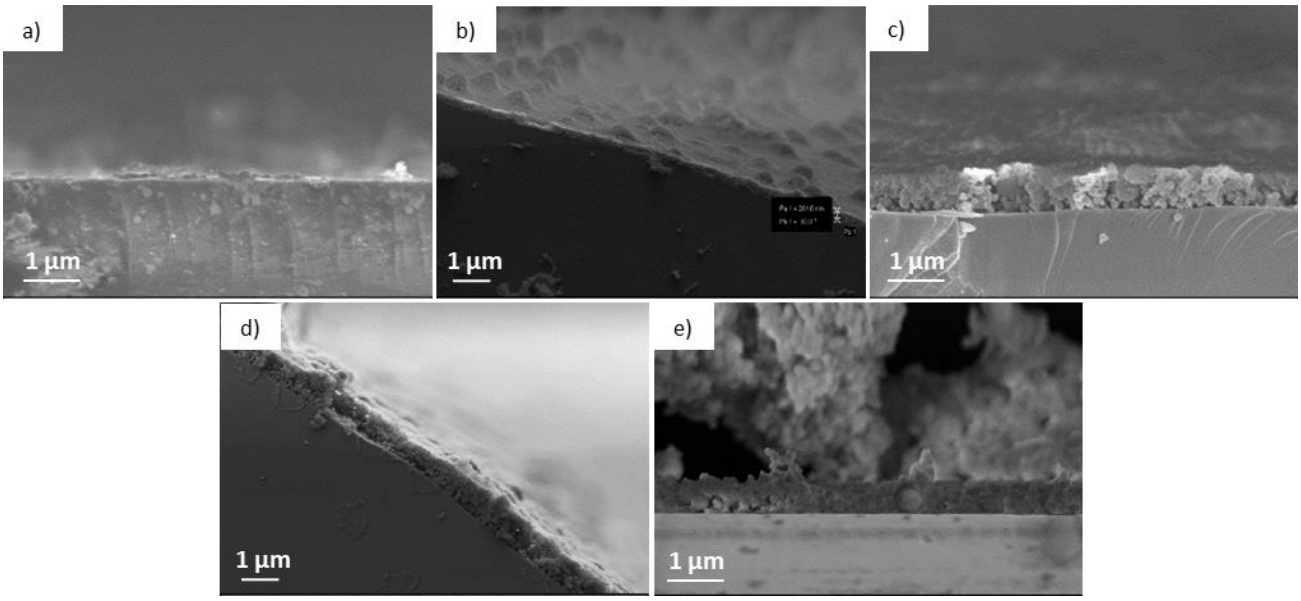

Figure 54 *SEM micrographs section of SiO_2F coatings deposited at different dipping/ withdrawal speed of a) 0.4mm/s b) 2 mm/s c) 4 mm/s d) 10 mm/s and e) 20 mm/s.*

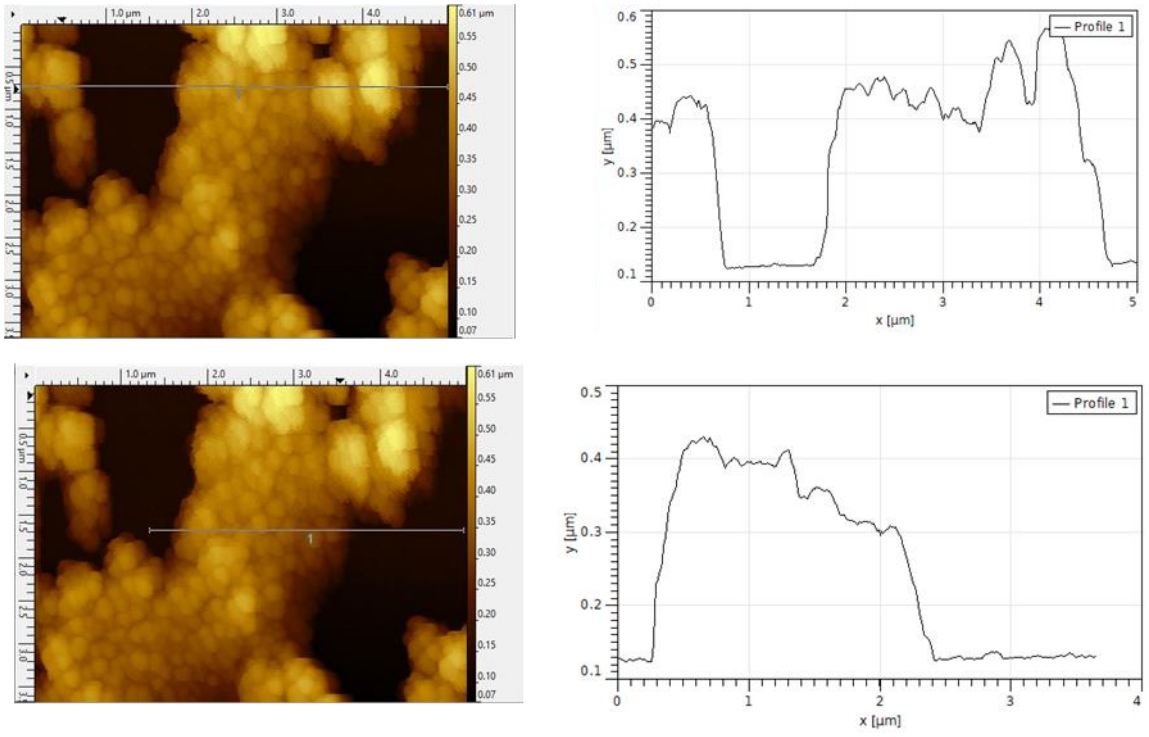

Figure 55 *AFM analysis (non-contact mode) and profilometry of SiO_2F coating at the dipping/withdrawal speed of 0.1 mm/s.*

Since SEM images (Fig 54) of SiO_2F coatings deposited at 0.1 mm/s did not provide exhaustive result in terms of thickness, AFM analysis was performed. A non-homogenous tendency of film formation is observed from cross sectional images, observing a stratification of nanoparticles at some thicker points, however deposition at 0.1 mm/s presents a homogenous layer.

This allows the AFM analysis (Fig. 54) of the surface, thus avoiding the breakage of the cantilever. The monolayer formed by the coating at low speed identifies in the profilometry a thickness of about 400nm corresponding to the diameter of the deposited particle.

Fluorinated silica based coating on steel

The 30 days aged suspension of fluorinated silica nanoparticles was deposited on AISI 316 steel alloy, dipping/ withdrawal speed of 2mm/s, soaking time 120s and annealing at 150°C for 30 minutes. Static (WCA) and contact angle hysteresis (CAH) are shown in table 21.

Table 21 *Static (WCA) and contact angle hysteresis (CAH) of SiO_2F based coating on AISI 316; standard deviation of data is also shown.*

Substrate	Layer	WCA (°)	ACA (°)	RCA (°)	CAH (°)
AISI 316	SiO_2F	160 ± 1	161 ±1	155 ± 2	6 ± 4

Morphologies of figure 56 confirm that a continuous layer is obtained on the surface, with some residual crack probably due to the evaporation of the solvent, occurring very quickly during the heat treatment. Again, nanoparticles of different sizes are present on the surface, which however, do not affect coating repellence against water.

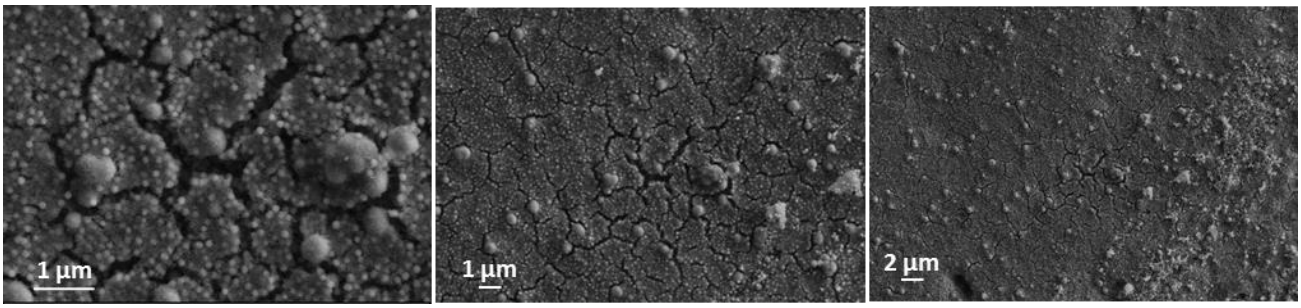

Figure 56 *SEM micrographs at different magnification of SiO_2F based coatings deposited on steel.*

Fluorinated silica based coatings on fiberglass

Dip-coating deposition of fluorinated silica suspension on fiberglass was optimized. With the only exception that, due to the limited temperature the fiberglass can bear, the thermal annealing was performed at 40°C for 24h. WCA of fluorinated silica based coatings at different withdrawal speed are summarized in table 22.

Table 22 *Static contact angle (WCA) of SiO_2F coating deposited on fiberglass substrate, standard deviation of data is also shown.*

Sample	Withdrawal speed (mm/s)	WCA (°)
FB_SiO_2F_1	1.0	135 ± 21
FB_SiO_2F_2	2.0	156 ± 10
FB_SiO_2F_4	4.0	166 ± 3
FB_SiO_2F_16	16.0	170 ± 2

The results indicate that dipping/withdrawal speed 4 mm/s induces superhydrophobicity overall surface (low values of standard deviation). Then, hereafter, a dipping/withdrawal speed of 4mm/s chosen with the additional aim of keeping the coating thickness as low possible to reduce the risk of delamination with loss of the performances over the time.

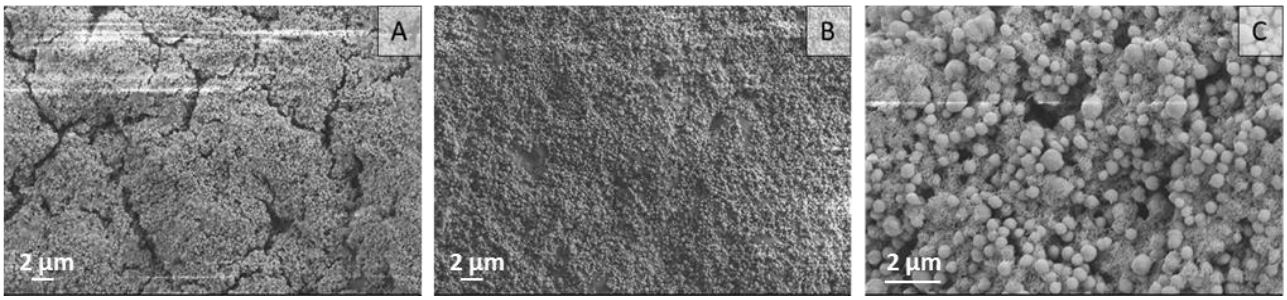

Figure 57 *SEM micrographs at different magnification of SiO_2F based coatings on fiberglass.*

SEM micrograph of SiO_2F based coatings on fiberglass (Fig. 57) highlight the complete covering of the substrate notwithstanding the presence of some deeper cavities whose formation is probably due linked to the evaporation step of the solvent.

8.2.2 Amino- functionalized silica based coatings

In the previous paragraph (3.2), the functionalization of silica nanoparticles amino groups was described. The introduction of NH_2 group in a silane chain allows groups such as epoxy, acrylate, carbohydrate or fluorinated ones to be better attached to materials (steel, aluminum and fiberglass) surface. In this work, the main idea was to create an epoxy primer loaded with SiO_2 particles functionalized by APTES (3-aminopropyltriethoxysilane) to significantly improve the adhesion between substrate and outer (more external) superhydrophobic coating. The epoxy resin has a very high viscosity, which does not allow thin films to be obtained. For this reason, it was decided to dilute the resin at percentage of 10% in isopropyl alcohol as solvent.

The reciprocal ratio solvent resin was subsequently optimized, as well as the speed withdrawal taking also into account, if any; multiple depositions process in order to obtain SiO_2-APTES based nanoparticles film covering the entire surface of the substrate. The diagram of the cladding manufacturing process is shown in the figure 58.

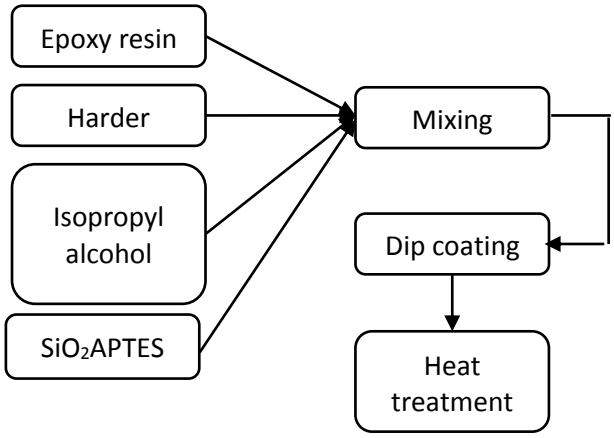

Figure 58 *Manufacturing scheme of epoxy coating with amine group functionalized silica nanoparticle.*

To obtain a homogenous layer of epoxy resin and SiO_2-APTES, the optimal percentage of resin and nanopowder by weight was first found. The ideal combination has been verified by SEM microscopy. It has been shown in Fig 59 that it is necessary a 4 times greater amount of silica with respect the resin to obtain a homogenous film entirely covered by nanoparticles. SiO_2-APTES film was obtained by withdrawal speed of 2mm/s, soaking time of 120s. After keeping samples at room temperature 60s, a further deposition under the same conditions was repeated.

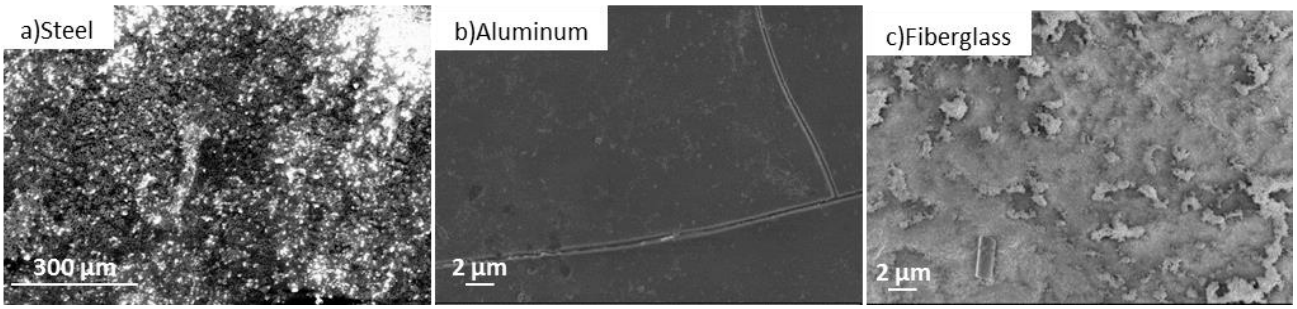

Figure 59 *SEM micrographs of a) steel b) aluminum c) fiberglass substrates dip-coated in the epoxy primer and SiO_2APTES filler.*

The figure 59 indicates that:

- Due to the very strong scattering of organic moieties, (unfortunately reducing images quality), steel substrate is completely covered by nanoparticles.

- Aluminum substrate sees a distribution of nanoparticles on but does not completely cover the sample; however, the presence of cracks suggests that the resin primer is present on the whole surface.
- An excellent distribution of nanoparticles is detected on fiberglass substrate with a clearly visible accumulation of aggregate particles.

The objective of the research is to obtain a homogeneous layer on the three types of substrate (aluminum, steel and, fiberglass). Was studied, in particular the quantities of resin, solvent and nanoparticles to obtain a primer that absorbed as little water as possible.

The use of nanoparticles filler also ensures that water is not absorbed when the epoxy primer is in contact with the liquid. The table shows the optimized formulation for three types of substrates: steel, aluminum and fiberglass, and the absorption of a drop of water after 2 minutes of contact with the surface. The percentage of water absorption of the primer is calculated by measuring the static contact angle at time zero (when the drop has just been deposited), and the contact angle after 60 and 120 seconds with the following formula [Eq 11]:

$$\%ass = \frac{WCA_{60} - WCA_0}{WCA_0} \text{ [Eq 11]}$$

Table 23 *Percentage of absorption of a drop of water on an epoxy-based coating filled with SiO_2-APTES on aluminum, steel, and fiberglass substrates.*

Substrate	Sample	Curing	Dip speed (mm/s)	Immersion (sec)	% ass 60s	% ass 120s
Steel	Epox_SiO_2NH_2_1:4_iprOH	2h 40°C	2	60	-18	4
Aluminum	Epox_SiO_2NH_2_1:4_iprOH	2h 40°C	2	60	-3	-2
Fiberglass	Epox_SiO_2NH_2_1:4_iprOH	2h 40°C	2	60	-11	-12

Aluminum coating has the lowest water absorption shown in table 23, of about 3%. The increasing of the silica content within the resin promotes the absorption of water that anyway, allows a homogeneous distribution of filler over the entire surface.

8.2.3 Alkyl group functionalized silica based coatings

The potential great relevance in term of reduced environmental impact of fluorine free coatings has been described in the previous paragraphs (3.2). To these purposes, attention was paid to the formulation and deposition of alkyl group functionalized (fluorine-free) silica nanoparticles.

The deposition of HTS functionalized based coatings (molar ratio SiO_2:HTS 1:1) on aluminum substrates was undertaken under following different processing conditions: dipping/withdrawal speed in the 1 ÷ 10 mm7s range and soaking time of 120s. WCA and CAH of all adopted solutions are summarized in table 24 and Fig. 60.

Table 24 *Static contact angle (WCA) and dynamic contact angle (CAH) of aluminum samples coated with SiO_2-HTS at different deposition rates.*

Sample	Speed (mm/s)	WCA (°)	CAH (°)
SiO_2HTS_1	1	111 ± 6	66 ± 17
SiO_2HTS_2	2	108 ± 3	29 ± 10
SiO_2HTS_4	4	88 ± 3	17 ± 9
SiO_2HTS_10	10	85 ± 2	17 ±4

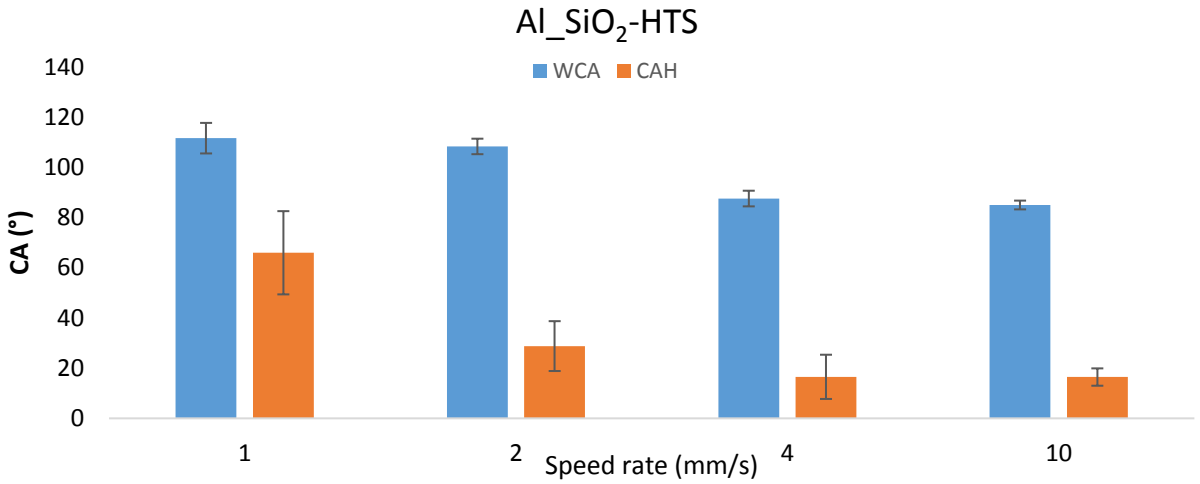

Figure 60 *Static contact angle (WCA) and contact angle hysteresis (CAH) of aluminum samples coated with SiO_2-HTS at different emersion rate (molar ratio SiO_2:HTS 1:1).*

Data of table 25 and Fig.60 the following conclusion can draw: if the dipping/ withdrawal speed is low (1, 2 mm/s) high static contact angles are obtained (130°) and hysteresis angle of 80°. At high dipping/withdrawal speed rates (4-10mm/s), instead, it obtained static contact angles around 80° and hysteresis angle of 15°.From the data presented in the table 24, and Fig. 60 it can be observed.

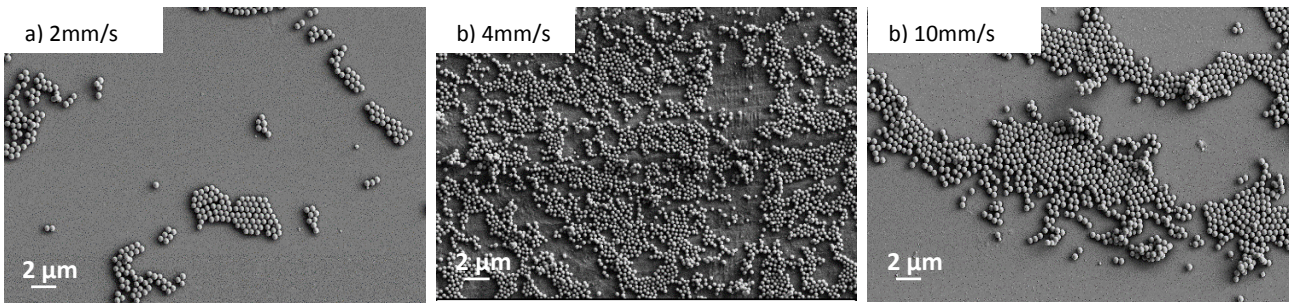

Figure 61 *SEM micrograph of SiO_2-HTS base coating deposited on aluminum substrate at different dipping-withdrawal speed a) 2mm/s b) 4mm/s c) 10mm/s.*

From the image Fig 61, we can see that with this synthesis spherical silica nanoparticles functionalized with alkyl chains are obtained.

The micrographs SEM in Fig 61 shown that only the coating deposited at 4mm/s has a homogeneous layer. Coatings deposited at speed 2 and 10 mm/s have surface nanoparticles aggregates. For this reason, the withdrawal speed selected for SiO_2-HTS based coatings is 4mm/s. With the aim optimizing the surface morphology, spray deposition of SiO_2-HTS formulation was also attempted by the adoption the set-up of Fig. 62.

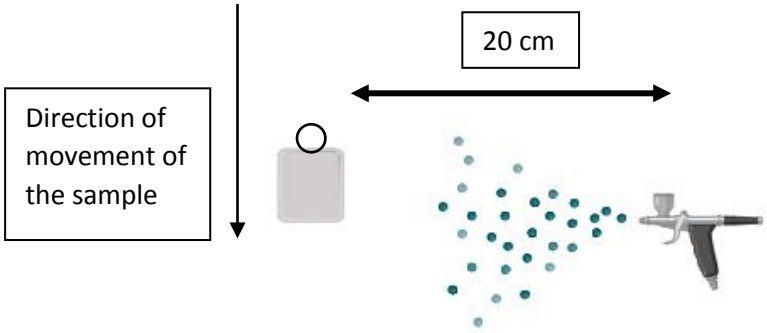

Figure 62 *Diagram of semi-automated spraying set-up used for SiO_2-HTS based coating.*

The optimized distance between the operator and the sample is 20 cm. This distance allows for controlled jet with a cone that is not too open and therefore the spraying is not dispersive. The speed at which the sample moves is 10 mm/s. With a lower speed, there is the risk of obtaining a sample with a layer that is too thick and the sample is too wet, and therefore a wrong structuring of the system. However, a high speed does not give time to the particles to deposit and therefore leads to a non-homogeneous layer. The static contact angle is WCA =85° ± 2 and the hysteresis is CAH=7 °± 4. The value of the hysteresis angle obtained is the lowest among those measured for this type of sample. As confirmed by the SEM micrographs (Fig 63), the wettability of the system improves because a homogeneous coating is obtained over the entire surface. In fact, this technique allows more material to be deposited and in this case, where there were adhesion problems with the dip-coating, it turns out to be optimal for suspension that are unable to form a homogenous film with dip-coating.

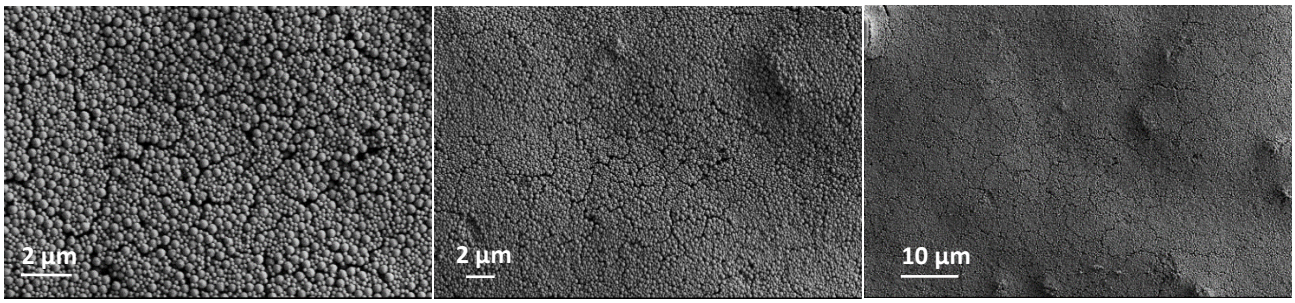

Figure 63 *SEM micrograph of SiO_2- HTS deposited via spray coating on aluminum at different magnification.*

9. SUPERHYDROHOBIC COATINGS: A ROUTE TO REGULATE BIOLOGICAL ADHESION ON LOW WETTABLE MATERIALS

9.1 State of art

The wettability of a material plays a key role in the context of materials and surfaces for underwater applications that come into contact many different biological species. According to the state of art, morphological and chemical modification of material surfaces can modulate their interaction with surrounding environment. The use of biomimetic inspired surfaces allows for the creation innovative of surfaces, whose wetting behavior can range from superhydrophilic to superhydrophobic, with interesting applications in many fields such as that of tissue engineering[156,157], cellular adhesion and biocompatibility[158], reduction of bacterial adhesion[159,160]. Among the most important key properties for the decreasing of cell adhesion on given substrate, roughness, and surface energy stand out due their ability to change the wetting behavior that, in turn, affects adhesion[161]/ repellence against organisms living in marine environment[162]. In cell biology, it's widely recognized that mammalian cell process an inherent tendency to attach to surfaces of different composition, this latter being a crucial aspect for executing their metabolic functions, proliferation and differentiation[163]. The cell adhesion on materials surfaces involves two primary molecular mechanism. Firstly, receptor mediated adhesion phenomenon occurs through interactions with extracellular matrix molecules (ECM) or their components. Interestingly, living cells don't directly interact with materials; instead, they readily attach to ECM proteins absorbed on substrates, originating from physiological fluid in vitro or the culture medium in vivo[164]. Several factors play a pivotal role in the physiological activities of cell, impact cell adhesion significantly. These factors include the cell's metabolic state, surface charge, hydrophobicity and the duration of cell-material contact[165,166]. Essentially, the adhesion of cells and the adsorption of proteins on a material surface are heavily influenced by the surface properties. The understanding of these intricate interactions provides valuable insights into the dynamic relationships between cells and materials surfaces.

Cells exhibit varied responses to patterns due to their ability to alter their morphology depending on the environment. As a result, different patterns elicit different responses in various type of cells[167].

There is a correlation between the superhydrophobic properties of surfaces and the cellular adhesion behavior. Using the wetting models mentioned in chapter 2 or Wenzel state, Cassie-Baxter state and SLIPS phenomena, recall that the first two stages are characterized by a roughness that affects the contact angle, in the case of Wenzel state, we have a microstructure, and in the Cassie Baxter state, we have a hierarchical structure. In the SLIPS phenomenon, there is a hierarchical structure where inside the porosities there is a lubricating oil that increases the ability to slips of the wetting liquid. Many studies highlight that when the surface roughness increased, cell adhesion decreased. The phenomenon can be attributed to the fact that trapped air in the surface cavities makes it non-wettable, thus preventing the cell from setting. In contrast, if there is microporosity attributed to the Wenzel state, where air is not trapped in the asperities of the microstructure, the cell adhesion will be promoted[168](Fig. 64 a). However, Cassie Baxter surfaces, which demonstrate non-cell adhesion, risk that, by extending the cell incubation time, the air trapped in the nanoroughness is replaced by liquid, promoting adhesion. In this regard, it may be crucial to act on the surface energy of the coating to prevent the phenomenon of liquid permeation (Fig. 64 b). The surfaces of the SLIPS type have been of interest in the field of non-cell adhesion. These superhydrophobic surfaces feature a thin and completely smooth layer of lubricant that penetrates into a porous matrix. After the oil infusion treatment, a perfectly smooth surface is formed, preventing interaction between the cell and the surface (Fig. 64 c).

Slippery surfaces, have demonstrated good resistance to cell adhesion and proliferation. However, the loss of lubricant over the time surface use poses significant challenges, leading to a loss of their anti-cellular property. Nevertheless, as reported in the literature[169], SLIPS surfaces exhibit greater durability compared to superhydrophobic surfaces and maintain their properties under extreme conditions. For this reason, they hold promise for future applications in the biological and biomedical fields[170].

The experimental study analyzed the correlation among coatings designed with different approaches leading respectively, to Wenzel, Cassie-Baxter state and SLIPS model, each of them providing different value (and different ratio) along with their respective static and dynamic repellence against water. With this aim, the influence of surface roughness and chemistry on the surfaces' ability to face up cell adhesion was deeply investigated and discussed.

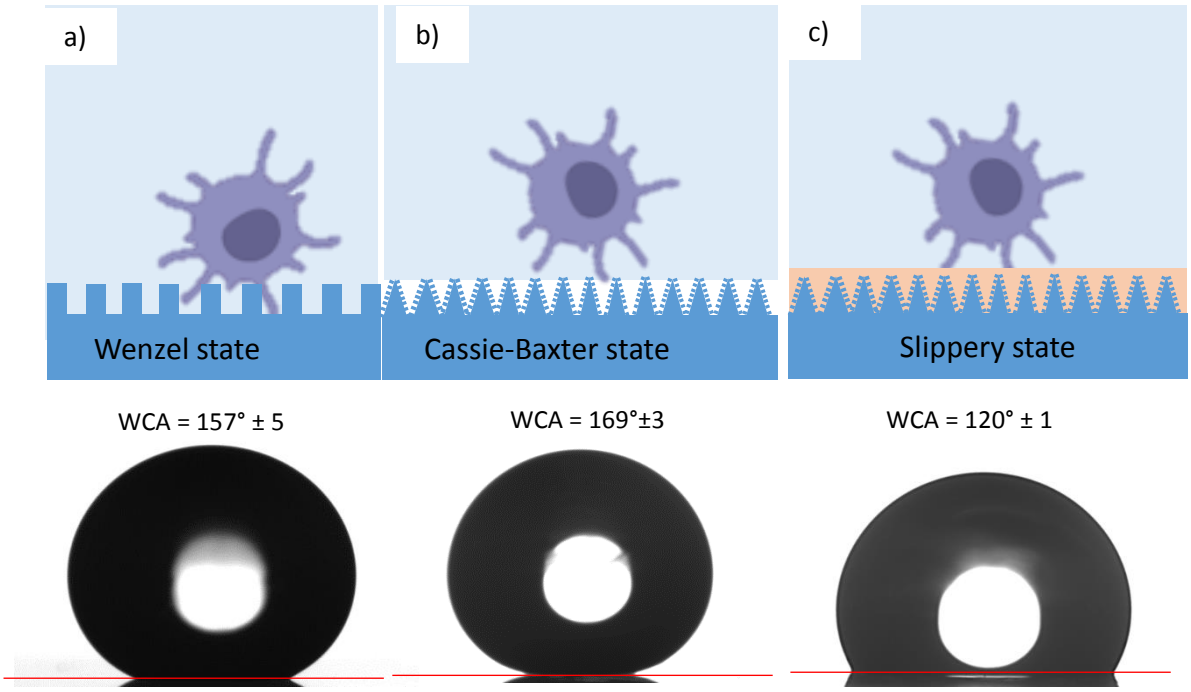

Figure 64 *Evolution of cell adhesion along the different surfaces wetting state a) Wenzel model b) Cassie Baxter model c) SLIPS model.*

9.2 Materials and methods

Coatings were deposited on thin glass commercially knows "microscope cover slips" size 20 x20 mm. First, the deposition process parameters of selected coatings were optimized based on the substrate typology. All specimens were cleaned with soapy water in an ultrasound bath for 5 minutes. After rinsing with ethanol, the specimens underwent additional 5 minutes treatment of ultrasound bath in ethanol. Abundant final rising with acetone was performed to remove all the impurities. Clean the specimens were stored in a desiccator to preserve them from atmospheric moisture.

The glasses were coated by fluorinated silica (90 days aged) nanoparticles or an alumina sol-gel as inorganic layers, then covering them with fluoroalkylsilane as outer layer, SLIPS approach was adopted the inner alumina layer, already covered FAS, infused with perfluoropolyether lubricants of the series Krytox^{tm} GLP.

Glass samples were coated with SiO_2F sol by dip-coating technique with withdrawal speed 2mm/s and soaking time of 120s. After drying at room temperature, they were thermally consolidate at 150°C for 30 minutes. Indeed, as far as the deposition of alumina sol, dipping/withdrawal speed was the same, soaking time is reduced at 5s and annealing took place at 400°C for 60 min to get the amorphous aluminum oxide.

Samples were them immersed in hot water (90°C) for 30 min to form boehmite and thermally treated again (400°C 10min) to reach an equilibrium state. Subsequently, FAS solution was dip-coated on the underlying boehmite layer (withdrawal speed of 2 mm/s and soaking time of 120s); followed by thermal treatment at 150°C for 30 min. Moving towards SLIPS, with Krytox 103, providing a liquid working interface was additionally deposited on the surface.

To obtain a thin and homogeneous liquid film, a perfluoropolyether lubricant Krytox^{tm} GLP 105 was spin-coated onto the surfaces with the following procedure: after the deposition of a 2µL oil drop at the center of the glass sample, the sample rotate at a spinning speed of 1000 rpm for 10sec. After the lubricant has been spread all over the surfaces, we proceed with another deposition of a 2µL oil drop. Every 10 seconds the spinning speed is increased (from 250 rpm to 3500 rpm with an intermediate speed of 1000 rpm). Then a high centrifugal force was employed to simulate a high shear conditions to remove the oil excess. Specifically, the infused surfaces have been subjected to a spinning speed of 3500 rpm for a prolonged time of 10 minutes. Once removed from the spin-coated, the sample have been left in a vertical position for 3 hours on each of the four borders. Furthermore, before the contact angle measurements, the sample has been left in vertical position overnight along the direction of the dip-coating process.

Cell adhesion and viability experimental plan

Cell adhesion tests require several preparation steps. Firstly, it is necessary to cultivate the selected available cells for the tests and, at the same time, to prepare the surfaces on which adhesion will occur by standardized procedures. A test of the eluate was carried out after 24 hours at 37°C while the adhesion test was evaluated after 1,3 and 7 days. The following adhesion and cytocompatibility tests were selected: MTT cell, viability test, observation morphology (Actin + DAPI) and after 24 hour by SEM. Hereafter the adopted experimental procedure are briefly described.

Cell culture

Mouse fibroblast BALB/3T3 cell line (Clone A31, ATCC® CCL-163™) was cultured in DMEM high glucose medium (Gibco) supplemented with 10% Calf Bovine Serum (Gibco) and 1% Penicillin and Streptomycin solution (100 U/ml-100 µg/mL, Gibco) and kept at 37°C under 5% CO2 atmosphere conditions and controlled humidity. Cells were detached from culture flasks by trypsinization and were centrifuged; cell number and viability were assessed with trypan-blue dye exclusion test. Each sample (2 cm x 2cm) was sterilized by 70% ethanol followed by 30 minutes UV irradiation under the biological laminar-flow sterile hood.

Samples were placed one per well in a 6-well plate and a drop of 100 µl containing 45×103 cells (11.2×103 cells/cm2) was seeded on the center of the treated glass coverslip surface allowing cell attachment for 20 min in the incubator, before addition into each well of 2 ml of cell culture medium. All cell-handling procedures were performed in a sterile laminar flow hood. All cell-culture incubation steps were performed at 37°C with 5% CO2. MTT assay was performed after 1, 3 and 7 days to evaluate the viability of cells grown in contact with the different coating surfaces, glass coverslip without coating was used as a control.

In order to evaluate the cellular effect of ions and/or molecules potentially released by the samples in the cell culture conditions, the test of the eluate cytotoxicity has been performed. Briefly, each sample was placed in a complete medium and incubated for 24 hours in standard cell culture conditions. Then the culture media (called eluate) were collected and tested for cytotoxicity using BALB/3T3 cell line. Cells, cultured as mentioned before, were seeded 1500 cells/well in 96 well-plates; 24 hours after seeding 150 µl of eluate were added to the culture for 1, 3 and 7 days. MTT assay was tested to evaluate the effect of eluate on cell viability.

Coating sterilization and Cell seeding

All the coated coverslips were sterilized by a wash in MilliQ water, followed by two washes in EtOH 70%, 30 min of ultraviolet germicidal irradiation and 20 min at 121°C in an autoclave. The cytotoxicity of the coatings was directly and indirectly evaluated. The murine fibroblasts were seeded at a density of 45.000 cells/coated slide by dripping the cell suspension on the coated surface, followed by 20 minutes of pre-adhesion incubation at 37°C before cell media addition. Alternatively, the fibroblasts were seeded in a 96 well plate at 5.000 cells/well density let grow for 24 hours and then the media replaced with media that was incubated for 24h with the coated slides (eluate). The biological behaviour of murine fibroblast seeded on top of the coatings in close relation to the different hydrophobic coatings was investigated in terms of cell viability, proliferation, and cell morphology evaluation. Moreover, the eluate cytotoxicity on BALB-3T3 cells was analysed.

MTT cell viability assay.

The MTT assay is a colorimetric protocol quantitatively to assess cell viability. 3-(4,5-dimethylthiazol-2—yl)2,5-diphenyltetrazolium bromide (MTT) can be reduced into formazan crystals by metabolically active cells. MTT reagent was resuspended in 1X Phosphate Buffered Saline (PBS) at 5 mg/mL final concentration and added to cell culture media 1:10 ratio.

After 2h incubation at 37°C, the solution was discarded and formazan crystals were dissolved by adding DMSO and shaking for 15 minutes (Fig.65). The absorbance of three biological replicates for each condition was read at 570 nm using a Multiskan FC Microplate Photometer (Thermo Scientific). Three biological replicates were tested and the results are represented on graphs with % respect to cells only.

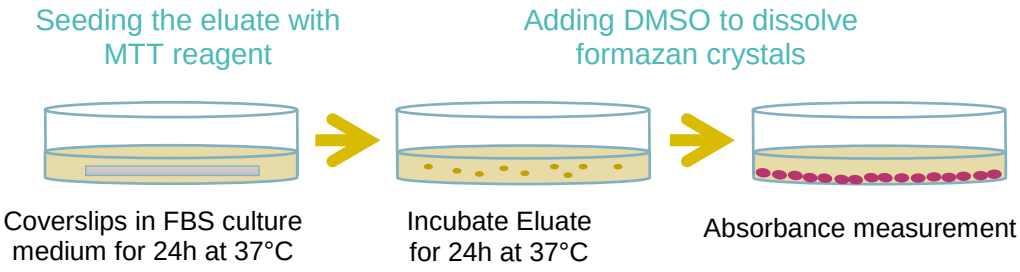

Figure 65 *Scheme of MTT cell viability test.*

Cell morphology evaluation

Actin/Dapi staining. The MTT assay is a colorimetric protocol to quantitatively assess cell viability. 3-(4,5-dimethylthiazol-2—yl)2,5-diphenyltetrazolium bromide (MTT) can be reduced into formazan crystals by metabolically active cells. MTT reagent was resuspended in 1X Phosphate Buffered Saline (PBS) at 5 mg/mL final concentration and added to cell culture media 1:10 ratio. After 2h incubation at 37°C, the solution was discarded and formazan crystals were dissolved by adding DMSO and shaking for 15 minutes. The absorbance of three biological replicates for each condition was read at 570 nm using a Multiskan FC Microplate Photometer (Thermo Scientific). Three biological replicates were tested and the results are represented on graphs with % respect to cells only.

9.3 Results

Wettability of glasses (cover slips) chosen for cell adhesion tests was quantified by WCA, ACA and RCA measurement and CAH calculation. The results is reported in table 25.

Table 25 *Static (WCA) advancing (ACA) receding (RCA) and hysteresis (CAH) contact angle of against water and hysteresis (CAH) of the glass substrates functionalized by Al_2O_3 hybrid coatings SiO_2F and Al_2O_3K105 (SLIPS) chosen for the adhesion test, standard deviation of data is also reported.*

	WCA (°)	**ACA (°)**	**RCA (°)**	**CAH (°)**
Al_2O_3-FAS	167 ± 3	171 ± 4	157 ± 1	14 ± 1
SiO_2F	157 ± 5	165 ± 2	148 ± 3	17 ± 4
Al_2O_3-FAS-K105	120 ± 1	122 ± 1	119 ± 1	3 ± 1

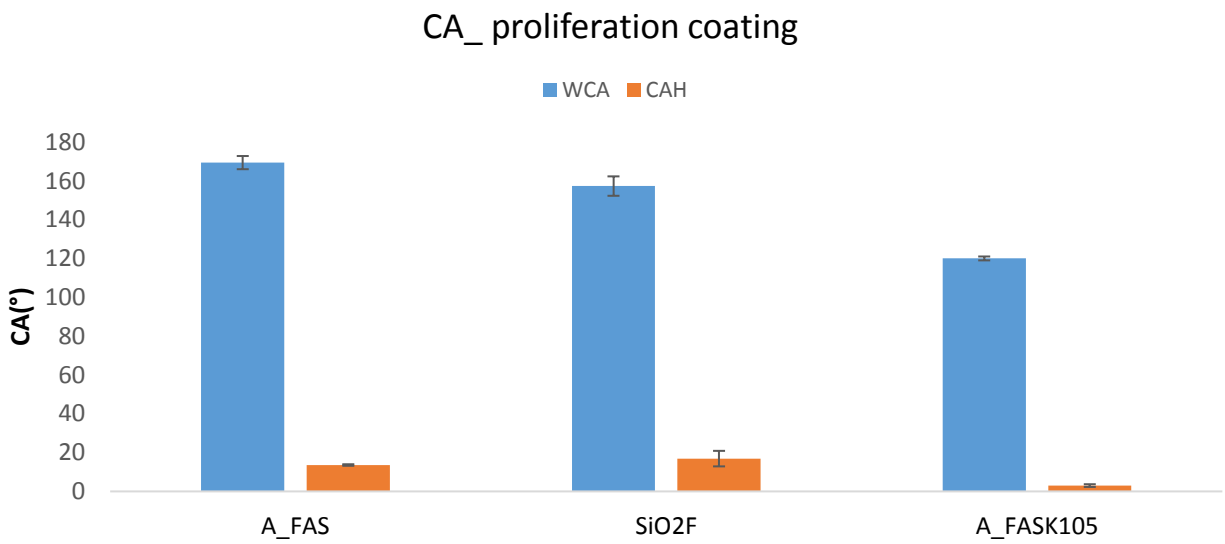

Figure 66 *Static (WCA) and hysteresis (CAH orange) contact angle measurement of coating tested for cellular adhesion.*

Among the coated glass substrates, SiO_2F has a hysteresis of 17°, in fact, the drop during the receding process tends to be stuck in the porosity, making it difficult to measure, and this effect called "pinning effect" is common in the surfaces that have a microporosity. The Al_2O_3 flower-like based coating with FAS allows a static contact angle >170° and hysteresis of about 14°. In this case, the drop during the receding phase retracts easily, thanks to both hierarchical nanostructure present and the silane that lowers the surfaces energy of the coating. When the lubricant is further introduced as a liquid interfaces (Al_2O_3-FASK105) although WCA is not higher than (120°), hysteresis is significantly lowered to a few degrees 3°. These three different coated substrates, together with uncoated reference, were subjected to cell adhesion testing.

In vitro tests with BALB/3T3 Clone A31 Murine Fibroblasts are performed on three different coatings. Metabolic quantification of active cells over time days (1-7) indicates that cell adhesion on day 1 has a high cell adhesion for the Wenzel model; the cells lose adhesion on the coating to the 3rd and 7th day. Differently, the Cassie-Baxter and SLIPS models represented by Al_2O_3-FAS and Al_2O_3-FASK105, show low cell adhesion from the first day of cell settlement, to the third and seventh day, the cells tend to disappear altogether. The evaluation of eluate toxicity demonstrate that cell viability was not compromised by substances potentially realised from the different coatings (Figure 67 B).

The viability of the cells grown in contact with all three different coatings showed a decrease over time and these differences result in statistically significant respect to the control at all the experimental times (δ= p ≥ 0.0001). Looking in detail, after 1 day of culture, Al_2O_3 –FAS and Al_2O_3-FASK105 showed a statistically significant reduction of cell viability with respect to SiO_2F (p ≥ 0.05 and p ≥ 0.001, respectively). Over the time of the experiment, Al_2O_3-FASK105 significantly reduced the cell viability compared to both SiO_2F and Al_2O_3 (p ≥ 0.0001) (Fig 67).

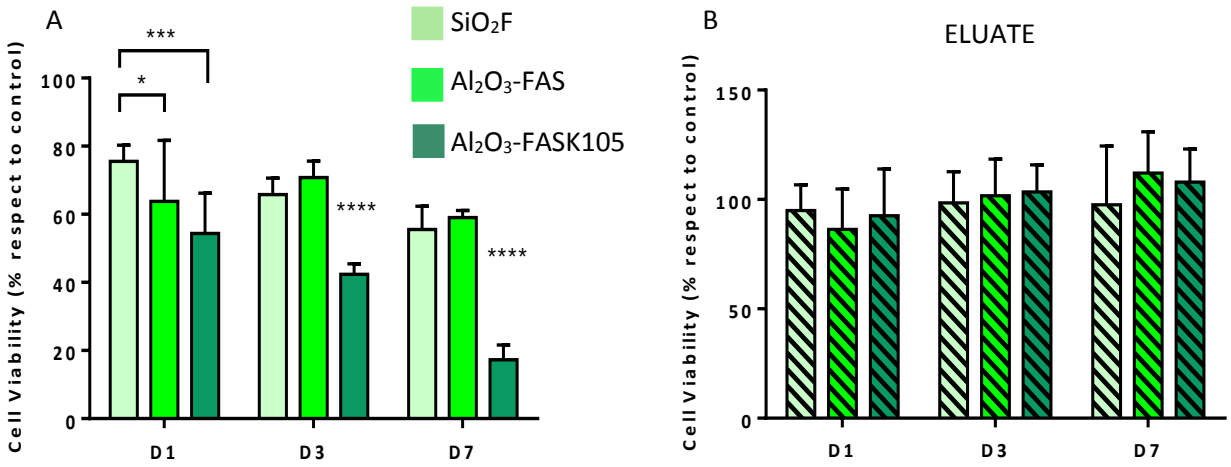

Figure 67 *Cell viability analysis. MTT assay was performed on the cells grown in direct contact with the coating surfaces (A) and in contact with eluate (B). The graphs show the percentage of viable cells compared to the control, and the mean ± standard error of the mean is presented. δ= p ≥ 0.0001; * p ≥ 0.05; *** p ≥ 0.001; **** p ≥ 0.0001.*

The morphological analysis in the figure 68 confirms the results shown with the MTT viability assay. In particular, the slide coated with SiO_2F on day 1 shown a greater settlement of cells compared to the seventh day and compared to the other two exposed coatings. The Cassie-Baxter and SLIPS coatings, indeed, present low cell adhesion from day one, with the SLIPS coating showing a presentation of adhesion on the seventh day of testing.

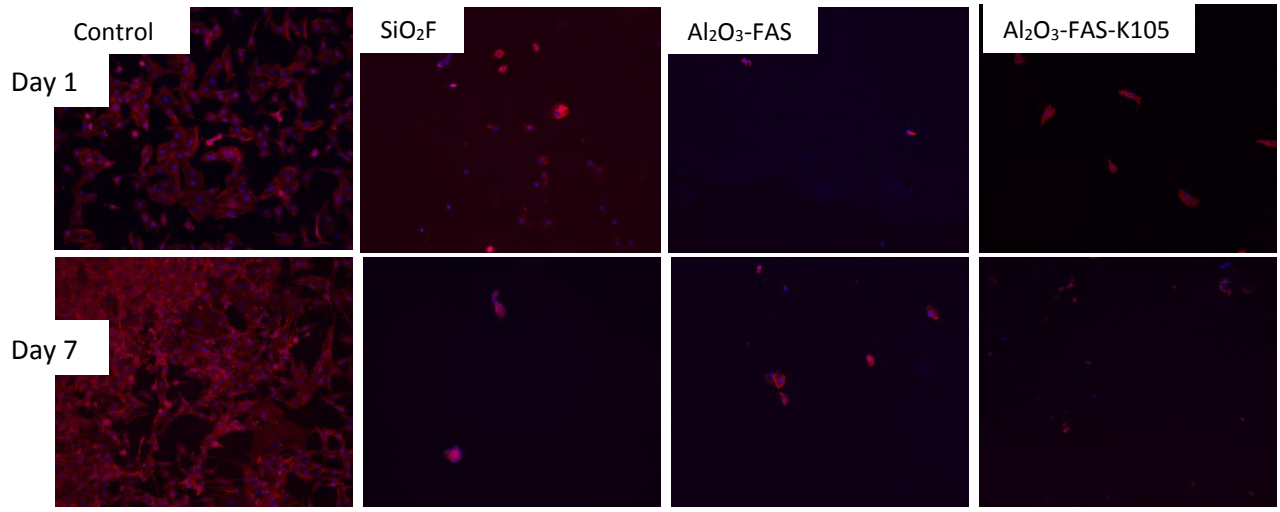

Figure 68 *Analysis of cell morphology on day 1 and 7 on different coating: SiO_2-F, Al_2O_3-FAS, Al_2O_3-FAS-K105. The first image refers to uncoated control surface.*

The cell anti adhesion tests lead to the following conclusion. The Wenzel coatings do not demonstrate an efficacy anti-cellular adhesion due to the morphological properties and wettability, indeed, the high hysteresis (17°) allows the attachment of cell to the coating. The Cassie-Baxter model promotes non-cellular adhesion from day one, showing that a decrease in hysteresis of only 3-4°with respect to the SiO_2F coating allows cells not to adhere. The SLIPS model is the most promising anti-adhesion property. After the first settlement occurred on day 1, the slide on day 7 does not have any cells on the coating, since; the oil promotes the slippage of cells over time. Finally, all coatings are non-toxic to the cells, as they do not exhibit significant cell deformation after tests.

9.4 Physical characterization of the coated surface after adhesion testing

For any application making coated surfaces attractive to be adopted at a higher scale with respect to the laboratory one, it is important that anti adhesion properties are kept stable over the time.

Coatings subjected to cell adhesion test (contact time of 1, 3, and 7 days) were washed thoroughly with trypsin and saline solution and then dried at room temperature overnight. WCA and CAH of coated surfaces were checked again.

Figure 69 highlights WCA and CAHs of SiO_2F, Al_2O_3-FAS and Al_2O_3-FASK105 coated surfaces before and after the cell adhesion test.

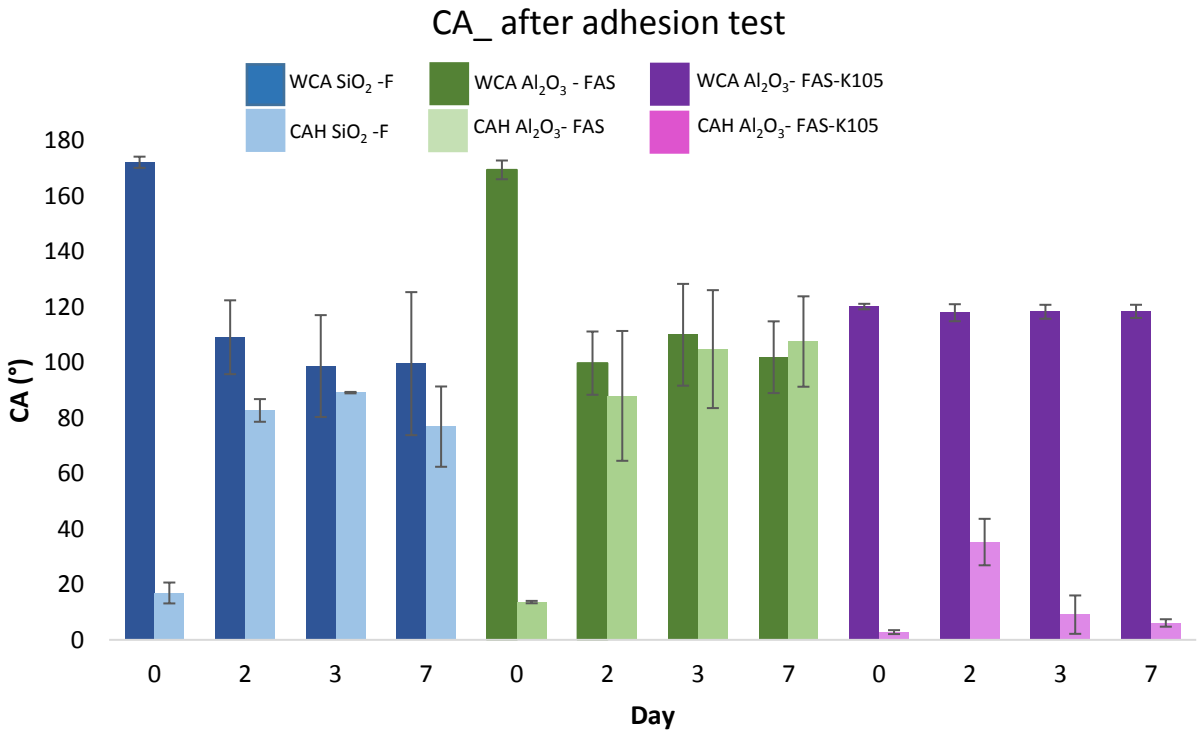

Figure 69 *Static (WCA) and dynamic (CAH) contact angle of SiO_2F, Al_2O_3-FAS and Al_2O_3-FAS-K105 coated surfaces, before and after cell adhesion tests at 2,3 and 7 days (washing for cell removal after testing was performed).*

From data of Figure 69, it can be noticed that:

- The fluorinated silica coating before washing shows a high static contact angle and hysteresis below 20°, after testing and washing the slide from the cells, the static angle drops by 60°, and the surface completely loses the properties of dynamic hydrophobicity.
- The Al_2O_3-FAS coating demonstrates the same behaviour as the fluorinated silica, further improving the static contact angle (100°).
- However, surfaces designed by SLIPS approach model have a different behaviour keeping unchanged their wetting properties even after quite aggressive washing conditions.

Morphologies are investigated by SEM analyses in figure 70. The SLIPS surfaces cannot be inserted within in SEM-FEG, due to surface moisture.

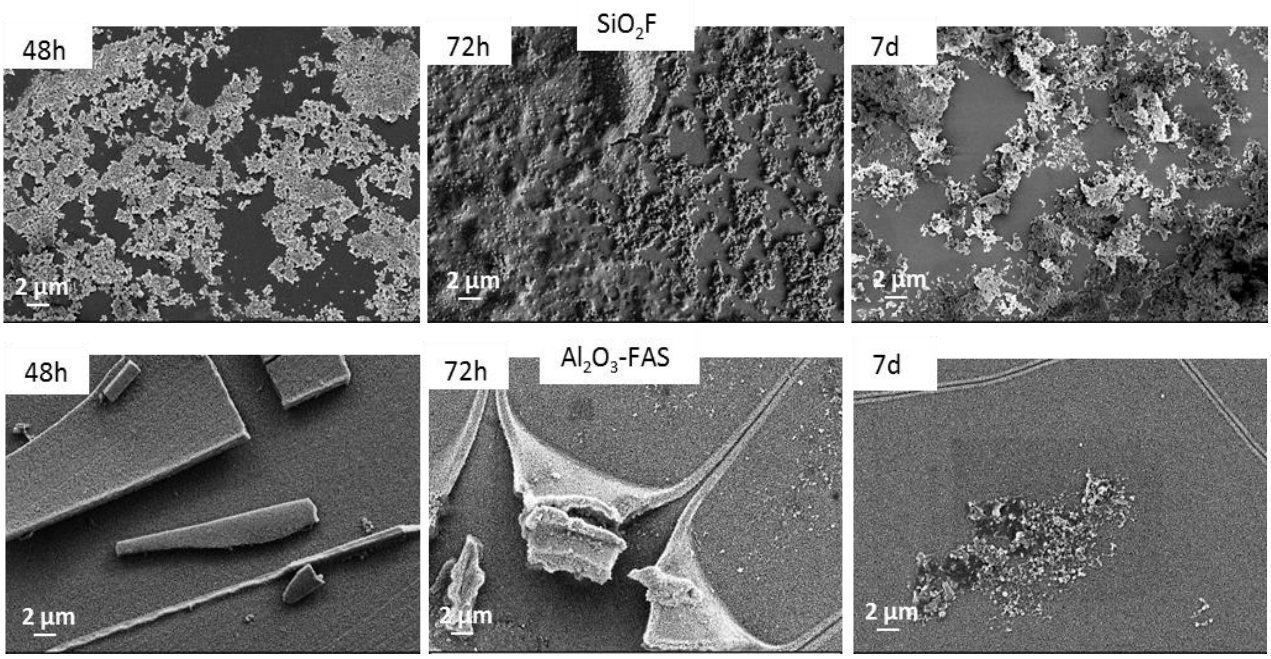

Figure 70 *SEM micrographs a) SiO_2F coating after cell adhesion test at 48, 72 hours and 7 days and after washing b) Al_2O_3 –FAS coatings after cell adhesion test at 48, 72 hours and 7 days, and after washing.*

Micrographs in Figure 70 a) show that the fluorinates silica coating is damaged during the tests, which is why it does not show the same contact angle before and after test. However, the alumina coating Fig 70 b), remains unchanged after testing, some exfoliated areas are observed but below is still the flower-like structure. The deterioration of the superhydrophobic properties in this case is attributable to the organic coating FAS, which during the tests is damaged, enhancing the hydrophilic character of the alumina below.

Conclusion

Resistance testing to cell adhesion and washing Al_2O_3-FAS-K105 revealed that SiO_2F coatings have do not withstand working conditions and deteriorate after only one-day anti-cellular test. The Al_2O_3-FAS coating undergoes a deterioration of the organic layer, while the infusion withstand test of cellular adhesion test.[1]

[1] Part of the section 8 are under submission to Coatings Journal as " Corozzi A., Montesi M., Panseri S, Caruso M., Raimondo M.," – Wetting control for cell adhesion and viability

10. SUPERHYDROPHOBIC COATINGS IN SIMULATED MARINE ENVIROMENTS

In recent years, the problem of fouling is a highly debated scientific issue. After the elimination from the trade of varnishes and paint containing biocidal heavy metals, the research moved towards alternative surfaces treatments and formulations (including coatings) designed by anti-adhesive strategies aimed at blocking the material/biofilm interaction at an early stage.

This section refers to larval settlement tests on different coated substrates to obtain preliminary information on their antifouling efficiency of coating, somehow of predicting the behavior in field conditions[171–173].

10.1 Preliminary Settlement test

The larval settlement tests were performed with Cypris larvae of barnacle crustacean *Amphibalanus Amphitrite* Fig 71.

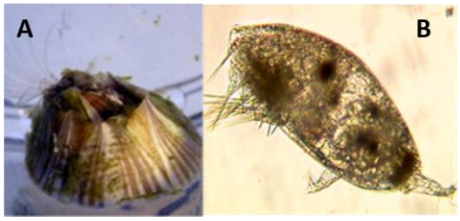

Figure 71 *A) Adult specimen of Amphibalanus Amphrite and B) Cypris larva.*

Amphitrite presents six Naupliar states in its life cycle, followed by a larval stage called “Cypris”, which represents the phase during which the larva explores the substrate in order to complete the process of larval settlement, which ends with the adhesion of the Cypris larva to the substrate (attachment”) and its metamorphosis into a young adult (Fig 71). The Cypris larvae used for the larval settlement test were obtained from a farm of A. Amphitrite adults maintained at the CNR IAS (Institute for the study of anthropogenic impacts and sustainability in the marine environment) located Genoa (Italy). The breeding conditions adopted in a thermostatic chamber (temperature of 20± 1°C and photoperiod 16:8 LD) allow the maintenance of adult specimens, their reproduction and the obtaining of larvae in the first Naupliar stage. Once collected, these larvae are fed and maintained in optimal conditions until they reach the Cypris larval stage (generally after 6 o 7 days from the emission of the fist Naupliar stage by the adults)[174].

The larval settlement test is known as the “droplet test” or also the “no choice assay”.

This test consists of placing a defined number of Cypris larvae (equal to 15/20) in contact with the substrate under investigation; the Cypris are then counted manually with the aid of a stereomicroscope and transferred into a volume of 600µl of natural seawater filtered at 0.22µm (FNSW 0.22). This drop in the placed on the substrate under test. In this way, the Cypris immersed in water are in contact only with the surface in question on which to settle, without alternative surfaces to choose ("no choice"). Two drops of 600µl of FNSW 0.22 µm containing 15/20 Cypris larvae were placed on each specimen; the specimens were then placed inside a polystyrene petri dish; closed with the lid and wrapped with film in order to prevent the evaporation of water. The plates containing the specimens were then placed in a thermostatic cabinet at a temperature of 26±1 °C, in the dark, and maintained in these conditions for 5 days. At the end of the test, the number of organism settled on each specimen (in both drops) was counted (via stereomicroscope).

Figure 72 *Example of "droplet test" on fiberglass substrate.*

Larval settlement tests were performed on specimens of size 3x8 cm using aluminum and fiberglass as substrates (Fig 72). Tables 27 and 28 lists the acronym and composition of coatings deposited on the fiberglass and aluminum substrate.

Table 26 *Fiberglass specimens used for larval settlement test.*

Abbreviation	Description
FB	Fiberglass
FBS	Fiberglass + SiO_2F
FB_SK103	FB_SiO_2F+Krytox103
FB_SK105	FB_SiO_2F+Krytox105
FB_SK107	FB_SiO_2F+Krytox107
FB_AK103	FB_Al_2O_3FAS +Krytox 103
FB_AK105	FB_Al_2O_3FAS +Krytox 105
FB_AK107	FB_Al_2O_3FAS +Krytox 107

Table 27 *Aluminum specimens used for larval settlement test.*

Abbreviation	Description
Al smooth	Aluminum substrate
Al_AK105	Al_Al_2O_3FAS+Krytox105

In parallel “negative controls” (Ref_1) were organized consisting of polystyrene specimens on which 600 µL “ drops” of 0.22µm FNS containing 15 to 20 Cypris larvae were placed. The percentage of larvae settlement obtained on the specimens with the experimental coating was then compared with that obtain by the negative controls, as well as with that obtain on the control specimens consisting of the uncoated substrate (fiberglass Fb, aluminum) referred to as “positive controls” (CrtFB).

Before proceeding with the analysis of the results, it is necessary to point out that the test on the aluminum control specimens could not be considered. In fact, the control specimens for the aluminum substrate (smooth Al) in contact with seawater (FNSW 0.22 µm) corroded developing aluminum oxides and hydroxides (Figure 73) which resulted in an acute toxic toward all organisms (Cypris larvae) used for the settlement test.

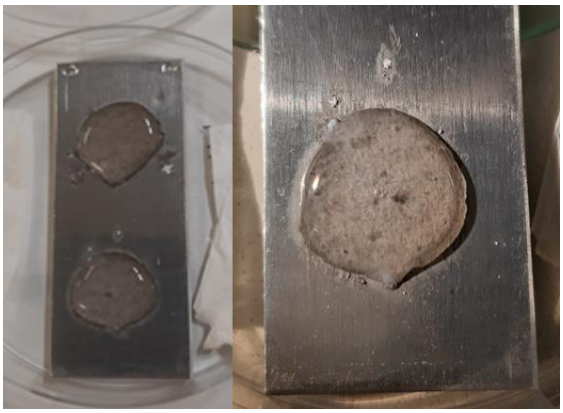

Figure 73 *Smooth aluminum substrate at the end of “droplet assay”. Substrate corrosion and the development of aluminum oxides and hydroxide are observed.*

10.2 Results

The results of larval settlement tests performed on coatings deposited on fiberglass and aluminum coated surfaces are shown in the Figure 74.

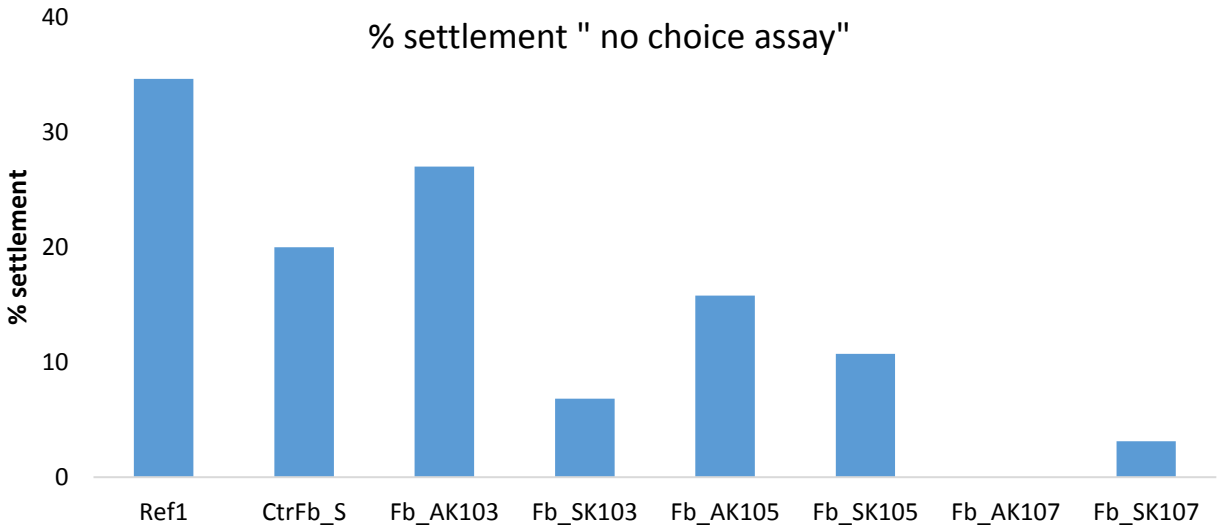

Figure 74 *Percentage of Cypris larval settlement of A. Amphitrite revealed by the droplet assay method.*

Figure 74 shows that the larval settlement percentages detected on the (coated fiberglass and aluminum) are significantly lower than that detected on the controls ones. This holds true for both the negative control (polystyrene plate), for which the settlement percentage reaches 60%, and the "positive" controls for the fiberglass specimens (CtrFb and CtrFb_S), for which a settlement of more than 50% was obtained. In contrast, for all functionalized specimens, the larva settlement rate is less than 5%.

The preliminary laboratory screening performed on the specimens listed in table provided some useful insights into the antifouling behavior of the experimental coatings under study.

Data obtained through the larval settlement test (droplet assay) show, with the same substrate, a significant reduction in the number of larvae settled on the specimens on which the SLIPS coating was present (Fig. 74). This reduction in the percentage of larvae settlement should be considered valid particularly with reference to the fiberglass specimens, for which data could also be obtained for the positive controls (non-functionalized fiberglass specimens, namely CTR bis and CtrFbS). For the aluminum specimens it was possible to observe a low percentage of larval settlement (maximum 3%) on the specimens with the AK105 coating, applied on both smooth aluminum , but the data for the corresponding positive controls (smooth aluminum without coating) is not present.

Although the result of this preliminary laboratory test relates to only one species of biofouling (A. Amphitrite), the information provided by the results of the larval settlement represent useful data indicative of the potential antifouling action by the tested coatings.

11. ENVIROMENTAL EFFECT OF SUPERHYDROPHOBIC COATINGS

11.1 Release test

The purpose of this test is to verify the possible release of toxic substances from the experimental coatings. The test involves a first step that consists of collecting the leaching products. The collection of leachable was carried out in order to subsequently set up a toxicity test aimed at verifying the possible release of substances with toxic action by the experimental coatings, i.e., to obtain information on the potential environmental impact. The leaching product of the coatings was collected according to the methods outlined in ASTM Method 6442, making some modifications that will be detailed below. The ASTM protocol for determining the rate of biocide release form conventional antifouling paints (Arai et al., 2009 D6442/2005) proposes a method for collecting leaching products from antifouling paints that involves applying paint to a cylinder with a diameter of 64mm and a total paint-covered area of 200 cm^2. The cylinder in placed in "holding " tanks, fed by a continuous flow of seawater and, at defined time intervals (from 24 hours up to 45 days), is taken from the holding park and placed in the contained for collecting the leachate, i.e., a glass container with a capacity equal to 2 liters, containing 1500 mL of artificial seawater. Here, through an automated system, the cylinder is kept in continuous rotation at 60 rpm for 1 hour (at T=25°C). After this time interval has elapsed, the water, representing the paint leachate, is collected. This operation is repeated for all defined times (up to 45 days of "aging" of the cylinders in the "holding tank").

The procedure adopted in our experiment for leachate collection differs from that described above (ASTM Method 6442; Piazza et al; 2018) in the following points:

- The present's experimental coating is applied on one side of aluminum samples (3x3cm), the total surface area on which the coating is present in 9 cm^2.
- During the collection of the leachate, the specimen was kept in a glass container immersed in 70 mL of water (0.22µm filtered natural seawater FNSW), in order to maintain a surface are/volume ratio corresponding to that applied in ASTM method 6442. An aerator was also inserted into the container in such a way as to create water movement (fig 73). The containers with the specimens were kept at T=25°C for the leachate collection time.
- The leaching products were collected after three different times of immersion of the specimens in the volume equal to 70 mL of FNSW, i.e.: 1h (as indicated in ASTM method 6442), 24hand 72h.

In the Figure 75 is reported the experimental set-up.

Figure 75 *Collection of leaching products of aluminum specimens (3x3 cm) covered by the experimental coatings.*

The prepared leaches were frozen (-20°C) and kept under these conditions until the toxicity test, which consist of the acute toxicity (mortality) assay on Nauplii (2nd larval stage) of A. Amphitrite, was carried out. This larval stage has indeed been shown to be sensitive toward a wide range of pollutant, which is adequate for the evaluation of potential toxic action. There is a standardized protocol for such bioassay (M.U. 2245/2012).

The aluminum sample used for obtaining the leaching products, which are 3x3 size, are listed in table 28.

Table 28 *Aluminum specimens used for leaching test.*

Abbreviation	Coatings
Al	No
Al-A	Al_2O_3
Al_SF	SiO_2F
Al_AK103	Al_2O_3 +FAS+ Krytox 103
Al_AK105	Al_2O_3 +FAS+ Krytox 105
Al_AK107	Al_2O_3 +FAS+ Krytox 107
Al_SFK_103	SiO_2F +Krytox 103
Al_SFK_105	SiO_2F +Krytox 105
Al_SFK_107	SiO_2F +Krytox 107

Let us briefly describe the model organism of the mortality/immobility trials. Amphibalanus (Balanus) Amphitrite (Darwin, 1854) is a barnacle crustacean with a sessile adult stage (Fig.76) preceded by a series of planktonic larval stages.

Already formed embryos are emitted from adults at Naupliar stage II. Larval development then proceeds through a series of planktonic Naupliar stages (instars III-VI) followed by lecithotrophic larval stage called Cypris. This larval stage represents the competent phase for settlement, irreversible adhesion to the substrate and metamorphosis into the adult stage. This species has suitable characteristics to be proposed as a model organism for ecotoxicological assays. It has a wide geographic distribution, ecological relevance and it is relatively easy to breed under controlled laboratory conditions. It also exhibits rapid larval development and high sensitivity to a wide range of toxic substances.

Figure 76 *Adult specimens of the barnacle crustacean Amphibalanus Amphitrite.*

Nauplii at the 2nd larval stage were obtained from cultures of A. Amphitrite adults maintained in the laboratory (Fig 76). Approximately 20-30 adult A. Amphitrite specimens are maintained in glass containers with a volume equal to 700/800 mL of 0.45µm filtered natural seawater (FNSW, salinity 37%) aerated at a temperature of 20±2°C with a light: dark photoperiod of 16:8h. Adults are fed every two days by feeding Nauplii of *Artemia salina* (100mL, 20-35 larvae/mL) and an aliquot of the microalga *Tetraselmis suecica* (100mL, 2 x 105 cells/mL).

The release of Nauplii by the adults is stimulated by a change of water in the beakers, placing the adults in water at a temperature about 5-6°C higher than the holding temperature. The larvae (stage II Nauplii) are collected using a pipette (5mL volume) and placing the beaker near a light beam, thus taking advantage of the positive photoactive effect of the Nauplii. After being collected, the Nauplii are filtered through a nylon filter (80µm mesh) and transferred to a beaker containing 0.22 µm filtered natural seawater at a density of 15-20 larvae/mL.

The toxicity assay is set up within 2-4 hours after the Nauplii are released. The set-up involves the use of a polystyrene multiwall plate, 15-20 stage II Nauplii are placed in each well along with 2 mL of the solution to be tested (leached as is, undiluted). The plates are then stored at 20± 2°C, and after 24 and 48 hours, dead and immobile organisms are counted using a stereomicroscope. Larvae are considered dead if they show no movement for an observation time of 10 seconds.

The number of immobile organisms is given by the sum of the dead and the “non-swimmers” (i.e., those organisms that move their appendages but are unable to move their center of gravity). A negative control (Ctr, i.e., Nauplii maintained under the same exposure conditions in cleans FNSW) was also set up. Three replicates were set up for each elutriate dilution and for the control, the result corresponds to the mean value of the three replicates (± standard error). Two different types of ecotoxicological responses (end points) were considered: mortality and immobility. The former represents a classic “acute” type of end point while the latter is considered to be of the “sub-lethal” type, that is it is able to show milder toxicity effects, which do not lead to death of the organism but still result in a severe effect (the inability to make movements).

11.2 Results

The mortality and immobility rates obtained after 24 and 48 hours of exposure of A. Amphitrite Nauplii to leaching products collected after 1 hour, 24 hours and 72 hours shown below. For the leaching product collected after 1 hour, the mortality and immobility rates (obtained after 24 and 48 hours of contact with the larvae) are shown in figures 77 respectively.

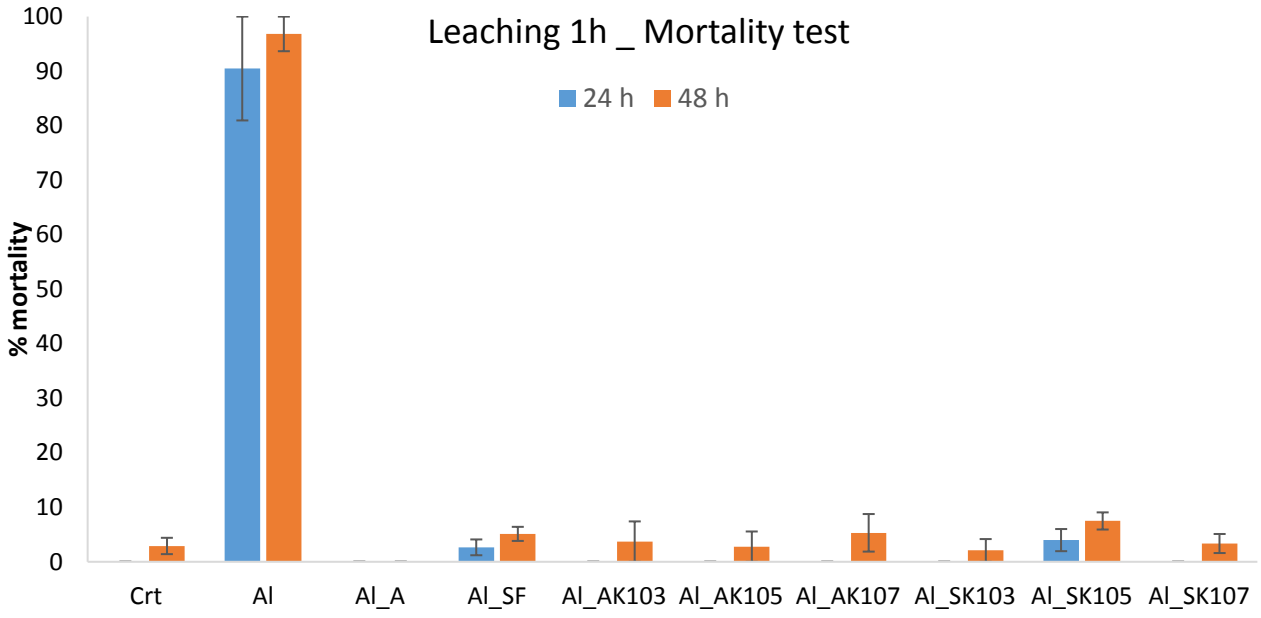

Figure 77 *Percentage of mortality of A. Amphitrite stage II Nauplii obtained after 24 and 48 hours of larval exposure to leaching products collected after one hour.*

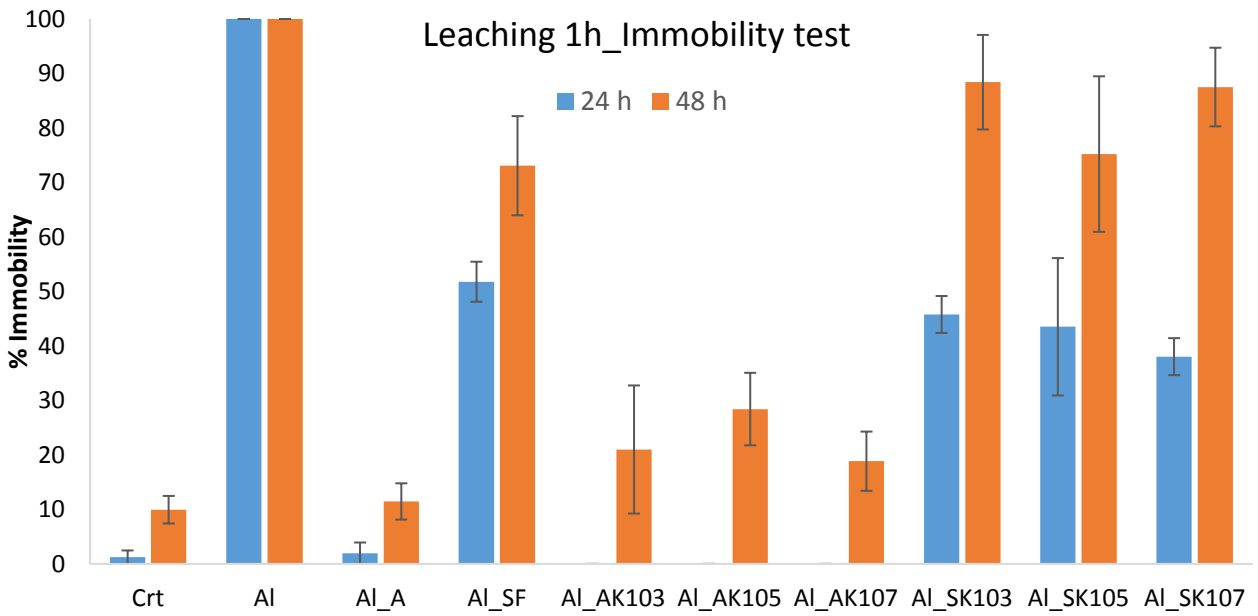

Figure 78 *Percentage of immobility of A. Amphitrite stage II Nauplii obtained after 24 and 48 hours exposure of larvae to leaching products collected after one hour.*

The mortality end point shown (Fig 77) a high effect rate (<80% after both 24 and 48 hours) only for the leached aluminum specimen, i.e., the aluminum specimen without any coating. In contrast, for all other coating types, the mortality rates are less than 10% after both 24 and 48 hours. For the immobility endpoint, which is more sensitive than mortality because it takes into account not only dead larvae but also those larvae that are still alive but unable to make any kind of movement, higher effect rate are shown, especially with reference to specimens coated with fluorinated silica (SiO_2F) with and without Krytox (Al_SF, Al_SFK103, Al_SFK105, Al_SFK107). These show immobility rates above 60% after 48 hours of exposure (Fig 78). On the other hand, specimens coated with alumina (Al_2O_3) together Krytox (Al_AK103, Al_AK105, Al_AK107) show no toxicity effect after 24 hours even for this endpoint, while after 48 hours, rates between 18% and 28% are observed.

For products collected after 24 hours of leaching, percentages less than 20% are observed for the mortality end point after 48 hours of larval exposure for all specimens (Fig 79) including the exposure to the leachates (orange bars). A percentage of immobility above 20% is observed only for the leachate of the fluorinated silica-coated specimen (Al_SF). Percentages between 10% and 13% for the uncoated aluminum (Al) specimens and two coated with fluorinated silica together Krytox 105 and 107 (Al_SFK105 and Al_SFK107) (Fig. 80). In contrast, the result obtained after 48 hours of exposure shown consistently significantly higher effects rates than the negative control (Ctr) even with larval immobility rates greater than 80% and particularly for the specimens with the coating containing fluorinated silica with and without Krytox (Al_SF; Al_SFK103, Al_SFK105 and Al_SFK107).

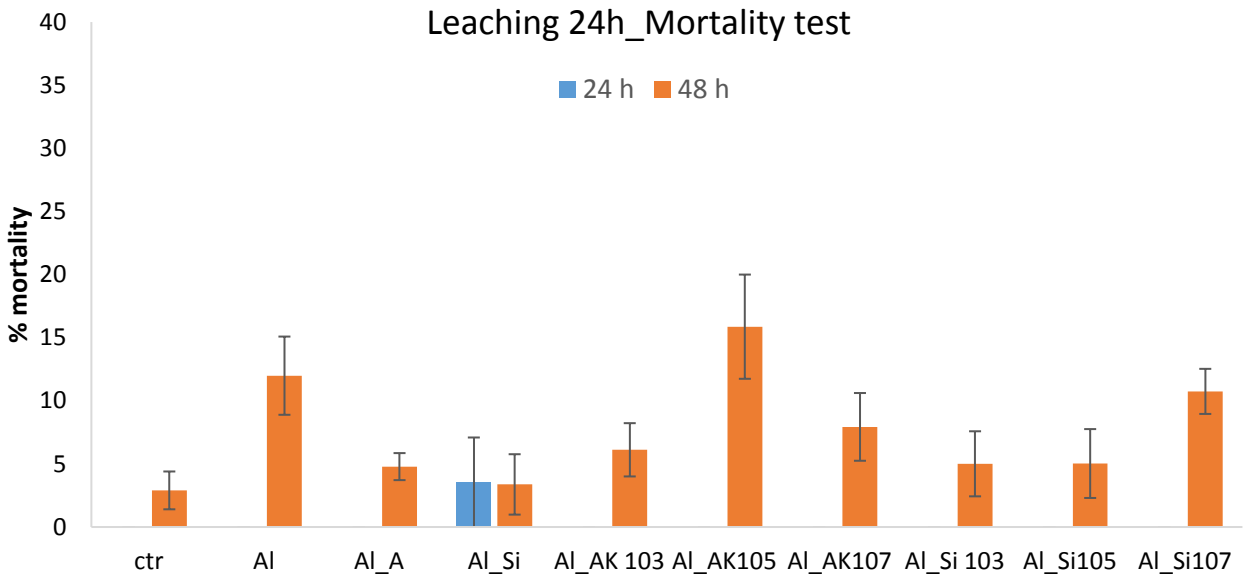

Figure 79 *Percentage of mortality of A. Amphitrite stage II Nauplii obtained after 24 and 48hours exposure of larvae to leaching products collected after 24 hours.*

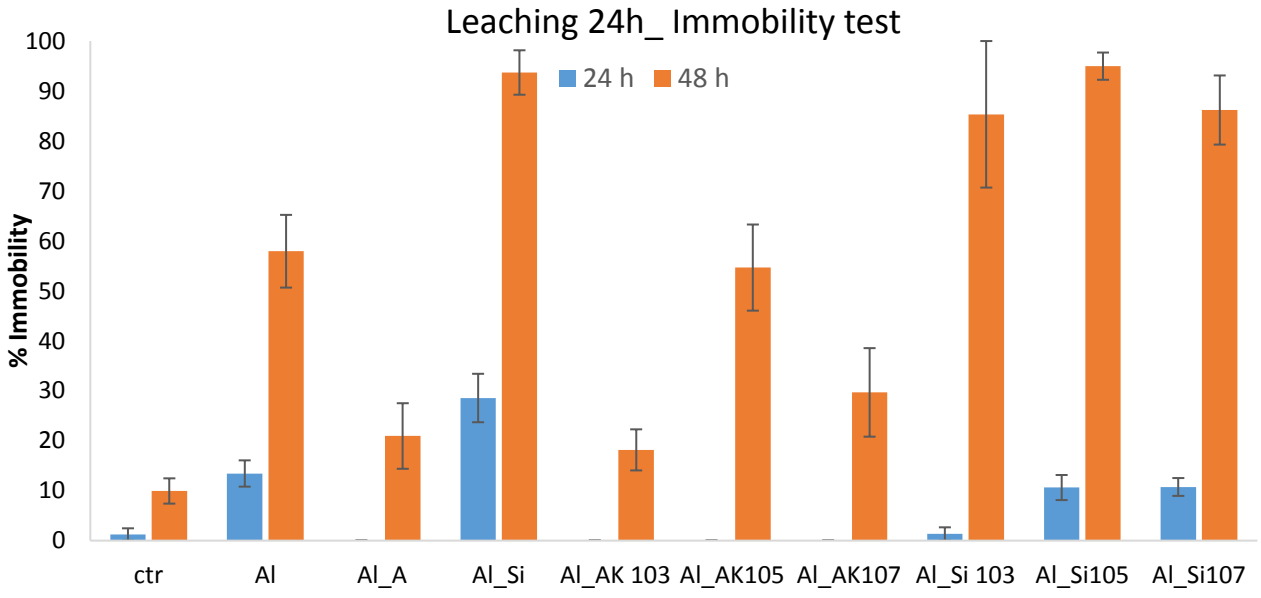

Figure 80 *Percentage immobility of A. Amphitrite stage II Nauplii obtained after 24 and 48 hours exposure of larvae to leaching products collected after 24 hours.*

For the products collected after 72 hours of leaching, the mortality endpoint (Fig. 81) after 24 hours of larval exposure shows zero effect rates for almost all leachates (1.5% for the leachate of the specimen coated with alumina + Krytox 103), while after 48 hours the effect is higher, particularly for the leachates of the specimens coated with alumina (Al_A) with alumina together Krytox 103 (Al_AK103) and the aluminum control (Al), but still less than 20% (Fig 81).

In figure 82, it can be seen that even for the immobility endpoint, the leachates of all specimens did not result in effect rates above 5% after 24hours of exposure of the larvae, thus not significantly different from the negative control (Ctr). After 48 hours of exposure for the same leachates, percentages above 20% were observed for almost all leaching products (excluding the leachate from the specimens coated with fluorinated silica and Krytox 107 (Al_SFK107).

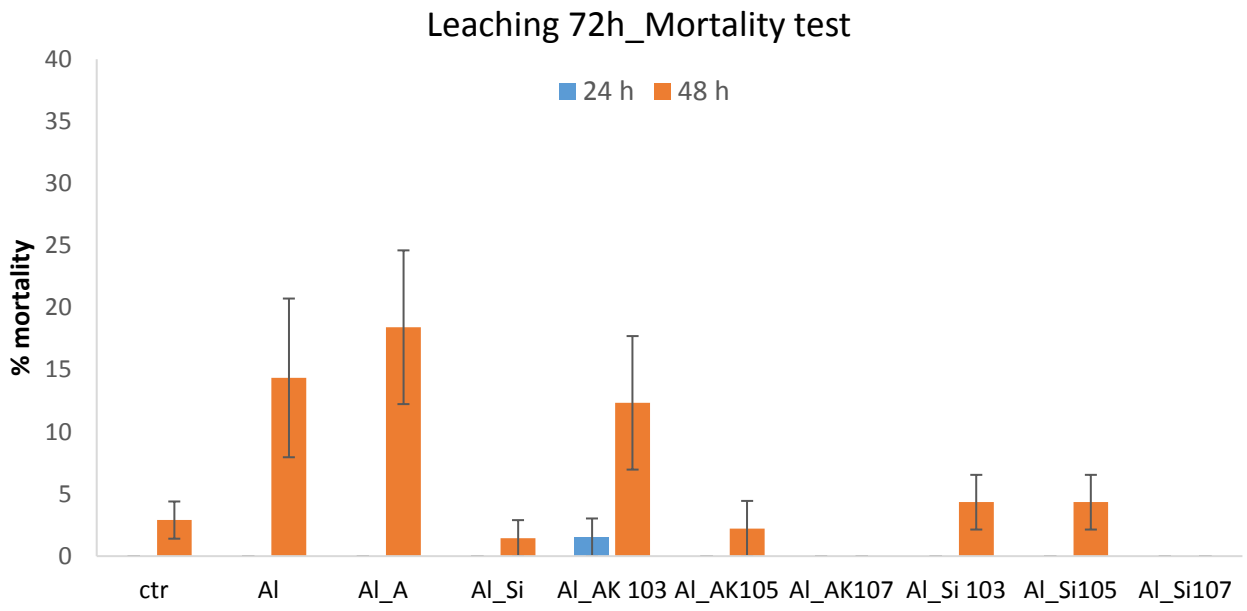

Figure 81 *Percentage mortality of A. Amphitrite stage II Nauplii obtained after 24 and 48 hours exposure of larvae to leaching products collected after 72 hours.*

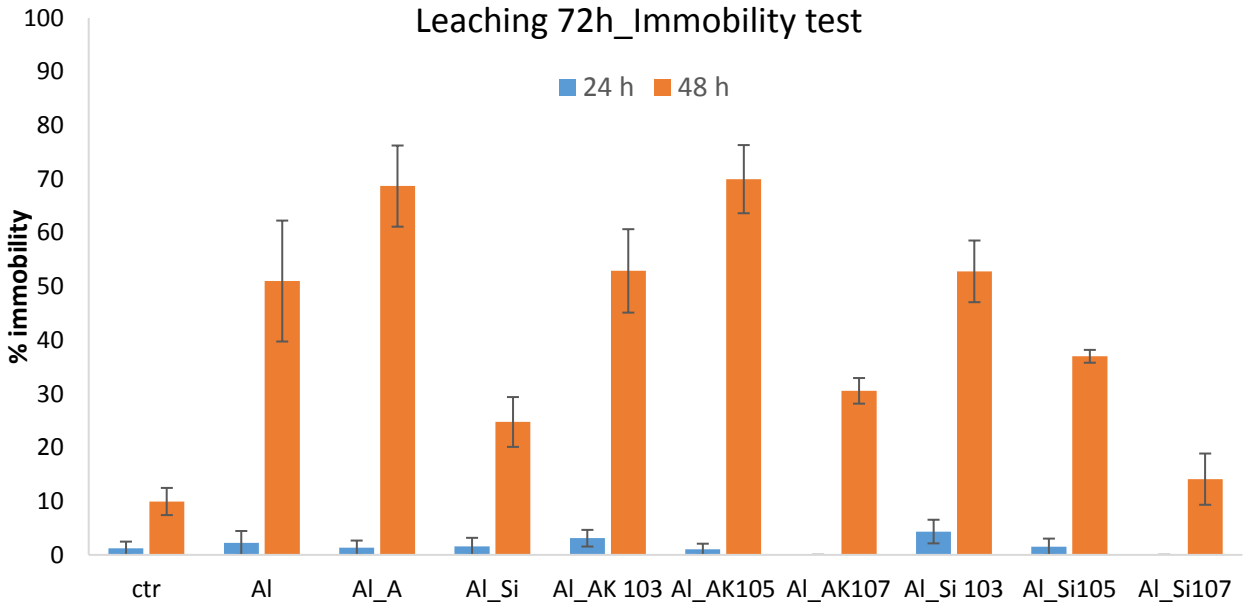

Figure 82 *Percentage immobility of A. Amphitrite stage II Nauplii obtained after 24 and 48hours exposure of larvae to leaching products collected after 72 hours.*

In summary, it is important to observe the rates of larvae mortality and immobility of A. Amphitrite obtained after 24 hours of exposure (orange bars histograms) of organisms to the products obtained after 1, 24, and 72 hours of leaching of aluminum specimens coated with different types of experimental coatings. High effect rates can be observed only for organisms exposed to the leachate collected after 1 hour (Fig. 77), while the leachates collected after 72 hours never show significant toxicity effects (Fig. 81) after 24 hours of contact with larvae. This figure 76 highlights how the release of toxic-acting products is presumably limited to the first hour of immersion in water, but already after 24 and 72 hours of immersion in seawater, the coatings are no longer capable of releasing toxic effects on the model organism tested. In figure 77, high and significantly different immobility rates compared to the negative control (Ctr) are observed for all leaching products. However, it should be noted that this result was obtained after 48 hours of larval exposure and for the most sensitive end point (immobility). Since habitually (included in L.D. 152/2006) only the mortality end point observed after 24 hours considered only the data on this response recorded after 24 hours of exposure of the organisms is taken into account. It is possible to conclude from this study that all types of experimental coatings applied on the aluminum specimens do not release products with toxic action, as evidenced by the mortality rates (after 24 hours) shown in Figure 77, 79, and 81.

For the most sensitive end point (immobility), however, this result is obtained for larvae exposed for 24 hours to leaching to products collected after 72 hours of immersion in seawater. The immobility data observed after 48 hours of exposure of larvae to leachates collected after 1 hour and 24 hours (Fig. 78 and 80), also highlighted a difference in toxicity effect between leachates from specimens with alumina-containing coating (Al_A; Al_AK103; Al_AK105 and Al_AK107) and those with fluorinated silica (Al_SF; Al_SFK103; Al_SFK105 and Al_SFK107): the leaching products obtained for the latter are able to result in higher immobility rates. However, this observation is not valid for leaching products collected after 72 hours (Fig. 82).

12. SUPERHYDROPHOBIC COATINGS IN MARINE EXPOSURE

12.1 Static field exposure (raft test) of coated surfaces

This type of test aims to verify the antifouling effectiveness of different surfaces with hybrid coating under static exposure conditions in the marine environment. The evaluation of antifouling effectiveness is carried out by means of a Raft-test performed at the Experimental marine Station (SMS) of CNR-IAS located in the Genoa's Harbor (Fig.83). The field test (raft test) is performed according to the ECHA Guideline "Guidance on the Biocidal Products Regulation –Volume II Efficacy-Assessment and Evaluation Part B+C (December 2017).

Specifically, the reference chapter for antifouling products is Chapter 5.7 (Other Biocidal Products, p. 239), Section 5.7.1 Antifouling products, and subsection 5.7.1.1.8 efficacy test p.242 Static Raft testing. The referenced ASTM standard is D3623-78a (2004) "Standard Test method for Testing Antifouling Panels in Shallow Submergence".

Figure 83 *Experimental marine Station (SMS) of the IAS-CNR in Genoa.*

The panels (10x10 cm) to which the coatings under study were applied are submerged for a minimum period of 6 months (and up to 12 months), taking care to include in this period the months characterized by a greatest pressure from biofouling (May August). The panels are placed on the perimeter on the floating dock present at the SMS in order to recreate the different lighting conditions present on the hull of a boat. In fact, the efficacy of the products in terms of antifouling performance will be evaluated both on the face of the specimen exposed to light and on the face of the specimen left in dark conditions. IAS CNR will carry out the evaluation of antifouling effectiveness on a monthly basis throughout the period exposure at sea. This evaluation will consist of two phases:

- Photographic sampling: performed by digital acquisition of the following high-resolution images of:

- Whole image of the individual Frame of both the side exposed to light and the side in shadow.
- Whole image of both sides (light/dark) of each individual specimen.

- Assessment of biological cover (biofouling): is performed by quantitative and qualitative analysis of the different images using Photogrid® software appropriately set up in order to be able to estimate the contribution of each individual Taxon to the diversity of biofouling present on the specimens (Fig. 84).

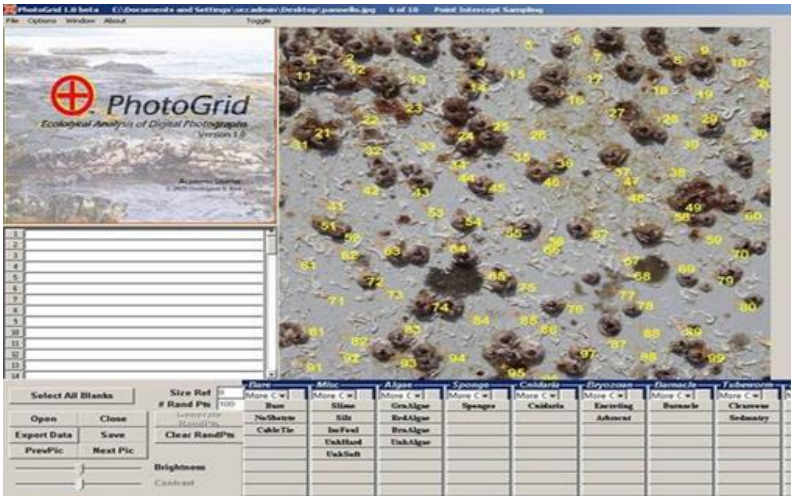

Figure 84 *Photogrid image analysis software interface.*

This analysis allows for the assessment of the antifouling effectiveness of the coating in terms of total biofouling cover (% cover) divided into three categories, namely “PA-B” (algal patina-biofilm), “soft fouling” i.e., organisms without calcareous structures such as, for example, sponge, bryozoans and ascidians, and “hard fouling”, organisms with calcareous structures such as balanus, serpulids and bivalves. In parallel, the analysis of the settled community is also conducted, pushing to the classification of the different types of settled organisms (taxa) for each category. An example of the graphical output of the expected classification is shown in the Figure 85.

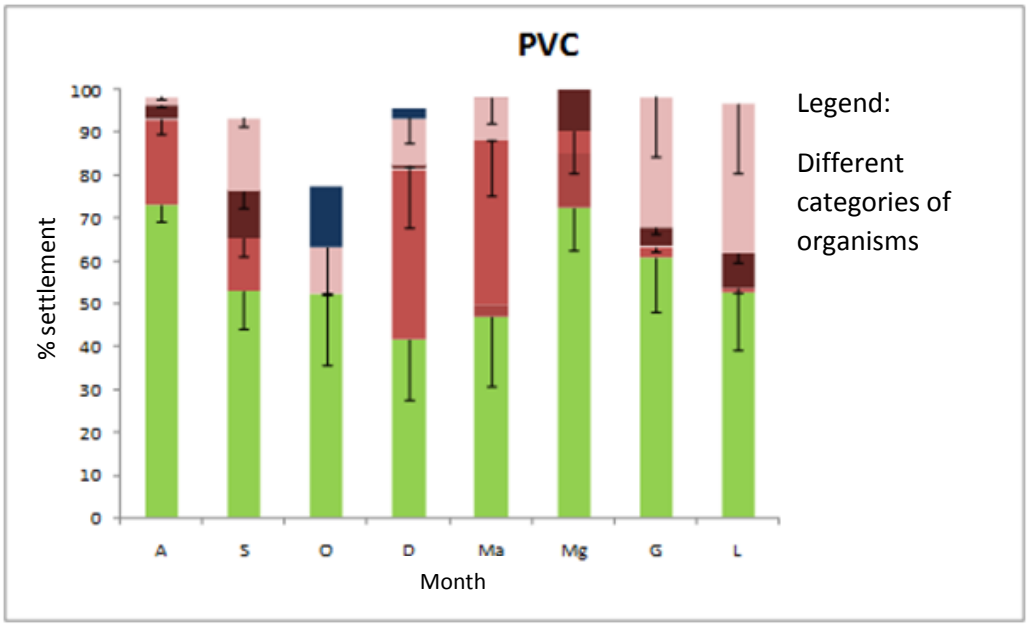

Figure 85 *Example of graphical output representing the degree of cover-expressed as a percentage of the analyzed area of the different categories of fouling organisms.*

The aluminum and fiberglass substrate (with dimension of 10x10 cm equipped with four holes with a diameter of about 6 mm positioned at the corners) on which the coating listed in table 29. The coatings were deposited –selected on the basis of the results obtained during the experimental phases previously described (larval settlement test aimed at verifying the antifouling potential of the coatings and eco-compatibility test) were already immersed on 15/6/2021. For each type of coating subjected to the "raft test", three replicas (3 panels) were prepared and immersed. The aluminum panels (Al) have coating on both sides, while for the fiberglass panels (FB) it was not possible to apply the coating on both sides, so they were prepared in duplicated and then dipped "sandwich" with the side coated by the coating facing outward, so that one side with the coating is exposed to the light and one the dark during exposure at sea.

In addition, a series (3 replicates) of PVC control panels were also immersed, uncoated and to be used as a reference, in order to monitor the growth of fouling on a third type of material, for which there are numerous coating data obtained in previous experiments.

A brief description is given on the sampling produced on aluminum substrate with a smooth surface finish and an epoxy-based fiberglass. The table 29 shows the coatings deposited and the abbreviation used for the subsequent data produced.

Table 29 *Outline of sampling for sea exposure testing.*

Substrate	Abbreviation	Coating	Note
Aluminum	Al	Uncoated	3
Aluminum	Al_A	Al_2O_3/FAS	x3-2 coated face
Aluminum	Al_S	SiO_2F	"
Aluminum	Al_AK105	Al_2O_3/FAS +Krytox 105	"
Fiberglass	Al_SK105	SiO_2F+Krytox 105	"
Fiberglass	FB	Uncoated	x6
Fiberglass	FB_S	SiO_2F	x6-1 coated face
Fiberglass	FB_AK105	Al_2O_3/FAS +Krytox 105	"
Fiberglass	FB_SK105	SiO_2F+Krytox 105	"

A brief schematic of the deposition process of alumina-based coatings on both substrate is shown.

Description of Al_2O_3 deposition process for aluminum and fiberglass substrate. The dip-coating parameters are described: extraction rate (u) and dip time. TT is an acronym for Thermal Treatments. EtOH Ethyl alcohol; iPrOH Isopropyl alcohol.

Substrate Aluminum: Al_2O_3/FAS coating.

Washing in soapy water: EtOH → dip coating Al_2O_3 u= 2mm/s 5s immersion → TT 400°C 1h → boiling water 30 min→ TT 400°C 10 min → dip coating FAS u=2mm/s 120s immersion → TT 150°C 30 min.

Substrate Aluminum: Al_2O_3/FAS coating +Krytox 105.

Washing in soapy water: EtOH → dip coating Al_2O_3 u= 2mm/s 5s immersion → TT 400°C 1h → boiling water 30 min→ TT 400°C 10 min → dip coating FAS u=2mm/s 120s immersion → TT 150°C 30 min → Krytox 105 infusion.

Substrate Fiberglass: Al_2O_3/FAS coating.

Washing in iPrOH→ dip coating Al_2O_3 u= 4mm/s 5s immersion → TT 60°C 24h → water vapor 30 min→ dry 48h T_r → dip coating FAS u=0.1 mm/s 120s immersion → dry 12h T_r.

Substrate Fiberglass: Al_2O_3/FAS coating + Krytox 105.

Washing in iPrOH→ dip coating Al_2O_3 u= 4mm/s 5s immersion → TT 60°C 24h → water vapor 30 min→ dry 48h T_r → dip coating FAS u=0.1 mm/s 120s immersion → dry 12h T_r→ Krytox 105 infusion.

The diagram of fluorinated silica (SiO_2F) deposition on aluminum and fiberglass substrate is shown.

Description of SiO_2F deposition process for aluminum and fiberglass substrate. The dip-coating parameters are described: extraction rate (u) and dip time. TT is an acronym for Thermal Treatments. EtOH Ethyl alcohol; iPrOH Isopropyl alcohol.

Substrate Aluminum: SiO_2F coating.

Washing in soapy water: EtOH → dip coating SiO_2F u= 2mm/s 120s immersion→ TT 150°C 30 min.

Substrate Aluminum: SiO_2F coating + Krytox 105.

Washing in soapy water: EtOH → dip coating SiO_2F u= 2mm/s 120s immersion→ TT 150°C 30 min→ Krytox 105 infusion.

Substrate fiberglass: SiO_2F coating.

Washing in iPrOH→ dip coating SiO_2F u= 4mm/s 120s immersion→ TT 60°C 24h.

Substrate fiberglass: SiO_2F coating+ Krytox 105.

Washing in iPrOH→ dip coating SiO_2F u= 4mm/s 120s immersion→ TT 60°C 24h→ Krytox 105 infusion.

The panels were immersed using a stand (called “frame”) made of rigid PVC on which they were arranged using cable ties and in a random pattern to ensure statistical independence of the observation. Each frame is approximately 100 x 60 cm in size and can accommodate a number of panels ranging from 12 to 15. Each individual panels was named with an acronym (shown in table 30) to allow its unique identification through the experiment. Following (Fig. 85) are diagrams showing the arrangement of the panels list in table in the frames used for the sea immersion. Three frames were immersed, for a total of 30 exposed panels (N° 15 aluminum, N°12 fiberglass and N° 3 PVC).

The three frames thus set up were dipped on one side on the floating raft in Figure 86 at the IAS SMS, with one side of the panels facing outward from the dock to which the raft is anchored (light side) and one facing inward (dark side).

Figure 86 *Immersion of the frames on the side of the raft at the SMS of IAS-CNR.*

Following the immersion, the growth of biofouling on the panels was monitored on a monthly basis in the manner described above (photographic monitoring and image analysis using Photogrid). The result of the field test are summarized below, with details on the 2nd and 5th months of immersion. The field trial, as written earlier, lasted for 12 months, and images of the overburden were collected monthly.

The 2nd and 5th months of immersion at sea are chosen as representative months as the corresponding immersion period (i.e. from June 2021 to October 2021 inclusive) includes the summer months, which are those in which the most favorable conditions occur to the growth of fouling (higher water temperature and greater number of hours of light during the day). The bulk of the settlement by fouling organisms occurs in fact during the period between May and October, the winter months usually show a slower growth of fouling, and therefore the results obtained in the fifth month (October 2021) can already be significant and indicative considerations of the potential antifouling effectiveness of the coatings under study.

12.2 Results

II month of immersion

The photos taken of the samples immersed in the sea after two months of immersion are shown, the aluminum and then fiberglass sample coated as in table are shown first. The side exposed to light is distinguished from the side exposed to the dark.

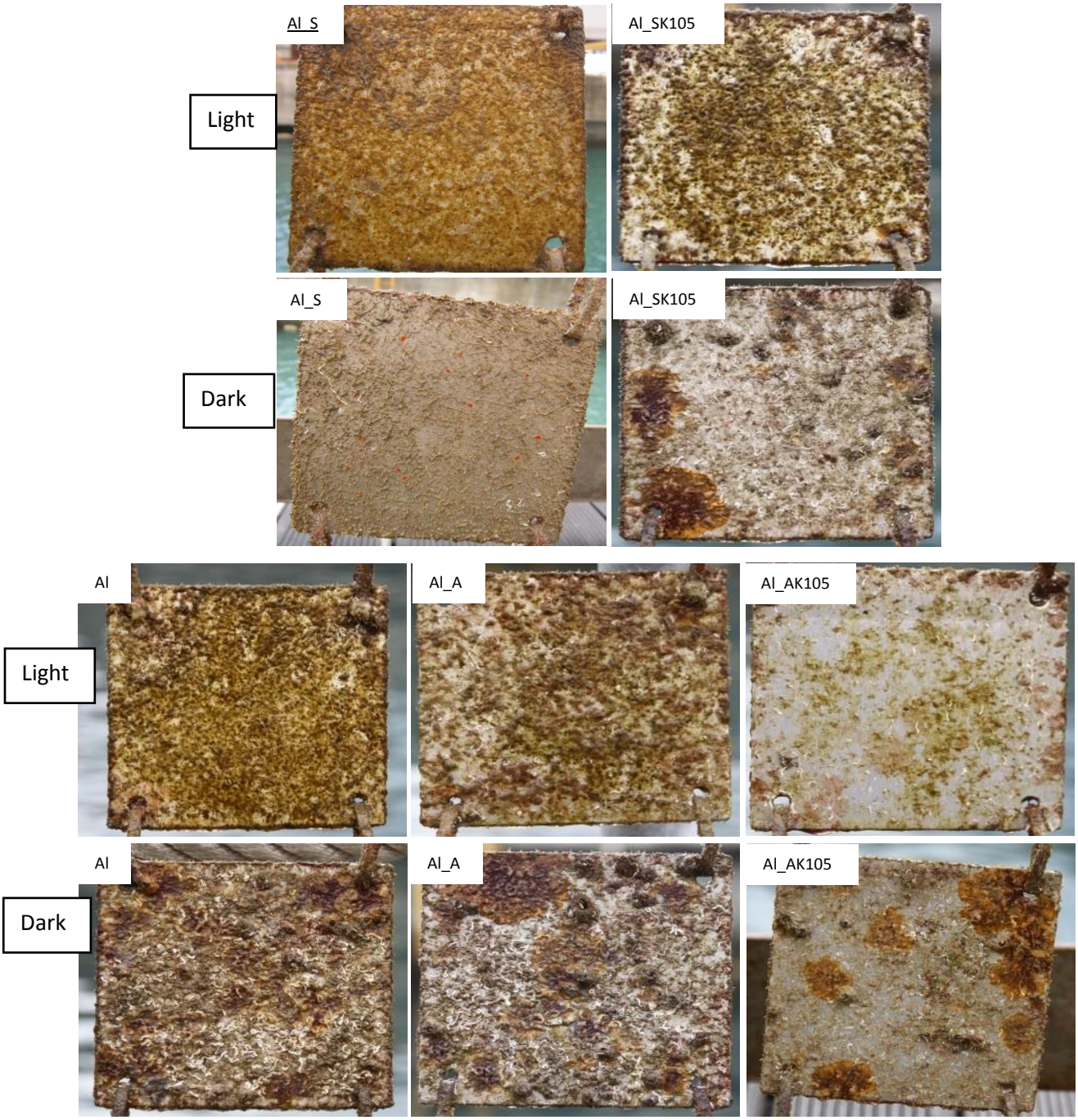

Figure 87 *A) Photo exposure at sea of aluminum samples after 2 months of immersion in the summer period June-July coated with Al_2O_3 with one face exposed to light and one exposed to darkness. B) Photo exposure at sea of aluminum samples after 2 months of immersion in the period summer June-July coated with SiO_2F with one face exposed to light and one exposed to darkness.*

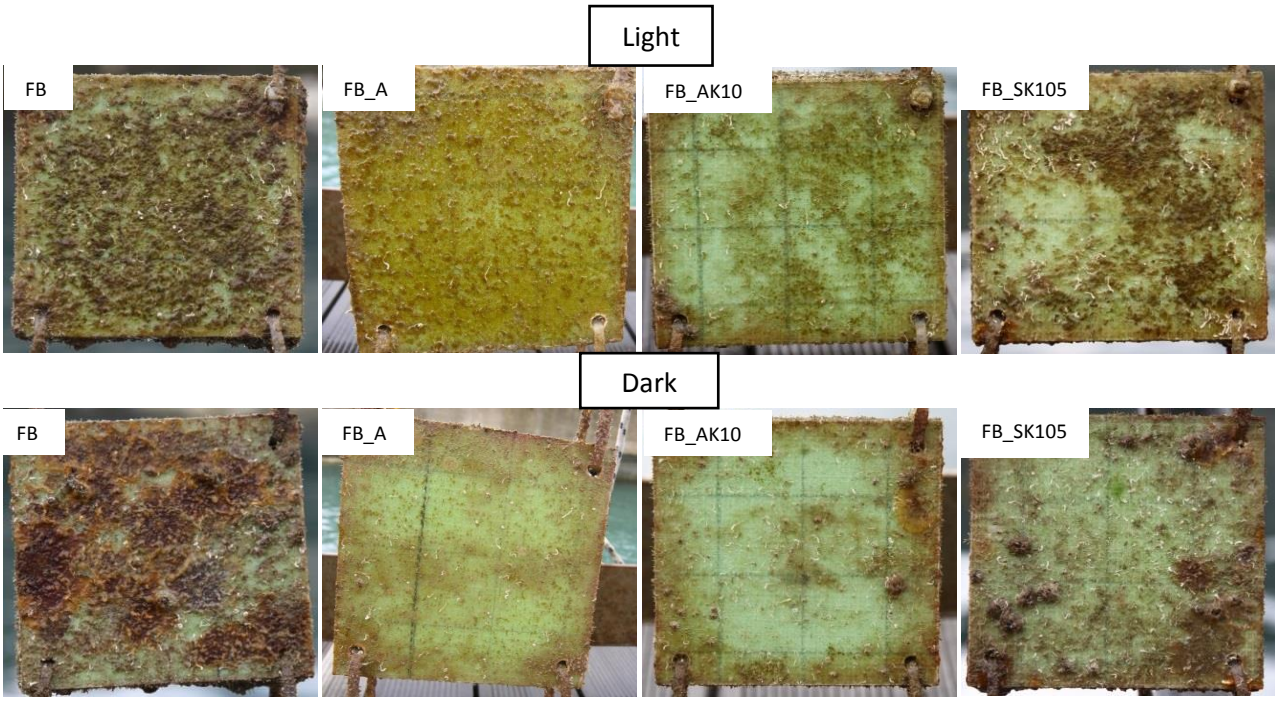

Figure 88 *Photo exposure at sea of Fiberglass samples after 2 months of immersion in the summer period June-July coated with Al_2O_3 and SiO_2F with one side exposed to light and one exposed to darkness.*

Each frame (Fig 87 and 88) was then analyzed with the Photogrid software to evaluate the coverage percentages and which attacked type of fouling the sample. For each type of coating, three replicates were carried out, and the percentages are an average of the data obtained.

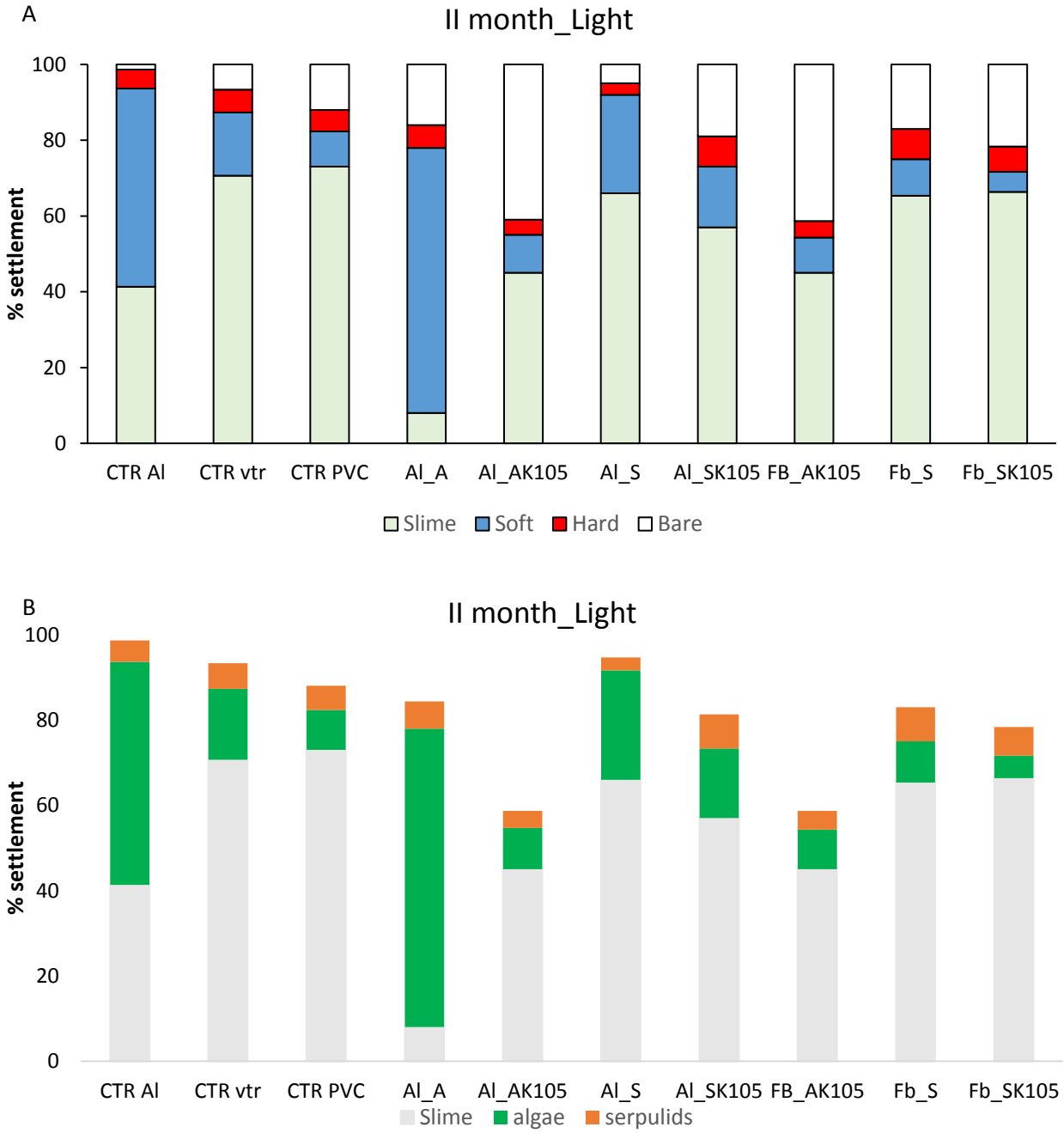

Figure 89 *Histograms relating to the second month of immersion of the panels in light conditions. Figure A reports the results in terms of coverage by hard fouling (red bars), soft fouling (blue bars) and slime (algal film). Figure B reports the results in terms of coverage of fouling macrocategories.*

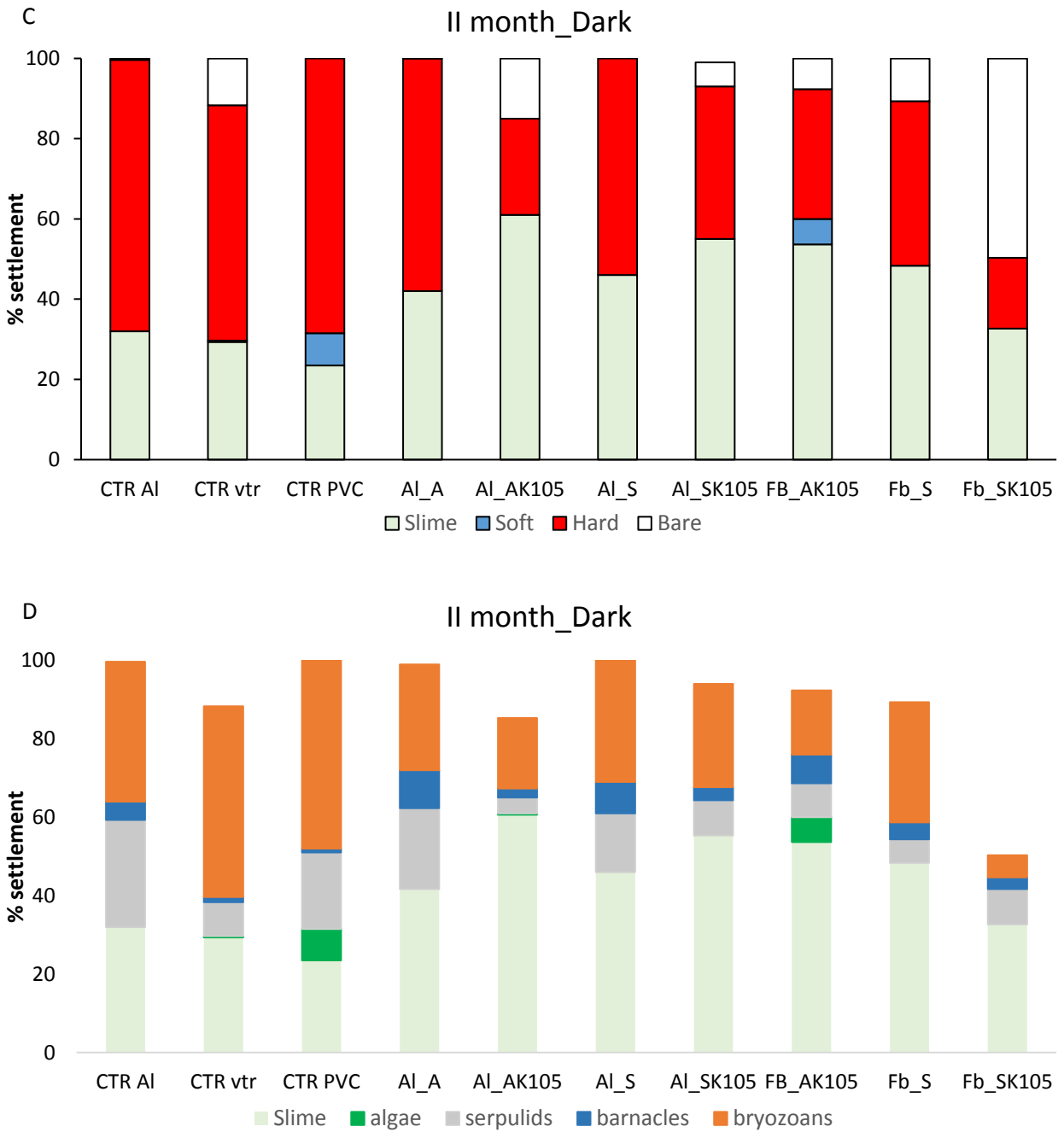

Figure 90 *Histograms relating to the second month of immersion of the panels in dark conditions. Figure C reports in terms of coverage by hard fouling (red bars) and soft fouling (blue bars) and slime (algal film). Figure D reports the results in terms of fouling macrocategories.*

After the initial two months immersion in the sea, the panels exposed to light condition (as shown in the figure 87 and 88) exhibit relatively low coverage percentages for all coatings. Specifically, the percentages of hard fouling denoting organisms with calcareous structures are consistently below 10% for all coatings. Conversely, the percentage of soft fouling, comprising organisms without calcareous structures such as algae, are higher. In some instances, the soft fouling percentage exceed 60% notably observed in the case of the Al_2O_3 +FAS coating applied on aluminum (Al_A).

Particularly for this Al_2O_3 +FAS coating, a significant discrepancy noticeable between the percentage of soft fouling (algae) on the coating without the Krytox 105 components (Al_A with soft fouling ≥ 70% Figure 89) and the one where Krytox 105 is present (Al_AK105 with soft fouling = 10% figure 89). In general, it is evident that panels with coatings applied on fiberglass substrates exhibit lower percentages of soft fouling compared to those with formulation applied on aluminum (as shown in the figure 89 a), while the percentages of hard fouling remains comparable across all coating type. Regarding the composition of fouling on the panels (in figure 89 b), two major categories are observed after the initial two-month immersion: hard fouling appears to consist exclusively of serpulids, while algae primarily represent soft fouling.

Upon analyzing the coverage percentages on the side exposed to low light conditions (the dark side in the figure 87 and 88), it becomes evident that the hard fouling percentages are notably higher compared to the well-lit side (in figure 90 c). Hard fouling percentages exceed 30% for all coatings on this dark side. Specifically, for the aluminum panels with the Al_2O_3 +FAS and SiO_2F coatings (abbreviation as Al_A and Al_S), the hard fouling percentages surpass 50% (57% and 54%, respectively) approaching levels only slightly lower than those observed on control aluminum panels (68% CRT). Conversely, coatings with lower hard fouling percentages are Al_AK105 (hard fouling = 24%) and Al_SK105 (hard fouling = 18%). This same trend is also apparent for fiberglass coating. Sample coated with Krytox 105 (FB_AK105 and FB_SK105) exhibit remarkably low hard fouling percentages (16% and 6% respectively). The consistent presence of Krytox 105 component in both coatings reaffirms its role in providing protection, as previously highlighted in the results from the well-lit side.

V° month immersion

Figures 91 and 92 shown the photos of the aluminum and fiberglass panels coated in month V of immersion (October). The figure 93 and 94, followed by graphs with the percentage of coverage present on the panels after 5 months of immersion in the sea (from June to October).

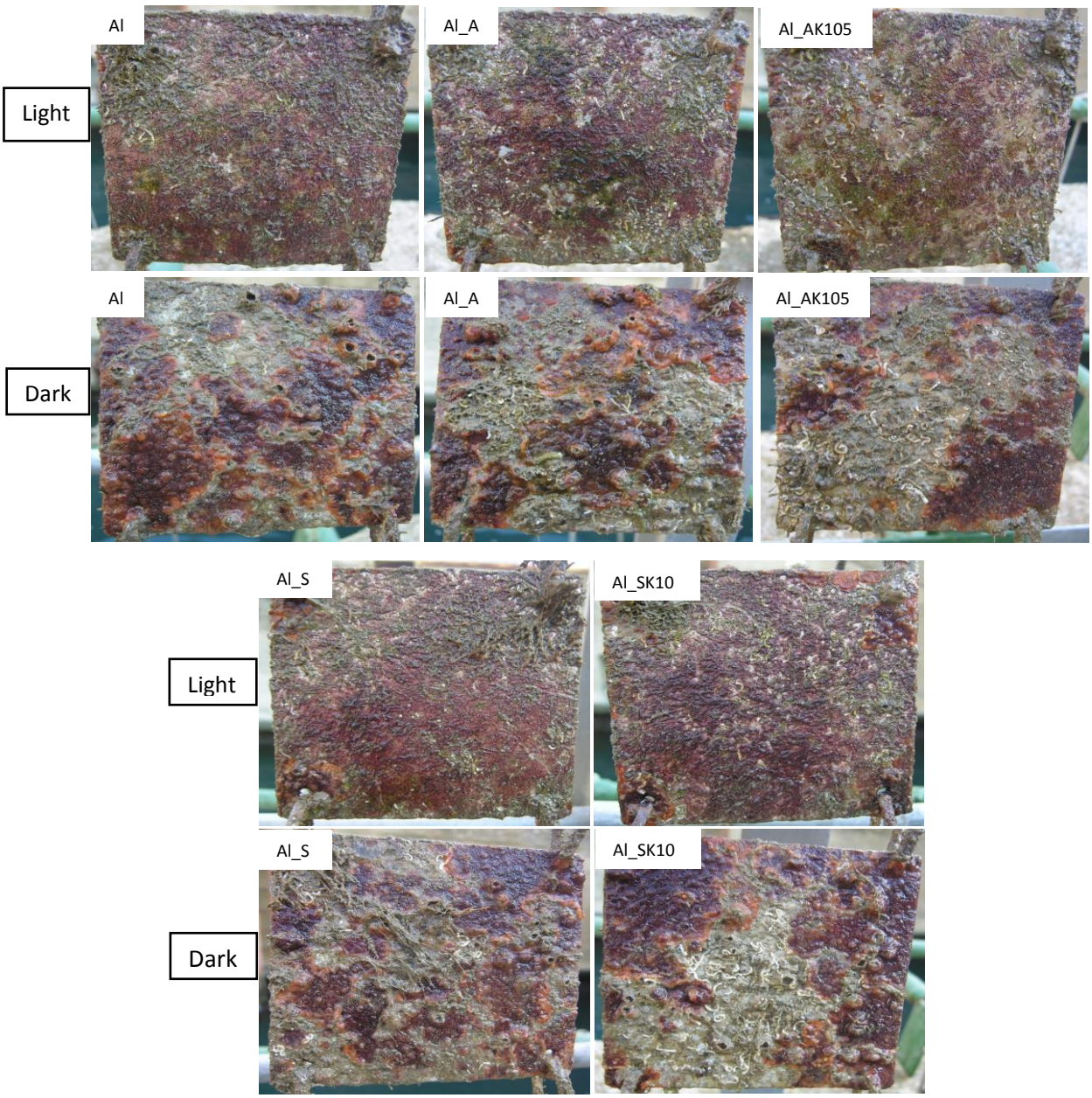

Figure 91 *A) Photo exposure at sea of aluminum sample after 5 months of immersion in the summer period June-October coated with Al_2O_3 with one face exposed to light and one exposed to darkness. B) Photo exposure at sea of aluminum samples after 5 months of immersion in the period summer June-October coated with SiO_2F with one face exposed to light and one exposed to darkness.*

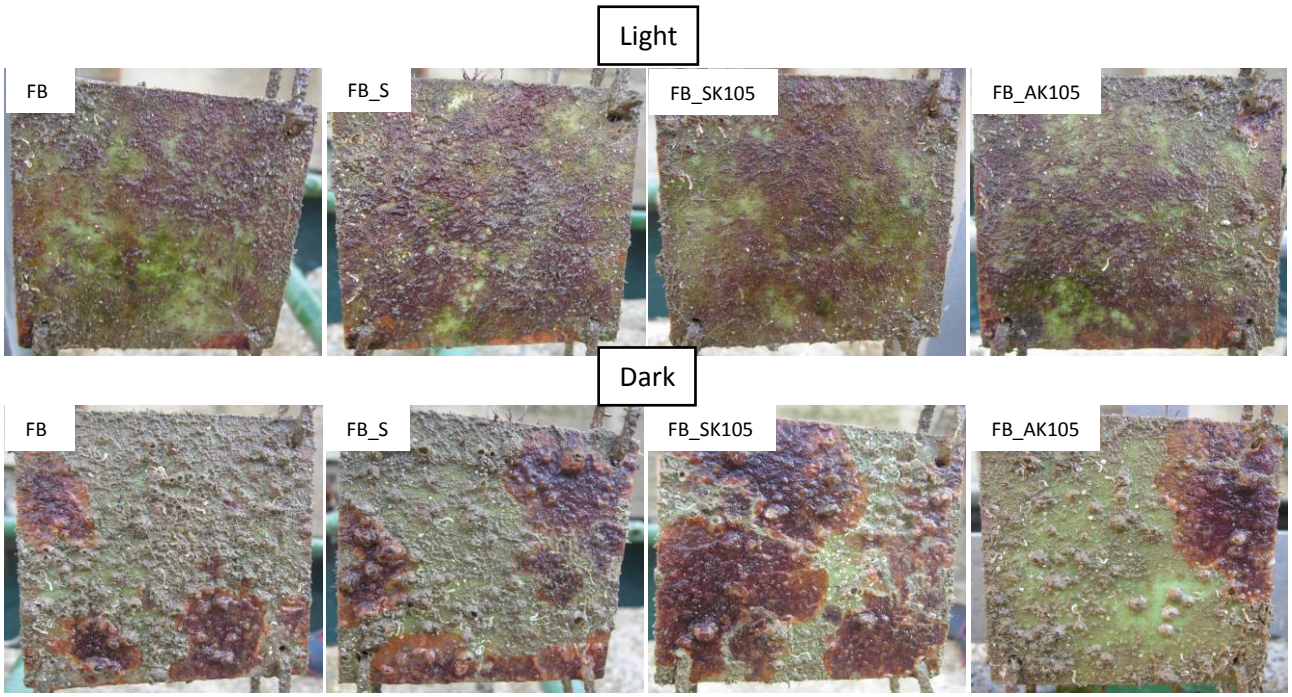

Figure 92 *Photo exposure at sea of fiberglass samples after 5 months of immersion in the summer period June-October coated with Al_2O_3 and SiO_2F with one side exposed to light and one exposed to darkness.*

Frame obtained at the fifth month of immersion were also analyzed at the Photogrid, the graph below represent the measured fouling rates (soft and hard) (Fig 93 and 94).

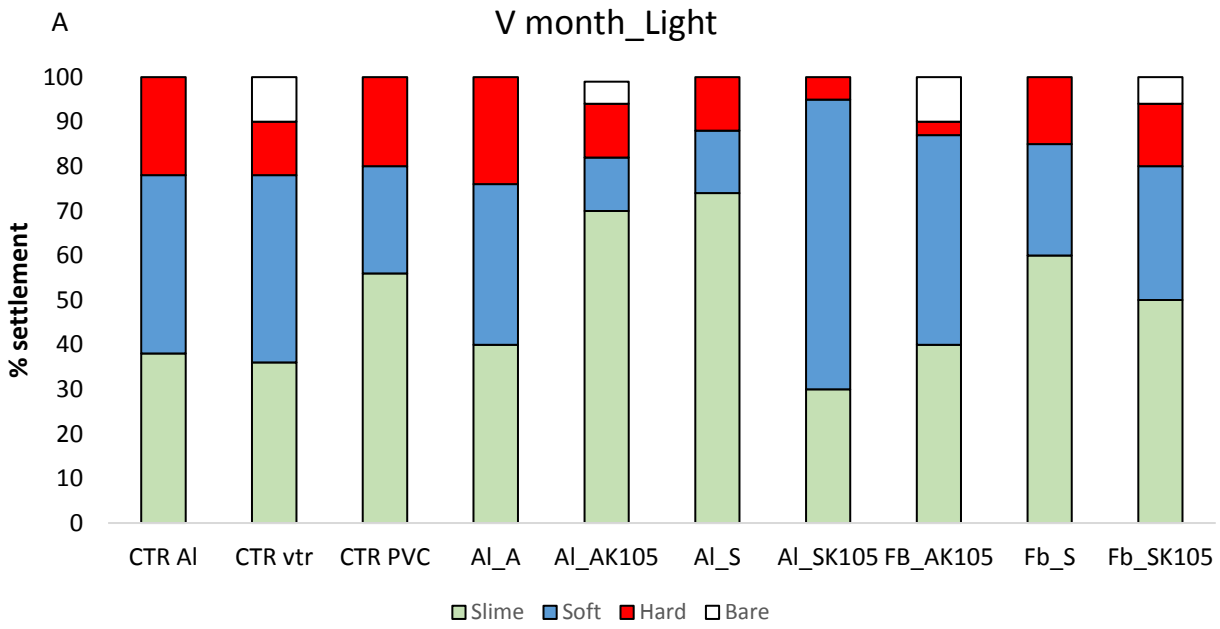

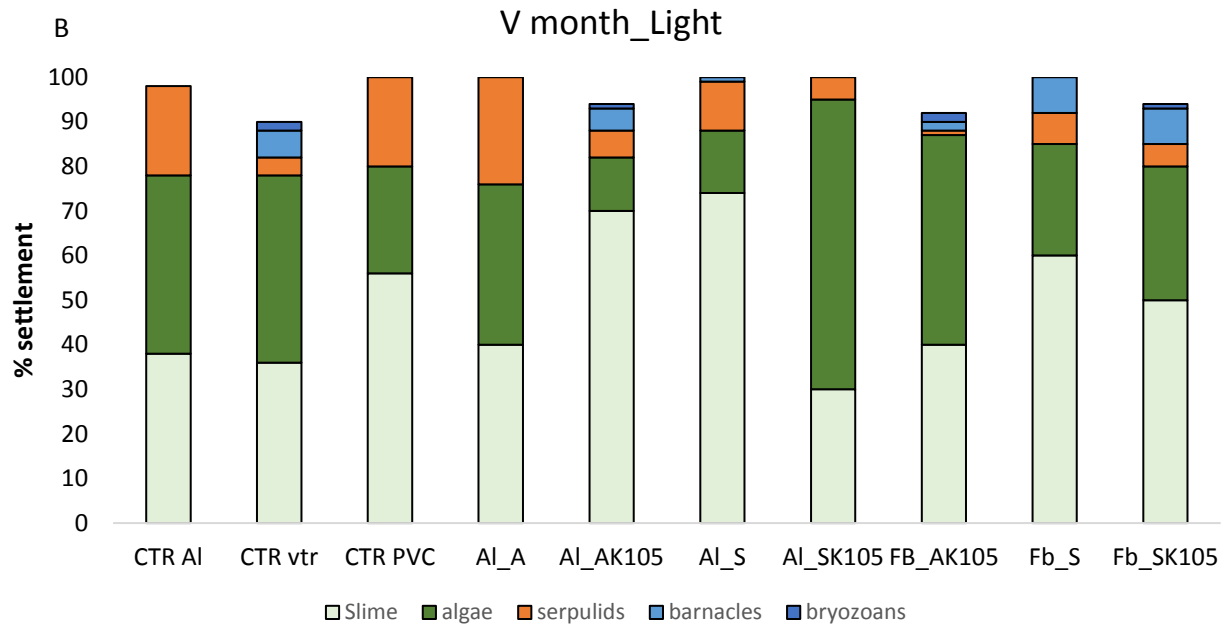

Figure 93 *Histograms relating to the fifth months of immersion of the panels in light conditions. Figure A reports the results in terms of coverage by hard fouling (red bars), soft fouling (blue bars) and slime (algal film). Figure B reports the results in terms of coverage of fouling macrocategories.*

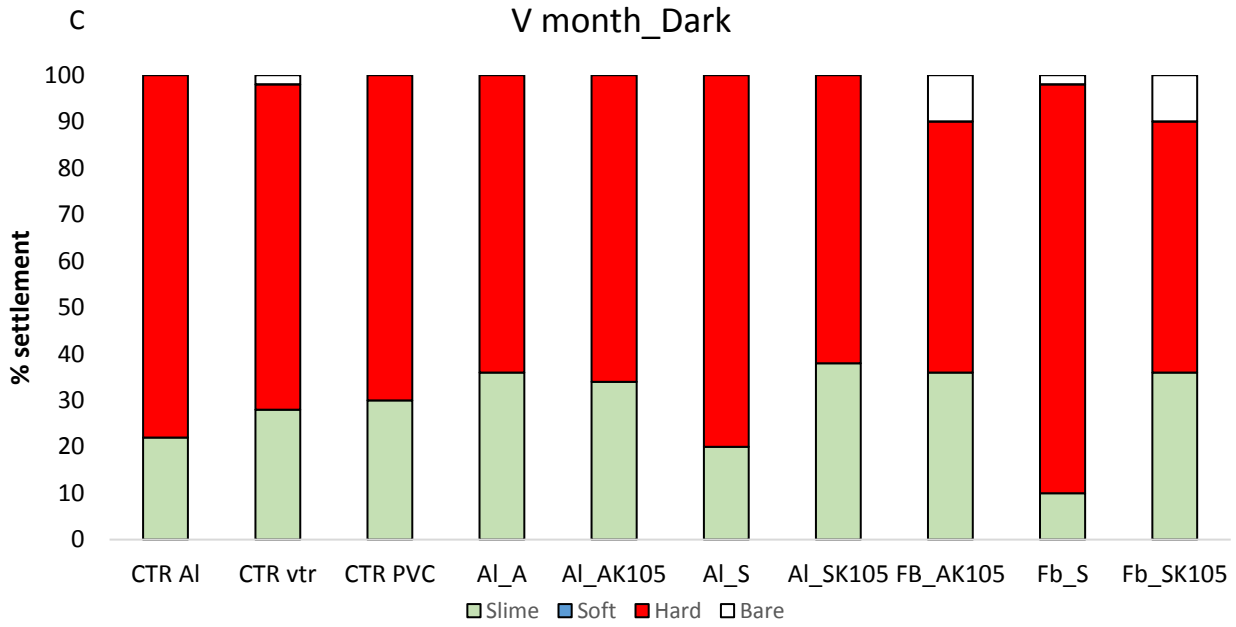

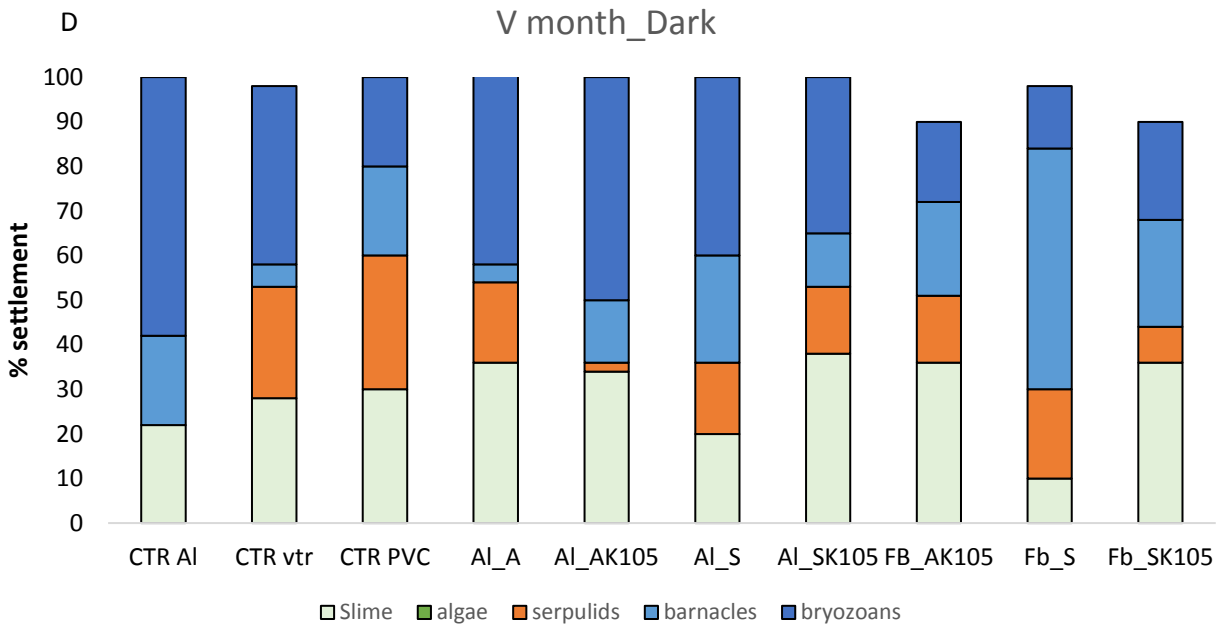

Figure 94 *Histograms relating to the fifth months of immersion of the panels in dark conditions. Figure A reports the results in terms of coverage by hard fouling 8red bars), soft fouling (blue bars) and slime (algal film). Figure B reports the results in terms of coverage of fouling macrocategories.*

Following a five months immersion in the sea, on the panels exposed to well-lit conditions (light side, as shown in the figure 91 and 92), the percentage of coverage by hard fouling organisms continue to remain relatively low, consistently staying below 35% for all samples. Conversely, there is a notable increase in the percentages of soft fouling, particularly exceeding 35% for coatings denoted as Al_A, Al_ASK105 and FB_AK105 (as illustrated in the figure 93, showcase soft fouling percentages of 35%, 67% and 47% respectively).

The presence of Krytox 105 components within the formulation does not seem to confer enhanced protection against algae proliferation, as previously noted in the results after the secondo month of immersion. It is probable that during the five-month period, Krytox is released from the porous structures where it was initially situated. Consequently, the samples lose the observed characteristics over time.

It's important to emphasize that the control panels, whether made of aluminum (CRT_Al) or fiberglass (CRT_FB) and PVC, exhibit hard fouling percentages comparable to those observed on panels with various types of coatings (excluding the Al_SK105 and FB_AK105 coatings mentioned earlier). These findings suggest a potential role for the Krytox 105 component in deterring the settlement of hard fouling organisms, although its effectiveness varies across different coatings where it is incorporate.

Regarding the composition of fouling on the panels (as shown in the Figure 93 b), and 94 d)) after 5 months of immersion, the following major categories are evident: hard fouling primarily comprises serpulids, with small percentages of barnacles and encrusting bryozoans. Conversely, soft fouling continues to be primarily represented by algae.

On the side exposed to dim light conditions (dark side figure 94), as previously observed after the II° months of immersion, higher percentages of hard fouling are noted compared to the light side (figure 93) exceeding 50% for all coatings. Specifically, for the SiO_2F applied on aluminum and fiberglass (Al_S and FB_S) the hard fouling percentages are 80% and 88% respectively, indicating limited antifouling protection by this coating. Similarly, for all other types of coatings (applied on both aluminum and fiberglass), generally on the side exposed to darkness, the high presence of hard fouling underscores insufficient antifouling protection under these exposure conditions, with growth of organisms comparable to that observed in controls. The presence of soft fouling is extremely reduced or absent in most cases, confirming previous observations from the II° month of immersion. Regarding the composition of fouling on the panels (figure 94 d), hard fouling primarily consists of encrusting bryozoans (with percentages ranging between 25% and 56%) barnacles (percentages ranging between 4% and 26%) and serpulids (between 3% and 22%).

Conclusion

The antifouling effectiveness of the experimental superhydrophobic (SLIPS) coatings under study was evaluated under static exposure conditions in marine environment through a “Raft test” lasting up to 12 months. The fouling organisms coverage percentages observed after the II° and V° months of immersion (Fig. 89 a 90 c and 93 a 94 c) lead to the following summary evaluations: under light (Fig. 89 b and 93 b), the percentages of hard fouling (fouling organisms with calcareous structure) remain relatively low (below 10% after 2 months and around 25% after 5 months of immersion). Additionally, a potential role of the Krytox 105 component (K105) in enhancing antifouling capacity when integrated into the coating can be hypothesized.

Under the same panels exposure conditions (light side), the growth of soft fouling (algae) does not be particularly inhibited by the tested experimental coatings, especially those without the Krytox 105 component. This observation is evident after the II month of immersion (Fig. 89 a, 90 b): the fouling coverage data obtained for the side of the panels exposed to lower light conditions (dark side) indicated a significantly lower antifouling protection compared to the light side generally for all type of coatings.

After two months of immersion the percentages of hard fouling on the dark side are consistently quite high for all types of coatings (ranging between 25% and 57%, figure 88 c), but still lower than the percentages of hard fouling observed on the control panels (after 2 months: 68% CRT_AL; 59% for CRT_FB and 69% for CRT PVC, Figure 90 c).

After five months of immersion, the percentage of hard fouling on the dark side range between 53% and 88% for panels coated with SLIPS coating (Figure 94 c). These percentages are comparable to, and in some case even higher than, the percentage of hard fouling observed on the control panels (76% for CRT_AL, 70% CRT_FB, and 66% for CRT PVC, figure 94 c). The potential contribution of the Krytox 105 component in enhancing protection against fouling organism settlement is less evident after five months of immersion, particularly on the dark side. In general, the experimental superhydrophobic (SLIPS) coatings under study seem to exhibit decent antifouling effectiveness for shorter periods of immersion and under higher lighting conditions, while their efficacy appears to diminish under low natural light conditions.

The causes for the limited durability of the coating can vary. Coatings based on fluorinated silica may have poor adhesion to the surface, both on aluminum and fiberglass substrate. In addition, on the fiberglass substrate, a mild heat treatment might be applied, which, however, does not allow for effective nano-structuring of our ceramic layer. Consequently, the lack of nano-structuring in the flower-like alumina hinders the creation of a nano-roughness essential for effectively retaining the Krytox.

One of the viable strategies is to apply a primer compatible with the substrate, containing a filler that facilitates chemical adhesion with the superhydrophobic coating.

13. DURABILITY OF SUPERHYDROPHOBIC PROPERTIES UNDER STATIC AND DYNAMIC SEA WATER CONDITIONS

13.1 Materials and method

From the previous chapter 12, it is evident that the proposed coatings demonstrate antifouling properties in the short term. The issue lies not in the formulation of the coatings, but rather in the poor adhesion between the coating and the substrate. Consequently, the antifouling properties diminish over time (lasting for 5 months). To address this concern, two types of experiments were conducted to determine when and under what conditions the coating loses its effeteness.

The resistance of the superhydrophobic samples in seawater was evaluated under two different conditions: static and dynamic. The prepared sample are listed in the following table, along with a brief description of the sample preparation. The static test was conducted as follows: the sample were immersed in filtered seawater from the Naples aquarium for approximately two months. At predefined intervals, static and dynamic contact angles were measured. On the other hand, dynamic resistance tests were conducted as follows: one sample at a time was placed in the setup illustrate in the figure 95. At regular intervals (shorter than those for the static test), static and dynamic contact angle were measured. Each time the sample were taken out the immersion tank, they were thoroughly rinsed with distilled water and then dried for 24 hours at room temperature.

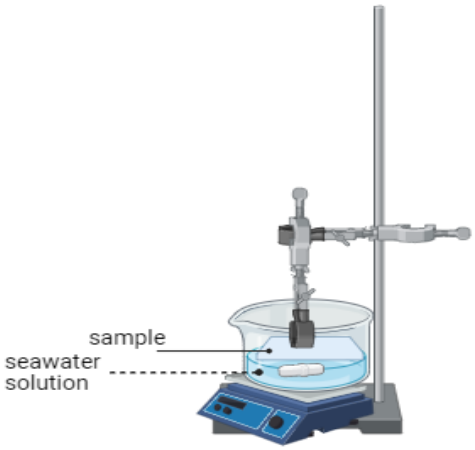

Figure 95 *Set-up for the dynamic seawater endurance testing.*

The coating used for the resistance test are similar to those subjected to fouling experiments reported in table 30. Additionally, a non-fluorinated coating was deposited on an aluminum substrate for comparison purposes. The fluorine-free coating consist of an inorganic ceramic layer based on alumina (as seen in previous chapters 12). The organic layer is composed of hexadecyltrimethoxysilane diluted to 6% in ethanol.

Table 30 *Samples subjected to static and dynamic water resistance test.*

Sample	I layer	II layer	Infusion oil
Al_Al_2O_3_FAS	Al_2O_3	Fluoroalkylsilane	/
Al_Al_2O_3_FAS_K105	Al_2O_3	Fluoroalkylsilane	Krytox 105
Al_Al_2O_3_HTS	Al_2O_3	Hexadecyltrimethoxysilane	/
Al_Al_2O_3_HTS_oil	Al_2O_3	Hexadecyltrimethoxysilane	Silicon oil 100 Cst
Al_SiO_2F	SiO_2F	/	/
Al_SiO_2F_K105	SiO_2F	/	Krytox 105

Description of deposition process on aluminum substrate. The dip-coating parameters are described: extraction rate (u) and dip time. TT is an acronym for Thermal Treatments. EtOH Ethyl alcohol; iPrOH Isopropyl alcohol.

Substrate Aluminum: Al_2O_3/FAS coating.

Washing in soapy water: EtOH → dip coating Al_2O_3 u= 2mm/s 5s immersion → TT 400°C 1h → boiling water 30 min→ TT 400°C 10 min → dip coating FAS u=2mm/s 120s immersion → TT 150°C 30 min.

Substrate Aluminum: Al_2O_3/FAS coating+ Krytox 105.

Washing in soapy water: EtOH → dip coating Al_2O_3 u= 2mm/s 5s immersion → TT 400°C 1h → boiling water 30 min→ TT 400°C 10 min → dip coating FAS u=2mm/s 120s immersion → TT 150°C 30 min → Krytox 105 infusion.

Substrate Aluminum Al_2O_3/HTS.

Washing in soapy water: EtOH → dip coating Al_2O_3 u= 2mm/s 5s immersion → TT 400°C 1h → boiling water 30 min→ TT 400°C 10 min → dip coating HTS u=2mm/s 120s immersion → TT 150°C 30 min.

Substrate Aluminum Al_2O_3/HTS +Silicon oil 100 Cst.

Washing in soapy water: EtOH → dip coating Al_2O_3 u= 2mm/s 5s immersion → TT 400°C 1h → boiling water 30 min→ TT 400°C 10 min → dip coating HTS u=2mm/s 120s immersion → TT 150°C 30 min → Silicon oil 100 Cst infusion.

Substrate Aluminum: SiO_2F coating

Washing in soapy water: EtOH → dip coating SiO_2F u= 2mm/s 120s immersion→ TT 150°C 30 min.

Substrate Aluminum: SiO_2F coating + Krytox 105.

Washing in soapy water: EtOH → dip coating SiO_2F u= 2mm/s 120s immersion→ TT 150°C 30 min→ Krytox 105 infusion.

Static and dynamic contact angles were measured before subjecting the specimens to strength tests in seawater.

13.2 Results

Static endurance test on Al_2O_3 based coating

The coated substrates were placed face up inside a plastic tray and covered with seawater. Immersion time 7, 14, 30 and 60 days were taken into account. Then samples were rinsed with distilled water and air-dried overnight. Once dry, their static and dynamic wettability was measured. Graphs of figure 96 exhibit the WCA and CAH contact angle results.

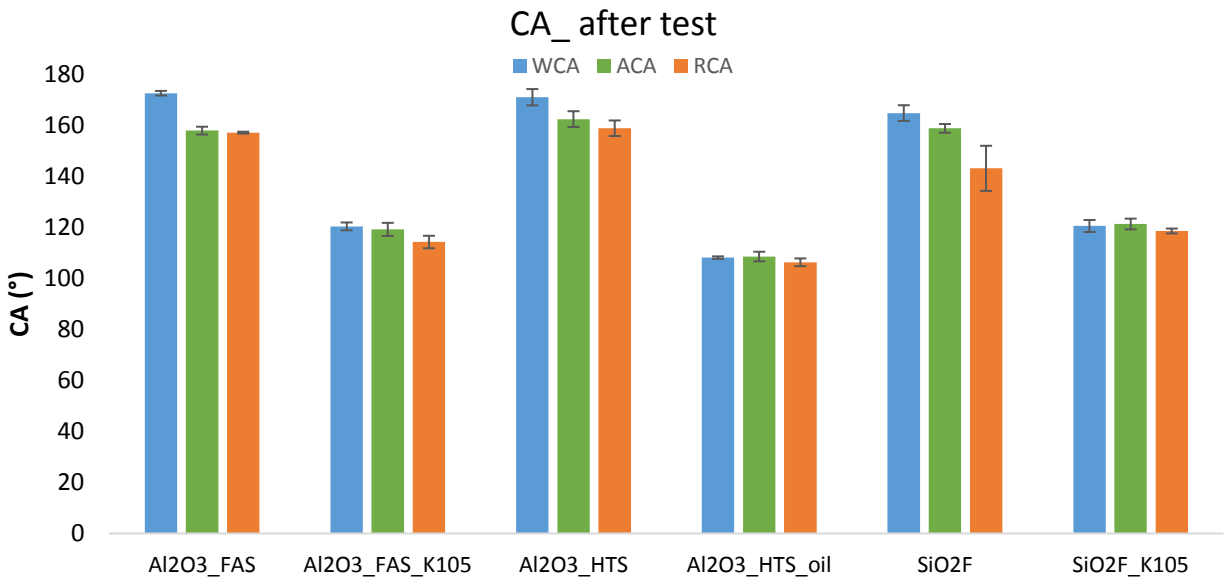

Figure 96 *Static and dynamic contact angle graph for the samples subjected to static and dynamic water resistance tests. Static Contact Angle (WCA) in blue, Advance Contact Angle (ACA) in green and Receding Contact Angle (RCA) in orange and respective deviation standard.*

The superhydrophobic surfaces exhibit WCA greater than 160°C and CAH less than 5°, except for fluorinated silica, which shows hysteresis of about 15°. On the other hand, SLIPS surfaces have WCA around 120° with CAH less than 5°.

First, salt water tests were conducted with the coating SHS (Al_2O_3-FAS) and SLIPS (Al_2O_3-FASK105) and SHS fluorine free (Al_2O_3-HTS) and respective SLIPS (Al_2O_3-HTS-silicon oil), the measurement were monitored up to 60 days.

Table 31 *Static wettability (WCA), and dynamic wettability (CAH) data of Al_2O_3+FAS coatings and corresponding Al_2O_3+FAS+K105 SLIPS in static conditions, the respective standard deviations are shown alongside.*

Sample	Time (d)	WCA (°)	CAH(°)	Sample	WCA(°)	CAH (°)
	0	170 ± 4	3 ± 2		120 ± 1	3 ± 3
	7	138 ± 3	45 ± 3		122 ± 2	8 ± 2
Al_2O_3+FAS	14	56 ± 10	60 ± 10	Al_2O_3+FAS+K105	120 ± 3	17 ± 11
	30	95 ± 27	69 ± 6		110 ± 10	32 ± 7
	60				83 ± 11	71 ± 15

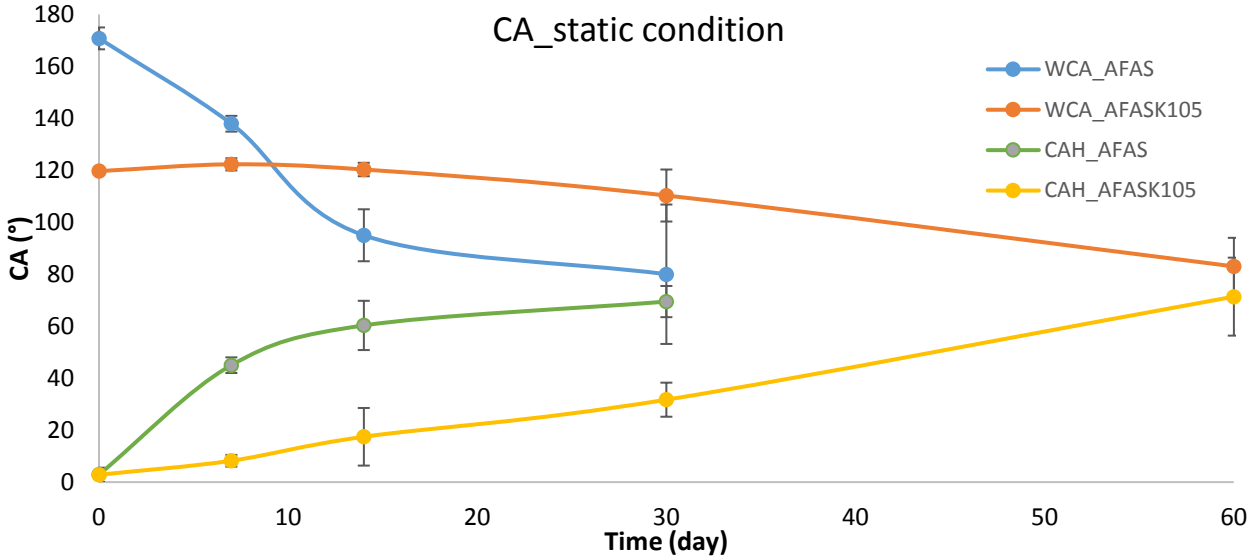

Figure 97 *Graph of trend of static (blue) and dynamic (green) wettability of the Al_2O_3+FAS coating over time; and trend of static (orange) and dynamic (yellow) wettability of the Al_2O_3+FAS+K105 coating. The respective standard deviation of the data are also shown.*

From data shown in the table 31, it can be seen that the Al_2O_3-FAS based coating has a very high WCA angle (170°) and very small CAH (<5°). As days progress, the WCA decrease to 100° and the CAH tends to be similar to the static contact angle. This trend indicates that the organic coating that imparts water repellency in contact with seawater tends to deteriorate, given also the standard deviation that increases over time, it has also been noted that in some areas there are salt incrustation, which did not allow to measure the angles after 60 days to immersion (Fig 97). On the other hand, it is observed that the Al_2O_3+FAS+K105 sample WCA is 120° and CAH of less than 5°. The static wettability in the progression of durability tests has decrease of 40° while the hysteresis tends to increase up to 80° with a very high standard deviation. Probably the increase in hysteresis and the increase in standard deviation are due to the presence of salt encrustations on the surface.

Table 32 *Static wettability (WCA) and dynamic wettability (CAH) data of Al_2O_3+HTS coatings and corresponding Al_2O_3+HTS+oil SLIPS in static conditions, the respective standard deviations are shown alongside.*

Sample	Time (d)	WCA (°)	CAH (°)	Sample	WCA (°)	CAH (°)
	0	169 ± 4	5 ± 5		110 ± 1	4 ± 3
	7	131 ± 10	6 ± 2		105 ± 4	4 ± 2
Al_2O_3+HTS	14	122 ± 4	11 ± 3	Al_2O_3+HTS+oil	105 ± 2	3 ± 1
	30	104 ± 10	58 ± 14		108 ± 1	5 ± 2
	60	98 ± 10	90 ± 7		109 ± 2	11 ± 6

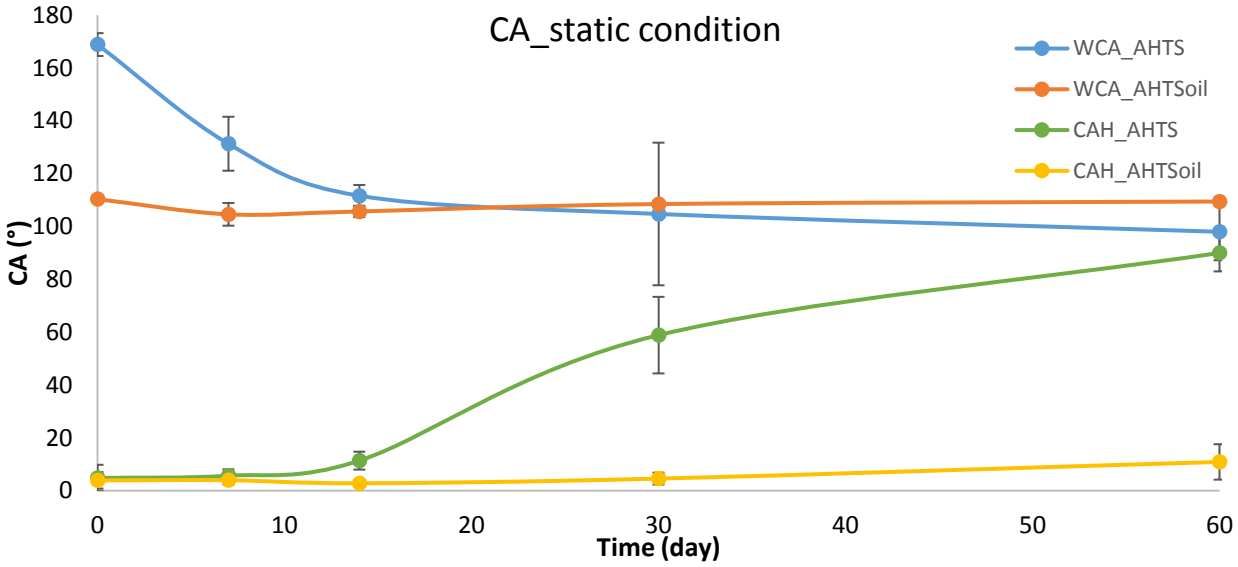

Figure 98 *Graph of trend of static (blue) and dynamic (green) wettability of the Al_2O_3+HTS coating over time; and trend of static (orange) and dynamic (yellow) wettability of the Al_2O_3+HTS+oil coating. The respective standard deviation of the data are also shown.*

From the data present in the figure 98 and in table 32 of the Al_2O_3 -HTS sample, a high WCA (169°) and CAH of 5° can be seen. With the passing, the static angle reaches 100° and the hysteresis increases up a level where there is no longer a hysteresis contact angle phenomenon. This occurs because of the saline environment damages, which gives the coating hydrophobicity.

On the contrary, the Al_2O_3+HTS +silicone oil (100cst) sample has lower WCA than no-SLIPS coating of 100° and CAH of 4°. At the end of the test, however, WCA remains unchanged while CAH increases by 10°. This happens because during the static test probably only part of silicone oil was lost, but no completely as in the previous case where the sample in which the infused oil is Krytox. Therefore, the silicon oil is more performing, remaining within the nanoroughness and more resistant to the aggressive environment.

Dynamic endurance test on Al_2O_3 based coating

The samples proposed in the table are subjected to the dynamic durability tests. The sample is then washed with distilled water and dried overnight. The test times are shorter than the static tests for more accurate monitoring to predict when the superhydrophobic performance actually falls.

Table 33 *Static wettability (WCA) and dynamic wettability (CAH) data of Al_2O_3+FAS coatings and corresponding Al_2O_3+FAS+K105 SLIPS in dynamic conditions, the respective standard deviations are shown alongside.*

Sample	Time (h)	WCA (°)	CAH (°)	Sample	WCA (°)	CAH (°)
Al_2O_3+FAS	0	172 ± 1	1 ± 0.3	Al_2O_3+FAS+K105	120 ± 2	4 ± 2
	1	142 ± 3	57 ± 7		120 ± 1	4 ± 2
	6	100 ± 5	76 ± 10		120 ± 1	6 ± 2
	24	98 ± 3	87 ± 7		120 ± 2	7 ± 4
	48	108 ± 3	116 ± 4		120 ± 4	10 ± 5
	72	106 ± 2	112 ± 8		118 ± 4	13 ± 4
	98				116 ± 4	8 ± 2
	122				120 ± 1	13 ± 5

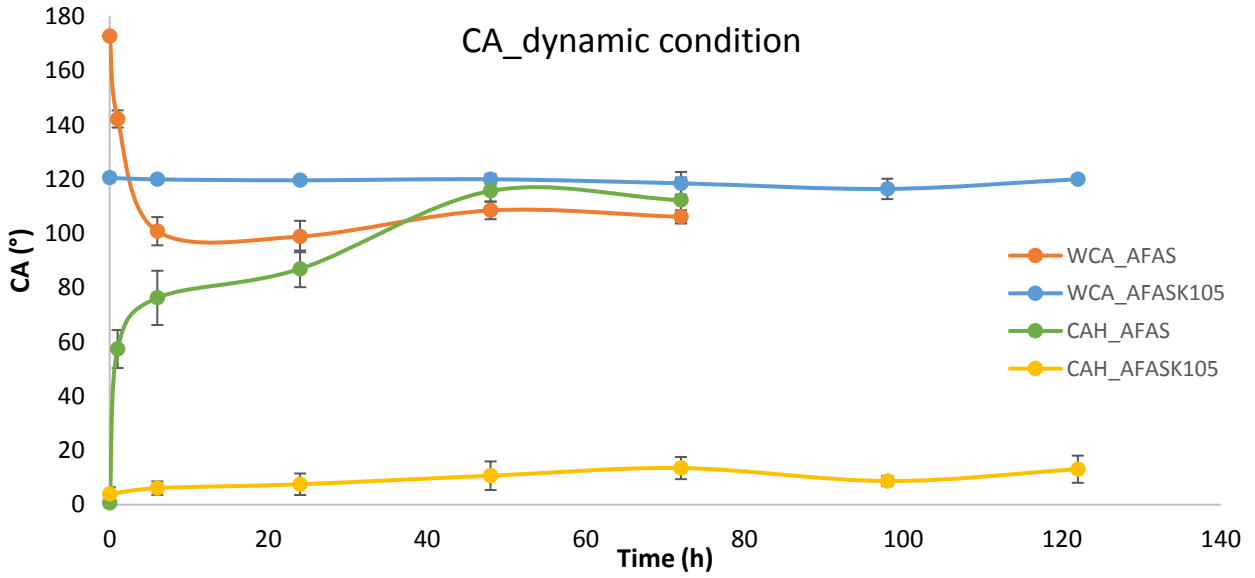

Figure 99 *Graph of trend of static (blue) and dynamic (green) wettability of the Al_2O_3+FAS coating over time; and trend of static (orange) and dynamic (yellow) wettability of the Al_2O_3+FAS+K105 coating. The respective standard deviation of the data are also shown.*

From the data in the table 33 and figure 99 for the Al_2O_3+FAS sample, it can be seen that the superhydrophobicity performance drops dramatically only after 3 days of testing under dynamic conditions. On the other hand, it exhibits zero-time CAH of less than 5° and only after 6 hours, the CAH increases to 60°. The proposed conditions turn out to be very aggressive with organic layer, and in fact, exhibits a rapid decay of hydrophobicity can be seen only after a few hours.

In contrast, the SLIPS Al_2O_3+FAS+K105 sample exhibits a constant trend throughout the duration of the test (5 days), with static angles around 120° and hysteresis that has a slight increase toward the end of the test around 13°. Probably the lubricant has a protective effect against the layer, being more resistant than the sample without Krytox, but as the hour's progress, the excess lubricant deposited is lost and there is a slight increase in wettability.

Table 34 *Static wettability (WCA) and dynamic wettability (CAH) data of Al_2O_3+HTS coatings and corresponding Al_2O_3+HTS+oil SLIPS in dynamic conditions, the respective standard deviations are shown alongside.*

Sample	Time (h)	WCA	CAH	Sample	WCA	CAH
Al_2O_3+HTS	0	171 ± 3	4 ± 3	Al_2O_3+HTS+oil	108 ± 1	2 ± 1
	1	140 ± 8	58 ± 1		109 ± 1	3 ± 1
	6	112 ± 5	95 ± 12		107 ± 1	2 ± 1
	24	104 ± 1	72 ± 15		110 ± 1	6 ± 8
	48	105 ± 10	89 ± 25		110 ± 1	16 ± 10
	72	106 ± 2	78 ± 10		112 ± 4	18 ± 10
	98	101 ± 5			112 ± 1	22 ± 10
	122	88 ± 4			101 ± 2	29 ± 11

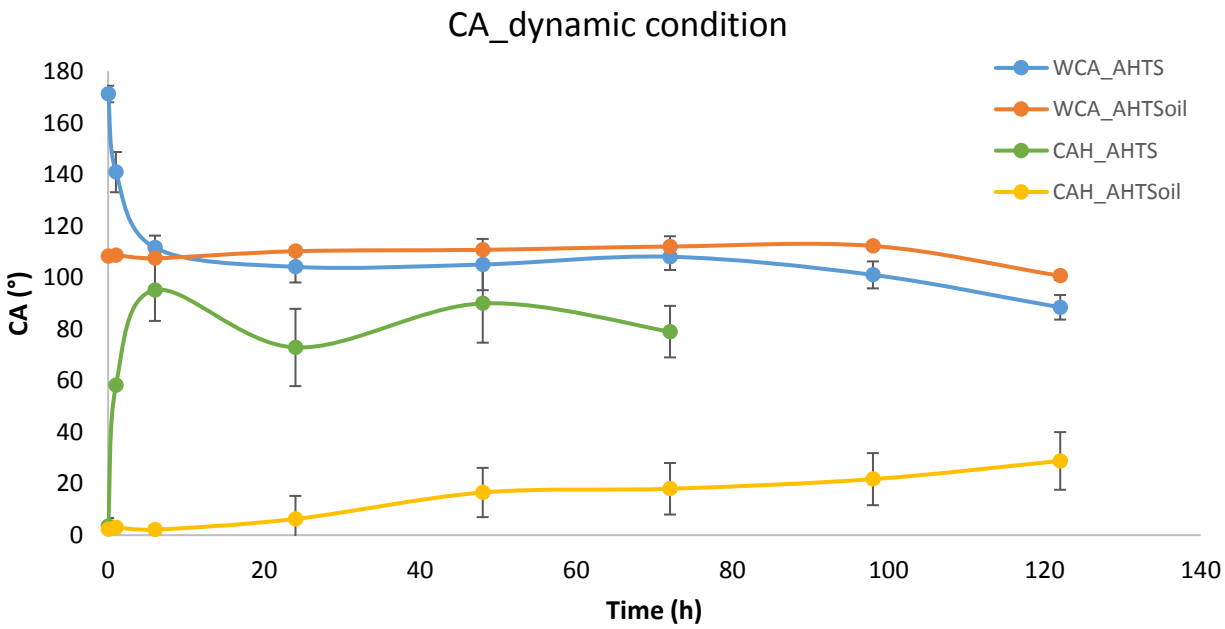

Figure 100 *Graph of trend of static (blue) and dynamic (green) wettability of the Al_2O_3+HTS coating over time; and trend of static (orange) and dynamic (yellow) wettability of the Al_2O_3+HTS+oil coating. The respective standard deviation of the data are also shown.*

From the data represented in graph Fig.100 and in the table 34, the Al_2O_3+HTS sample presents a decline in static wettability performance as time progresses, in particular after only 6 hours there is a drop of 80° in the static angle, up to the complete loss the superhydrophobicity properties of the coating at the end of 72 hours. Dynamic wettability also presents the same characteristics, with a complete loss of dynamic water repellency properties after only 6 hours of testing. Differently, the Al_2O_3+HTS+oil sample presents an almost unchanged static angle trend with a decrease of 10° towards the fifth day. Dynamic water repellency tests, on the other hand, show an increase in the hysteresis angle of up to 30 degrees over time.

Static endurance test on SiO_2F based coating

The static and dynamic durability tests were carried out on samples coated with fluorinated silica and fluorinated silica infused with Krytox 105. The static and dynamic durability test were carried out using the same procedure as the alumina coating.

Table 35 *Static wettability (WCA) and dynamic wettability (CAH) data of SiO_2F coatings and corresponding SiO_2F Krytox SLIPS in static condition, the respective standard deviations are shown alongside.*

Sample	Time (h)	WCA (°)	CAH (°)	Sample	WCA (°)	CAH (°)
	0	164 ± 3	15 ± 6		120 ± 3	5 ± 1
	7	42 ± 10	53 ± 31		99 ± 13	24 ± 17
SiO_2F	14			SiO_2F K105	106 ± 7	43 ± 25
	30				101 ± 8	93 ± 13
	60				102 ± 9	123 ± 81

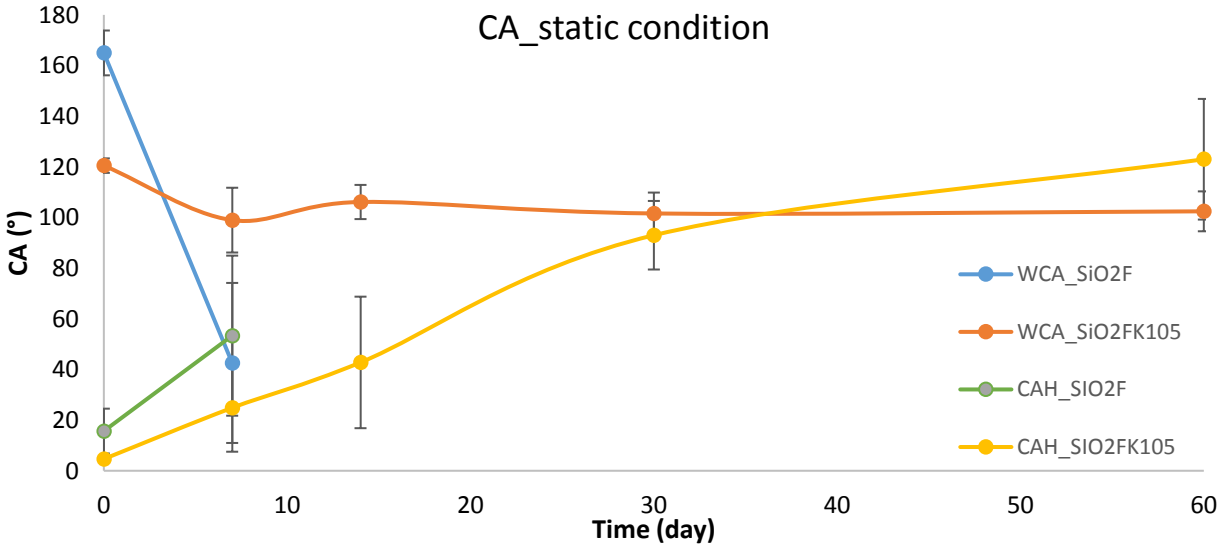

Figure 101 *Graph of trend of static (blue) and dynamic (green) wettability of the SiO_2F coating over time; and trend of static (orange) and dynamic (yellow) wettability of the SiO_2F K105 coating. The respective standard deviation of the data are also shown.*

It is observed from data in the table 35 and shown in Figure 101 that the SHS coating based on fluorinated silica loses its superhydrophobic properties after only 7 days of immersion, in fact static wettability increases from 150° to 40°. Furthermore, salt scale and signs of corrosion are observed on the aluminum sample, making it impossible to continue with the immersion test. The coating type SLIPS, however, has WCA unchanged over time, the CAH increases during the immersion time. After 60 days the SLIPS sample also shows sing of fouling, the two phenomena together indicate a complete loss of lubricant.

Table 36 *Static wettability (WCA) and dynamic wettability (CAH) data of SiO_2F coatings and corresponding SiO_2F Krytox SLIPS in dynamic conditions, the respective standard deviations are shown alongside.*

Sample	Time (h)	WCA (°)	CAH (°)	Sample	WCA (°)	CAH (°)
	0	164 ± 3	15 ± 8		120 ± 2	3 ± 1
SiO_2F	1	77 ± 7	64 ± 36	SiO_2F K105	121 ± 3	5 ± 1
	24				108 ± 16	27 ± 16

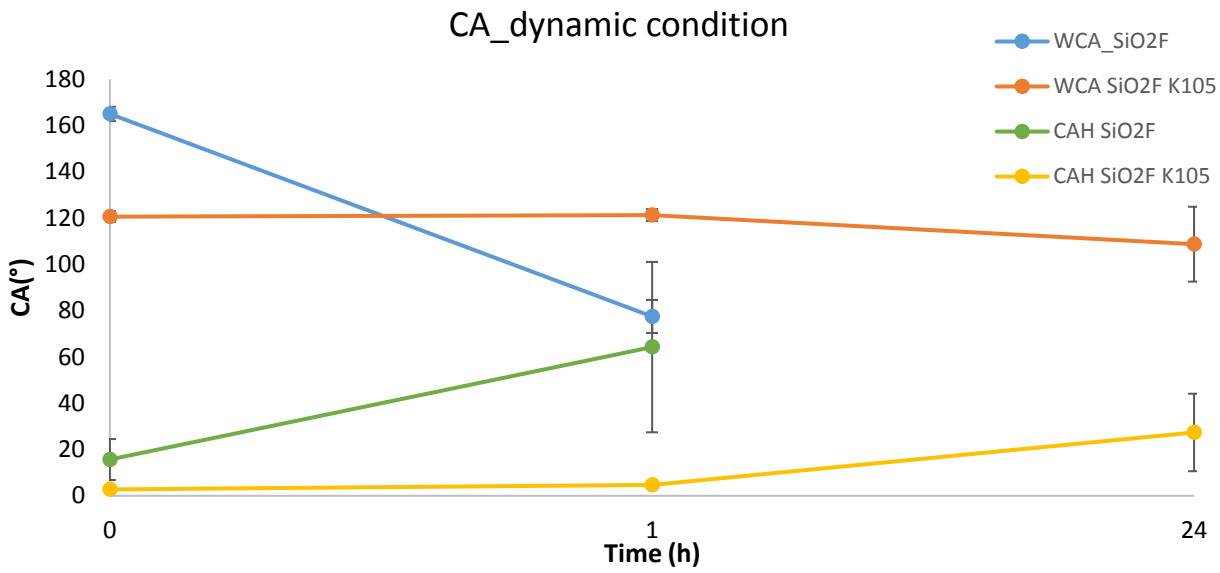

Figure 102 *Graph of trend of static (blue) and dynamic (green) wettability of the SiO_2F coating over time; and trend of static (orange) and dynamic (yellow) wettability of the SiO_2F K105 coating. The respective standard deviation of the data are also shown.*

From data in the table 36 and in Figure 102 the trend of dynamic resistance to seawater shown that the fluorinated silica after only one hour of immersion loses the properties of superhydrophobicity, with a decrease in wettability from 140° to 80°. In addition, the SLIPS type coating loses its properties, especially in terms of dynamic wetting, with an increase in CAH to 30°, indicating also in this case the loss of the infused oil.

Conclusion

The static and dynamic seawater resistance tests have the following results:

- SHS coatings have low resistance under underwater conditions, with a loss of superhydrophobicity after only one month (under static conditions) and a few days under dynamic conditions.
- SHS fluorine free coatings, therefore, lose their superhydrophobic properties but not in such a marked way. After one more moth of immersion the coating is still hydrophobic (WCA>100).
- SLIPS type coatings, both with fluorinated lubricating oil and silicone, show a greater resistance to underwater conditions, superhydrophobicity persist throughout the exposure time in water.

14. FRICTION REDUCTION ON SUPERHYDROPHOBIC COATINGS

14. 1 Friction reduction of flat plates

Due to climate change and rising fuel costs, it was necessary to design vehicles that would reduce fuel consumption and gas emissions. The design of marine vehicles energy efficiency improvement has been a subject of enormous interest in recent years. From the state of the art and previous experimentation, the design of the surface, not only leads to an improvement of the antifouling properties of naval components, but it can also generate benefits in terms of the fluid dynamic of the wall through the design of the surface interface from physical solid to the liquid in contact with the liquid/fluid in which it is immersed.

From the relevant literature and the knowhow developed in CNR-ISSMC in recent years, lowering the surface energy (SE) of substrate appears to be one of the crucial points for controlling the surface wettability of materials. The value of SE is determined by the ratio of cohesion/adhesion forces of the substrate surface, and it is strongly dependent on the surface chemistry. To reduce the interaction between surface and liquid/fluid, it is necessary to maximize the difference between SE and the surface tension of the liquid/fluid, etc. To be reject. The lower the solid's SE, the greater its repellence against liquids of different natures over a wide range of surface tension. Tsujii, Tuteja, Hensel, et al[175–177], have extensively reported successful design of such surfaces, for example. These valuable studies reveal that a surface should have a micro and nano-scale hierarchical morphology and low SE to achieve the omniphobic status.

When practical applications for SH materials are taken into account, the main hindrance is generally represented by their limited durability, since under severe conditions the peculiar structural features might be easily destroyed [178], allowing water drops to penetrate the structure, annihilating the Cassie-Baxter wetting state and nullifying the hydrophobic behaviour. To overcome the issues connected to the structural weakness of traditionally designed Lotus leaf-like surfaces, in the last years, scientists considered new design approaches and, among them, the one leading to slippery liquid-infused porous surfaces (SLIPS)[179]. These innovative surfaces are based on the infusion of a liquid, e.g., a lubricant, which wicks into the undelaying porous structure making it repellent to a wide range of liquids under conditions where the Lotus Leaf approach usually fails, i.e. in high-pressure environments.

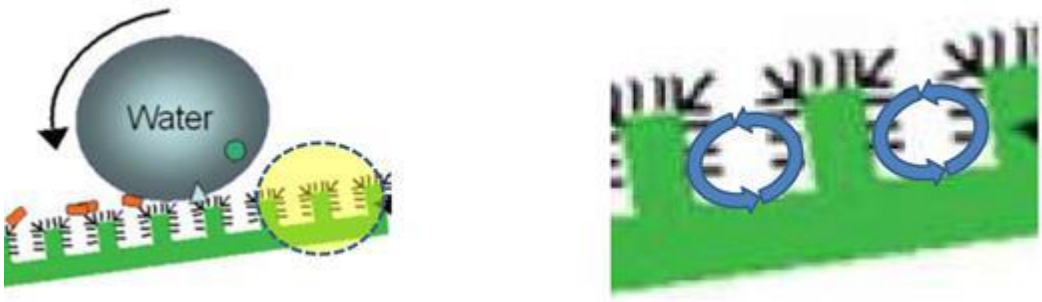

Figure 103 *Principle of operation of a superhydrophobic coating, illustrated in the case of a drop of water rolling along an inclined plane coated with superhydrophobic surfaces.*

The figure 103 illustrates the behavior of the SLIPS surface, the role of the microporosity in which the lubricant recirculates and allows the drop to slip, while the nanoporosity favors the retention of the lubricant increasing both the retention by capillarity and the chemical affinity.

The lubricant contained in the porosities of the ceramic scaffold is not stationary but is moved by the water flux with which it is in contact. The water flowing on the surface at an average speed other than zero does not adhere (zero speed) on the solid walls but flows concerning the reference system on the portions occupied by the lubricant. This results in a lower overall surface resistance on the water flow.

The main goal of coating design were:

- Maximizing the ratio between the surface area covered by the lubricant and the total surface.
- Ensure the maximum mobility of lubricant within the individual porosities.

Intuitively the lower the porosity's size the greater the influence of the walls, which tend to dampen the motion of lubricant inside the cell. However, the magnitude of the porosity cannot exceed some limits. In addition to a certain scale, the force exerted by the external turbulent flow, breaking the lubricant film, overcomes the surface tension forces and the chemical bond between the substrate and the lubricant, which allows the retention of the lubricant, and the water penetrates inside the porosities.

The ideal morphological surface configuration to ensure both mobility to the lubricant fluid and retention of energy it is an anisotropic geometry, with elongated porosity at the direction of flow. The intuition has been supported by recent theoretical and numerical work.

However, isotropic configurations, obtained from pores of uniform size, are randomly distributed on the surfaces. Although less performing it is easier to be implemented industrial level. For laboratory-scale testing it was decided to work on a substrate that has a geometry with Longitudinal microscopic grooves. The grooves have a cross-section in triangular shape, with depth H and width W, and were obtained by milling the test samples with a tool designed ad-hoc. The transverse dimensional of the grooves are derived from specific mathematical models.

Mathematical models, albeit with simplifications, can provide the mean velocity value of the outermost layer of the lubricant in function of the geometric parameters of the substrate and the physical characteristics of the two fluids in contact. Therefore, the structured coating can be perceived by the flow of water and thus have an appreciable effect on the value of the feed resistance. The lubricant speed must be comparable with the water flow velocity near the surface itself. This condition is normally translated in terms of characteristic lengths instead of speed. The length of the briefs depends on the geometric parameters and characteristics of two fluids and must be comparable with the spatial scale by the turbulent flow near the wall, quantified as “wall scale” I*. The wall scale is defined that I*= va/uτ when va is the kinematic viscosity of water, and uτ is friction speed; that depends on the friction stress to wall τ and water density ρa; uτ= (τ/ ρa)1/2.

The scale shall be of the order of 10-50 microns under the test conditions laid down. Analytical predictions of the slip length (derived from Schoenecker) allow estimating a slip length based on the ratio (N) between the dynamic viscosity of the water and the viscosity of the lubricant, of the fraction (A) of surface occupied but the interface between water and lubricant and the groove size (W). The sliding length increased by W, N and A assuming A equal 0.9 (given by triangular geometry of the groove) and for N values shown in the table, the value of W for which the slip length is 20-30 micron. The selected W values are W=300 μm and W= 900 μm.

Then, static and dynamic wetting properties of SHS and SLIPS materials were evaluated via goniometric measurements, while Scanning Electron Microscopy (SEM) obtained morphology information. Micro-structured surfaces, chemically treated according to the protocols mentioned above, have been tested in a water channel to verify the possibility of reducing the viscous drag of turbulent wall-bounded flows.

For these purposes, both SHs and SLIPS-designed coated surfaces have been investigated. A wing model, equipped with a microstructured SHS coating, has been tested in the same water channel, to assess the influence of the coating on the hydrodynamic performances of the model (in particular on the behavior of the form drag component). According to our previous experience, the deposition processes have been selected among those having potentially the highest transfer degree at the industrial scale, based on their spreading, simplicity of processing parameters to be adopted, limited cost of equipment, and requirement of a lower amount of coating formulations to reduce the environmental impact as well.

Focus is on selecting lubricants to have chemical affinity with the selected superhydrophobic coating. The coating characteristics allowed both air and lubricant films to be used. The air guarantees better performance in terms of reduction of friction, thanks to its reduced viscosity. However, air films are often unstable and subject to rupture at time of external pressure fluctuations occurring within the turbulent boundary layer, causing an increase in the number of Reynolds number. Using an incompressible fluid that has a higher viscosity than air, this phenomenon is avoided. The lubricating oils used are shown in the table 37, showing the main characteristics, dynamic viscosity, and density.

Table 37 *Physics characteristic of lubricant used in drag reduction test.*

Lubricant	**η [mPA/s]**	**ρ [Kg/m^3]**	**N =η_a/η**
Krytox®	19.5	1820	0.05
n-Hexadecane	2.66	773	0.33
Air	0.02	1.2	48

Lubricant retention

One a critical aspect of superhydrophobic coatings is the decay of performance over time. The deterioration of the film is due to the effect of the turbulent external flow. To limit the phenomenon, the geometry of the surface is carefully designed. By reducing the size, the effects is amplified due to the stabilizing forces (surfaces tension and chemical affinity lubricant and substrate) that counteract the action due to external disturbances (viscous stresses, pressure and gravity). By reducing the size of W of the cells, the value of the slip length of the coating and the reduction of friction resistance is limited.

Visualizations were made to check the ability of the coating to retain the lubricant. In the case of oils, a small amount of fluorescent substance has been diluted inside the lubricant. The intensity of the illuminated signal with LED light in the UV field. The intensity of the fluorescent signal, proportional to the amount of lubricant retained in the coating, is monitored over time. The presence of the air film instead is simply monitored with a fast camera and a simple diffused light.

14.1.1 Materials and methods

The hybrid coating are made of an inorganic porous layer based on ceramic nanoparticles (Al_2O_3), obtained via sol-gel. The size plates (260 x 450 x 5) mm after the boil treatment and second heat treatment were further functionalized for the realization of SLIPS; two types of plates were obtained:

- Functionalization with FAS and infused with Krytox 100 with low viscosity. The choice of the low viscosity of fluorinated oil is motivated by the fact that this property affects the ability to reduce the friction by the SLIPS; lower viscosity oils oppose a lower slip resistance.
- Functionalization with HTS 6% Vol and infusion with n-hexadecane. The fluorine free choice has environmental impact effect in the case of coating detachment, also the n-hexadecane has a viscosity 7 times lower than Krytox, therefore a better result is expected than the fluorinated oil. Hexadecane is an alkane with a long alkyl chain so it should show less stability problems (evaporation of the compound) when exposed to air.

The measure of static and dynamic contact angle as reported in table 38.

Table 38 *Static (WCA) and dynamic (CAH) contact angle measurement of plates coated and uncoated.*

	WCA (°)	**CAH (°)**	**Ra [μ m]**
Uncoated	92 ± 5	42 ± 6	1
Al_2O_3-FAS K100	121 ± 1	4.1 ± 0.7	1.5-4
Al_2O_3-HTS-N-Hex	140 ± 5	2 ± 0.4	1.5-4

In this case, it is also important to report the roughness of the coating applied. Coatings roughness was measured by optimal profilometry.

Implementation of an experimental set-up to measure the friction resistance of superhydrophobic flat surfaces, lapped by a uniform flow of water.

The set-up to measure of the friction resistance of flat surfaces with coatings produced with SLIPS approach has been designed, manufactured, and tested.

The device allows to measure the resistance exerted by the flow lapping a sample plate housed inside one of the walls of the test section of the CEIMM cavitation tunnel in INM-CNR (Institute of Marine Engineering) (Rome, Italy) (Fig. 104, 105).

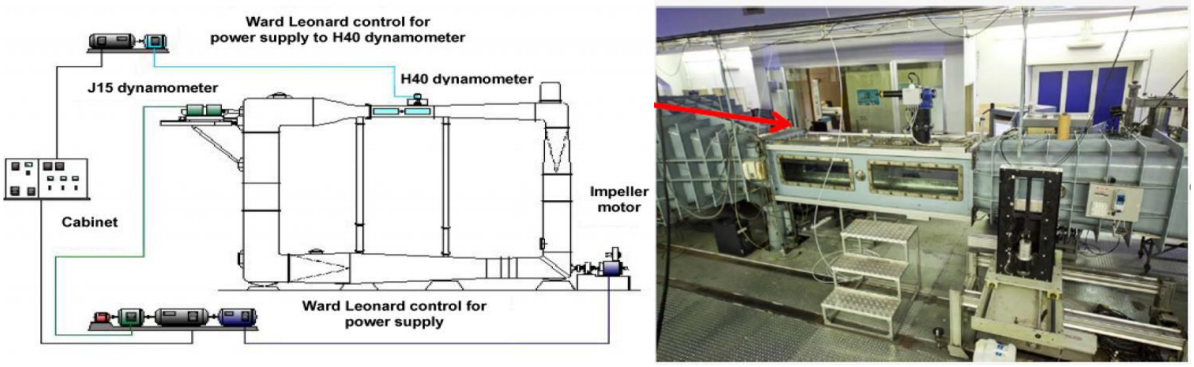

Figure 104 *Diagram of the CEIMM cavitation tunnel. The test section, shown in detail in the photo on the right. The test section is 2.6m long, 0.6 m wide and 0.6 m high. The arrow indicates the upper wall in which the test plate used for strength tests is housed.*

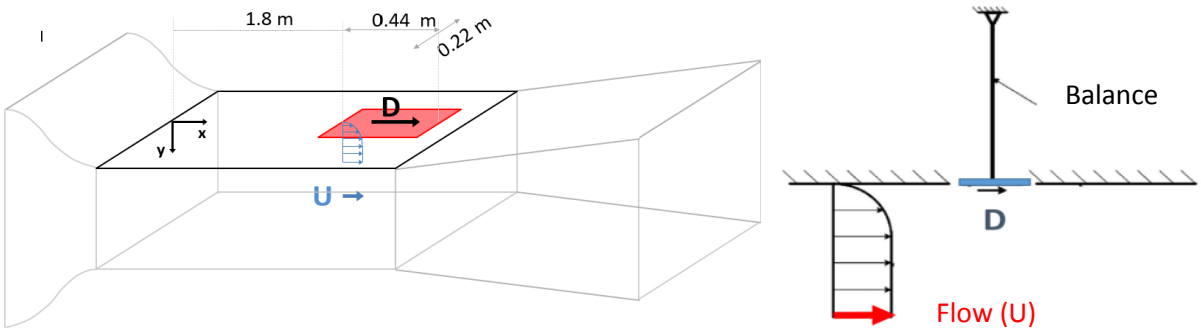

Figure 105 *Simplified layout of the tunnel test section. Illustration of the principle of measuring the strength of the plate-simple.*

The strength of the individual plates is measured according to the diagram shown in the figure 105. The test plate is inserted into a rectangular opening in the upper wall of the test section of the tunnel. The positioning of the slab must be done with extreme precision in order to avoid geometrical discontinuities between the slab and the surrounding wall. Once the reference speed U is set (measured with the Pilot of Laser Doppler Velocimetry), a canonical turbulent boundary layer is created.

The water flow tends to drag the sample plate with a force D (friction resistance). The displacement of the plate in the horizontal direction is limited by the deflection of the elastic element (load cell) to which the sample plate is connected. By means of strain gauges inserted in Wheatstone bridge, the deflection of the elastic element is transduced into an electrical signal that is digitized and acquired. After preliminary calibration, the proportionality constant between acquired voltage and applied force is obtained, it is possible to find the value of the resistance D corresponding to the test speed U.

The system just illustrated in Fig 106 for the measurement of the resistance through floating plate is extremely sensitive to some disturbing factors. In particular, any misalignment between the floating plate and the wall in which it is housed may create a pressure distribution along the edge of the measuring element. The resulting pressure forces clearly alter the value of the measuring plate (steps), and the gap around the plate, are minimized. The realized system represented in figure 106 introduces the main components so described: the floating plate (1) of measure, as such or coated, lapped by the flow of water on the inferior face. The plate is attached to the load cell, which for initial tests has a depth of 10N± 0.003%, a maximum deflection of 500µm and is insensitive to temperature changes. The cell allows to measure with sufficient accuracy the friction forces on the plate in the speed range identified (1-4 m/s). The balance is connected to a support C (3). The support (2) is fixed by two feet adjustable to the frame (4). The system allows to accurately varying position of the frame, in order to align the plate to the measuring system inside the rectangular hole made in the frame itself. The frame is screwed onto the upper wall of the tunnel.

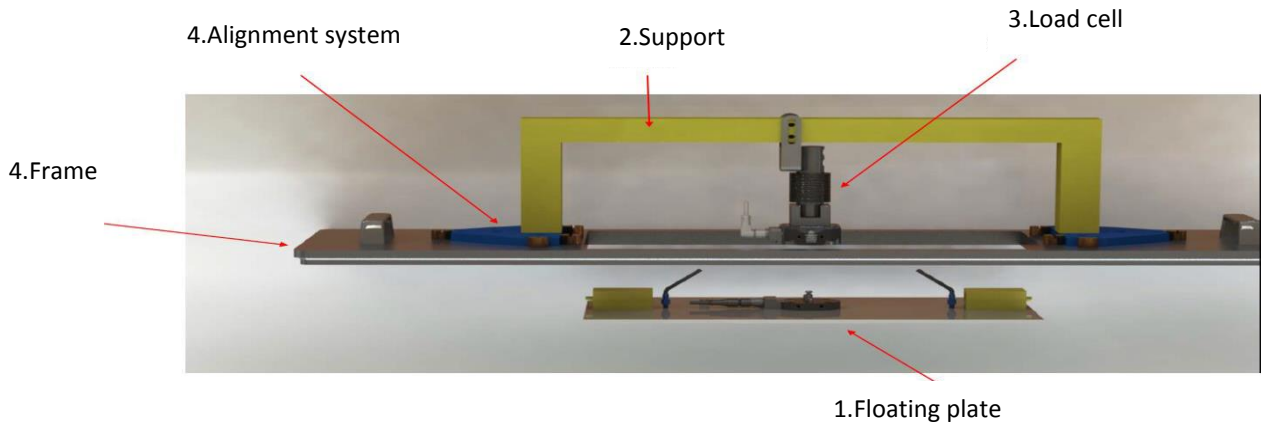

Figure 106 *Overall view of the resistance measurement system with highlighted different components.*

Note that since the gap between the measuring plate and the frame would allow the tunnel water to escape, it is necessary to enclose the entire system inside a watertight container. The container must also be equipped with appropriate air vent valves to allow the equalization of the internal and external pressures. With the tunnel in operation (Fig 107), the water inside the container stabilizes at a certain level and covers all the mechanical and electronic elements described above. The figure 107 shows the system actually constructed (under operating conditions). The red arrow indicated the level reached by the water inside the transparent box.

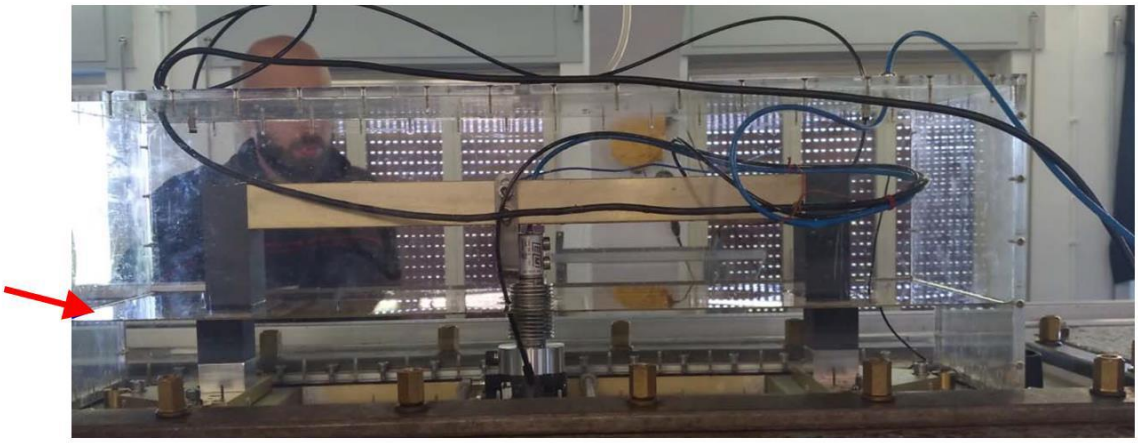

Figure 107 *The resistance measurement system in operation at the CEIMM.*

14.1.2 Results

1_ Geometry W=900 µm

The solution with larger grooves (width W=900) was examined to maximize the slip length of the superhydrophobic coating. As the size of the cells increases, the speed of the internal lubricant also increases. The water that touches the coating can then slip with a higher speed, giving a lower resistance to friction, as the influence of the friction of solid walls on the fluid tends to decrease. The figure 108 shown the trend of the coefficient of friction C_f of the test piece infused with hexadecane as the test speed varies Ue. The coefficients of friction of a smooth plane are indicated by continuous black line. In this case, it is observed that the superhydrophobic coating fails to retain the lubricant, probably due to the forces of insufficient surface tension. Once the lubricant is removed, the wet surface of the specimen increases, and the plate behaves in all respects like a completely wrinkled plate. In this case, the resistance of the specimen is dominated by the shape component, independent of the Reynolds number, and is higher than the smooth reference of specimen.

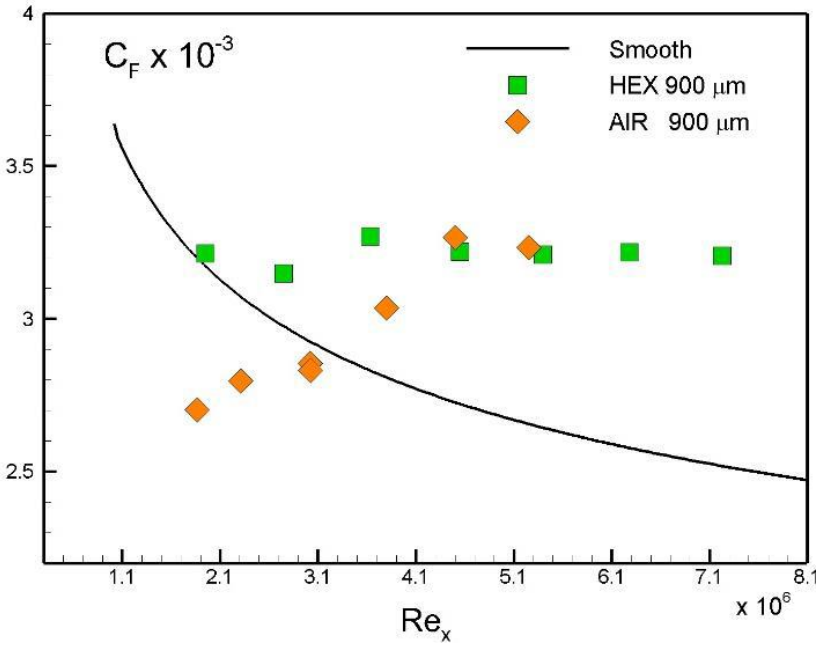

Figure 108 *Variation of the friction coefficient (C_f) as function of the Reynolds number (Re_x), of the superhydrophobic coating with grooves of width W=900 μm, combining air and oil (hexadecane). The black line represent the friction of smooth flat plate.*

The use of air as a lubricant decreases friction resistance at low speeds (Fig 108). In particular, a 25% reduction is achieved when the speed is around 1m/s. However increasing the speed to 2m/s the effect is reduced, as the water flow breaks the air film inside the grooves.

2_ Geometry W=300 μm

The coating applied on a plate with grooves of W=300 μm, has promising performance over a wider speed range. The friction resistance behaviour is also partly due to the type of lubricant used (Fig 109). The tracer indicates that this type of geometry is able to retain some oils, in particular the alkanes, in sufficient quantity for a prolonged time (40min). The results indicate that hexadecane, with it is viscosity ratio μ_w/ μ_{HEX} = 1 / 2.6, achieve resistance reductions of up to 10-15% at low speeds. By increasing the speed, the lubricating film tends to thin out, and the oil tends to stabilize only in the final part of the plate. On the contrary, the use of viscous oil such as Krytox 100, with a viscosity 20 times greater than water, does not lead to any reduction in friction resistance. Due to the viscosity and the high density, it is quickly dragged away. The microstructure emptied by the lubricant, tends to behave like a Riblet-like structure, the resistance of which compared to the smooth plate, changes according to the W/l* ratio. In fact, there is a decrease in resistance for the corrugated plate at the lowest speed and a slight increase when the speed increases with a W/l* ~ 30.

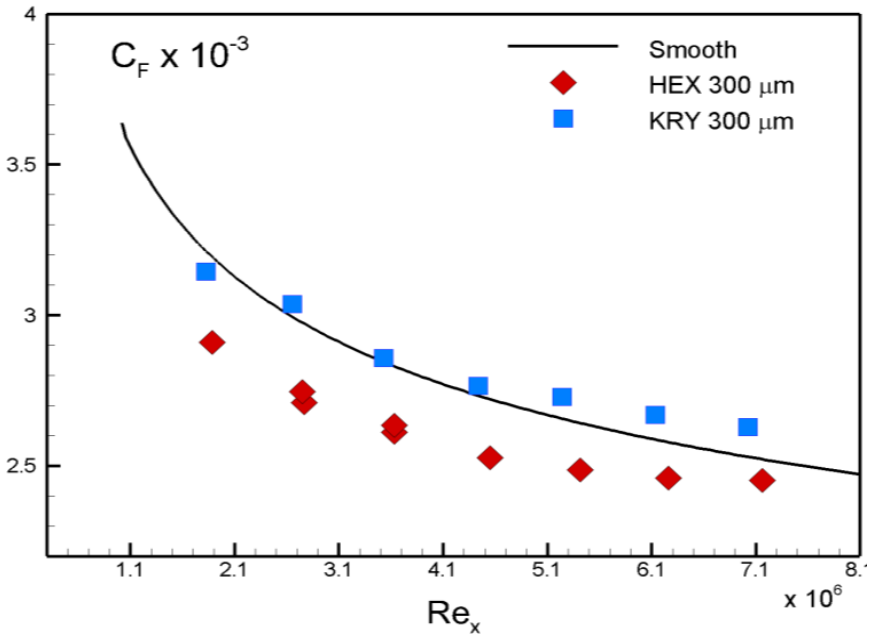

Figure 109 *Friction coefficient (C_f) of coating with grooves of width W=300 µm used in combination with two different lubricating oils (hexadecane and Krytox 100), depending on the Reynolds number (R_e).*

The decay of the friction reduction properties is mainly attributable to the loss of the lubricant during the test. A fluorescent molecule has been inserted as a tracer to monitor the presence of lubricant. The figure 110 shows the relative state of lubricant (n-Hexadecane) infused into the grooves 300 µm, before and after 20 minutes of operation at a speed of 2.5m/s.

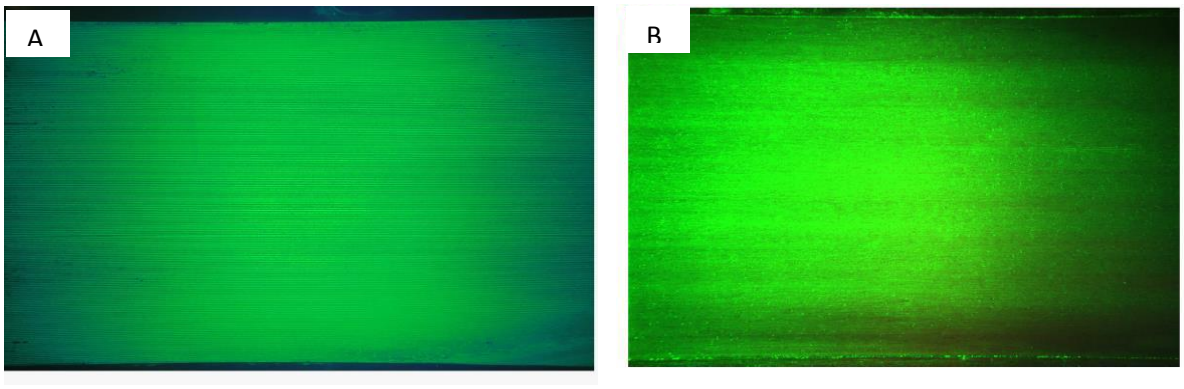

Figure 110 *Fluorescence of lubricating oil (Hexadecane). A) Depicts the initial situation (with the water flow stopped). B) The situation after 20 minutes of testing (the water speed is 2.5m/s and the flow is left to right.*

It is observed that the coating is able to retain the lubricant on a large part of the treated surface, with the exception of the initial parte (where the tangential stress exerted by water on the oil is higher). In conclusion, to obtain a flat surface friction resistance on the wall, it is necessary to combine several morphological and chemical factors, increasing the retention of the lubricant as much as possible.

14.2 Development of Ad-Hoc Porous Ceramic Based Scaffold for creating a SLIPS in controlled environment

The development of ad-hoc porous ceramic-based scaffolds for creating SLIPS in a controlled environment has been achieved through the design of nanostructured porous scaffolds using sol-gel and hydrothermal methods. These processes yield ceramic scaffolds with a high surface area, tuneable crystal and pore size distribution, and a surface texture optimized to host and trap low surface tension lubricants. The nanostructured scaffolds are obtained through direct growth on substrates, or deposition of thin xerogel films via dip coating.

The hydrothermal method use a slow kinetics at any given temperature, because of the fact that less reaction time usually means less energy consumptions. For a more eco-friendly design, it is still an unremitting pursuit to develop time-saving boehmite synthesis routes, which will greatly facilitate their future industrial applications[180]. The hydrothermal synthesis provides the use of aqueous solution at elevated temperature (>100°C) and pressure (> 0.1 MPa). Properties and morphology depend on thermodynamic[181,182] and chemical condition[183,184]. Lower temperatures generally yield smaller nanoparticles size. For example, in alkaline conditions, thicker plate-like boehmite could be formed a with longer reaction time[185]. Generally, system pH controls the boehmite morphology. In acid conditions, boehmite tend to form 1D nanorods or nanofibers, whereas, in basic conditions, 2D nanoplates or 3D near-nanocubes are observed[186,187].

It is necessary to use a neutralization aging of aluminum salt solution at moderate temperatures and hydrothermal transformation of hydroxide into oxide-hydroxide are well documented. The neutralizing agents usually added are sodium hydroxide, sodium carbonate, sodium bicarbonate[188] and ammonia components[189]. In several important studies the use of urea as precipitating or nucleation agent for the synthesis[189] have also been reported.

Urea is widely used as a Bronsted base for homogenous precipitation of metal ions and synthesis of oxides or hydroxide[190]. In this way increasing the pH leads to increasing the equilibrium concentration of $Al(OH)_4$ which makes the kinetics of crystallization faster[191]. When urea hydrolyzed at temperature above 90°C, it can produce carbon dioxide and ammonia, which can increase pH solution and lead to the formation of metal ions or metal/oxide hydroxide particles. Under weakly basic hydrothermal conditions, the electrostatic attraction between the OH groups on the surface on boehmite crystal and metal ions in the solution can promote the growth of the crystal into nanoflakes[191].

The homogenous distribution of OH ions in the solutions is important because the local concentration of ions or molecules can have significant effects on the kinetics and mechanism of chemical reactions, including crystallization[192].

In 1937 Willard and Tung used the reaction of urea with water to precipitate Al^{3+} ions form homogenous solutions. At temperature above about 70°C urea reacts with water in the overall reaction[192]:

$$CO(NH_2)_2 + 3H_2O \rightarrow 2NH_4^+ + 2OH^- + CO_2$$

In the boehmite lattice, oxygen, ions are arranged in a disorder octahedral configuration around aluminum atoms, which leads to the formation of parallel layers linked by hydrogen bonds. Therefore thanks to hydrogen bonds formed in the reaction, oriented one-dimensional nanocrystals are expected[193].

The hydroxide in solution helps to hydrolyze the aluminum thanks to the cationic species present and an increase is pH is obtained[194]. The composition of the ligand sphere of the Al^{3+} ions in aqueous solution is strongly included by the pH of the solution[194].

There are new methods for synthesizing γ-AlOOH nanostructures directly from pure aluminum, i.e. without the introduction of any other anions[190,195] The factors influencing crystal growth were found to be pH, reaction time, temperature, as well as the role of urea as a neutralizing agent.

The porous scaffold has been chemically modified to host the infused commercially available Vaseline lubricant oil. The infusion of such a degassed lubricant on the porous ceramic scaffold is carried out under low vacuum condition.

14.2.1 Materials and method

All reagents were of analytical grade and were used as received without further purification. Rheometer aluminium alloy disposable plates with a diameter of 50 mm (D-PP50/AL/S07D by Anton Paar Fig 108 C) were used as substrates. All the samples were degreased in consecutive ultrasonic baths for 5 minutes prior with deionized water and then with ethanol. We fabricated the coating of the samples with an alumina xerogel obtained via the sol-gel method, following the previously described procedure (refer to paragraph 1.2.1), while the direct growth of nanostructured scaffolds on the samples was realized through a typical hydrothermal route. The samples to be treated hydrothermally were immersed in a 1 M NaOH (Sigma Aldrich) solution for 20 minutes to eliminate the oxide layer, washed four times with distilled water.

In a typical hydrothermal procedure, placed into a Teflon-lined stainless autoclave (1L capacity) with 3M Urea [$CO(NH_2)_2$] (Sigma Aldrich) dissolved in 350 mL of deionized water and the sodium hydroxide concentration necessary to achieve the desired pH value. To rationalize crystal growth, hydrothermal treatments were conducted at various temperatures and reaction times, while to understand the role of the additive, hydrothermal experiments were conducted even without adding urea. To obtain SLIPS surfaces, the infusion of degassed Vaseline oil onto the porous ceramic scaffold was carried out under low vacuum conditions. After infusion, all the candidate samples for the hydrodynamic resistance test were characterized in terms of repellence against water. The static water contact angle (WCA) was measured with sessile water drops (volume 3µL) using the Drop Shape Analyzer DSA30. The dynamic wetting, expressed by the contact angle hysteresis (CAH), was evaluated with the needle-in technique. CAH was calculated as the difference between the advancing and receding contact angles of a sessile drop with a changing volume from 3µL to 6µL. Contact angle values were calculated as the average of three measurements at different points on the surface. The different morphologies of surfaces were investigated with a field emission scanning electron microscope (FESEM Gemini Columns SIGMA, Carl Zeiss Microscopy GmbH, Oberkochen, Germany).

Hydrodynamic resistance

The surfaces obtained have been analysed in experiments at laboratory scale.

Figure 111 *A) Scheme of the hydrodynamic resistance measurement set-up B) Aluminum alloy Rheometer Disk D-PP50/AL/S07D by Anton Paar used as substrates C) Anton Paar Rheometer MCR 301.*

All the experiments were performed using a rheometer Anton Paar MCR 301 equipped with a rotor of 50 mm in diameter and 1.5 mm in thickness. In this experimental setup (Fig. 111), the rotor is immersed in a rectangular vessel filled with distilled water A-B). All measurements were performed at a rotor's immersion depth of 40 mm. The contribution of the rotating shaft to the total torque is negligible with respect to that of the disk and inferior to the error bar in the experimental data.

The choice of a rectangular container instead of a cylindrical one is related to the desire to minimize the negative effect due to the formation of a vortex around the rotor when the rotational speed exceeds 400 rpm. This effect does not occur in the rectangular container because the geometry breaks the symmetry. A similar effect can be obtained by adding baffles to the cylindrical container.

14.2.2 Results

Using the previously described sol-gel procedure (previous paragraph 4.1), a xerogel coating of alumina has been transferred on the aluminum alloy plates. The alumina nanoparticles, after the structuring process in boiling water, leads to the formation of the typical hierarchically organized "flower-like" boehmite structure (Fig 112). The surface structure presents voids with dimensions of about 50 nm, able to host and trap the lubricants. As clearly visible in figure A-B, the dilatometric disagreement between the substrate and coating leads to the formation of cracks in the ceramic coating, despite the perfectly homogeneous nanoroughness induced across the entire surface.

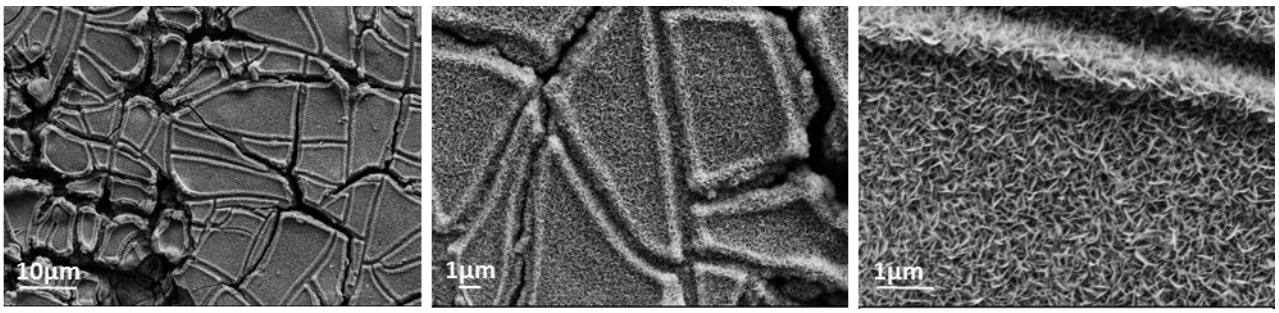

Figure 112 *From left to right, increased magnification of the sol-gel coating on the aluminum alloy plates.*

To achieve a scaffold suitable to realize SLIPS surfaces with optimized porosity and morphology capable of permanently hosting the infused lubricant oil, we opted for the hydrothermal synthesis of boehmite. In such a synthesis, it is possible to influence the direction of crystal growth, although several parameters play a crucial role in controlling the outcome of a hydrothermal reaction and the properties of the synthesized materials. Understanding the reaction conditions in solution that govern the growth of boehmite crystals, their sizes, and morphology is the main path to develop synthesis protocols for controlling the surface area, shape, and reactivity of crystal facets. In this study, we have explored the variations in reaction parameters, including temperature, reaction time, pH level, and urea as additive, in table 39 are hydrothermal synthesis performed. The temperature at which the reaction occurs is a critical factor that can influence the reaction rate, phase formation, crystal size, and other material properties. Similarly, the reaction time is vital for achieving the desired level of crystallinity and phase formation.

To investigate the influence of reaction time and temperature, we conducted hydrothermal synthesis with a fixed NaOH concentration of 0.01M and keeping all other variables constant. In the subsequent sections, we present the morphology of the sample surfaces obtained.

Table 39 *List the sequence of hydrothermal synthesis conducted.*

	T(°C) 200			T (°C) 160			T (°C) 120		
Reaction Time (h)	**24**	**12**	**6**	**24**	**12**	**6**	**24**	**12**	**6**
pH 13	X	X		X	X			X	
pH 12	X	X	X			X	X		
pH 11	X	X	X	X		X	X		
pH 11 no Urea	X		X			X	X		

In the Fig.113, the surface of the samples subjected to hydrothermal treatment at 200°C, with a pH fixed at 13, and reaction times of 24 hours, 12 hours, and, are presented in Fig. 113 A-B, respectively. The SEM micrographs Fig 113 obtained do not indicate any significant effect on the structuring and crystal dimensions of boehmite growth when reducing the reaction time from 24 hours to 12 hours.

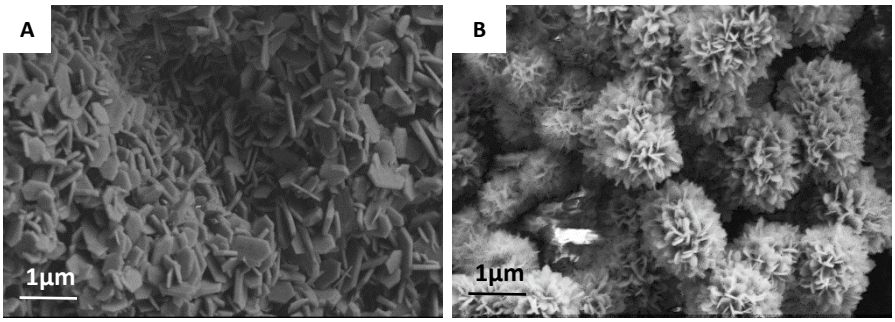

Figure 113 *From left to right, SEM micrograph of sample surfaces of hydrothermal treatment at 200°C, pH 13, [Urea] 3M, and reaction times of 24 hours (A), 12 hours (B).*

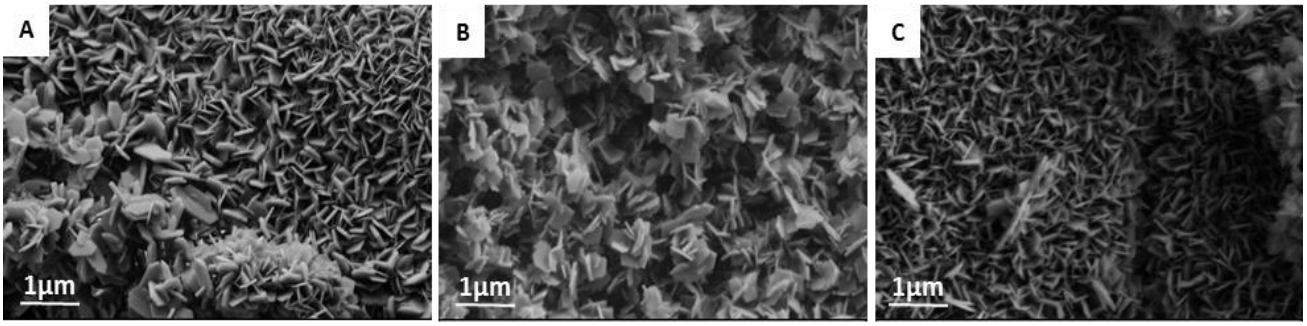

Figure 114 *from left to right, SEM micrograph of sample surfaces of hydrothermal treatment at 200°C, pH 12, [Urea] 3M, and reaction times of 24 hours (A), 12 hours (B), and 6 hours (C).*

In figure 114, the SEM micrographs of the sample surface after a hydrothermal treatment at 200°C, pH 12, [Urea] 3M, with reaction times of different time at reaction temperatures. In figure 114 A, B, and C. The plate-like hexagonal crystals are the same but with a crystal size a lot smaller. The effect of crystal size reduction with decreasing reaction time is also confirmed. In SEM micrographs of samples treated hydrothermally for a longer reaction time (24 hours) but at temperatures of 200°C 160°C and 120°C, respectively, are presented in Fig 115 A-B-C. Crystal size reduction is favorable to the formation of micropores in the view of advanced material production but it is undesirable in the view of reaction kinetics. Micropores formation prevents the diffusion of water into the volume of particles to the surface of aluminum and this reduces the rate of reaction and conversion degree of aluminum.

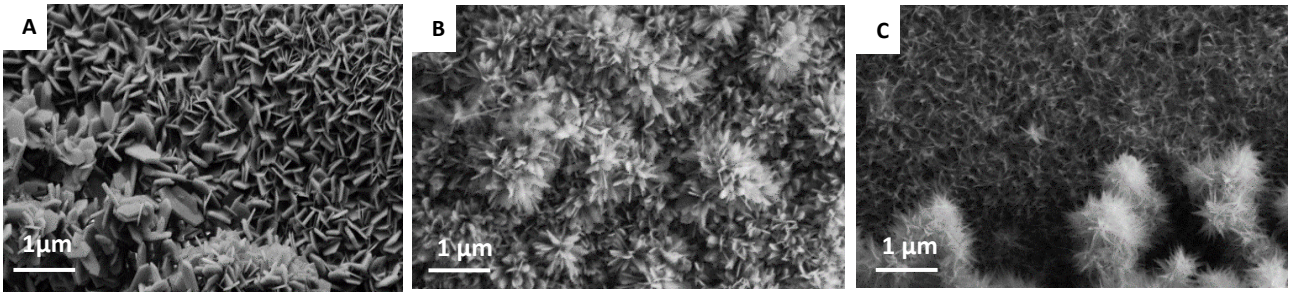

Figure 115 *From left to right, SEM micrograph of sample surfaces of hydrothermal treatment at pH12, 3M [Urea] reaction time 24h, with temperature is A) 200°C, B)160°C and, C) 120°C.*

Synthesis pH has a prominent influence on the resulting nanocrystal morphology, allowing some insight into the pH dependence of the growth rate of specific crystal faces.

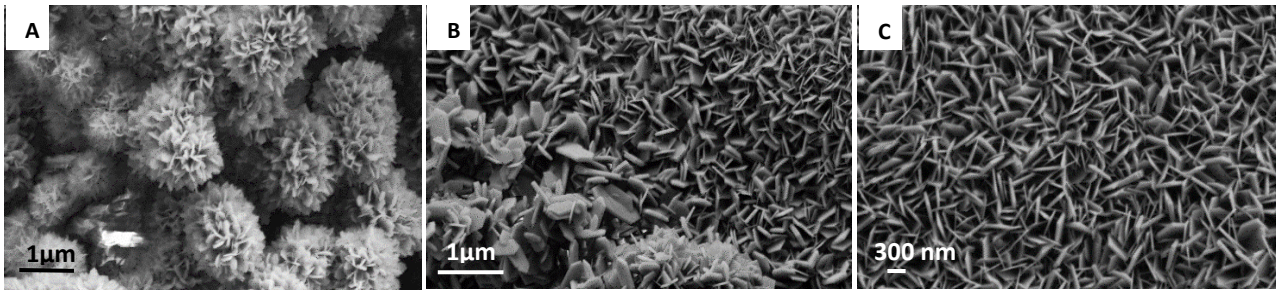

Figure 116 *From left to right, SEM micrograph of sample surfaces of hydrothermal treatment at 200°C, 3M [Urea] reaction time of 24h at pH 13, pH 12, and pH 11.*

From the obtained results, the variation in solution pH, by influencing the solubility of the reactants, appears to be a principal parameter for controlling the crystal growth rate. In Fig 116, SEM micrographs of sample surfaces treated hydrothermally while decreasing the pH from 13 to 11, at a temperature of 200°C, a reaction time of 24 hours, and [Urea] 3M, are presented.

Specifically, at pH <11, lamellae of approximately the same size are obtained, grown without a preferential orientation.

At pH ≥ 12, spherical crystallites composed of sheets arranged to form spheres in an uncontrolled manner are obtained; indeed, greater growth points are observed in certain non-preferential areas.

Without adding the urea additive, under alkaline conditions, boehmite initially grows along the [101] direction, followed by a transition to growth along the [010] direction. An extended reaction time can lead to the formation of thicker plate-like boehmite structures [196]. In Fig. 117 are reported the SEM micrograph of the sample surfaces after hydrothermal experiments before of the previously mentioned transition from [101] to [010] direction. With a reaction time of 6h we obtained lath-like crystals at both temperatures of 200°C and 160°C, with SEM micrographs respectively shown in A-B and C-D.

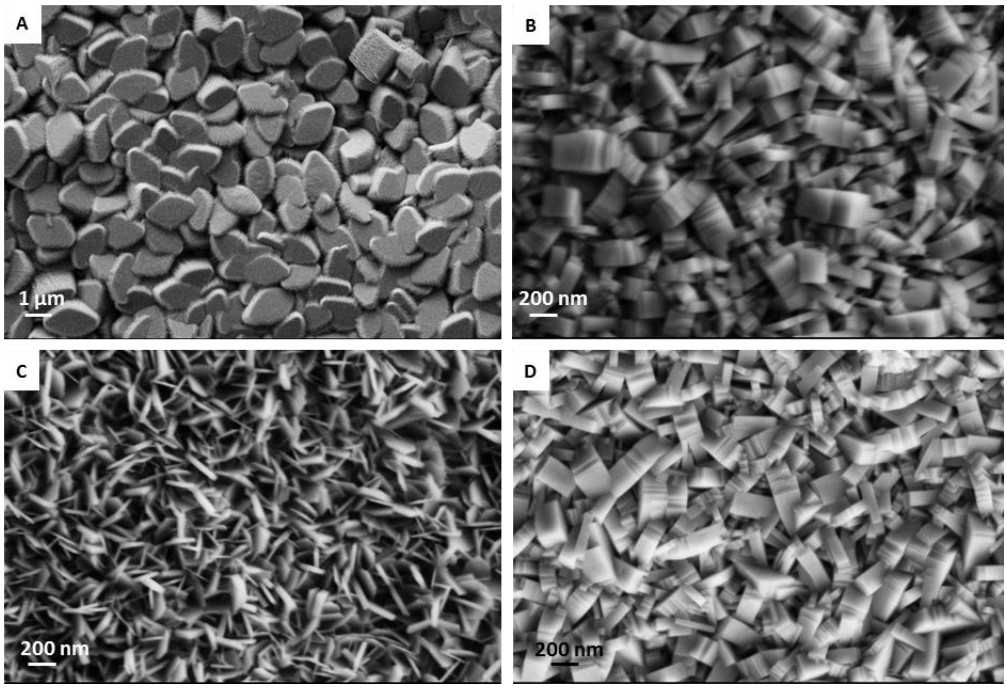

Figure 117 *SEM micrograph of sample surfaces of hydrothermal treatment with a reaction time 6 hours, pH 11, without urea additive, and a reaction temperature of 200°C (A-B), and 160°C (C-D).*

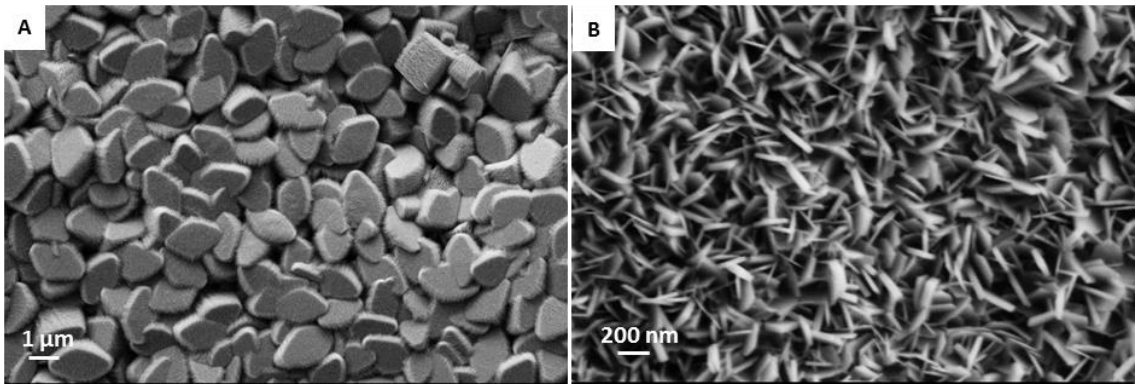

Figure 118*. SEM micrograph of sample surfaces of hydrothermal treatment at pH 11 Urea No 24h T 200°C (A) T 120°C (B).*

As clearly seen in figure 118 without the urea additive, regardless of the reaction temperature, increasing the reaction time led to such a transition in the crystal growth direction. The surface of the samples after 24 hours of treatment is characterized by hexagonal plate-like crystals that become larger and thicker as the reaction temperature increases in figure 118 A). From our experimental results, urea confirms its role as an alkaline buffer, helping to maintain the desired pH range for the formation of boehmite, other than acting as complexing agent that prevents the rapid precipitation of aluminum ions and allows for the controlled growth of plate-like boehmite crystals [197]. For this preliminary series of hydrodynamic resistance tests, three ceramic scaffolds with different morphologies in figure 119, but the same composition of aluminum oxide crystals were selected:

1) The scaffold obtained as a ceramic xerogel coating (A), as described in the sol-gel procedure of paragraph 2.1, and referred to as "sol-gel".
2) The scaffold obtained by hydrothermal synthesis at a temperature of 200°C with 3M [Urea] as an additive, a reaction time of 24 hours at pH 12 (B) and referred to as "pH12 Urea" with plate-like crystals approximately twice the size of the sol-gel sample.
3) The scaffold obtained by hydrothermal synthesis at a temperature of 200°C without the use of additives, a reaction time of 6 hours at pH 11 C) and referred to as "pH11 No Urea," characterized by lath-like crystals.

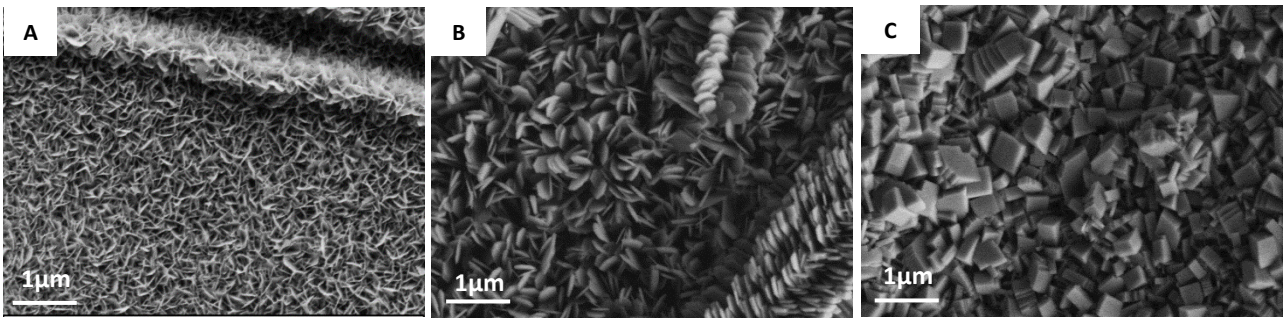

Figure 119 *SEM Micrographs of ceramic scaffolds selected for the hydrodynamic resistance tests: sol-gel and hydrothermal alumina coating.*

Table 40 *Static (WCA) and dynamic contact angle (CAH) of three different sample infused with Vaseline, standard deviation of data is also reported.*

SLIPS [scaffold + lubricant]	**WCA (°)**	**CAH (°)**	**CAH (°)**	**CAH (°)**
Sol-gel + Vaseline	104 ± 1	13	6	9
pH12 Urea + Vaseline	21 ± 3	Not Applicable*	Not Applicable*	Not Applicable*
pH11 No Urea + Vaseline	91 ± 4	Pinning	32	42

After the infusion with Vaseline oil, the characterization of the obtained SLIPS surfaces in terms of the sessile contact angle with deionized water (WCA Sessile) and contact angle hysteresis (CAH) is presented in Table 40.

Snapshots of the contact angles for the three SLIPS surfaces are provided in 118 “Sol-gel” + Vaseline (Fig. 120 A), “pH12 Urea” + Vaseline (Fig. 120 B), “pH11 No Urea” + Vaseline (Fig. 120 C).

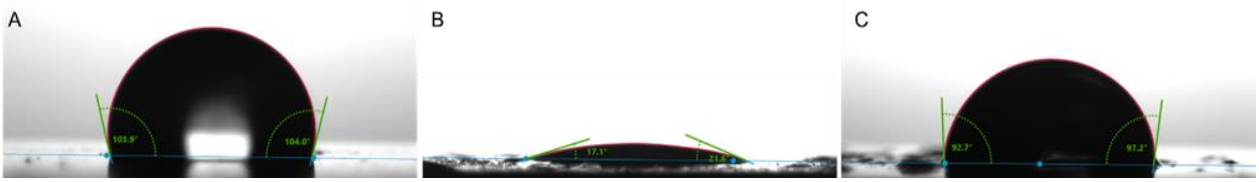

Figure 120 *Sessile contact angle of water of the SLIPS surfaces used as candidate for hydrodynamic resistance test: A) “Sol-gel” + Vaseline ,B) “pH12 Urea” + Vaseline, C) “pH11 No Urea” + Vaseline.*

The SLIPS created using the “sol-gel” alumina scaffold is characterized by greater hydrophobicity compared to other surfaces, with a contact angle hysteresis of 10° ± 2, indicating pronounced water mobility at the interface and, as a consequence, a limited adhesion force [198]. As for the “pH12 Urea” scaffold, compared to the “sol-gel” scaffold, it is presumed that the increased size of plate-like crystals, combined with phenomena of aggregation with preferential orientations, leads the surface to exhibit hydrophilic characteristics.

Consequently, the contact angle hysteresis could not be measured for this substrate. Lastly, the SLIPS with the “pH11 No Urea” scaffold exhibits a moderate hydrophobicity, contact angle hysteresis, and droplet pinning zones, as well as a pronounced wetting ridge, indicating a partial permeation of the oil into the scaffold's porosity (Fig 120)[2].

[2] Part of Chapter 11.2 is under submission in Crystal Growth Journal as Caruso M., Corozzi A., Ruffini A., Raimondo M., “ development of porous ceramic scaffolds for the fabrication of SLIPS coatings”

The disk rotors coated with Sol-gel, pH 12 Urea and pH11 no Urea are reported in Figure 121.

The torque trends for to the rotational speed for the smooth aluminum disc rotor used as a reference and the three coatings can be observed in Figure 121. All three coated surfaces have the same torque in the speed range up to 1500 rpm. After this value for the samples are more hydrophilic the torque increases as the samples are more hydrophilic than the reference. The vaseline infusion of the rheometer rotors of the differently coated specimens are shown in the graph in fig. 123. It is noted that the infusion coatings have the same trend as those that have not undergone the infusion process (fig 122), in fact, the torque increases when the rotation speed is greater than 1500 rpm. However, some interesting behaviors can be observed: in particular, the torque of the sample coated with alumina sol-gel infused with vaseline compared to its analog without, decreases, this result depends in fact as observed by the SEM images (fig 119), the coating blades are small about 30 nm, which allow to better retain the lubricant. On the contrary, this phenomenon is not observed for the coatings obtained with hydrothermal treatment. The torque obtained before and after the infusion is very similar, probably the porosity introduced with the coating is not suitable for have retention of the optimal lubricant.

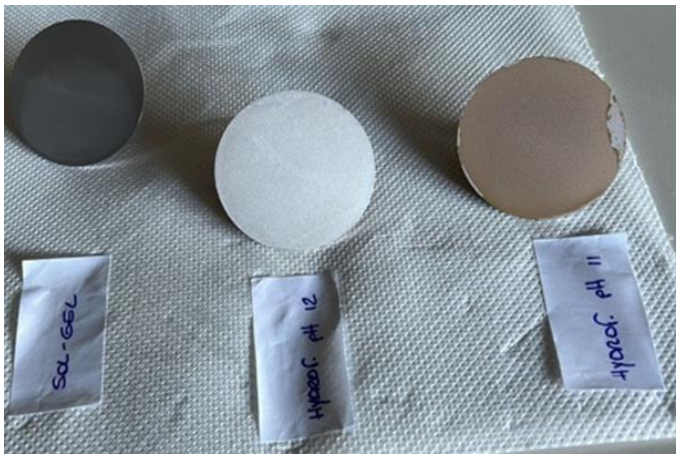

Figure 121 *Comparison of the hydrodynamic resistance results of the smooth aluminium disc used as reference and of the coated surfaces: "Sol-gel", "pH12 Urea", and "pH11 No Urea", before the liquid infusion.*

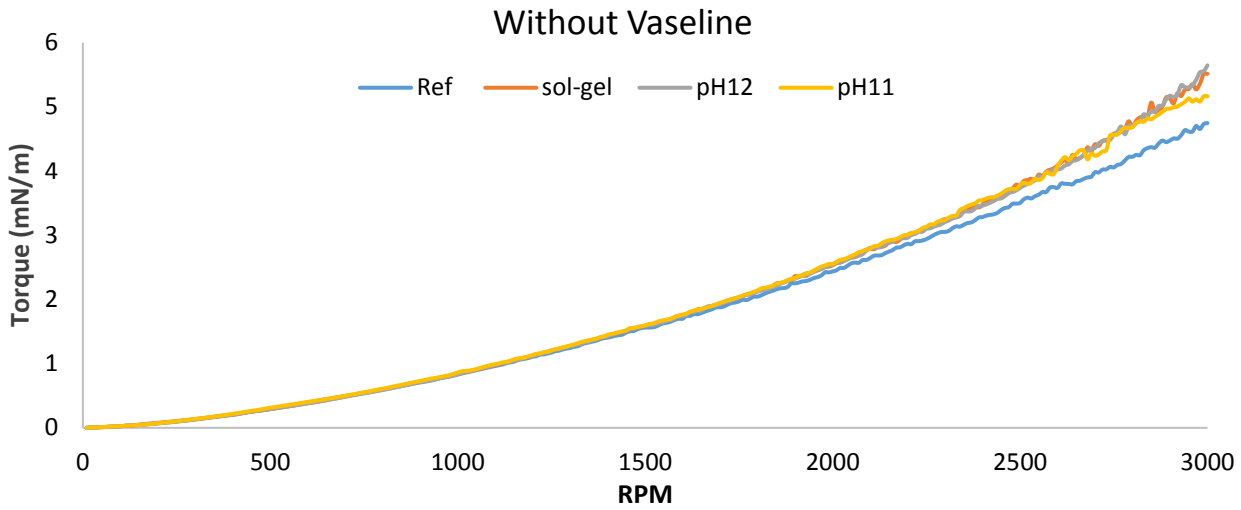

Figure 122 *Comparison of the hydrodynamic resistance results of the smooth aluminium disc used as reference "ref", and of the coated surfaces: "Sol-gel", "pH12 Urea", "pH11 No Urea", before the liquid infusion.*

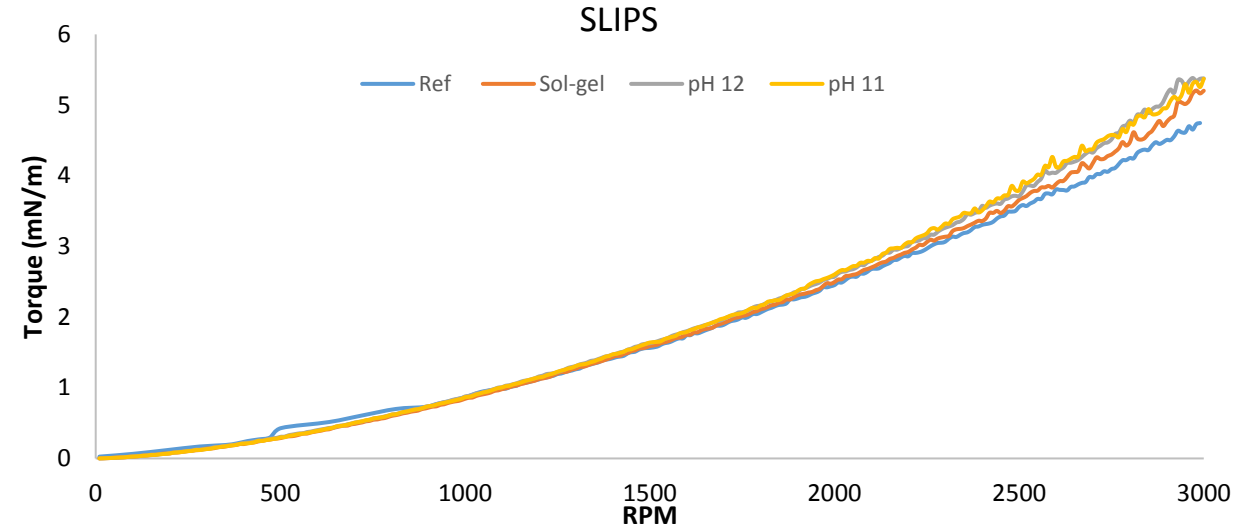

Figure 123 *Comparison of the hydrodynamic resistance results of the smooth aluminium disc, used as reference, "ref", and of the SLIPS obtained by infusion of the coated surfaces: "Sol-gel", "pH12 Urea", "pH11 No Urea".*

Since an initial investigation phase, the implantation of nanoroughness on rheometer discs has not led to optimal results in rheometer tests.

It is necessary to induce a micrometric roughness, such as large flat plates, on the surface (5-10 µm) and subsequently introduce a nanoroughness with hydrothermal or sol-gel method for the retention of lubricant.[3]

[3] Part of the chapter 11.2 is under submission in Coating and Surface Technology as Corozzi A., Caruso M, Lagazzo A., Innocenti G., Bottaro A., Raimondo M. " Stable and durable lubricant infused Slippery Surfaces for marine applications"

The results obtained suggest that the lubricant was not retained during the test and was partly lost. The release of Vaseline oil, used as a lubricant to decrease drag reduction, such as other types of oil, such as fluorinated, can cause a long-term marine pollution problem. In this regard, among the future goals of the research on coating that reduce wall friction will be to optimize the retention of the lubricant and the discovery of oils that do not cause environmental problems.

15. CONCLUSION

The control of surface properties, specifically, wettability, holds significant importance in various industrial applications. The ability of surface to repel water, but also, other liquids, involve, let's say derived properties, exploitable in sector such as aeronautic (prevention of icing adhesion), mechanical (slippery, corrosion component), construction (self-cleaning exterior paint), renewable solar energy (solar and wind turbines), textile (anti-soiling cloths) just to mention a few. Among the strategic and exploitable working environments marine and naval ones are looking a low wettable superhydrophobic surfaces as a solution to counteract more effectively way the heavy drawbacks promoted by fouling adhesion. In this framework, the Ph.D. research activities focused on the design and fabrication of superhydrophobic surfaces to be applied in underwater conditions, particularly antifouling and drag reduction purpose. In this field, it is expected that the use of properly designed low wettable coatings can enhance vehicle performance also in terms of durability with great positive impact on energy efficiency, reduction of fuel consumption together with a lower utilization of chemicals as cleaning formulations. From the experimental point of view, two different biomimetic design approaches were proposed: a) the achievement of hierarchically organized micro-and nano- texturing according to many natural examples (the most famous being that inspired by Lotus Leaf) and b) SLIPS (Slippery Liquid-Infused Porous Surfaces) technique inspired by Nepenthes Pitcher plant. In both cases, hybrid multilayer coatings were formulated involving the deposition of inorganic ceramic oxides and polymeric based layers. As far as the ceramic oxides, we selected:

- Silica nanoparticles, synthesized in our labs that have been functionalized with various silanes, including fluoroalkylsilane (FAS) and hexadecyltrimethoxysilane (HTS), to achieve superhydrophobicity with a single deposition step.
- Alumina boehmite hierarchically organized nanoflakes.

After hybridization with organic layers, SLIPS surfaces were obtained by infusion of lubricant oil, both fluorinated and alkyl based fluorine-free ones, on the underneath hybrid organic/inorganic scaffolds.

It is important to underline that properties of coatings such as morphology, chemistry of outer layers and surface energy, were taken into account as the most influencing design variables. The size of hydrodynamic diameter of Al_2O_3 and SiO_2 particles aiming to achieve the desired nanoroughness was finely controlled to reach superhydrophobicity. As far as the deposition techniques of the coatings formulations, the choice fell on those techniques, such as dipping and spraying, already available in industries devoted to the treatments of ship hulls. Fundamental parameters and deposition processing conditions were assessed according to the different nature of the substrate, which include alloy, metals and composites as representative materials adopted in the marine fields.

Each coating has been characterized by determining both static and dynamic wettability by optical tensiometry with a DSA30 Kruss instrument. Alumina based coatings with FAS and HTS as outer layers reach WCA > 170° and CAH< 10°, while SLIPS provide WCA of about 120° but CAH even lower than 5°. The silica based coating, functionalized with fluorine reaches WCA>150° and CAH< 15°, the best value owing to SiO_2 –HTS nanoparticles with WCA of about 85° and CAH< 7.

In addition, to assess the effectiveness of the adopted processing conditions, all coated surfaces underwent deep morphological SEM analyses, including thickness measurements and detection of defects. As described in section 8, two different inorganic layers morphologies have been dealt with respectively hierarchically organized flower like alumina and well-organized aggregation of spherical silica nanoparticles. Focusing on superhydrophobic and SLIPS coatings as solution for fouling control, and water repellency prevent microorganism's adhesion, making the surface resistant to their growth. When both Al_2O_3 coatings functionalized with FAS and SiO_2F layers, their surface energy falls down to very low values (just a few mN/m units) then significantly improving the anti-adhesion abilities against micro-organisms and cells. Moreover, in most case, SLIPS coatings revealed to be more effective enabling a much better control of the ratio between static and dynamic superhydrophobicity. As further discussed in paragraph 10.2 about the settlement results of "no droplet choice", the test in open sea emphasized the antifouling properties of the SLIPS with respect to the SHS solutions, particularly when property durability is analyzed over longer time exposure of materials in working conditions. Test performed at IAS-CNR in Genoa, clearly indicate that only SLIPS surfaces withstand somehow the severe conditions of sea immersion with a residual anti-adhesion attitude still present after 5 month of testing, avoiding the deposition of marine organisms on 100% of their surface.

On this last topic, the main concern of the coating solution discussed in this thesis, badly influencing the durability of antifouling performance was their low adhesion to the substrates, especially when dealing with composites. For this reason, a preliminary study was undertaken to obtain a primer that, grafting on the substrate through the formation of stable covalent bonds, allows for a greater of estate the superhydrophobic coating. The primer is composed of silica nanoparticles with amino function has been optimized, in particular with APTES (3-aminotriethoxysilane). The nanoparticles were loaded in epoxy resin and then deposited on the composite by dip coating. The study was carried out in order to obtain a homogenous primer where the particles completely cover substrate. Future prospects will be tested the antifouling activities of superhydrophobic coatings where there is the optimized primer and evaluated the performance of durability.

Overall, other antifouling performance, the wetting modification of substrates by coatings deposition has proven to be of fundamental relevance in terms of energy saving and efficiency of naval vehicles.

The reduction of the friction to wall is among the biggest challenges for the design of slippery surface also in terms of emission reduction. The achievement of reduction friction is quite complex combination of several factors. First of all the geometry, since it is necessary to introduce a microporosity of the same size of the slips length. Additionally, the choice of lubricant with the suitable viscosity is crucial to effective sliding mechanisms on the surface. To address these requirements a surface with grooves of 300 nm was designed on which the deposition of nanoroughness lamellae helps retain the lubricant, thereby enhancing durability. Hydrodynamic tests were conducted in the CEIMM cavitational tunnel made available by INM-CNR (Rome). The results of the subsection 14.1 highlight that for SLISP designed coatings, as the flow rate increases not only the hydrodynamic force decrease but also it stay constant when the speed increases.

Therefore, the use of Al_2O_3 flower-like based coating has demonstrated to be exploitable but keeping strict control of materials and processing parameters in order to obtain appropriate morphology. To streamline the whole process and enhance the potential scaling up, a research effort was undertaken to obtain a flower-like morphology in a single step through hydrothermal synthesis. The objective was to obtain the already structured nanoboehmite directly on aluminum substrate under hydrothermal conditions, with careful consideration of reaction parameters, which significantly influence the required hierarchically organized morphology.

SEM observation outline that when coatings are obtained by hydrothermal synthesis three different nanostructures (spherical, platelet, and lamellae) can be obtained at different pH; the crystal size of boehmite decrease with the decreasing of both processing temperature and reaction time. Friction reduction tests were conducted comparing the Al_2O_3 morphology obtained by sol-gel and hydrothermal methods. Some friction tests were preliminary conducted with a rheometer, whose rotor was functionalized, and torque measured as the rotation speed increased.

The first results indicated that no relevant differences are detectable, due to the absence of initial microporosity on the substrate.

In conclusion, the design of SHS and SLIPS type coatings, led to obtaining of antifouling properties, non-toxic for marine fauna. These coatings have also been shown to have friction reduction properties. The results showed in particular that SLIPS coatings are able to prevent vegetative adhesion and to maintain these properties over time. This model of surface (designed with a scaffold of alumina and infused with both fluorinated and non-fluorinated lubricants), has proven to have friction-reducing properties on the wall.

In particular, the design of fluorine-free superhydrophobic coatings is necessary for replacement of environmentally toxic biocidal paints. Moreover, the reduction of the synthesis and deposition steps of the various coatings allows it to be competitive and substitute in the global market of the antifouling paints.

ACKNOWLEDGMENT

First, I want to thank my research group at ISSMC-CNR. Thanks to Dr.ssa Mariarosa Raimondo for believing in me and supporting my growth as a scientist. Thanks for giving me the opportunity to complete this Ph.D. course. Thanks, to Guia for being close to me, for having taught me, so many things and for having been very patient. Thanks to Alessandro, for giving me scientific and moral support whenever there was a problem, also for accompanying me on many business trips. A special thanks to my colleagues who have been close to me, for having made friends and shared many experiences.

Thanks to the collaborators of the CNR of Rome, in particular E. Ciappi and B. Jacob, and the CNR of Genoa, V. Piazza, F. Garaventa and finally to Prof. A. Lagazzo of the Genoa University for supporting my research.

Very special thanks goes to my family. Especially my mother who in all these years has always supported my dreams and has always made sure to realizer them, being close to me in every moment of my life.

Thanks to Andrea, Antonella and my nephew who celebrated my every achievement. Thanks to Iacopo that despite not being always present in my like has helped make me happy in recent years.

A special thanks to my friend, my second family, for spending good times together, for giving me support and always being close.

Thanks you all, once again

16. REFERENCES

1. Song, M., Liu, Y., Cui, S., Liu, L. & Yang, M. Fabrication and icing property of superhydrophilic and superhydrophobic aluminum surfaces derived from anodizing aluminum foil in a sodium chloride aqueous solution. *Appl. Surf. Sci.* **283**, 19–24 (2013).
2. Dafforn, K. A., Lewis, J. A. & Johnston, E. L. Antifouling strategies: history and regulation, ecological impacts and mitigation. *Mar. Pollut. Bull.* **62**, 453–465 (2011).
3. Li, Z. & Guo, Z. Bioinspired surfaces with wettability for antifouling application. *Nanoscale* **11**, 22636–22663 (2019).
4. Bonanno, A., Raimondo, M. & Zapperi, S. Surface Nano-structured Coating for Improved Performance of Axial Piston Pumps. in *Factories of the Future* (eds. Tolio, T., Copani, G. & Terkaj, W.) 295–314 (Springer International Publishing, Cham, 2019). doi:10.1007/978-3-319-94358-9_14.
5. Ensikat, H. J., Ditsche-Kuru, P., Neinhuis, C. & Barthlott, W. Superhydrophobicity in perfection: the outstanding properties of the lotus leaf. *Beilstein J. Nanotechnol.* **2**, 152–161 (2011).
6. Bechert, D. W., Bruse, M. & Hage, W. Experiments with three-dimensional riblets as an idealized model of shark skin. *Exp. Fluids* **28**, 403–412 (2000).
7. Ball, P. Engineering Shark skin and other solutions. *Nature* **400**, 507–509 (1999).
8. Autumn, K. *et al.* Adhesive force of a single gecko foot-hair. *Nature* **405**, 681–685 (2000).
9. Bixler, G. D. & Bhushan, B. Fluid drag reduction and efficient self-cleaning with rice leaf and butterfly wing bioinspired surfaces. *Nanoscale* **5**, 7685–7710 (2013).
10. Wong, T.-S. *et al.* Bioinspired self-repairing slippery surfaces with pressure-stable omniphobicity. *Nature* **477**, 443–447 (2011).
11. Chaudhari, M., Ahirrao, R. & Bagul, S. Thin film Deposition Methods: A Critical Review. **9**, 5215–5232 (2021).
12. Abegunde, O. O. *et al.* Overview of thin film deposition techniques. *AIMS Mater. Sci.* **6**, 174–199 (2019).

13. XPS and contact angle study of N2 and O2 plasma-modified PTFE, PVDF and PVF surfaces - Vandencasteele - 2006 - Surface and Interface Analysis - Wiley Online Library. https://analyticalsciencejournals.onlinelibrary.wiley.com/doi/abs/10.1002/sia.2255.

14. Kaliyannan, G. V. *et al.* Investigation on sol-gel based coatings application in energy sector – A review. *Int. Conf. Adv. Mater. Res. - 2019* **45**, 1138–1143 (2021).

15. Caldarelli, A., Raimondo, M., Veronesi, F., Boveri, G. & Guarini, G. Sol–gel route for the building up of superhydrophobic nanostructured hybrid-coatings on copper surfaces. *Surf. Coat. Technol.* **276**, 408–415 (2015).

16. Faustini, M., Louis, B., Albouy, P. A., Kuemmel, M. & Grosso, D. Preparation of Sol−Gel Films by Dip-Coating in Extreme Conditions. *J. Phys. Chem. C* **114**, 7637–7645 (2010).

17. Chen, W. & McCarthy, T. J. Layer-by-Layer Deposition: A Tool for Polymer Surface Modification. *Macromolecules* **30**, 78–86 (1997).

18. Zhu, P., Zhu, L., Ge, F., Wang, G. & Zeng, Z. Robust and transparent superamphiphobic coating prepared via layer-by-layer spraying. *Surf. Coat. Technol.* **426**, 127793 (2021).

19. Rudra, J. S., Kelly, S. H. & Collier, J. H. 2.4 Self-Assembling Biomaterials☆. in *Comprehensive Biomaterials II* (ed. Ducheyne, P.) 67–89 (Elsevier, Oxford, 2017). doi:10.1016/B978-0-12-803581-8.10210-3.

20. Li, Y. & Ning, C. Latest research progress of marine microbiological corrosion and bio-fouling, and new approaches of marine anti-corrosion and anti-fouling. *Bioact. Mater.* **4**, 189–195 (2019).

21. Sarkar, P. K., Pawar, S. S., Rath, S. K. & Kandasubramanian, B. Anti-barnacle biofouling coatings for the protection of marine vessels: synthesis and progress. *Environ. Sci. Pollut. Res.* **29**, 26078–26112 (2022).

22. Tian, L., Yin, Y., Bing, W. & Jin, E. Antifouling Technology Trends in Marine Environmental Protection. *J. Bionic Eng.* **18**, 239–263 (2021).

23. Xie, Q. *et al.* Self-Stratifying Silicone Coating with Nonleaching Antifoulant for Marine Anti-Biofouling. *Adv. Mater. Interfaces* **6**, 1900535 (2019).

24. Miralles, L. *et al.* Barcodes of marine invertebrates from north Iberian ports: Native diversity and resistance to biological invasions. *Mar. Pollut. Bull.* **112**, 183–188 (2016).

25. Jain, A. & Bhosle, N. B. Biochemical composition of the marine conditioning film: implications for bacterial adhesion. *Biofouling* **25**, 13–19 (2009).

26. S, A. & S, J. Biotechnological investigation for the prevention of biofouling. I. Biological and biochemical principles for the prevention of biofouling. *Mar. Ecol. Prog. Ser.* **123**, 301–312 (1995).

27. G. Nurioglu, A., C. Esteves, A. C. & With, G. de. Non-toxic, non-biocide-release antifouling coatings based on molecular structure design for marine applications. *J. Mater. Chem. B* **3**, 6547–6570 (2015).

28. Callow, J. A. & Callow, M. E. Trends in the development of environmentally friendly fouling-resistant marine coatings. *Nat. Commun.* **2**, 244 (2011).

29. Laspidou, C. S. & Rittmann, B. E. A unified theory for extracellular polymeric substances, soluble microbial products, and active and inert biomass. *Water Res.* **36**, 2711–2720 (2002).

30. Maan, A. M. C., Hofman, A. H., de Vos, W. M. & Kamperman, M. Recent Developments and Practical Feasibility of Polymer-Based Antifouling Coatings. *Adv. Funct. Mater.* **30**, 2000936 (2020).

31. Amara, I., Miled, W., Slama, R. B. & Ladhari, N. Antifouling processes and toxicity effects of antifouling paints on marine environment. A review. *Environ. Toxicol. Pharmacol.* **57**, 115–130 (2018).

32. Ytreberg, E. *et al.* A novel XRF method to measure environmental release of copper and zinc from antifouling paints. *Environ. Pollut.* **225**, 490–496 (2017).

33. Yebra, D. M., Kiil, S. & Dam-Johansen, K. Antifouling technology—past, present and future steps towards efficient and environmentally friendly antifouling coatings. *Prog. Org. Coat.* **50**, 75–104 (2004).

34. Chambers, L. D., Stokes, K. R., Walsh, F. C. & Wood, R. J. K. Modern approaches to marine antifouling coatings. *Surf. Coat. Technol.* **201**, 3642–3652 (2006).

35. Han, X. *et al.* Special issue on advanced corrosion-resistance materials and emerging applications. The progress on antifouling organic coating: From biocide to biomimetic surface. *J. Mater. Sci. Technol.* **61**, 46 (2021).

36. Pei, X. & Ye, Q. Development of Marine Antifouling Coatings. in *Antifouling Surfaces and Materials: From Land to Marine Environment* (ed. Zhou, F.) 135–149 (Springer, Berlin, Heidelberg, 2015). doi:10.1007/978-3-662-45204-2_6.

37. Webster, D. C., Pieper, R. J. & Nasrullah, M. J. Zwitterionic/amphiphilic pentablock copolymers and coatings therefrom. (2014).

38. Ciriminna, R., Bright, F. V. & Pagliaro, M. Ecofriendly Antifouling Marine Coatings. *ACS Sustain. Chem. Eng.* **3**, 559–565 (2015).

39. Baier, P. R. The Law Clerks: Profile of an Institution. *Vanderbilt Law Rev.* **26**, 1125 (1973).

40. Salta, M. *et al.* Designing biomimetic antifouling surfaces. *Philos. Trans. R. Soc. Math. Phys. Eng. Sci.* **368**, 4729–4754 (2010).

41. Schumacher, J. F. *et al.* Species-specific engineered antifouling topographies: correlations between the settlement of algal zoospores and barnacle cyprids. *Biofouling* **23**, 307–317 (2007).

42. Leonardi, A. K. & Ober, C. K. Polymer-Based Marine Antifouling and Fouling Release Surfaces: Strategies for Synthesis and Modification. *Annu. Rev. Chem. Biomol. Eng.* **10**, 241–264 (2019).

43. Xiao, L. *et al.* Topographic cues guide the attachment of diatom cells and algal zoospores. *Biofouling* **34**, 86–97 (2018).

44. Gittens, J. E., Smith, T. J., Suleiman, R. & Akid, R. Current and emerging environmentally-friendly systems for fouling control in the marine environment. *Biotechnol. Adv.* **31**, 1738–1753 (2013).

45. Huang, W.-H. & Lin, C.-S. Robust superhydrophobic transparent coatings fabricated by a low-temperature sol–gel process. *Appl. Surf. Sci.* **305**, 702–709 (2014).

46. Ferrari, M. *et al.* Biofouling control by superhydrophobic surfaces in shallow euphotic seawater. *Colloids Surf. Physicochem. Eng. Asp.* **480**, 369–375 (2015).

47. Sun, K. *et al.* Anti-biofouling superhydrophobic surface fabricated by picosecond laser texturing of stainless steel. *Appl. Surf. Sci.* **436**, 263–267 (2018).

48. Golovin, K. B., Gose, J. W., Perlin, M., Ceccio, S. L. & Tuteja, A. Bioinspired surfaces for turbulent drag reduction. *Philos. Transact. A Math. Phys. Eng. Sci.* **374**, 20160189 (2016).

49. Boban, M. *et al.* Characterization of superhydrophobic surfaces for drag reduction in turbulent flow. *J. Fluid Mech.* **845**, 560–580 (2018).

50. Ralston, E. & Swain, G. Bioinspiration—the solution for biofouling control? *Bioinspir. Biomim.* **4**, 015007 (2009).

51. Carman, M. L. *et al.* Engineered antifouling microtopographies – correlating wettability with cell attachment. *Biofouling* **22**, 11–21 (2006).

52. Hellio, C. & Yebra, D. *Advances in Marine Antifouling Coatings and Technologies*. (2009). doi:10.1533/9781845696313.1.

53. Jang, M.-Y., Park, J.-W., Baek, S.-Y. & Kim, T.-W. Anisotropic Wetting Characteristics of Biomimetic Rice Leaf Surface with Asymmetric Asperities. *J. Nanosci. Nanotechnol.* **20**, 4331–4335 (2020).

54. Deo, D. *et al.* Biomimicking of phyto-based super-hydrophobic surfaces towards prospective applications: a review. *J. Mater. Sci.* **57**, (2022).

55. Schumacher, J. F. *et al.* Engineered nanoforce gradients for inhibition of settlement (attachment) of swimming algal spores. *Langmuir ACS J. Surf. Colloids* **24**, 4931–4937 (2008).

56. Li, X. *et al.* Lotus-Leaf-Inspired Flexible and Tunable Random Laser. *ACS Appl. Mater. Interfaces* **12**, 10050–10057 (2020).

57. Hou, D. *et al.* Biomimetic superhydrophobic membrane for membrane distillation with robust wetting and fouling resistance. *J. Membr. Sci.* **599**, (2020).

58. Reid, G. A. M. B. F. R. S. E. *et al.* Biomimetic Polymer Surfaces by High Resolution Molding of the Wings of Different Cicadas. *Materials* **14**, (2021).

59. Amini, S. *et al.* Preventing mussel adhesion using lubricant-infused materials. *Science* **357**, 668–673 (2017).

60. Wang, Y., Zhang, H., Liu, X. & Zhou, Z. Slippery liquid-infused substrates: a versatile preparation, unique anti-wetting and drag-reduction effect on water. *J. Mater. Chem. A* **4**, 2524–2529 (2016).

61. Solomon, B. R., Khalil, K. S. & Varanasi, K. K. Drag Reduction using Lubricant-Impregnated Surfaces in Viscous Laminar Flow. *Langmuir* **30**, 10970–10976 (2014).

62. Treatment agents for biofouling in internal pipework of recreational vessels A review of pipework configurations, biofouling risk, and operational considerations.

63. Arndt, E. *et al.* Factors that influence vessel biofouling and its prevention and management.

64. Sensors | Free Full-Text | Antifouling Strategies for Sensors Used in Water Monitoring: Review and Future Perspectives. https://www.mdpi.com/1424-8220/21/2/389.

65. Aldred, N. & Clare, A. S. Mini-review: Impact and dynamics of surface fouling by solitary and compound ascidians. *Biofouling* **30**, 259–270 (2014).

66. Granhag, L., Finlay, J., Jonsson, P., Callow, J. & Callow, M. Roughness-dependent Removal of Settled Spores of the Green Alga Ulva (syn. Enteromorpha) Exposed to Hydrodynamic Forces from a Water Jet. *Biofouling* **20**, 117–122 (2004).

67. Delgado, A., Briciu-Burghina, C. & Regan, F. Antifouling Strategies for Sensors Used in Water Monitoring: Review and Future Perspectives. *Sensors* **21**, (2021).

68. Paetzold, S. C. & Davidson, J. Viability of golden star tunicate fragments after high-pressure water treatment. *Aquaculture* **303**, 105–107 (2010).

69. Gauss, C. F. Principia Generalia Theoriae Figurae Fluidorum in Statu Aequilibrii. in *Werke: Fünfter Band* (ed. Gauss, C. F.) 29–77 (Springer Berlin Heidelberg, Berlin, Heidelberg, 1830). doi:10.1007/978-3-642-49319-5_3.

70. Celia, E., Darmanin, T., Taffin de Givenchy, E., Amigoni, S. & Guittard, F. Recent advances in designing superhydrophobic surfaces. *J. Colloid Interface Sci.* **402**, 1–18 (2013).

71. Wenzel, R. N. RESISTANCE OF SOLID SURFACES TO WETTING BY WATER. *Ind. Eng. Chem.* **28**, 988–994 (1936).

72. Cassie, A. B. D. & Baxter, S. Wettability of porous surfaces. *Trans. Faraday Soc.* **40**, 546–551 (1944).

73. Milne, A. J. B. & Amirfazli, A. The Cassie equation: How it is meant to be used. *Adv. Colloid Interface Sci.* **170**, 48–55 (2012).

74. S. Herminghaus. Roughness-induced non-wetting. *Europhys. Lett.* **52**, 165 (2000).

75. Gao, N. & Yan, Y. Modeling Superhydrophobic Contact Angles and Wetting Transition. *J. Bionic Eng.* **6**, 335–340 (2009).

76. Panchagnula, M. V. & Vedantam, S. Comment on How Wenzel and Cassie Were Wrong by Gao and McCarthy. *Langmuir* **23**, 13242–13242 (2007).

77. Brinker, C. J. & Scherer, G. W. Introduction. in *Sol-Gel Science* xvi–18 (Elsevier, 1990). doi:10.1016/B978-0-08-057103-4.50006-4.

78. Antireflective mesoporous silica coatings by optimization of water content in acid-catalyzed sol-gel method for application in glass covers of concentrated photovoltaic modules. *J. Colloid Interface Sci.* **534**, 370–380 (2019).

79. Novotná, P., Zita, J., Krýsa, J., Kalousek, V. & Rathouský, J. Two-component transparent TiO2/SiO2 and TiO2/PDMS films as efficient photocatalysts for environmental cleaning. *Appl. Catal. B Environ.* **79**, 179–185 (2008).

80. Brinker, C. J. & Scherer, G. W. Hydrolysis and Condensation I. in *Sol-Gel Science* 20–95 (Elsevier, 1990). doi:10.1016/B978-0-08-057103-4.50007-6.

81. Sohrabi, B., Mansouri, F. & Khalifan, S. Z. The study of glass superhydrophobicity by modified SiO2-hexadecyltrimethoxysilane (SiO2-m-HDTMS) nanoparticles and mixture of surfactants. *Prog. Org. Coat.* **131**, 73–81 (2019).

82. Zhu, Y., Chen, L., Zhang, C. & Guan, Z. Preparation of hydrophobic antireflective SiO2 coating with deposition of PDMS from water-based SiO2-PEG sol. *Appl. Surf. Sci.* **457**, 522–528 (2018).

83. Tadanaga, K., Katata, N. & Minami, T. Super-Water-Repellent Al2O3 Coating Films with High Transparency. *J. Am. Ceram. Soc.* **80**, 1040–1042 (1997).

84. Hu, B., Yao, M., Xiao, R., Chen, J. & Yao, X. Optical properties of amorphous Al2O3 thin films prepared by a sol–gel process. *Ceram. Int.* **40**, 14133–14139 (2014).

85. Xu, C. *et al.* Preparation and surface wettability of TiO2 nanorod films modified with triethoxyoctylsilane. *Thin Solid Films* **531**, 255–260 (2013).

86. Matin, A., Baig, U., Gondal, M. A., Akhtar, S. & Zubair, S. M. Superhydrophobic and superoleophilic surfaces prepared by spray-coating of facile synthesized Cerium(IV) oxide nanoparticles for efficient oil/water separation. *Appl. Surf. Sci.* **462**, 95–104 (2018).

87. John, S., Joseph, A., Jose, A. J. & Narayana, B. Enhancement of corrosion protection of mild steel by chitosan/ZnO nanoparticle composite membranes. *Prog. Org. Coat.* **84**, 28–34 (2015).

88. Si, Y., Dong, Z. & Jiang, L. Bioinspired Designs of Superhydrophobic and Superhydrophilic Materials. *ACS Cent. Sci.* **4**, 1102–1112 (2018).

89. Veronesi, F., Boveri, G., Mora, J., Corozzi, A. & Raimondo, M. Icephobic properties of anti-wetting coatings for aeronautical applications. *Surf. Coat. Technol.* **421**, 127363 (2021).

90. Sheen, Y.-C., Huang, Y.-C., Liao, C.-S., Chou, H.-Y. & Chang, F.-C. New approach to fabricate an extremely super-amphiphobic surface based on fluorinated silica nanoparticles. *J. Polym. Sci. Part B Polym. Phys.* **46**, 1984–1990 (2008).

91. Ruiz-Cañas, M. C., Corredor, L. M., Quintero, H. I., Manrique, E. & Romero Bohórquez, A. R. Morphological and Structural Properties of Amino-Functionalized Fumed Nanosilica and Its Comparison with Nanoparticles Obtained by Modified Stöber Method. *Molecules* **25**, (2020).

92. Tadanaga, K. & Minami, T. Precursor structure of chemically modified aluminum-tri-sec-butoxide in diethylene glycol and ethylene glycol monoethyl ether. *J. Ceram. Soc. Jpn.* **108**, 420–423 (2000).

93. Liu, H., Chen, J. & Ge, H. Chemical modification of ethylacetoacetate with ASB in aqueous medium. *J. Wuhan Univ. Technol.-Mater Sci Ed* **24**, 68–71 (2009).

94. Uchihashi, H., Tohge, N. & Minami, T. Preparation of amorphous Al2O3 thin films from stabilized Al-alkoxides by the sol-gel method. *Nippon Seramikkusu Kyokai Gakujutsu RonbunshiJournal Ceram. Soc. Jpn.* **97**, 396–399 (1989).

95. Tadanaga, K., Ito, S., Minami, T. & Tohge, N. Precursor structure and microstructure of Al2O3 xerogels prepared from aluminum-tri-sec-butoxide chemically modified with mono-, di-, tri-ethanolamines. *J. Non-Cryst. Solids* **201**, 231–236 (1996).

96. Fordham, S. & Freeth, F. A. On the calculation of surface tension from measurements of pendant drops. *Proc. R. Soc. Lond. Ser. Math. Phys. Sci.* **194**, 1–16 (1997).

97. Okubo, T. Surface Tension of Structured Colloidal Suspensions of Polystyrene and Silica Spheres at the Air-Water Interface. *J. Colloid Interface Sci.* **171**, 55–62 (1995).

98. Ravera, F., Santini, E., Loglio, G., Ferrari, M. & Liggieri, L. Effect of Nanoparticles on the Interfacial Properties of Liquid/Liquid and Liquid/Air Surface Layers. *J. Phys. Chem. B* **110**, 19543–19551 (2006).

99. Singh, T. K. & Jain, C. L. Preparation of dispersed silica by hydrolysis of tetraethyl orthosilicate.

100. Xiao, Xu, Niu, Zhu, & Kou. Effects of Surface Functional Groups on the Adhesion of SiO2 Nanospheres to Bio-Based Materials. *Nanomaterials* **9**, 1411 (2019).

101. Chen, S. *et al.* Sol–Gel Synthesis and Microstructure Analysis of Amino-Modified Hybrid Silica Nanoparticles from Aminopropyltriethoxysilane and Tetraethoxysilane. *J. Am. Ceram. Soc.* **92**, 2074–2082 (2009).

102. Xu, L., Wang, L., Shen, Y., Ding, Y. & Cai, Z. Preparation of hexadecyltrimethoxysilane-modified silica nanocomposite hydrosol and superhydrophobic cotton coating. *Fibers Polym.* **16**, 1082–1091 (2015).

103. Li, J., Wan, H., Ye, Y., Zhou, H. & Chen, J. One-step process to fabrication of transparent superhydrophobic SiO2 paper. *Appl. Surf. Sci.* **261**, 470–472 (2012).

104. Xu, B. & Zhang, Q. Preparation and Properties of Hydrophobically Modified Nano-SiO_2 with Hexadecyltrimethoxysilane. *ACS Omega* **6**, 9764–9770 (2021).

105. Zhang, Q., Liu, H., Zhao, S. & Dong, W. Hydrophobic and optical properties of silica antireflective coating prepared via sol-gel method. *Mater. Res. Express* **8**, 046403 (2021).

106. Landau, L. & Levich, B. Dragging of a Liquid by a Moving Plate. in *Dynamics of Curved Fronts* (ed. Pelcé, P.) 141–153 (Academic Press, San Diego, 1988). doi:10.1016/B978-0-08-092523-3.50016-2.

107. Grosso, D. How to exploit the full potential of the dip-coating process to better control film formation. *J. Mater. Chem.* **21**, 17033–17038 (2011).

108. Kavale, M. S. *et al.* Optically transparent, superhydrophobic methyltrimethoxysilane based silica coatings without silylating reagent. *Appl. Surf. Sci.* **258**, 158–162 (2011).

109. Mahadik, S. A., Kavale, M. S., Mukherjee, S. K. & Rao, A. V. Transparent Superhydrophobic silica coatings on glass by sol–gel method. *Appl. Surf. Sci.* **257**, 333–339 (2010).

110. Phani, A. R. & Santucci, S. Evaluation of structural and mechanical properties of aluminum oxide thin films deposited by a sol–gel process: Comparison of microwave to conventional anneal. *J. Non-Cryst. Solids* **352**, 4093–4100 (2006).

111. Kozuka, H. Stress evolution on gel-to-ceramic thin film conversion. *J. Sol-Gel Sci. Technol.* **40**, 287–297 (2006).

112. Kurisu, T. & Kozuka, H. Effects of Heating Rate on Stress Evolution in Alkoxide-Derived Silica Gel-Coating Films. *J. Am. Ceram. Soc.* **89**, 2453–2458 (2006).

113. Yuan, Y. & Lee, T. R. Contact Angle and Wetting Properties. in *Surface Science Techniques* (eds. Bracco, G. & Holst, B.) 3–34 (Springer Berlin Heidelberg, Berlin, Heidelberg, 2013). doi:10.1007/978-3-642-34243-1_1.

114. Chattoraj, D. K. & Birdi, K. S. Experimental Methods and Procedures. in *Adsorption and the Gibbs Surface Excess* (eds. Chattoraj, D. K. & Birdi, K. S.) 21–38 (Springer US, Boston, MA, 1984). doi:10.1007/978-1-4615-8333-2_2.

115. Bateni, A., Susnar, S. S., Amirfazli, A. & Neumann, A. W. A high-accuracy polynomial fitting approach to determine contact angles. *Colloids Surf. Physicochem. Eng. Asp.* **219**, 215–231 (2003).

116. Macdougall, G., Ockrent, C. & Kendall, J. P. Surface energy relations in liquid/solid systems I. The adhesion of liquids to solids and a new method of determining the surface tension of liquids. *Proc. R. Soc. Lond. Ser. Math. Phys. Sci.* **180**, 151–173 (1942).

117. Bonn, D., Eggers, J., Indekeu, J., Meunier, J. & Rolley, E. Wetting and spreading. *Rev. Mod. Phys.* **81**, 739–805 (2009).

118. Kwok, D. Y. & Neumann, A. W. Contact angle measurement and contact angle interpretation. *Adv. Colloid Interface Sci.* **81**, 167–249 (1999).

119. Owens, D. K. & Wendt, R. C. Estimation of the surface free energy of polymers. *J. Appl. Polym. Sci.* **13**, 1741–1747 (1969).

120. Kaelble, D. H. Dispersion-Polar Surface Tension Properties of Organic Solids. *J. Adhes. - J ADHES* **2**, 66–81 (2008).

121. Stetefeld, J., McKenna, S. A. & Patel, T. R. Dynamic light scattering: a practical guide and applications in biomedical sciences. *Biophys. Rev.* **8**, 409–427 (2016).

122. Shaw, R. Dynamic Light Scattering Training. *Malvern Instrum. Ltd* (2014).

123. Electrophoretic Light Scattering ELS | Measure Electrophoretic Mobility | Malvern Panalytical. https://www.malvernpanalytical.com/en/products/technology/light-scattering/electrophoretic-light-scattering.

124. McNeil-Watson, F. Electrophoretic Light Scattering. in *Encyclopedia of Biophysics* (ed. Roberts, G. C. K.) 648–654 (Springer, Berlin, Heidelberg, 2013). doi:10.1007/978-3-642-16712-6_288.

125. What is FTIR Spectroscopy? https://www.sigmaaldrich.com/IT/en/technical-documents/technical-article/analytical-chemistry/photometry-and-reflectometry/ftir-spectroscopy.

126. Settle, F. A. *Handbook of Instrumental Techniques for Analytical Chemistry*. (Prentice Hall PTR Upper Saddle River, NJ, Upper Saddle River, NJ, 1997).

127. Byrne, B., Beattie, J. W., Song, C. L. & Kazarian, S. G. Chapter 1 - ATR-FTIR spectroscopy and spectroscopic imaging of proteins. in *Vibrational Spectroscopy in Protein Research* (eds. Ozaki, Y., Baranska, M., Lednev, I. K. & Wood, B. R.) 1–22 (Academic Press, 2020). doi:10.1016/B978-0-12-818610-7.00001-3.

128. 11.3: IR-Active and IR-Inactive Vibrations. *Chemistry LibreTexts* https://chem.libretexts.org/Bookshelves/Organic_Chemistry/Map%3A_Organic_Chemistry_(Wade)_Complete_and_Semesters_I_and_II/Map%3A_Organic_Chemistry_(Wade)/11%3A_Infrared_Spectroscopy_and_Mass_Spectrometry/11.03%3A_IR-Active_and_IR-Inactive_Vibrations (2016).

129. Infrared Spectroscopy. *Chemistry LibreTexts* https://chem.libretexts.org/Bookshelves/Physical_and_Theoretical_Chemistry_Textbook_Maps/Supplemental_Modules_(Physical_and_Theoretical_Chemistry)/Spectroscopy/Vibrational_Spectroscopy/Infrared_Spectroscopy/Infrared_Spectroscopy (2013).

130. Campanella, B., Palleschi, V. & Legnaioli, S. Introduction to vibrational spectroscopies. *ChemTexts* **7**, (2021).

131. FTIR Sample Techniques: Attenuated Total Reflection (ATR) - IT. https://www.thermofisher.com/uk/en/home/industrial/spectroscopy-elemental-isotope-analysis/spectroscopy-elemental-isotope-analysis-learning-center/molecular-spectroscopy-information/ftir-information/ftir-sample-handling-techniques/ftir-sample-handling-techniques-attenuated-total-reflection-atr.html.

132. Ausili, A., Sánchez, M. & Gómez-Fernández, J. Attenuated total reflectance infrared spectroscopy: A powerful method for the simultaneous study of structure and spatial orientation of lipids and membrane proteins. *Biomed. Spectrosc. Imaging* **4**, 159–70 (2015).

133. Thermogravimetric Analysis - NETZSCH Thermal Academy. https://www.netzsch-thermal-academy.com/en/advanced-materials-testing/methods/thermogravimetric-analysis/.

134. Valdré, U. & ricerche, C. naxionale delle. Electron microscopy in material science. in (1971).

135. Goldstein, J. *et al. Scanning Electron Microscopy and X-Ray Microanalysis ISBN: 0306472929*. *Scanning Electron Microscopy and X-Ray Microanalysis.* vol. XIX (2003).

136. Inkson, B. J. 2 - Scanning electron microscopy (SEM) and transmission electron microscopy (TEM) for materials characterization. in *Materials Characterization Using Nondestructive Evaluation (NDE) Methods* (eds. Hübschen, G., Altpeter, I., Tschuncky, R. & Herrmann, H.-G.) 17–43 (Woodhead Publishing, 2016). doi:10.1016/B978-0-08-100040-3.00002-X.

137. Augsten. L. Reimer, Scanning Electron Microscopy — Physics of Image Formation and Microanalysis (Springer Series in Optical Sciences, Volume 45. Editiorial Board: J. M. Enoch, D. L. Macadam, A. L. Schawlow, K. Shimoda and T. Tamir). XVIII + 457 S., 247 Abb., 5 Tab. Berlin-Heidelberg-New York-Tokyo 1985. Springer Verlag. DM 112,00. ISBN: 3-540-13530-8. *J. Basic Microbiol.* **27**, 166–166 (1987).

138. Fluorescence Microscopy - Explanation and Labelled Images. *New York Microscope Company* https://microscopeinternational.com/fluorescence-microscopy/.

139. Fluorescent Microscopy. *Microscopy* https://serc.carleton.edu/microbelife/research_methods/microscopy/fluromic.html.

140. Paschotta, D. R. Optical profilometers. https://www.rp-photonics.com/optical_profilometers.html.

141. Profilometry - Nanoscience Instruments. https://www.nanoscience.com/techniques/profilometry/.

142. Pantano, C. G., Bojan, V. J. & Smay, G. AFM analysis of hot-end coatings on glass containers. *Glass Res.* **9**, 12–13 (1999).

143. Pompeo, G. *et al.* AFM characterization of solid-supported lipid multilayers prepared by spin-coating. *Biochim. Biophys. Acta BBA - Biomembr.* **1712**, 29–36 (2005).

144. Aliofkhazraei, M. & Ali, N. 7.09 - AFM Applications in Micro/Nanostructured Coatings. in *Comprehensive Materials Processing* (eds. Hashmi, S., Batalha, G. F., Van Tyne, C. J. & Yilbas, B.) 191–241 (Elsevier, Oxford, 2014). doi:10.1016/B978-0-08-096532-1.00712-3.

145. Raja, P. M. V. & Barron, A. R. Atomic Force Microscopy (AFM). https://chem.libretexts.org/@go/page/55928 (2022).

146. Malavasi, I. *et al.* Is a Knowledge of Surface Topology and Contact Angles Enough to Define the Drop Impact Outcome? *Langmuir* **32**, 6255–6262 (2016).

147. Feng, K., Rong, D., Ren, W. & Wen, X. Hierarchical flower-like <I>γ</I>-AlOOH and <I>γ</I>-Al₂O₃ microspheres: Synthesis and adsorption properties. *Mater. Express* **5**, 371–375 (2015).

148. Zhou, R.-S. & Snyder, R. L. Structures and transformation mechanisms of the η, γ and θ transition aluminas. *Acta Crystallogr. Sect. B* **47**, 617–630 (1991).

149. Minami, T., Katata, N. & Tadanaga, K. Preparation and characterization of super-water-repellent Al2O3 coating films with high transparency. in vol. 3136 168–175 (1997).

150. Bandi, P., K, V. M., Kausley, S. & Rai, B. Development of superhydrophobic and corrosion resistant coatings on mild steel—A greener approach. *Mater. Today Commun.* **25**, 101625 (2020).

151. Taskin, N. U. & Ordu, F. Effect of etching duration on roughness and wettability of different carbon steel substrates. *Mater. Chem. Phys.* **257**, 123746 (2021).

152. Feng, L., Zhang, H., Wang, Z. & Liu, Y. Superhydrophobic aluminum alloy surface: Fabrication, structure, and corrosion resistance. *Colloids Surf. Physicochem. Eng. Asp.* **441**, 319–325 (2014).

153. van Ooij, W. J. *et al.* Silane based chromate replacements for corrosion control, paint adhesion, and rubber bonding. *Surf. Eng.* **16**, 386–396 (2000).

154. Bernagozzi, I., Antonini, C., Villa, F. & Marengo, M. Fabricating superhydrophobic aluminum: An optimized one-step wet synthesis using fluoroalkyl silane. *Colloids Surf. Physicochem. Eng. Asp.* **441**, 919–924 (2014).

155. Choi, H.-J. *et al.* Fabrication of superhydrophobic and oleophobic Al surfaces by chemical etching and surface fluorination. *Thin Solid Films* **585**, 76–80 (2015).

156. Feng, C. *et al.* 3D Printing of Lotus Root-Like Biomimetic Materials for Cell Delivery and Tissue Regeneration. *Adv. Sci.* **4**, 1700401 (2017).

157. Contessi Negrini, N., Toffoletto, N., Farè, S. & Altomare, L. Plant Tissues as 3D Natural Scaffolds for Adipose, Bone and Tendon Tissue Regeneration. *Front. Bioeng. Biotechnol.* **8**, (2020).

158. Li, C. *et al.* In Vitro Bioactivity and Biocompatibility of Bio-Inspired Ti-6Al-4V Alloy Surfaces Modified by Combined Laser Micro/Nano Structuring. *Molecules* **25**, (2020).

159. Jaggessar, A., Shahali, H., Mathew, A. & Yarlagadda, P. K. D. V. Bio-mimicking nano and micro-structured surface fabrication for antibacterial properties in medical implants. *J. Nanobiotechnology* **15**, 64 (2017).

160. Glinel, K., Thebault, P., Humblot, V., Pradier, C.-M. & Jouenne, T. Antibacterial surfaces developed from bio-inspired approaches. *Acta Biomater.* **8**, 1670–84 (2012).

161. Arango-Santander, S. Bioinspired Topographic Surface Modification of Biomaterials. *Materials* **15**, 2383 (2022).

162. Schweikl, H. *et al.* Proliferation of osteoblasts and fibroblasts on model surfaces of varying roughness and surface chemistry. *J. Mater. Sci. Mater. Med.* **18**, 1895–1905 (2007).

163. Lauffenburger, D. A. & Horwitz, A. F. Cell migration: a physically integrated molecular process. *Cell* **84**, 359–369 (1996).

164. Ishizaki, T., Saito, N. & Takai, O. Correlation of Cell Adhesive Behaviors on Superhydrophobic, Superhydrophilic, and Micropatterned Superhydrophobic/Superhydrophilic Surfaces to Their Surface Chemistry. *Langmuir* **26**, 8147–8154 (2010).

165. Arnold, M. *et al.* Cell interactions with hierarchically structured nano-patterned adhesive surfaces. *Soft Matter* **5**, 72 (2009).

166. Ayala, R. *et al.* Engineering the cell–material interface for controlling stem cell adhesion, migration, and differentiation. *Biomaterials* **32**, 3700–3711 (2011).

167. Fan, H. & Guo, Z. Bioinspired surfaces with wettability: biomolecule adhesion behaviors. *Biomater. Sci.* **8**, 1502–1535 (2020).

168. Zhou, J., Fan, J.-B., Nie, Q. & Wang, S. Three-dimensional superhydrophobic copper 7,7,8,8-tetracyanoquinodimethane biointerfaces with the capability of high adhesion of osteoblasts. *Nanoscale* **8**, 3264–3267 (2016).

169. Raimondo, M., Blosi, M., Caldarelli, A., Guarini, G. & Veronesi, F. Wetting behavior and remarkable durability of amphiphobic aluminum alloys surfaces in a wide range of environmental conditions. *Chem. Eng. J.* **258**, 101–109 (2014).

170. Oliveira, S. M., Song, W., Alves, N. M. & Mano, J. F. Chemical modification of bioinspired superhydrophobic polystyrene surfaces to control cell attachment/proliferation. *Soft Matter* **7**, 8932 (2011).

171. Reddy, G. K. K., Rajitha, K. & Nancharaiah, Y. V. Antibiofouling potential of 1-alkyl-3-methylimidazolium ionic liquids: Studies against biofouling barnacle larvae. *J. Mol. Liq.* **302**, 112497 (2020).

172. Venkatnarayanan, S., Murthy, P. S., Kirubagaran, R. & Venugopalan, V. P. Effect of chlorination on barnacle larval stages: Implications for biofouling control and environmental impact. *Int. Biodeterior. Biodegrad.* **109**, 141–149 (2016).

173. Stafslien, S. J. *et al.* Comparison of laboratory and field testing performance evaluations of siloxane-polyurethane fouling-release marine coatings. *Biofouling* **32**, 949–968 (2016).

174. Faimali, M. *et al.* Swimming speed alteration of larvae of Balanus Amphitrite as a behavioural end-point for laboratory toxicological bioassays. *Mar. Biol.* **149**, 87–96 (2006).

175. Tsujii, K., Yamamoto, T., Onda, T. & Shibuichi, S. Super Oil-Repellent Surfaces. *Angew. Chem. Int. Ed. Engl.* **36**, 1011–1012 (1997).

176. Hensel, R., Neinhuis, C. & Werner, C. The springtail cuticle as a blueprint for omniphobic surfaces. *Chem. Soc. Rev.* **45**, 323–341 (2016).

177. Tuteja, A., Choi, W., Mabry, J. M., McKinley, G. H. & Cohen, R. E. Robust omniphobic surfaces. *Proc. Natl. Acad. Sci.* **105**, 18200–18205 (2008).

178. Zhao, X., Khandoker, Md. A. R. & Golovin, K. Non-Fluorinated Omniphobic Paper with Ultralow Contact Angle Hysteresis. *ACS Appl. Mater. Interfaces* **12**, 15748–15756 (2020).

179. Non-Fluorinated Omniphobic Paper with Ultralow Contact Angle Hysteresis | ACS Applied Materials & Interfaces. https://pubs.acs.org/doi/10.1021/acsami.0c01678.

180. Osmolovskaya, O. M., Osmolowsky, M. G., Petrov, M. P., Voitylov, A. V. & Vojtylov, V. V. Theoretical and experimental approaches to the electro-optical study of boehmite nanoparticles with given morphology. *Colloids Surf. Physicochem. Eng. Asp.* **586**, 124095 (2020).

181. Suchanek, W. L. & Riman, R. E. Hydrothermal Synthesis of Advanced Ceramic Powders. in 184–193 (2006). doi:10.4028/www.scientific.net/AST.45.184.

182. Zhang, X. *et al.* Size and Morphology Controlled Synthesis of Boehmite Nanoplates and Crystal Growth Mechanisms. *Cryst. Growth Des.* **18**, 3596–3606 (2018).

183. He, F. *et al.* Hydrothermal synthesis of boehmite nanorods from alumina sols. *Ceram. Int.* **48**, 18035–18047 (2022).

184. Shkolnikov, E. I., Shaitura, N. S. & Vlaskin, M. S. Structural properties of boehmite produced by hydrothermal oxidation of aluminum. *J. Supercrit. Fluids* **73**, 10–17 (2013).

185. Pardo, P. *et al.* Enhanced Lateral to Basal Surface Ratio in Boehmite Nanoparticles Achieved by Hydrothermal Aging. *Cryst. Growth Des.* **15**, 3532–3538 (2015).

186. Chen, X. Y., Huh, H. S. & Lee, S. W. Hydrothermal synthesis of boehmite (γ-AlOOH) nanoplatelets and nanowires: pH-controlled morphologies. *Nanotechnology* **18**, 285608 (2007).

187. Chen, X. Y. & Lee, S. W. pH-Dependent formation of boehmite (γ-AlOOH) nanorods and nanoflakes. *Chem. Phys. Lett.* **438**, 279–284 (2007).

188. Mishra, D., Anand, S., Panda, R. K. & Das, R. P. Hydrothermal preparation and characterization of boehmites. *Mater. Lett.* **42**, 38–45 (2000).

189. Willard, H. H. & Tang, N. K. A Study of the Precipitation of Aluminum Basic Sulfate by Urea. *Journal of the American Chemical Society* vol. 59 1190–1196 (1937).

190. Wu, X., Zhang, B. & Hu, Z. Large-scale and additive-free hydrothermal synthesis of lamellar morphology boehmite. *Powder Technol.* **239**, 155–161 (2013).

191. Ramanathan, S., Roy, S. K., Bhat, R., Upadhyaya, D. D. & Biswas, A. R. Alumina powders from aluminium nitrate-urea and aluminium sulphate-urea reactions — The role of the precursor anion and process conditions on characteristics. *Ceram. Int.* **23**, 45–53 (1997).

192. Vermeulen, A. C. & Geus, J. W. Hydrolysis-Precipitation Studies of Aluminum (111) Solutions I. Titration of Acidified Aluminum Nitrate Solutions. (1974).

193. Mazloumi, M. *et al.* Boehmite nanopetals self assembled to form rosette-like nanostructures. *Mater. Lett.* **62**, 4184–4186 (2008).

194. Hellgardt, K. & Chadwick, D. Effect of pH of Precipitation on the Preparation of High Surface Area Aluminas from Nitrate Solutions. *Ind. Eng. Chem. Res.* **37**, 405–411 (1998).

195. Feng, K., Rong, D., Ren, W. & Wen, X. Hierarchical flower-like <I>γ</I>-AlOOH and <I>γ</I>-Al₂O₃ microspheres: Synthesis and adsorption properties. *Mater. Express* **5**, 371–375 (2015).

196. Pardo, P., Montoya, N. & Alarcón, J. Tuning the size and shape of nano-boehmites by a free-additive hydrothermal method. *CrystEngComm* **17**, 2091–2100 (2015).

197. Wu, X., Zhang, B. & Hu, Z. Large-scale and additive-free hydrothermal synthesis of lamellar morphology boehmite. *Powder Technol.* **239**, 155–161 (2013).

198. Fumridge, C. G. L. Studies At Phase Interfaces I. the Sliding of Liquid Drops on Solid Surfaces and a Theory for Spray Retention. *J. Colloid Sci.* **17**, 309–324 (1962).

199. Féat, A., Federle, W., Kamperman, M. & Gucht, J. Coatings preventing insect adhesion: An overview. *Prog. Org. Coat.* **134**, (2019).

200. Sharma, V. & Bhardwaj, A. 29 - Scanning electron microscopy (SEM) in food quality evaluation. in *Evaluation Technologies for Food Quality* (eds. Zhong, J. & Wang, X.) 743–761 (Woodhead Publishing, 2019). doi:10.1016/B978-0-12-814217-2.00029-9.

17 List of Figures

1. INTRODUCTION

3. WETTING MODELS

4. SOL-GEL SYNTHESIS OF NANOPARTICLES

5. COATING DEPOSITION PROCESS

6. CONTACT ANGLE MEASUREMENT

7. CHARACTERIZATION

8. COATINGS COMPOSITION PROCESS

11. ENVIROMENT EFFECT OF SUPERHYDROPHOBIC COATINGS

12. SUPERHYDROPHOBIC COATINGS IN MARINE EXPOSURE

14. FRICTION REDUCTION ON SUPERHYDROPHOBIC COATINGS

18. List of tables

4. SOL-GEL SYNTHESIS NANOPARTICLE

8. COATINGS COMPOSITION PROCESS

11. ENVIROMENT EFFECT OF SUPERHYDROPHOBIC COATINGS

12. SUPERHYDROPHOBIC COATINGS IN MARINE EXPOSURE

13 DURABILITY OF SUPERHYDROPHOBIC PROPERTIES IN STATIC AND DYNAMIC SEA WATER CONDITIONS

14. FRICTION REDUCTION ON SUPERHYDROPHOBIC COATINGS